INFLUENCE OF ENVIRONMENTAL DISTURBANCES ON HYPERSONIC CROSSFLOW INSTABILITY ON THE HIFIRE-5 ELLIPTIC CONE

A Dissertation

by

IAN THOMAS NEEL

Submitted to the Office of Graduate and Professional Studies of
Texas A&M University
in partial fulfillment of the requirements for the degree of

DOCTOR OF PHILOSOPHY

Chair of Committee,	Rodney Bowersox
Committee Members,	Helen Reed
	David Staack
	Edward White
Head of Department,	Rodney Bowersox

May 2019

Major Subject: Aerospace Engineering

ABSTRACT

Crossflow instabilities on a 2:1 elliptic cone in hypersonic flow have been investigated in the M6QT and ACE wind tunnels at the Texas A&M National Aerothermochemistry and Hypersonics Laboratory. Experiments on a PEEK 38.1% scale model of the HIFiRE-5 flight test geometry were conducted to investigate the development of crossflow instabilities as well as to characterize the freestream and surface conditions responsible for their initial amplitudes. The freestream environment was varied not only by testing the model in both quiet and conventional tunnels but also by passively changing the fluctuation levels experienced in the conventional facility through systematic model placement. ACE freestream measurements, using a Kulite pressure transducer mounted in a pitot probe configuration and a hot-wire anemometer, indicated that fluctuation levels at the upstream model station were half those at the downstream stations. Fast-response PCB and Kulite surface mounted pressure transducers allowed examination of pressure fluctuation amplitudes and spectra within the model boundary layer. Kulite transducer data show evidence of traveling crossflow in the M6QT and a lower frequency disturbance in ACE. In all cases, frequencies near the expected second mode and secondary instability were observed in data from PCB transducers mounted in the shoulder region. IR thermography measurements examined surface heating levels, indicative of transition onset location and spatial extent. Surface heating magnitude and spatial extent were seen to vary with freestream disturbance level. Under quiet flow, narrow streaks of elevated heating, believed to be evidence of stationary crossflow vortices were observed. Under conventional noise levels, the heating front presents as more diffuse lobes of elevated heating covering a large portion of the cone shoulder and occurs at a much lower freestream Re. Moving the

model nosetip to a lower disturbance streamwise station results in more distinct streaks of elevated heating. Results are presented and discussed in context of computations and experimental data from the literature.

DEDICATION

To my family and friends for their continued love and support.

ACKNOWLEDGMENTS

I am extremely thankful for the opportunities afforded to me by my committee chair and advisor, Dr. Rodney Bowersox. His knowledge, optimism, and encouragement have been invaluable to me throughout my graduate career. Your mentorship and advice are greatly appreciated. I was and still am frequently in awe of your ability to manage the wide range of projects housed within the NAL and still find time to thoughtfully engage with, and make yourself available to, each student. Working at the NAL has been a great pleasure in no small part thanks to you.

My committee members, Drs. Helen Reed, David Staack, and Edward White, are thankfully acknowledged for their input and advice throughout this research effort. Their thoughtful questions, discussions, and suggestions provided great insight which strongly influenced and improved this research. The interactions I had with each of them and with their research groups were extremely helpful.

I thank Dr. Bill Saric for input into this research as well providing my undergraduate education in compressible flow theory and giving me the opportunity to participate in research at the TAMU Flight Research Laboratory. I would also like to acknowledge the other members of the FRL with whom I had the pleasure to work. I have never met a sharper, more hard-working group of people. You each provided an inspiration and encouraged me to continue my studies. The techniques and attention to detail I learned from you laid the foundation of my research.

I am thankful to Mr. Cecil Rhodes for providing his expertise to keep the facilities running smoothly. I can't count the number of times Mr. Cecil was able to quickly diagnose and solve a facility or instrumentation problem I'd been been fighting with for hours. I've taken to heart his

encouragement to take pride in my work and my workspace.

My gratitude is owed to the past and present members of the TAMU NAL for their knowledge, hard work, and patience. I was inspired early on by the willingness and dedication of the previous generation of students. I especially appreciate Alex Craig, Jerrod Hofferth, Chi Mai, Mike Semper, Nicole Sharp, and Nathan Tichenor who each in their own way involved me in work at the lab and passed on their hard-won expertise and knowledge. I have benefited greatly from working alongside the present NAL members. Many thoughtful questions and discussions contributed significantly to my understanding of my own research and the range of studies at the NAL. The dedication and excitement each student brings to their work at the lab makes it a special place. I wish you all continued success in your research and in life.

I cannot overstate my gratitude to Andrew Leidy for being my faithful colleague for the past 6 years. From manning the tunnel controls for nearly every single one of my runs, to theoretical and technical discussions all the way to helping me wrangle and direct summer undergrads, it has been a great pleasure to work with you. I sincerely appreciate that you were always willing to help me. Having someone at the lab I could trust with anything and rely on made working through the long nights and hot summers much more enjoyable.

The students and staff of the Oran W. Nicks Low Speed Wind Tunnel and the KlebanoffSaric Wind Tunnel provided tremendous support and are gratefully acknowledged. I've enjoyed working with each of you and the strong cooperation between our facilities. In addition, I will sorely miss sharing the excitement of running outside the lab to gawk at the latest visiting planes and rotorcraft. It was always a great reminder of life outside of the lab.

I am indebted to several machinists for providing support for these experiments. Zahir Udovicic is gratefully acknowledged for his work machining the models used in this work. His expertise and

craftsmanship were invaluable. I've learned a tremendous amount from you and greatly value the opportunity I had to work with you. I'd like to thank the machinists at the cyclotron machine shop for their excellent work finishing the improved model. I'd also be remiss not to thank William Seward for his excellent machine work on the SHR tunnel. I especially appreciate his willingness to sit down and work through drawings with me to identify improvements and cost savings. Thank you for always getting me into the queue and delivering parts ahead of schedule.

I am grateful to the members of the TAMU computational stability and transition lab. Discussions with the group, especially Travis Kocian, Alex Moyes, and Daniel Mullen greatly improved my knowledge and understating of boundary layer transition.

I'd like to thank Colleen Leatherman and Rebecca Marianno and the other staff of the AERO department for their administrative support and keeping things running smoothly.

Finally, I'd like to thank my family and my loving girlfriend Vianni. Your continued love and support made all of this possible.

CONTRIBUTORS AND FUNDING SOURCES

Contributors

This work was supported by a dissertation committee consisting of Professors Rodney Bowersox (advisor), Helen Reed, Edward White of the Department of Aerospace Engineering and Professor David Staack of the Department of Mechanical Engineering.

This work draws several comparisons to previous and concurrent experimental and computational data of outside groups. Contributions of outside sources are clearly noted and cited within the text.

All other work conducted for the dissertation was completed by the student independently.

Funding Sources

Graduate study was supported by Graduate Research Assistantships from Texas A&M University, AFOSR grant number FA9550-14-1-0365 (Program Manager Dr. Ivett Leyva), and the Vannevar Bush Faculty Fellowship Program grant number N00014-18-1-3020. Data analysis and writing of this dissertation occurred while the author participated in the Pathways internship program at NASA Langley Research Center within the Hypersonic Airbreathing Propulsion Branch.

The views and opinions expressed herein are solely those of the author and do not necessarily represent the views or opinions either expressed or implied of the AFOSR, NASA, or any part of the Government of the United States of America.

NOMENCLATURE

A_0	=	initial disturbance amplitude
A_{max}	=	maximum pressure fluctuation rms of the second mode normalized by the mean edge pressure
ACE	=	Actively Controlled Expansion Tunnel
$AEDC$	=	Arnold Engineering Development Center
$AFOSR$	=	Air Force Office of Scientific Research
$AFRL$	=	Air Force Research Laboratory
AoA	=	angle of attack
$BAM6QT$	=	Boeing/AFOSR Mach 6 Quiet Tunnel
C_R	=	receptivity coefficient
CFD	=	computational fluid dynamics
CTA	=	constant temperature anemometer/anemometry
DNS	=	direct numerical simulation
$DSTO$	=	Australian Defence Science and Technology Organisation
f	=	frequency
f_t	=	most unstable frequency at start of transition
$HIFiRE$	=	Hypersonic International Flight Research Experimentation
M	=	Mach number
MS/s	=	MegaSamples per second

$M6QT$	=	NASA Langley/Texas A&M 6 Quiet Tunnel
N	=	amplitude ratio
$PEEK$	=	polyether ether ketone
$PTFE$	=	polytetrafluoroethylene
q	=	heat flux
R_a	=	average roughness profile height
Re	=	unit Reynolds number
Re_N	=	nose-tip Reynolds number based on freestream quantities
RMS	=	root mean square
R_q	=	root mean square roughness
R_z	=	Average peak to valley roughness
St	=	Stanton number
T_0	=	stagnation temperature
T_w	=	wall temperature
T	=	temperature
t	=	time
TSP	=	temperature sensitive paint
VI	=	virtual instrument
x	=	global streamwise coordinate (measured from nosetip)
y	=	global spanwise coordinate (0 at model center axis)
α	=	thermal diffusivity

Γ_0	=	freestream noise amplification integrated over the second-mode bandwidth
γ_0	=	normalized pitot noise spectral amplitude
Δf	=	second mode bandwidth, 1/Hz
ζ	=	surface normal coordinate
κ	=	thermal conductivity
ρ	=	density

TABLE OF CONTENTS

Page

Page

LIST OF FIGURES

Page

Page

Page

Page

Page

LIST OF TABLES

TABLE Page

1. INTRODUCTION

1.1 Background & Motivation

Hypersonics, Heating, & Boundary Layer Transition

Boundary layer transition is a challenging problem which has received much attention due to its relevance to the aerodynamic design of both low- and high-speed vehicles. As a boundary layer transitions from laminar to turbulent flow, there is an increase in skin friction at the wall. At lower speeds, the main concern of this is increased drag, and prediction and control of this transition is sought-after to increase vehicle efficiency and performance. As vehicle speed increases to the high-speed regime into supersonic and hypersonic flight, surface heating becomes the order one problem associated with boundary layer transition. For hypersonic vehicles, adequate prediction and control of the processes leading to this transition are necessary for a wide range of vehicle design parameters. An example of this importance is found in the 1988 Report of the Defense Science Board Task Force on the National Aerospace Plane (NASP) (Shea, 1988). The NASP was planned to be a manned hypersonic X-plane meant to investigate hypersonic air breathing propulsion and hypersonic cruise. The report explains that estimates for the location of transition from laminar to turbulent flow ranged from 20% to 80% of the vehicle body length. The uncertainty in this location cascades throughout the design. Uncertainty in transition location translates into uncertainty in the heat transfer and skin friction on the vehicle surface. This in turn affects estimates of drag, engine performance, and structural heating. The report estimated that the total uncertainties in these quantities were enough to alter the vehicle weight by a factor of two or more! The NASP program fueled interest in the understanding and prediction of hypersonic boundary layer

transition and resulted in several advances. Lau (2008) provides an excellent history of the impact of boundary layer transition on high-speed vehicle design including NASP.

Decades of research, advancements, and computational progress have improved the boundary layer stability community's knowledge of boundary layer transition. Approaches based on understanding the underlying physics of the transition process have led to improvements in transition prediction and control (Fedorov, 2011). Background theory, foundational experiments, and modern computational tools are discussed in Chapter 2. As will be shown and discussed, there is still much to be learned. 3-D instabilities such as the crossflow instability, and their interactions with freestream disturbances, are not well understood. Design tools and CFD are frequently compared to and validated against data from conventional disturbance environment wind tunnel facilities which, at best, provide a worst case estimate for transition onset. However, in some cases the freestream disturbance levels in these facilities alter the transition process so profoundly that trends, especially in comparison between geometries, are opposite to those observed in quiet facilities and flight (Schneider, 2001). There is a distinct lack of quality experimental stability data at high speeds, partly owing to the lack of low disturbance environment wind tunnels. Few low disturbance facilities, capable of approximating atmospheric disturbances which real flight vehicles encounter, are available; fewer still are capable of super and hypersonic conditions, and none are capable of producing true flight enthalpies. To progress the state of boundary layer transition prediction and control, a better understanding of how crossflow instabilities develop and the role freestream disturbances play in their initiation and growth is needed.

1.2 Research Objectives & Contributions

The objective of the study described in this paper was to provide quantitative experimental characterization of the changes in the crossflow driven instability and transition process due to variations in the freestream environment at hypersonic speeds. This research was proposed to provide insight into the broad question: What is the role of freestream disturbances in the crossflow instability process? The testbed chosen for this study was the HIFiRE-5 2:1 elliptic cone geometry. The experiments were conducted in the Texas A&M Mach 6 Quiet (M6QT) and Actively Controlled Expansion (ACE) tunnels. This geometry and the unique characteristics of the ACE and M6QT facilities allow for direct comparison with the large body of recent HiFIRE-5 ground test and computational efforts. As detailed in Chapter 2, regions of this geometry are expected to be dominated by crossflow transition. This 2:1 elliptic cone geometry lends itself to the study of naturally developing crossflow instability due to the inherent pressure gradient between the windward major axis and the leeward minor axis. Previous experimental work in the Purdue University BAM6QT and in the TAMU ACE facility had shown large differences in transition onset location under noisy and quiet flow.

Experiments were performed to expose the model to differing freestream disturbance environments and observe changes in the characteristics of the transition process on the elliptic cone. The M6QT was operated in two modes: the high freestream disturbance "noisy" mode and low disturbance "quiet" mode. The freestream environment of the ACE tunnel was characterized using high-frequency pitot pressure measurements as well as hotwire anemometry. The observed variation of freestream fluctuation levels with streamwise position relative to the ACE nozzle exit plane was utilized to expose the model to different levels of freestream disturbances. Between the

two facilities, the model was exposed to centerline freestream pitot RMS fluctuation levels varying from M6QT quiet (<= 0.05%) to ACE (0.5%-1.5%) to M6QT "noisy" ($\sim$ 5%).

A major contribution of this work to the field is the large varied data set it provides for experimental comparison and CFD validation. Specific contributions of this work to the existing literature and study of this geometry include:

- duplication of key previous results using independent models and facilities
- detailed characterization of model roughness and as-built geometry
- characterization of disturbances present in the freestream and across the model shockwave
- tests at freestream disturbances in-between those of conventional and quiet facilities
- high-frequency pressure transducer measurements within the crossflow induced transition region as well as at and off centerline on the cone surface
- high-resolution sweeps of Reynolds number allowing observation of growth of disturbances from below the sensor noise floor to fully turbulent flow

1.3 Experimental Overview

The initial proposal and design of the experiments was conducted at the same time as a CFD effort focused on the same geometry within the TAMU Computational Stability & Transition Lab. In line with recommendations and previous lessons learned from the stability community (Reed *et al.*, 2018; Kocian *et al.*, 2018; Tufts *et al.*, 2018), the experiments reported herein were designed and performed to inform computational stability analysis. Discussions with the computational group guided the design of the model, selection of test instrumentation, and interpretation of experimental results.

Model design began with the selection of materials and design of the test article. IR thermography was selected to allow wide field imaging of the model surface to allow examination of spatial extent and development of expected transition fronts on the model surface. The model was constructed from PEEK to allow thermal imaging and was characterized by using surface profilometers to measure roughness and a micro-CT scanner for model as-built geometry. Global surface IR was used to examine the transition pattern under varied flow conditions. Initial IR runs were performed in the ACE facility. These runs were utilized to fine tune model alignment and to determine the optimal positioning of sensors on the model surface. Previous experimental literature and stability analyses were also used to determine selection and placement of high frequency PCB and Kulite pressure transducers. Data from these transducers give insight into the growth of fluctuations within the boundary layer and their spectral content. With the pressure transducers installed, a series of runs was conducted in ACE. These runs took advantage of previous experiments in the ACE facility which showed that freestream pitot fluctuations decreased in front of the tunnel nozzle exit. The nosetip of the model was positioned at 3 stations, 1 downstream and 2 upstream of the nozzle exit. This served to expose the model to different freestream disturbance levels. It is important to note that this is not a controlled reduction in the disturbance level but rather an exploitation of the natural disturbance field generated within the tunnel nozzle. The instrumented model was additionally run in the TAMU M6QT, exposing it a much lower freestream disturbance level. A follow-on series of experiments was conducted in the same manner in both facilities with an additional sensor configuration.

Prior to the experiments the model surface roughness was characterized using surface profilometry and its geometry examined using micro-CT scans. The freestream disturbance environment was examined at all stations with a pitot probe and hotwire campaign. At the downstream lo-

cation, an additional multiple overheat ratio hotwire campaign was conducted. Freestream and surface characterization provides useful data for comparison with experiments and flights and also as inputs for numerical simulations.

1.4 Dissertation Structure and Overview

The work presented herein represents several years of effort and is organized to provide a cohesive overview and details of the experiments performed and data obtained. The dissertation is structured as follows. The present chapter provides motivation, a project overview, and the research objectives of the present work. Chapter 2 provides further context for the study, detailing hypersonic boundary layer transition and a survey of previous work in hypersonic crossflow instability with particular emphasis on experiments on the 2:1 elliptic cone. Chapter 3 describes the facilities, infrastructure, and data acquisition systems that monitor and record tunnel conditions. Chapter 4 details the model geometry utilized, tunnel run procedures and sample conditions, and the experimental techniques utilized including a discussion of uncertainty. Results are reported and discussed from the ACE facility characterization (Chapter 5), instrumented model runs in ACE (Chapter 6) and in the M6QT (Chapter 7). Chapter 8 provides discussions of results including comparisons with previous results and computational studies. Chapter 9 presents a concluding summary and discussion as well as recommendations for future work. A series of appendices are included and give a more detailed explanation of select experimental techniques and data reduction, assessment of run repeatability, and sample data reduction codes.

2. BACKGROUND & RESEARCH ISSUES

2.1 Laminar-Turbulent Boundary Layer Transition

Boundary layer transition has received much attention as a significant design issue for all flight regimes and as such several extensive reviews of transition are available in the literature. Much of the focus of past work has been on incompressible flows, with compressible flows receiving increasing attention in the past few decades with the resurgence of interest in hypersonic vehicle systems. These reviews demonstrate that boundary layer transition is a very complicated process which can evolve along several different pathways depending on freestream conditions and parameters such as freestream disturbances, vehicle geometry, and vehicle surface roughness. Many of these pathways have received extensive study for low-speed cases with prediction techniques, CFD, and experimental campaigns achieving consistent results (Fedorov, 2011). The instabilities receiving most attention are Tollmien−Schlichting waves, Görtler vortices, and crossflow instabilities. Reviews of special relevance to the work detailed in this dissertation are Reed *et al.* (1996), Bippes (1999), Saric *et al.* (2002), Saric *et al.* (2003), and Saric *et al.* (1998) which focus on Linear stability theory, 3-D boundary layers, receptivity, and the crossflow instability at low-speeds, as well as Fedorov (2011), and Mack (1984) which focus on high-speed compressible stability theory, experiment, and computation.

High-speed flows are complicated by the presence of a mechanism that begins to dominate for Mach > 4. The Mack (or acoustic) mode is a uniquely high-speed mechanism physically expressed as an acoustic wave trapped within the boundary layer evolving as it propagates downstream, eventually causing breakdown to turbulence (Mack, 1984). Mack (1984) is a foundational reference and

report of boundary layer stability theory including compressible boundary layer theory. Part two of Mack's report presents a review and analysis of compressible linear stability theory formulation and discussion of bulk trends with wall temperature as well as viscous effects. Especially relevant to high speed flight is the observation that for all insulated flat plate boundary layers, a generalized inflection point where $D(\rho DU) = 0$ (D = $\frac{d}{dy}$ and y is the wall normal direction) within the boundary layer is present and is unstable to inviscid waves. First mode waves are dominant for Mach < 4 and stabilized by wall cooling. Increased wall cooling eventually results in the removal of the generalized inflection point. Second mode instability, however, is not dependent on the generalized inflection point and is in fact found to be destabilized with increased wall cooling. The second mode instability is the dominant mechanism observed on hypersonic 2-D geometries such as flat plates and slender circular cones at 0° AoA. Transition location on these geometries has been observed to be highly receptive to freestream noise with varying transition locations in ground test and flight (Schneider, 2001).

2.2 Crossflow Instability

For 3-D bodies, pressure gradients and swept geometry give rise to the crossflow instability. This instability develops owing to a velocity component induced normal to the local inviscid streamline direction by a pressure gradient on the vehicle surface. Near the edge of the boundary layer, this crossflow velocity is zero as the momentum and pressure gradient are balanced. As momentum decreases within the boundary layer, the crossflow component grows as the momentum and pressure gradient are no longer balanced. The no slip condition at the wall means that the crossflow component of velocity is again zero at the wall, indicating an unstable inflection point is present in the resulting combined velocity profile. For a compressible flow, a typical mass

flux profile is shown in Fig. 2.1 with the generalized inflection point of the crossflow component highlighted.

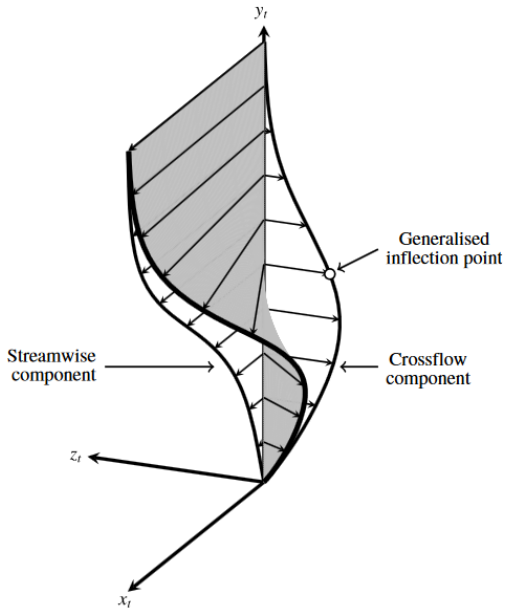

Figure 2.1: Typical crossflow mass flux profile, streamwise ρU and crossflow ρW. Reprinted from Craig & Saric (2016)

This generalized inflection point is a source of inviscid instability (Mack, 1984; Saric *et al.*, 2003). Stronger pressure gradients create stronger crossflow velocities, amplifying this instability.

The crossflow instability can manifest on a body as both traveling and stationary disturbances. Although linear stability theory predicts traveling crossflow wavelengths to be more unstable, stationary waves have been experimentally observed to lead to transition for low freestream disturbance environments at low speeds (Deyhle & Bippes, 1996; Saric *et al.*, 2003). Much research has focused on the crossflow instability isolated on a swept plate or airfoil configuration at low speeds. To date, it is these studies which give the community much of its insight into the onset and development of these instabilities. As explained by Saric *et al.* (2003), stationary crossflow v' and w' velocity disturbances are quite small and develop linearly. These small disturbances however

convect O(1) momentum into the boundary layer and rapidly produce strong u' distortion in the mean flow profile. This leads to the early development of nonlinear effects. These nonlinear effects are one reason transition prediction methods such as the e^N method have had limited success in predicting transition onset in cases of 3-D crossflow dominated boundary layers (Reed *et al.*, 1997). Waves present as an alternating pattern of accelerated and decelerated profiles. These stationary waves are seen to saturate at 10% - 30% of the streamwise U velocity amplitude. At some point after nonlinear saturation the waves are observed to rapidly undergo transition to turbulence. Breakdown of the saturated vortices is caused by the development and breakdown of secondary instabilities within the waves. Type-I and type-II secondary instability modes are caused by spanwise and wall normal gradients respectively. Type-I modes are seen to be lower in frequency and have higher growth rates. Type-II modes typically occur at higher frequencies. The development of these higher frequency secondary instabilities is an area of much interest in our understanding and modeling of crossflow dominated boundary layers. White & Saric (2005) performed a careful series of experiments to examine the growth and distribution of the secondary instabilities on a swept wing under quiet flow at low speeds. In each experiment, transition was observed within a few percentage chord of the onset of secondary instabilities and the authors conclude that it always appears to be the case that breakdown requires secondary instability growth.

As with other instabilities, crossflow is sensitive to influence from the coupling of external and surface disturbances through the process of receptivity. Receptivity is the process by which such disturbances couple to produce the initial disturbance amplitudes within the boundary layer which then grow and eventually break down to turbulence. Reed & Saric (2015) provides historical review of the concept of receptivity as well as a summary of modern progress in receptivity understanding for subsonic/transonic flight regimes. As noted before, traveling crossflow is predicted

to have higher growth rates than its stationary counterpart but is not observed to be the dominant mechanism in flows with a low disturbance environment. Deyhle & Bippes (1996) present a series of crossflow experiments performed in a range of wind tunnels with varying freestream disturbance environments. They found that crossflow transition was dominated by traveling waves only for turbulence intensities above 0.20%. For lower turbulence levels, stationary waves dominated and were tied to roughness on the model surface. Radeztsky *et al.* (1999) found that transition was insensitive to acoustic sound, even at amplitudes greater than 100 dB. Thus, the variations observed by Deyhle & Bippes (1996) were due primarily to variations in the vortical components of the freestream fluctuations and not to the acoustic mode (Saric *et al.*, 2003).

2.3 Crossflow Instability in High-Speed Flows

Hypersonic crossflow and transition are considerably less understood than instabilities associated with first and second modes. Relatively few experiments have been conducted to examine crossflow instabilities at hypersonic speeds. Experimental efforts have largely focused on straight cones at angle of attack and elliptic cones.

Recently published results by Craig & Saric (2016) provide insight into the crossflow instability on a yawed cone in the low-disturbance Mach 6 Quiet tunnel at Texas A&M University (TAMU). Utilizing a model-fixed traverse, hotwire boundary layer measurements were made across several runs, allowing for the study of both stationary and traveling crossflow waves. Up to saturation, the growth and development of these instabilities were in agreement with low-speed theory and experiments. One notable difference observed when compared to White & Saric (2005) is that secondary instabilities of the stationary crossflow vortices were not observed to grow rapidly and lead to breakdown immediately after developing. Edelman & Schneider (2018) present work investi-

gating secondary instabilities on a yawed circular cone under quiet flow in the Purdue BAM6QT. They had success using surface mounted, high frequency, PCB piezoelectric pressure transducers to measure the secondary instability on a yawed circular cone. In conjunction with temperature sensitive paint (TSP) measurements to compute the model surface heat flux, pressure data was utilized to examine the spatial extent and development of a presumed secondary instability. Two instabilities were observed within a narrow azimuthal distance. A higher frequency instability was observed in sensors located directly underneath streaks of elevated heating observed in TSP images. Low frequency instabilities grew in between the observed streaks. DNS computations Dinzl & Candler (2017) show, for a similar flow, that increased surface heating is found in the trough between vortices and decreased heating is found at the upwelling of the vortex. This observation, paired with observations in low-speed and high-speed experiments and CFD analysis of the position of secondary instabilities, indicates that the measurements of Edelman & Schneider (2018) are likely Type-I secondary instabilities.

In conjunction with these experiments, numerous computational efforts have provided insight into the crossflow instability for high speeds. The computational stability group at TAMU has utilized a toolkit which uses linear stability theory (LST), linear and nonlinear parabolized stability equations (LPSE, NPSE), and LST based on 2-D PDEs, called spatial BiGlobal (SBG) theory. LST and NPSE methods form the EPIC code which was developed in house at TAMU and is detailed in Oliviero *et al.* (2015). EPIC can be utilized for the initial linear growth of instabilities including crossflow as assumptions of two homogeneous spatial directions and small disturbance amplitudes made for LST hold in this region. NPSE is able to account for and model the large amplitudes and non-linearities of disturbances. SBG analysis allows for the analysis of the non-linearly distorted modified basic state created by the stationary vortices. Moyes *et al.* (2017) apply this toolkit to a

hypersonic yawed circular cone. Their findings show qualitative and quantitative agreement with Craig & Saric (2016) and provide insight into the results of another experiment performed in the Purdue BAM6QT. Similarity between secondary instabilities of incompressible and hypersonic stationary crossflow are noted.

2.4 Elliptic Cones and HIFiRE-5 Research

Several modern experiments have focused in on the elliptic cone as a geometry of interest. A computational study by Kimmel *et al.* (1997) in the mid 1990's identified the elliptic cone as a geometry ripe for study. Its shape naturally produces a favorable pressure gradient and amplifies the crossflow instability with linear stability N-factors reaching a maximum near the shoulder of the cone. Along the centerline, highly inflected profiles warranting further study were identified. Poggie *et al.* (2000) conducted experiments in AEDC Tunnel B at M=8 with hotfilm probes which revealed both stationary and traveling disturbances at frequencies in line with predictions from LST and computations.

This work expanded into part of the **H**ypersonic **I**nternational **Fl**i**g**ht **R**esearch **E**xperimentation (HIFiRE) program, a joint program between the AFOSR and the Australian DTSO. This program, described in Bowcutt *et al.* (2012), was a series of flight tests aimed at examining several areas of interest to hypersonic flight. The HIFiRE-5 flight model was a 2:1 elliptic cone designed to examine natural transition caused by the crossflow instability. The cone has a 7-degree minor axis half angle with blunt nosetip defined by a 2.5 mm radius arc which maintained an elliptic cross section to its tip. This geometry was mounted to a spin-stabilized, 2-stage, sounding rocket intended to boost the payload to Mach 7. The test article was first launched in April 2012 but the second stage of the rocket failed to ignite. This resulted in subsonic flight with preliminary results

reported by Kimmel *et al.* (2013). A relaunch in May 2016 was successful at obtaining the desired hypersonic flight velocity and has been reported by Kimmel *et al.* (2018) and companion reports.

Several ground based studies of the 2:1 elliptic cone geometry at Mach 6 have been conducted in support of these flight tests (Michael Holden and Timothy Wadhams and Matthew MacLean and Erik Mundy, 2009; Berger *et al.*, 2009; Juliano & Schneider, 2010; Borg *et al.*, 2012, 2013; Borg & Kimmel, 2016; Juliano *et al.*, 2016), and several CFD analyses have been performed (Choudhari *et al.*, 2009; Li *et al.*, 2012; Moyes *et al.*, 2017; Paredes *et al.*, 2016; Lakebrink *et al.*, 2017).

Choudhari *et al.* (2009) presents the initial CFD analysis performed on this geometry in support of the HiFIRE-5 program. Included are full scale and wind tunnel scale analyses for flight and the Purdue BAM6QT. The LST and PSE based analysis predicts moderate N-factors near the cone shoulder for both traveling and stationary crossflow vortices. Spatial maps of these N-factor calculations are reproduced here from Choudhari *et al.* (2009) in Fig. 2.3. The pressure gradient from the model attachment line drives flow towards the centerline resulting in an mushroom shaped upwelling along the model centerline and streamline curvature over large portions of the cone shoulder. This is illustrated by the CFD result examples reproduced in Fig. 2.2 which shows surface limiting surface streamlines and contours of local Mach number as well as density contours at different streamwise stations along the cone. In the model centerline region two instabilities have been observed in computational stability studies. The dominant instability in the stability analysis of Paredes *et al.* (2016) on the full scale HIFiRE-5 vehicle was a shear-layer instability in the 3-D structure of the centerline upwelling. Oblique second mode instabilities were also present.

The ground based campaigns of Juliano *et al.* (2015) and Borg & Kimmel (2016) have examined a 38.1% scale model of the HF-5 geometry. Juliano *et al.* (2015) performed a series of experiments using temperature sensitive paint to examine transition on the model surface. His

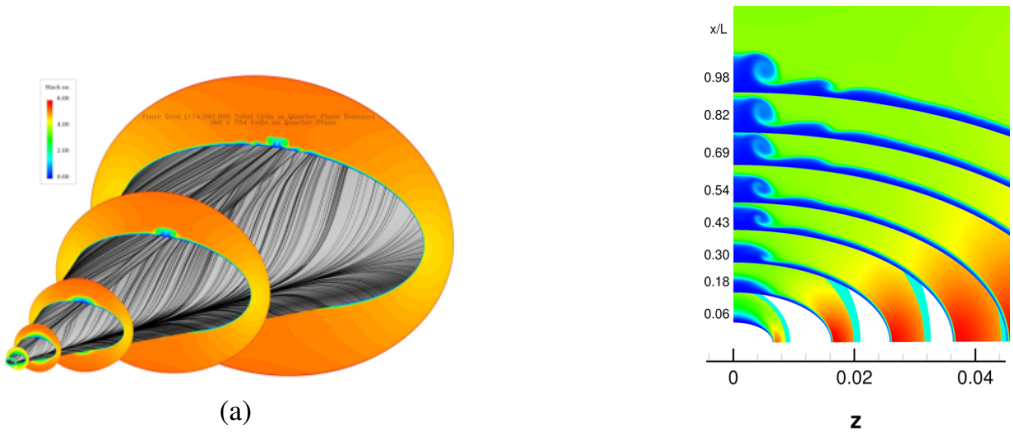

(a) (b)

Figure 2.2: Example CFD results highlighting 2:1 elliptic cone flow features. (a) Limiting surface streamlines on a 2:1 geometry with slices colored by local Mach number (Reprinted from Li *et al.* (2012)). (b) Contours of density for slices parallel to cone base (Reprinted from Kocian *et al.* (2016)).

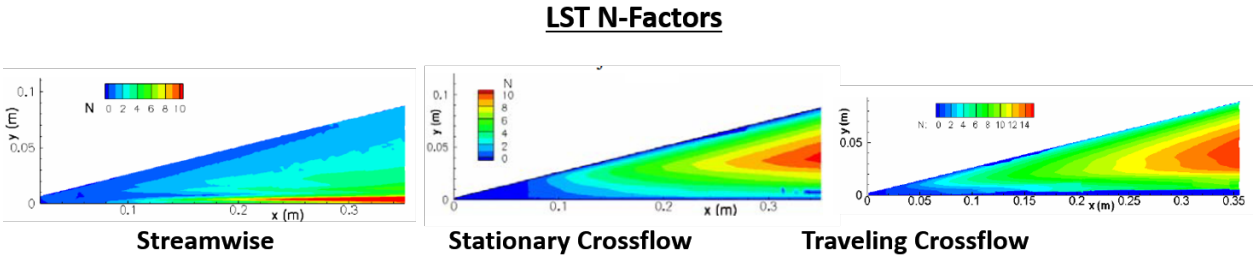

Figure 2.3: LST N-factors of instabilities on the 38.1% HIFiRE-5 geometry (Reprinted from Choudhari *et al.* (2009)).

experiments showed good agreement under quiet flow with the LST and PSE calculations of Li *et al.* (2012) and Choudhari *et al.* (2009). Juliano analyzed the model centerline transition location and boundary layer frequency content utilizing temperature sensitive paint and surface mounted pressure transducers.

Borg and colleagues have run a series of campaigns focusing on various elements of the transition process on this geometry with an eye to supporting the full scale design and flight test. Borg has focused on the model attachment line and its sensitivity to roughness, the effect of freestream disturbances, stationary crossflow vortices, traveling crossflow waves, and angle of attack effects

(Borg *et al.*, 2011, 2012, 2013, 2015*a*; Borg & Kimmel, 2016). Borg et al.'s studies have seen evidence of dominant stationary crossflow under quiet flow with the accompanying presence of traveling crossflow waves (Borg *et al.*, 2015*b*). These tests utilized arrays of surface mounted Kulite pressure transducers to measure pressure fluctuations within the transitional boundary layer. Spectra from the Kulites revealed a peak centered near 45 kHz believed to be the traveling instability. The peak magnitude is seen to increase with increasing Re and then seen to broaden and fill the transducer's frequency range, indicating fully turbulent flow. The sensor arrays utilized allowed for the computation of wave properties including phase speed and wave angle. Borg *et al.* (2015*b*) and Borg & Kimmel (2017*a*) present such data indicating largely oblique waves (77°-81° relative to the model centerline). Borg *et al.* (2015*b*) provide comparison with predicted wave properties from LST which show excellent agreement at the Re = 8.1×10^6/m case tested. Evidence of stationary vortices has been observed under noisy flow conditions in oil flow images (Borg *et al.*, 2012) but does not appear in either TSP or IR thermography (Juliano & Schneider, 2010; Borg & Kimmel, 2016). In addition, evidence of traveling crossflow, in surface pressure transducer data, has not been seen under noisy flow.

Borg *et al.* (2015*a*) presents work conducted in the Purdue BAM6QT operated in noisy mode with bleed valves closed as well as the conventional TAMU ACE hypersonic tunnel to examine the effect of freestream disturbance levels on the same test article. Although low frequency disturbances were observed in surface mounted Kulites, traveling crossflow was not definitively identified. Comparisons of the spectral content measured from the Kulites revealed strong similarity between the BAM6QT in noisy mode and the conventional ACE facility. The exact cause of the transition under noisy flow or the effect of significantly varying noise levels was not obtained. These experiments and the apparent contradiction of experimental evidence and conventional wis-

dom prompted interest in the present research.

Borg & Kimmel (2016) and Juliano *et al.* (2016) examined a newly constructed steel-tipped PEEK version of the 38.1% model geometry using simultaneous IR thermography and surface pressure measurements. Similar to the results from Borg *et al.* (2012, 2015*a*,*b*), both stationary and traveling crossflow were detected on the model under quiet flow but neither was observed under noisy flow, despite an observed region of transition apparent as increased heating near the cone shoulder. Borg has also recently made measurements along the model centerline using high frequency pressure transducers revealing spectral content of the centerline instability (Borg & Kimmel, 2017*b*).

The computational stability group at TAMU has utilized the combination of modeling techniques described in section 2.3 to examine the stability of both the flight and reduced scale models of the HIFiRE-5 geometry. Kocian *et al.* (2017) examine the 3-D crossflow instabilities and nonlinear secondary instabilities on both the full and a wind tunnel scale HIFiRE-5 geometry. Type I & II secondary instabilities, traveling crossflow, and second mode instabilities were identified and their growth rates and spectral extent examined. The results presented seem to explain the spectral broadening observed by Borg *et al.* (2015*b*) in the 0-200 kHz range of the Kulites utilized. Initially the traveling crossflow instability dominates the spectral content with a peak centered near 45 kHz, but it is quickly surpassed in growth rate by type- I & II secondary instabilities in a broad frequency band that fills the 0-200 kHz spectral range. These techniques form a powerful tool set for examining the transition process. The understanding gained can help inform experimental requirements, from necessary sensor response and placement, to need for surface roughness characterization of critical model areas.

2.5 Effect of Freestream Disturbances

Freestream disturbances have been shown to play a large role in the development of instabilities within the boundary layer. These disturbances can be divided into modes such as entropy variation, vorticity, and acoustic or sound (irrotational velocity or pressure fluctuations) (Schneider, 2001; Kovasznay, 1953; Bushnell, 1990). Conventional hypersonic tunnels are known to have elevated freestream turbulence, owing to the high-pressure piping supplying the facilities. With increasing Reynolds numbers the sidewalls of such tunnels undergo boundary layer transition adding disturbance to the freestream flow. Based on the early decomposition work of Kovasznay (1953) and measurements of Laufer (1961), as well as modern analysis summarized in Duan *et al.* (2018), the disturbances are believed to consist mainly of acoustic disturbances radiated from turbulent boundary layers on the tunnel nozzle contours and sidewalls. The effect of this noise on the transition process is not well understood but has been seen to have a large effect. Comparisons of data between "quiet" and "noisy" facilities have shown differences between the transition on the same model. Schneider (2001) presents an extensive review and summary of the existing comparisons between quiet and noisy experimental data as well as flight experiments, and demonstrates that trends in transition may even be reversed when tested under noisy conditions. Such differences have been observed experimentally on the elliptic cone geometry in the experiments of Borg *et al.* (2015*b*). It is believed that both stationary and traveling crossflow vortices in low-speed flows are largely insensitive to sound, based on low-speed experimental evidence. It might be expected then that at high-speeds the same would be true. For a conventional facility, stationary waves would still dominate in the acoustic noise dominated flow. This line of thinking, however, runs counter to the observation by Borg *et al.* (2015*b*) that neither traveling nor stationary waves were detected on

the scale HIFiRE-5 geometry under noisy flow despite transition being observed.

2.5.1 Freestream Disturbance Example:

Second Mode Transition Onset Prediction Technique

An illuminating example of the role of freestream noise and its usefulness in predictions of transition onset can be found in the work of Marineau (2017). Marineau and collaborators performed an extensive study to characterize the freestream disturbances of AEDC tunnel 9 and, using that characterization, allow the prediction of transition onset for cone flows dominated by the second mode.

The freestream disturbance environment was characterized using both Kulite and PCB pressure transducers. Several cones with varied nosetip bluntness were instrumented with a dense array of fast response pressure transducers, skin friction sensors and thermocouples. This dense array of transducers allowed for the measurement of the spatial evolution of the second mode instability in the form of pressure fluctuations on the cone surface. For several cases the density of instrumentation was sufficient to allow measurements ahead of the second mode instability neutral point, allowing examination of the initial disturbance amplitudes. This data was utilized as part of an iterative process to determine the transition onset location for a given geometry.

The goal of the iterative process is to proceed from an initial estimate for transition onset location (S_{Ti}), and use CFD and a stability solver along with experimental correlations to iteratively refine this estimate. The process is diagrammed in Fig. 2.4, reprinted from Marineau (2017)'s Fig. 8. The process begins by using CFD and a stability solver to estimate edge Mach number and expected second mode frequency. These values are then converted to an initial amplitude A_0 and a maximum amplitude A_{Max}. Both amplitudes represent RMS pressure fluctuations normalized

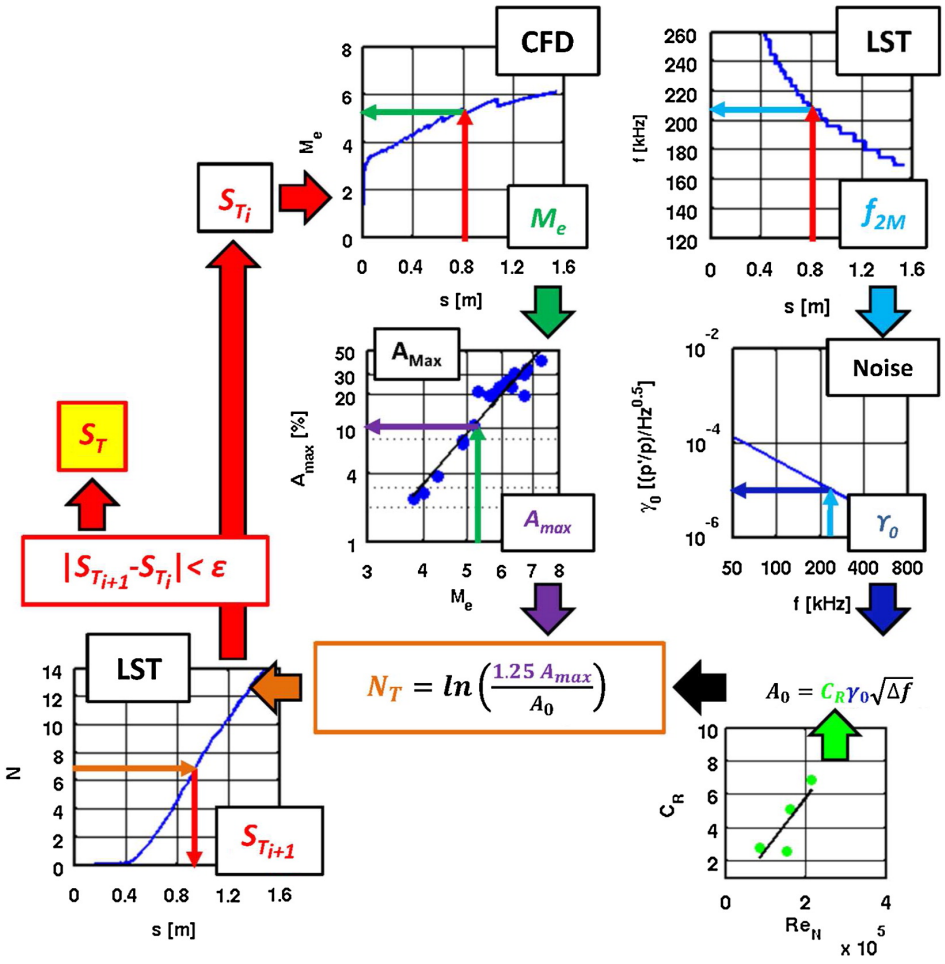

Figure 2.4: Schematic of algorithm for estimating transition onset. Reprinted from Marineau (2017).

by the mean edge pressure. These values allow the computation of a transitional amplification or N-factor N_T via equation 2.1. Stability equations then are utilized to determine the location this N-factor is reached, S_{Ti}.

$$N_T \approx ln\left(\frac{1.25A_{max}}{A_0(f_T)}\right) \tag{2.1}$$

Iteration of this process is carried out until an error threshold is met in the difference of S_{Ti} and S_{Ti+1}.

The process requires a series of correlations. Again following the diagram from the initial

estimate S_{Ti} to the right, CFD is utilized to simulate the mean flow basic state flow around the cone. This simulation is utilized to determine the edge Mach number along the region of interest on the cone. A correlation is then utilized to relate M_e and A_{max}. This correlation is obtained from plotting and fitting the measured values of A_{max} vs M_e from previous experiments in AEDC Tunnel 9. For sharp cones and cones with small radii bluntness, this correlation is shown to be a linear function (Marineau, 2017).

Stability simulations (LST or PSE) are utilized to obtain the most dominant second mode frequency expected. Freestream pitot pressure fluctuation measurements are then integrated over a band of frequencies centered around the expected second mode frequency, giving the normalized pitot noise spectral amplitude. This step critically gives a measure of the freestream disturbance field present near the nosetip of the cone. This information is utilized to calculate A_0 via equation 2.2.

$$A_0 = C_R \gamma_0 \sqrt{\Delta f} \tag{2.2}$$

C_R in equation 2.2 is Marineau's receptivity coefficient. This coefficient is defined as the ratio of normalized initial RMS pressure fluctuations at the second mode neutral stability point and the normalized RMS pressure fluctuations of P_{T2} measured in the tunnel freestream via a pitot probe (equation 2.3). Both are integrated over the expected second mode frequency range.

$$C_R \equiv \frac{A_0}{\Gamma_0} \tag{2.3}$$

This receptivity coefficient is simply as defined a direct relation between the measured pitot pressure fluctuations in a band of frequencies centered around the second mode frequency and the

fluctuations observed in the surface pressure transducer data in the same frequency band. In using this ratio, it couples a number of uncertain receptivity factors into one term. First is the process by which disturbances in the freestream propagate through the pitot probe shockwave and are measured by the transducer. Second is the disturbance propagation of the freestream disturbances through the model shockwave and shock layer. Third is the interaction of the disturbance with the model boundary layer and surface roughness. Marineau has built this correlation from experimental data of A_0 and measured freestream disturbances. He casts this as a correlation between Re_N and C_R. With this correlation and those above, equation 2.1 can be utilized to calculate the transition N-factor. Again using stability calculations, the location of this N-factor on the cone can be determined and utilized as the new estimate for S_T.

This technique in general illustrates the value added by the understanding of the impact of freestream disturbances on the transition process. The correlations utilized by Marineau allow for several unknowns to be combined to simplify this process. In the paper Marineau demonstrates that this iterative technique is superior to a constant N-factor technique, such as assuming that transition occurs at N = 5.5. For the cases examined he reports an uncertainty in S_T of 14% vs a 43% uncertainty in the traditional estimate.

The correlations used are not directly applicable to crossflow dominated boundary layers. The central observation that fluctuation amplitude A_{max} at transition onset is a simple linear function of M_e is unlikely to exist for crossflow dominated boundary layers. A better understanding of the underlying nature of crossflow primary and secondary instabilities and their breakdown process may lead to correlations that would allow a similar technique to be possible.

2.6 Effect of Surface Roughness

It has been shown, at low-speed, that stationary crossflow vortices are model fixed and related to roughness on the model surface. Discrete roughness elements have been utilized in several experiments to excite the crossflow instability and promote stationary wave growth. In low-speed swept wing flows, small micron-sized discrete roughness near model attachment line has been shown to strongly influence the crossflow transition process (Saric *et al.*, 2003). Periodically spaced roughness has been used in several efforts to excite stationary crossflow disturbances. Discrete roughness elements (DRE) placed as a periodic spanwise array with a wavelength equal to, or a multiple of, the most unstable crossflow wavelength hastens transition reducing the observed transition Reynolds number. Roughness with wavelengths below the dominant crossflow wavelength excite shorter wavelength disturbances and delay the onset of transition.

A review of experiments employing this DRE technology for swept wing laminar flow control is presented by Saric *et al.* (2019). The results underscore the necessity of characterizing model surface roughness, including its spectral content. For example, a swept wing model with a painted leading edge with 2 μm RMS roughness was observed to move transition forward. The roughness was characterized and found to have spatial spectral content near 9 mm which excited the 4.5 mm most unstable wavelength.

Recent computational efforts by Dinzl & Candler (2017) used DNS to examine the effect of distributed roughness on the transition on 2:1 elliptic cones in high-speed flow. Increasing RMS surface roughness heights from 0.5 to 4 μm was shown to change the extent and shape of surface heating due to the crossflow transition process. Moyes *et al.* (2018) studied the effect of initial disturbance amplitude on hypersonic crossflow instability for the 38.1% scale HIFiRE-5 geometry.

They found that increased initial amplitude shifted vortex saturation forward, which is similar to the effect observed in low-speed flows. Both of these studies highlight the importance of initial disturbance amplitude on the evolution of stationary crossflow for the HIFiRE-5 geometry.

2.7 Experimental Challenges

Because they depend so heavily on initial conditions, stability experiments must be carefully designed to isolate the parameters under study. Careful characterization of the freestream disturbance environment as well as model surface roughness are necessary for valid conclusions and comparisons with other experiments and computations to be made. To these ends, the facilities and models used need to be well characterized and documented. Measurements performed need to both be broad enough to enable the study of the 3-D boundary layer on the model and also provide local measurements within the boundary layer to track fluctuating quantities and their evolution. Global measurements need to be sensitive enough to resolve the small variations caused by the instabilities present. Local measurements similarly need sufficient resolution and frequency response to detect the weak rapid fluctuations within the boundary layer.

3. TECHNICAL APPROACH

3.1 Facilities

Experiments leveraged the unique combination of capabilities of two facilities at the National Aerothermochemistry and Hypersonics Laboratory (NAL) at Texas A&M University. The Actively Controlled Expansion (ACE) tunnel and NASA Langley/Texas A&M Mach 6 Quiet tunnel (M6QT) were utilized to test a 38.1% scale HIFiRE-5 model under varied freestream conditions. A photograph of the two facilities is given as Fig. 3.1.

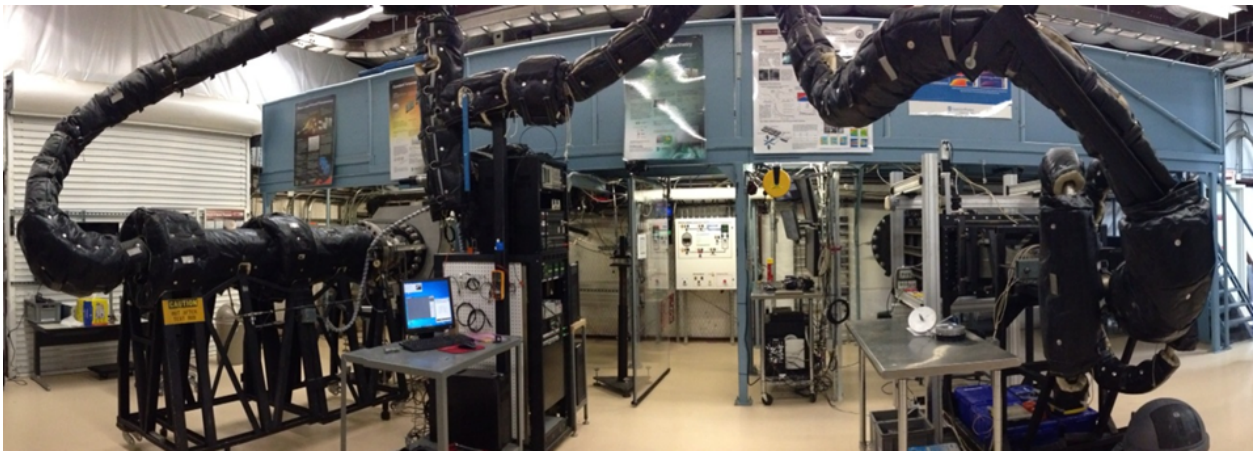

Figure 3.1: NAL facilities. Left: M6QT, Right: ACE.

3.1.1 Infrastructure

High pressure air and vacuum for tunnel operation were provided by dedicated infrastructure at the NAL. Both facilities operated in a pressure-vacuum blow-down mode. Vacuum was supplied by a two-stage Fox brand Venturi air-ejector system capable of generating a vacuum of 530 Pa using approximately 25 kg/sec of compressed air at 1 MPa. This system, pictured in Fig. 3.2, was connected to knife gates downstream of each tunnel's diffuser. High-pressure air is provided

by two CompAir Reavell 5442 compressors. The compressed air was filtered using a cyclone separator for large contaminants and a series of two 99% efficient sub-micron filters to remove oil and particulates introduced in the compression process. It was then dried by a twin-tower heatless desiccant drier to a dewpoint of 233 K and stored in a 23.2 m^3 tank at 17.2 MPa. The motive air for the ejector system was delivered through a 10.16 cm (4") carbon steel pipe. A separate 5.08 cm (2") schedule 80 stainless steel pipe supplied air from the storage tank to the laboratory. Both lines were controlled by remotely operated ball valves. Before entering the laboratory, the tunnel supply air was heated by a 0.5 MW Chromalox electric resistance heater (rated up to 530 K at 3.4 MPa) and filtered again (99.9% efficient 1-micron particle filter) just before entering the tunnel. To achieve the typical operating total temperatures ($\sim$ 400-450 K depending on Mach number, selected to avoid liquefaction within the nozzle expansion), the tunnels were preheated convectively, running low-speed air through the tunnels at a total pressure of 200-500 KPa prior to each run. Several heating-wire type resistance heaters mounted to each of the tunnel settling chambers and supply piping, in conjunction with fiberglass insulation, were used to help ensure thermal stability during a run. A typical tunnel run consists of a few minute subsonic tunnel preheat followed by approximately 40 seconds of hypersonic run. During tunnel preheat, the tunnel and any test articles in the test section are subjected to subsonic flow with an increasing total temperature as the tunnel nozzle and test section are heat soaked. For the present experiments operating procedures of both tunnels were altered to permit the test article to be removed during preheat and reinserted before a run. This allowed for direct comparison to impulse facilities which typically ran with an unheated room temperature model. Detailed specifications, schematics, and photographs of the tunnel supply infrastructure are available in Tichenor (2010).

Figure 3.2: Photograph of NAL two-stage ejector system.

3.1.2 Actively Controlled Expansion Tunnel (ACE)

The ACE tunnel is a variable Mach number tunnel with a rectangular 22.9 cm $\times$ 35.7 cm test section. The facility was designed such that the Mach number could be varied continuously by adjusting the throat height of its planar method of characteristics designed nozzle. For the present study, the Mach number was set to a nominal value of 5.9 to match that of the M6QT. A schematic of the facility, from settling chamber through diffuser, is shown in Fig. 3.3. Flow within the settling chamber is conditioned using two aerogrids and a series of 3 mesh screens. The aerogrids provide backpressure promoting uniformity of flow through the settling chamber. The series of mesh screens is arranged with decreasing mesh size to help break up any large scale structures further promoting flow uniformity.

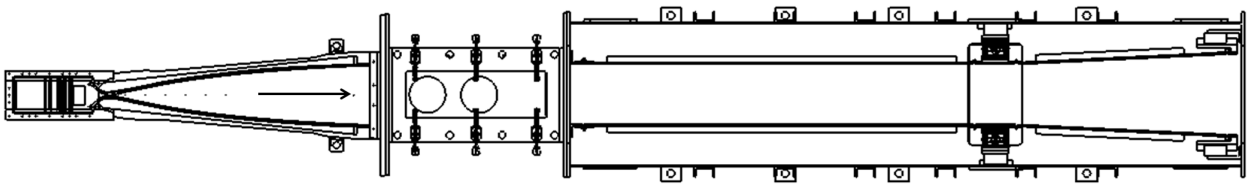

Figure 3.3: Schematic of ACE tunnel.

The tunnel test section is 508 mm in length and provisioned with portholes on each of the test-

section walls allowing for optical access and model mounting. A cage constructed of XT-95 optical railing is installed surrounding the tunnel allowing for mounting of cameras, illumination sources, and traverse mechanisms. Photographs and schematics of the ACE facility settling chamber, nozzle, and test section are available in Mai (2014), Tichenor (2010), and Semper *et al.* (2012). The tunnel diffuser was updated shortly before this experimental campaign, allowing higher Re testing. The design and development of this diffuser is detailed by Leidy (2019).

The tunnel has been calibrated from Mach 5 to 7 and documented as uniform across the test section to within $\pm$ 1.5% at Mach 5 and $\pm$ 0.5% above Mach 6 (Mai, 2014). Previous work has characterized freestream pitot and mass flux disturbance levels in the ACE facility (Semper *et al.*, 2012; Mai, 2014; Borg *et al.*, 2015*a*). Disturbance levels in the facility exhibit an interesting characteristic. There is a sharp increase in freestream disturbance levels at a freestream unit Reynolds number of 3×10^6/m. Below Re = 3×10^6/m, boundary layers along the nozzle and sidewall boundary layers are laminar, and hence the freestream turbulence levels are small. At Re > 3×10^6/m, the nozzle wall boundary layers transition to turbulence and freestream pressure fluctuations increase. The freestream fluctuations are believed to be dominated by noise radiating from the nozzle sidewalls. The freestream pitot fluctuations vs unit Re are shown in Fig. 3.4 and compared with the TAMU M6QT and Purdue BAM6QT.

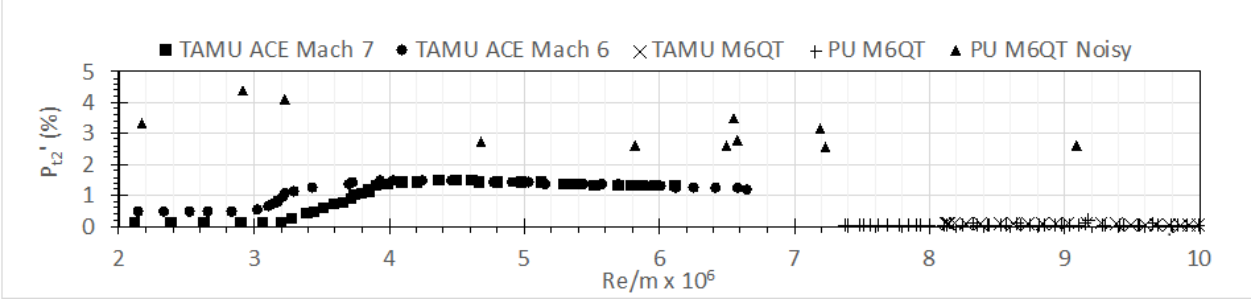

Figure 3.4: Freestream disturbance levels in ACE.

3.1.3 TAMU / NASA Langley Mach 6 Quiet Tunnel (M6QT)

The Texas A&M/NASA Langley Mach 6 Quiet tunnel is a low disturbance facility which was originally designed and operated at NASA Langley Research Center. Its design was the result of extensive efforts at LaRC to understand and develop low disturbance supersonic and hypersonic facilities. The facility contains a number of design features tailored to produce low disturbance flow. Flow enters the facility through a smooth bore PTFE-lined stainless-steel braided hose. The facility's large settling chamber houses a perforated spreading cone to expand the flow to the full settling chamber diameter. The spreading cone is followed by a series of meshes arranged from coarse to fine spacing to provide flow conditioning by straightening the flow and breaking up any large-scale structures. The Mach 6 facility nozzle expansion was designed to minimize streamwise curvature to delay growth of göertler vortices in the nozzle wall boundary layer. Additionally, a bleed slot at the nozzle throat allowed for the removal of the boundary layer formed in the converging section of the nozzle, allowing a fresh laminar boundary layer to develop downstream. The nozzle is highly polished to reduce the amplitude of disturbances within its boundary layer. These features combined allow for operation of the facility at a unit Re range of approximately 7×10^6/m to 11×10^6/m with laminar boundary layers over a large portion of the nozzle streamwise extent.

The tunnel was initially relocated to Texas A&M in 2005 and an upgraded test section was installed in 2008. Early work focused on restoring and characterizing the facility's quiet performance. The freestream was characterized and its quiet performance verified by Hofferth *et al.* (2010) who found that the performance of the re-established facility was in line with its previous performance at LaRC. The nozzle was approximately 1 m in length with an exit diameter of 18.4 cm. The nozzle was housed within a large enclosed-free-jet style test section. Within this test

section a model fixed traverse system was installed and utilized for freestream and boundary layer surveys by Craig & Saric (2016). Test articles were typically placed well within the nozzle, attempting to take advantage of the test revolved-rhombus of on condition quiet flow defined by the limiting characteristic and the radiated noise from transition of the nozzle sidewall boundary layer. Optical access was severely limited with the majority of the model in the nozzle. Nevertheless previous efforts have successfully used IR thermography and focusing schlieren on the portions of the model extending past the nozzle exit plane.

Hofferth (2013) presents the results of an extensive freestream characterization effort performed after initial installation and shakedown operations. A Kulite XCEL-152-10A was utilized to create spatial maps of the freestream pitot pressure and pitot pressure fluctuations at two typical tunnel operating Reynolds numbers. These scans reveal freestream noise levels at or below the noise floor of the pressure transducer (0.05% P'_{t2}/P_{t2}) for a large area of the nozzle. Moving radially from the centerline, this quiet core is bordered by a cone of fluctuations radiating from apparent nozzle wall transition. Hofferth also presents frequency spectra indicating that content in the quiet freestream is contained below 10 kHz. At positions within the noise radiated from the nozzle wall, the spectra show a broadband profile across the Kulite's spectral range (0-60 kHz). With the probe positioned at the model centerline at a position of x/L = 0.72 along the nozzle's streamwise length, Re sweeps performed reveal intermittent packets of disturbances appearing near 10.5×10^6 and a complete loss of quiet flow near 11×10^6/m. Spot checks of this characterization are performed, typically before and after entry and exit of models for various campaigns and any model changes or facility modifications. Before the current experiments, the facility nozzle was cleaned and a Re sweep pitot survey was performed. The probe utilized lacked the resolution and noise floor level necessary to precisely measure the quiet flow fluctuations but was used as a binary

detector of quiet flow. The appearance of disturbances above the sensor noise floor occurred at a Re consistent with the measurements of Hofferth.

3.2 Tunnel Instrumentation & Data Acquisition

3.2.1 Tunnel Data Acquisition: NALDAQ

Conditions of both facilities were monitored using a LabView VI. Between tunnel runs the VI was operated in a monitoring mode allowing the monitoring of the facility transducers, supply tank pressures, and compressor status. Test data acquisition was triggered by the opening of the ejector supply line, the first step in a run of either tunnel. A 16-bit NI USB-6255 M-Series DAQ with BNC connections was used for this system. This VI was also capable of producing a 5V TTL signal allowing for triggering and synchronization of other measurement devices. For the present work this signal was utilized to trigger a high-speed camera as part of a schlieren system as described in Chapter 4. For both tunnels, this system recorded settling chamber total pressure and temperature, test section static pressure, and diffuser pressure. In addition, several measurements of tunnel infrastructure performance were acquired. These include supply line pressures, ejector stage pressures, heater temperature, and tank pressure. Data were recorded at 100 Hz. The VI produces a comma separated ASCII output file of the raw data as well as an averaged version of the run data down-sampled to 10 Hz. This down-sampled output was compiled into a spreadsheet and plotted. These plots were used after each run to quickly survey the run conditions achieved and diagnose potential infrastructure issues.

In both facilities, stagnation temperature and pressure were measured utilizing a pressure transducer mounted to a pitot tube within the settling chamber and a type K thermocouple near the exit of the chamber. Static pressure was measured via a static pressure port on the nozzle sidewall

downstream of the limiting characteristic of either facility nozzle. From these measurements, assuming isentropic flow through the facility nozzle, Mach and Reynolds number were computed. Sutherland's viscosity law was utilized to determine freestream dynamic viscosity. This choice for viscosity was made to allow comparison with other facilities and CFD simulations (Lakebrink *et al.*, 2017; Edelman & Schneider, 2018; Kocian *et al.*, 2017). The equation and reference conditions utilized are presented in Eq. 3.1 and Table 3.1.

$$\mu = \mu_{ref} \left(\frac{T}{T_{ref}} \right)^{3/2} \frac{T_{ref} + S_\mu}{T + S_\mu} \tag{3.1}$$

Table 3.1: Sutherland's law computation parameters for air.

μ_{ref} $(\frac{\text{kg}}{\text{ms}})$	T_{ref} (K)	S_μ (K)
1.716×10^6	273.15	110.4

3.2.2 Tunnel Instrumentation: ACE

The ACE facility settling chamber conditions were measured downstream of the facility flow conditioning porous plates and screens. Stagnation temperature was measured using an Omega type K thermocouple exposed to the flow. Its frequency response was estimated by Mai (2014) from Omega specifications as O(1s). Stagnation pressure was measured using an Endevco 8540-200 pressure transducer. This sensor was mounted to the settling chamber and attached to a pitot tube facing in the upstream direction made from a 3.2 mm (0.125 in.) diameter stainless steel tube. Static pressure was measured at a static pressure port 11.4 cm upstream of the nozzle exit plane along the tunnel centerline. Static pressure was measured using an MKS Baratron 631C-10 capacitance manometer, actively heated to 423 K to avoid error due to thermal shift during tunnel

operation.

3.2.3 Tunnel Instrumentation: M6QT

In the M6QT, stagnation pressure is measured using an MKS Baratron 615A high-accuracy capacitance manometer with a full-scale range of 10 kTorr. Nozzle static pressure is measured by an MKS Instruments 902 series absolute piezo-vacuum transducers. The transducer is connected to a static pressure port mounted approximately 12.7 mm inches upstream of the nozzle exit via a stainless-steel tube $\sim$ 1 m in length. This transducer is utilized as an indication that the tunnel has started but lacks the resolution for accurate determination of tunnel Mach number. Previously performed pitot surveys measured the facility Mach number to be 5.9 across the quiet range of the facility. Thus M = 5.9 is assumed and utilized for calculations of freestream pressure and temperature through standard isentropic flow relations.

3.2.4 Instrumented Model DAQ: M6QTDAQ

A suite of in-house developed LabVIEW VIs was utilized for model data acquisition. Signals were acquired using two synchronized 16 bit NI USB-6366 X-Series DAQ boards each offering 2 MS/s per channel on 8 differential channels with simultaneous sampling. The system was utilized in several configurations for each of the experimental campaigns presented here. Instrumented model runs utilized 12 of the 16 channels acquired at 2 MS/s per channel for 100 ms per sample. Tunnel conditions were down-sampled by averaging over the sample length. pressure transducers utilized additional signal conditioning before being sampled. This conditioning and setup are described in detail in Subsection 4.1.7.

3.3 Experimental Techniques

Infrared thermography, surface pressure measurements, and hotwire anemometry were used to examine the development of instabilities on the cone and freestream disturbances. This section details each technique and how it was utilized in the present experimental campaigns.

3.3.1 Infrared Thermography

IR thermography has been successfully used in several studies to examine the location and extent of the onset of transition in both high- and low-speed flows (Borg & Kimmel, 2016; Duncan *et al.*, 2013). Distortions of the boundary layer on a model surface alter the local heat flux producing changes in temperature. With a suitable high emissivity material very small temperature changes may be detected with a sensitive IR camera. This technique can provide a large field of view allowing for a non-intrusive global measurement of surface temperature. A time history of this surface temperature can then be utilized to compute the heat flux at the model surface.

In the present experiments, the model surface was imaged using a FLIR SC8100 which was a mid-wavelength infrared (MWIR) camera sensitive to wavelengths from 3-5 μm. The camera has a resolution of 1,024 $\times$ 1,024, allowing for high resolution images through an IR window mounted in the tunnel roof or sidewall. The camera was connected via an Ethernet cable to a Windows PC running FLIR Systems ResearchIR IR camera control and acquisition software. For the 40 second typical run times of ACE and the M6QT, it was necessary to record files directly from the camera to the PC's hard disk drive. This limited the usable frame rate of the camera to approximately 30 fps. Higher recording rates up to 135 fps are possible using a FLIR Systems high speed data recorder which should be utilized in future testing at the NAL.

Time histories of model surface temperature were recorded at 15 Hz each at two integration

times (8 ms and 4 ms for ACE runs and 4ms and 2ms for M6QT runs). The camera output raw 14-bit data in counts which was then converted to temperature using a calibration curve. An *in situ* calibration was performed by imaging, through the actual test IR window utilized, a matte black plate approximating a black body with its temperature measured via an embedded thermocouple. The calibration process was performed and is described in detail by Leidy (2019). The IR processing procedures are described below with more basic theory and sample reduction codes found in App. A and App. E

The time histories of surface temperature obtained were used to compute the heat flux at the model surface. For a low thermal conductivity model, minimal lateral heat transfer along the model surface is expected and 1-D heat conduction within the model can be assumed. A MATLAB script was developed to use a 1-D forward time, central difference scheme to process the temperature time history and compute heat flux. This script was inspired by the FORTRAN code QCALC (Boyd & Howell, 1994), and its successful adaptation and use in the modern studies of Borg & Kimmel (2016) & Juliano *et al.* (2016). This script assumes 1-D heat conduction normal to each image pixel and computes the temperature distribution within the model at each time step and then computes the first derivative at the surface to obtain the surface heat flux. This method was utilized and reported in Neel *et al.* (2017), Neel *et al.* (2018*a*), & Neel *et al.* (2018*b*). The descriptions in those papers are reproduced and expanded upon here.

To reduce the visibility of reflections observed on the model from the IR camera itself and tunnel sidewalls, the first processing step was to subtract an initial frame. This initial frame was created using an average of 20 frames acquired immediately before the tunnel air supply was opened. An average temperature from a manually chosen location on the model near the cone shoulder was then added back as the initial model temperature. The initial temperature distribution

within the model was assumed to be equal to this initial temperature. The time evolution of the temperature distribution within the model was then estimated by the general 1-D heat equation, Eq. 3.2:

$$\frac{\partial T}{\partial t} = \alpha \frac{\partial^2 T}{\partial \zeta^2} \tag{3.2}$$

In Eq. 3.2, α is the thermal diffusivity, defined as Eq. 3.3:

$$\alpha = \frac{\kappa}{\rho c_p} \tag{3.3}$$

where the material properties of PEEK κ, ρ, and c_p were obtained from the manufacturer of the PEEK rod used to construct the model. The derivatives in Eq. 3.2 were approximated using a Forward-Time, Central-Space (FTCS) scheme. This finite difference scheme is presented as Eq. 3.4:

$$\frac{T_{(i+1,j)} - T_{(i,j)}}{\Delta t} = \frac{\alpha(T_{(i,j-1)} - 2T_{(i,j)} + T_{(i,j+1)})}{(\Delta\zeta)^2} + \mathscr{O}(\delta\zeta^2) \tag{3.4}$$

where the first temperature index is temporal and the second is spatial, Δ t is the temporal step size, given by the camera sampling frequency of 15 Hz, and $\Delta\zeta$ is the spatial step size, which was set to $\sqrt{2\alpha\Delta t}$ for scheme stability. The initial temperature distribution within the plate was set to the initial wall temperature as described above. The time dependent surface temperature provided by the IR thermography was used as the surface boundary condition. For the second boundary condition, the temperature was assumed constant at a maximum heat penetration depth. This was set at 5 mm, meaning the temperature at that depth remains the initial temperature for the duration

of the run. With the temperature distribution within the model approximated for the entire run, the heat flux for each pixel at each time step was determined using Fouriers law given below as Eq. 3.5:

$$q = -\kappa \frac{\partial T}{\partial \zeta} \tag{3.5}$$

The first spatial derivative of temperature was approximated using a 3 point scheme. The heat flux approximation is given in Eq. Eq. 3.6:

$$q = -k \frac{-\frac{3}{2}T_{(n,0)} + 2T_{(n,1)} - \frac{1}{2}T_{(n,2)}}{\Delta \zeta} \tag{3.6}$$

where i=n is a given time and j=0 is the surface. The heat flux was then averaged over 3 frames (1/5 sec) to reduce noise in the resulting heat flux maps.

The temperature observed and heat flux computed will depend on the state of the flow over the model surface and initial model conditions. To account for the variance in freestream properties and wall temperature throughout the run, the heat flux was normalized to Stanton number using Eq. 3.7 where the subscript ∞ indicates freestream properties, 0 indicates stagnation properties, and w indicates wall properties.

$$St = \frac{q}{\rho_\infty U_\infty c_p (T_0 - T_w)} \tag{3.7}$$

Triggering of the IR camera via the tunnel DAQ system was attempted but proved unreliable. Instead the camera was manually triggered in sync with the tunnel operator opening the tunnel ejector supply line valve. The computed heat flux was synchronized with the tunnel freestream

conditions by examining the model surface temperature. Tunnel unstart is detected by an impulse step in tunnel static pressure and a rapid increase in model surface temperature. Heat flux is synchronized with tunnel conditions by matching the time of the surface pressure increase and static pressure rise.

The assumptions in the method above (i.e. 1-D conduction normal to each pixel, constant temperature at a 5 mm depth) are considered valid for the regions of the cone examined in the current study. All areas shown are more than 5 mm thick. The shape of the elliptical cone is such that the angle between the normal to the camera sensor and the model surface is very shallow for much of the surface acreage of the cone, limiting the effects of viewing angle on surface emissivity. There are two major sources of distortion present in the images obtained by the IR camera. The first is distortion introduced by the physical lens. In the ACE tunnel a 17 mm lens was utilized which introduced significant barrel distortion into the images making spatial scaling somewhat difficult. For campaigns within the ACE tunnel this lens distortion was corrected by utilizing the image processing toolbox within MATLAB. A checkerboard of 1.27 cm squares was created by applying a machine cut vinyl adhesive to a polished aluminum plate. This checkerboard proved to be easily detectable by the IR camera. Images were obtained and used to characterize the lens distortion parameters and apply a correction to the images. The 50 mm lens used in the M6QT tunnel runs was not observed to create similar barrel distortion in a series of calibration images, so a lens calibration was deemed unnecessary. The second source of distortion is perspective. In the case of the ACE images the perspective distortion is minimal as the camera is mounted directly above the test article. In the quiet tunnel the optical setup is more difficult and required the cone to be viewed at an approximately 20° angle which introduces quite significant perspective distortion. As a result the spatial scales on the IR derived images should be taken as approximate.

3.3.2 High Frequency Pressure Transducers

Pressure transducers are useful for tunnel characterization and direct measurement of static and fluctuating pressure on a model's surface. The anticipated surface fluctuation frequencies of interest, from previous experiment, CFD, and theory are such that high frequency (O (100 kHz - 1 MHz)) transducers are necessary to characterize the fluctuations present. For this reason high frequency Kulite piezoresistive and PCB piezoelectric pressure transducers were selected. A freestream pitot mounted Kulite and surface mounted Kulite and PCB pressure transducers were utilized to measure fluctuating pressure in the freestream and on the model surface respectively. Such transducers have been successfully characterized and utilized to provide measurements of fluctuating surface pressure in supersonic and hypersonic boundary layers (see Beresh *et al.*, 2011; Edelman & Schneider, 2018). The following section discusses the pressure transducers, power supplies and filters utilized. Discussion of mounting and placement of the transducers can be found in Chapter 4.

Kulite XCE-062-15A[1] pressure transducers are piezoresistive transducers with a 0-103.4 kPa pressure range and compensated temperature range from 298 to 508 K. The sensor housing is a stainless-steel cylinder 1.7 mm in diameter and 9.5 mm long. The units are typically included with a screen covering the opening of the cylinder. For this experimental campaign screen-less (type-A screen in manufacturer notation) transducers were chosen as it has been demonstrated that they achieve a more linear spectral response over a larger range of frequencies. This type of transducer has been characterized under a supersonic turbulent boundary layer and the screen-less variety are expected to have a linear frequency response up to 30-40% of their resonant frequency (Beresh

[1] Kulite XCE-062-15A Spec Sheet: URL

et al., 2011). Power and signal conditioning for these transducers was provided by a custom built circuit created at the NAL by Dr. Jerrod Hofferth based on circuit designs by Prof. Steve Schneider at Purdue University. This circuit provides a clean 10V excitation voltage to the Kulites and gains the DC coupled Kulite output signal 100×. The circuit also contains a first-order RC circuit which is used to low-pass filter the signal at 482.5 kHz. This provides an inbuilt measure of anti-aliasing. An AC coupled output is also available which converts the DC signal by high-pass filtering at 842 Hz and gaining by 28.9×. The DC signals from the signal conditioning box were then low-pass filtered using Khron-Hite brand 200-kHz Bessel filter modules in a set of Khron-Hite FMB3002 filter boxes.

Table 3.2: Kulite XCE-062-15A sensor properties.

Property	**Value**
Pressure Range	0-103.4 kPa
Housing Diameter	1.7 mm
Full-Scale Output	100 mV
Combined Non-Linearity, Hysteresis and Repeatability	± 0.1% BFSL
Resonant Frequency (Experimentally Observed)	250-270 kHz
Compensated Temperature Range	298-508 K

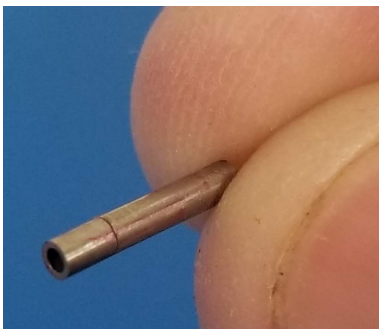

Figure 3.5: Photograph of XCE-062A15 pressure transducer.

PCB 132B38 [2] transducers are high frequency response piezoelectric type transducers. They

[2]PCB 132B38 spec sheet: URL

have a measurement range of 345 kPa with a typical sensitivity of 140 mV/psi and factory stated typical resolution of 0.007 kPa. By their piezoelectric nature, they are effectively high-passed at 11 kHz and have a high frequency response up to 1 MHz. Transducer specifications are given in Table 3.3. At the time the experiments detailed herein were conducted, the sensor was still under development by PCB and a development version of the sensors (DEV132B38 in manufacturer nomenclature) was obtained and used. The specifications of this development version are identical to those provided for the 132B38 sensors available at the time of writing. Power and signal conditioning were provided by PCB Model 482C05 sensor signal conditioning boxes. These boxes provided power and excitation and output the transducer voltage with unity gain. The raw PCB signal was low-pass anti-alias filtered using Khron-Hite brand, 1 MHz, 8-pole Bessel filter modules in a set of Khron-Hite FMB3002 filter boxes.

This type of transducer has been heavily utilized recently for characterization of spectral content in supersonic and hypersonic boundary layers. Beresh *et al.* (2011) found good spectral agreement in an experiment which compared a similar PCB transducer to previously characterized transducers. The PCB was estimated to have a flat frequency response from approximately 20-300 kHz. The present study as well as a series of shock boundary layer interaction experiments conducted with the same transducers showed similar performance. The lack of response below 11 kHz makes calibration of the sensors somewhat difficult. The transducers are supplied from the manufacturer with a single point shock tunnel calibration. Recent work has been conducted at Purdue University within Prof. Steve Schneider's research group to perform more thorough calibrations (Gray *et al.*, 2017).

A Kulite XCEL-100-5A transducer was utilized for freestream pressure measurements. This transducer was mounted in a pitot configuration, flush with the end of a probe constructed from

Table 3.3: PCB 132B38 sensor properties.

Property	Value
Measurement Range	345 kPa
Housing Diameter	3.18 mm
Sensitivity (typical)	20.3 mV kPa^{-1}
Resolution	0.007 kPa
High Frequency Response	1 MHz
Operating Temperature	248-350 K

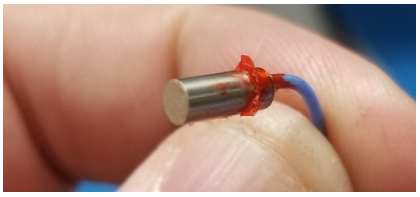

Figure 3.6: Photograph of PCB 132B38 pressure transducer. Orange fingernail polish used for mounting is visible after removal of sensor from model.

progressively decreasing diameters of concentric stainless-steel tubing. This probe and its construction are detailed in Mai (2014). The pressure range was chosen to maximize the use of the DAQ resolution with the goal of measuring freestream fluctuations which can be quite small in absolute terms (<1% of 5 psia). Sensor properties are given in Table 3.4.

Table 3.4: Kulite XCEL-100-5A sensor properties

Property	Value
Measurement Range	0-34.5 kPa
Housing Diameter	2.6 mm
Full-Scale Output	100 mV
Combined Non-Linearity, Hysteresis and Repeatability	0.1% BFSL
Resonant Frequency (nom.)	150 kHz
Compensated Temperature Range	298-508 K

Figure 3.7: Photograph of XCEL-100-5A pressure transducer in pitot configuration. Screen shown at left and probe construction at right.

3.3.3 Schlieren Imaging

Schlieren imaging is a common technique utilized in high-speed wind tunnel facilities to visualize flow features such as boundary layers, shockwaves and vortices. A Z-type schlieren system was utilized to visualize shockwave locations and the examine the layer on the model surface. The system consists of a high-powered light source, two parabolic collimating mirrors, a knife edge cutoff and a high-speed camera. The light source used was a high output LED (Luminus, Inc. PT-121-RAX-L15l-MPH) which was operated with a supply power of approximately 70 W. The LED was actively water-cooled to support this level of power output. The light from the LED was collected and focused on to a Thorlabs VA100 adjustable slit using a 55 mm Nikon camera lens. The light was colimated using a 152.4 mm f-number f/6 parabolic mirror and directed through the tunnel test section. It was then refocused onto an adjustable knife edge before being focused onto the camera sensor plane using an appropriate spherical lens. The camera utilized was a Photron FASTCAM SA-Z CMOS camera with a resolution of 1024x1024 pixels and a minimum exposure time of 159 ns. Resolution of the images varied depending on the frame rate utilized. The camera was equipped with an external trigger allowing the acquisition of images to be synced with data acquisition using the NALDAQ TTL output.

3.3.4 Hotwire Anemometry

An A.A. Lab Systems AN-1003 constant temperature anemometer (CTA) anemometer was utilized to measure fluctuations in the tunnel freestream and across the model shockwave. Hotwires are sensitive to mass flux and temperature fluctuations. The sensitivity to temperature fluctuations can be reduced to negligible levels by utilizing a high temperature loading factor. This factor is computed using Eq. 3.8.

$$\tau = \frac{T_w - T_e}{T_0} \tag{3.8a}$$

$$T_e = \eta T_0 \tag{3.8b}$$

η has previously been determined to be 1.05 for the wires used in this study. The temperature loading factor for the present experiments was set to 0.8 ($T_w = 776K$). The response of the wire to mass flux can then be computed by a general form of King's law, Eq. 3.9.

$$E^2 = A + B(\rho U)^n \tag{3.9}$$

E is the anemometer bridge voltage. Calibration parameters A, B, & C were obtained by an in situ calibration in the ACE freestream. The resulting parameters are shown in Table 3.5.

Table 3.5: Hotwire calibration parameters.

A	B	n
0.495	0.824	2.333

The sensor utilized was a TSI 6.3 μm diameter, 1.27 mm long platinum iridium wire (L/D =200) which was mounted to a TSI model 1220 high temperature straight probe with a model 1151 probe

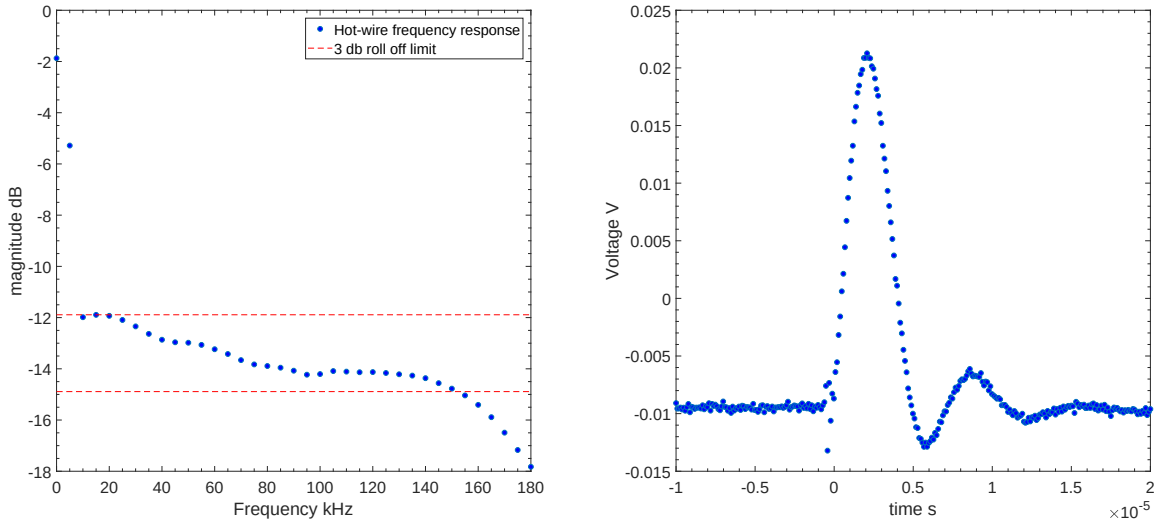

(a) (b)

Figure 3.8: Hotwire square pulse response. (a) frequency response (b) time response

support. The wire was initially tuned on the bench-top in nominally quiescent air and then during a constant Reynolds number run at a condition representing the highest Reynolds number expected during experiments. A digital oscilloscope was utilized to monitor the pulse response during tuning and calculate the frequency response of the probe. Using the criteria of a 3 dB roll off from the lowest frequencies, a typical 140 kHz response was obtained. This response is shown in Fig. 3.8.

3.3.5 Probe Traverse

Freestream characterization runs in the ACE tunnel utilized a two-stage traverse mounted to a 95 mm optical rail system around the tunnel. The system consists of two Aerotech PRO165 linear stages. The traverse was specifically chosen for use in the M6QT due to its low electronic noise characteristics, allowing it to be operated at the same time as the sensitive CTA hotwire anemometry system. The specifications and rational for initial selection are detailed by Hofferth (2013). The factory calibrated positional accuracy of the system is $\pm$ 5 µm. For this work this

traverse was utilized for freestream measurements rather than the more precise boundary layer measurements it was designed for.

As part of the freestream survey effort, a new probe sting and pass-through system was designed and constructed. This system was designed to be capable of positioning and traversing a probe within a plane parallel to the model exit plane. It consists of a 20° wedge shaped sting with a probe mounting provision at one end allowing for various probe mounting angles. A computer rendering of the probe sting and pass-through system is shown in Fig. 3.9. This probe holder was utilized for hotwire runs while a previously manufactured holder and sting was utilized for the freestream pitot surveys. The previously manufactured probe holder was similar in design and is detailed in Mai (2014).

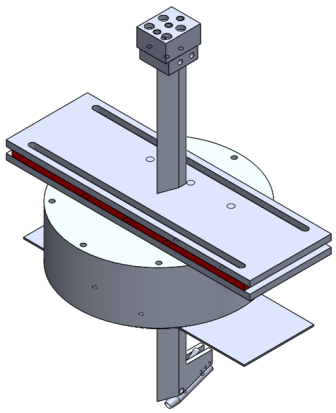

Figure 3.9: CAD drawing of probe sting and pass through.

3.3.6 Model and Surface Metrology

A series of measurements were conducted to characterize the roughness present on the model surface. A Keyence laser profilometer constructed by Crawford *et al.* (2014) was utilized and compared against a Mitituyo Surftest contact profilometer. Both systems allow for precise line measurements of surface roughness. From these scans the surface roughness height, length scales

as well as spatial distribution can be determined.

A challenge associated with both measurement techniques is their limited throw and depth capability. To maintain sub-micron accuracy ($\pm$ 0.02 μm), the laser profilometer is constrained to a measurement range of $\pm$ 3 mm. This complicates the scanning procedure allowing the model surface to deviate only 6 mm across the profile being scanned. For this 2:1 elliptic cone geometry there are several sections where this limit means that only a small area on either side of the model centerline are able to be scanned without large manipulation of the model. The traverse also has a limited throw of 60 mm. The model was mounted to an optical rail allowing it to be positioned underneath the laser traverse allowing for quick realignment of the model. A photo of this setup is given as Fig. 3.10.

For the model surface characterization, scans were made about the model centerline, extending at least 18 mm on either side. Scans were made in lines along the model span with 5 mm spacing in the streamwise direction. The raw output of the laser profilometer is a table of displacements, distances from the surface to the head of the laser, in ASCII format. This output was then analyzed using a MATLAB script to smooth, remove profile shape, separate waviness from roughness and finally compute characteristic roughness parameters. Subsection 4.1.6 presents the results of this characterization and App. B provides a detailed description of the methodology utilized for post-processing and analysis of the scans.

To augment the somewhat limited spatial resolution of the scans made with the profilometers, additional scans were made with a North Star Imaging x50 2D Digital Radiography & 3-D Computed Tomography system. CT scans were acquired to image roughly the first 100 mm of the cone with slices, planes parallel to the cone base and major axis plane, taken every 75 μm. A smaller section of the nosetip region was imaged with 37 μm slices. The factory stated max accuracy of

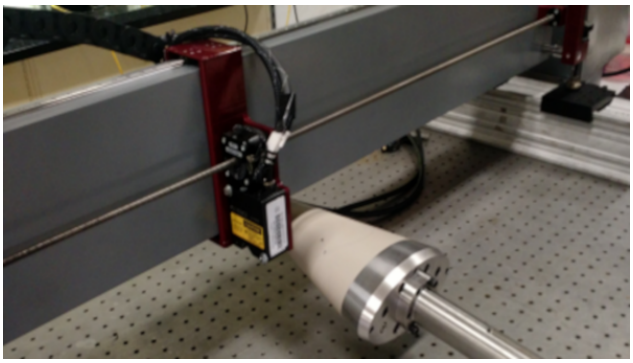

Figure 3.10: Keyence laser displacement sensor installed on two-stage traverse.

the system is 0.5 μm. These measurements are not finely resolved enough to make detailed measurements of roughness but do allow characterization of the as-machined outer mold line of the model.

4. EXPERIMENTAL CONFIGURATION

The techniques of the previous chapter were utilized to investigate the evolution of instabilities on the HIFiRE-5 elliptic cone geometry. Several 2:1 ellipse models were constructed and run in both the M6QT and ACE wind tunnel facilities. This chapter describes the model design process, model construction, model instrumentation, facility configuration, and concludes with discussion of experimental uncertainty.

4.1 Model Geometry and instrumentation

4.1.1 Original HIFiRE-5 Geometry Requirements

As described previously, the 2:1 elliptic cone geometry was selected for further study as part of the HIFiRE experimental flight test program. A full-scale flight model was designed. It's basic geometry consisted of a 7° half angle 2:1 elliptic cone, 861.05 mm in length and having a 431.8 mm major axis base diameter. The vehicle has a nosetip defined by a 2.5 mm circular arc in the minor axis plane and maintains a 2:1 elliptical aspect ratio until its stagnation point (Kimmel & Adamczak, 2012). A diagram of this basic geometry is given in Fig. 4.1 with the nosetip geometry highlighted in Fig. 4.2.

4.1.2 Model Design and Construction

The model chosen for this study was a 38.1%-scale model of the forebody of the HIFiRE-5 flight research vehicle. This particular geometry and scale is of great interest because of the existing flight data as well as a number of ground tests at the same scale as detailed in Chapter 2. The model is 328.1 mm in length with a major axis base diameter of 431.8 mm. A diagram of

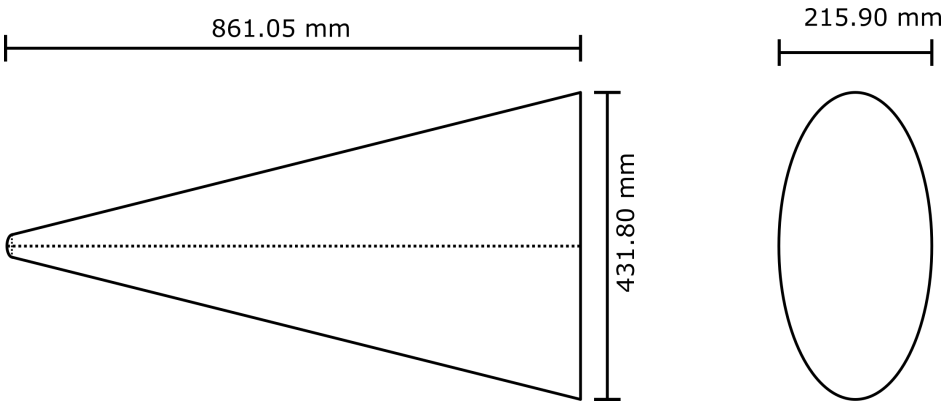

Figure 4.1: Full-scale HIFiRE-5 geometry. Left: view onto major axis plane. Right:View onto cone base plane.

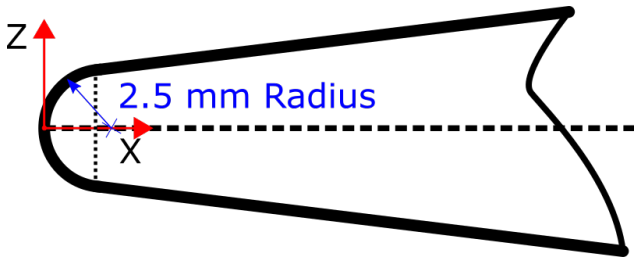

Figure 4.2: Full-scale HIFiRE-5 Nosetip geometry. View onto minor axis plane.

this geometry is shown in Fig. 4.3. The nosetip of the model as machined here was modified from that of the full geometry. The super ellipse nosetip utilized is discussed in Subsection 4.1.5. An aluminum "blockage" model version of this cone was constructed and run in both facilities to ensure that this model scale would allow the tunnels to start and remain operational throughout their typical Reynolds number range. These runs were successful in both facilities.

Because the growth and development of boundary layer instabilities has been shown to be highly influenced by general model geometry and roughness it is important to detail the design and construction of the model utilized for these experiments. Polyether ether ketone (PEEK) plastic was chosen as a suitable material for the test article due to its low thermal conductivity and high emissivity, ensuring that heating patterns readily radiate energy and do not diffuse across the surface of the model. This material has been utilized previously by Borg & Kimmel (2016) and others

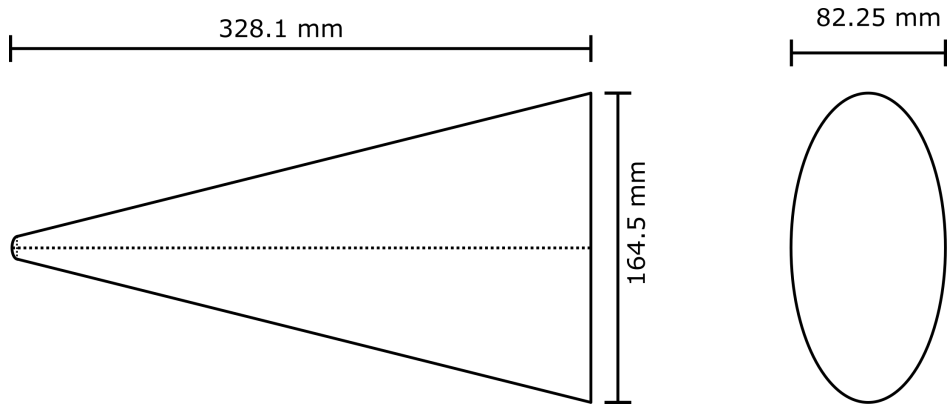

Figure 4.3: 38.1% model-scale HIFiRE-5 geometry. Left: view onto major axis plane. Right:View onto cone base plane.

and yielded good signal to noise ratios in similar flows (Borg & Kimmel, 2016; Juliano *et al.*, 2016). Models were machined from a solid piece of extruded unfilled PEEK rod. This monolithic construction was chosen to avoid any issues with steps, thermal expansion, and pressure sealing at material interfaces which might alter instability development in an uncontrolled way. Steel dowel pins were added to the models to ensure rigidity and aid alignment during machining. Pockets were drilled from the rear of the cone upstream along the cone centerline and shoulders. These pockets enabled flush mounting of surface pressure transducers for analysis of surface pressure fluctuations in the transitional regions of the cone. A photograph of this geometry is shown in Fig. 4.4 and the sensor cavity shown in Fig. 4.5. For the present study the improved model sensor cavities were expanded by removing the material between them allowing for more inboard placement of pressure transducers.

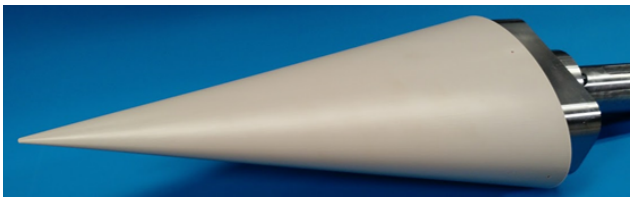

Figure 4.4: Improved 38.1% scale PEEK elliptic cone model.

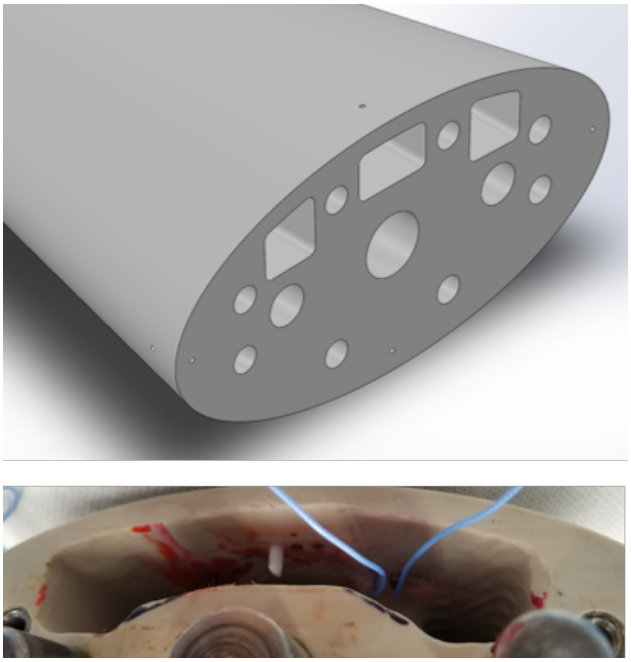

Figure 4.5: 38.1% Scale model sensor cavity. Above: As designed CAD drawing. Below: Extended sensor cavity.

4.1.3 Initial PEEK Manufacturing Attempt

A model was initially machined on a 3-axis computer numeric control milling machine. This type of mill is only capable of machining one side of the 2:1 ellipse at a time. A 152 mm diameter unfilled PEEK rod was mated to a holding assembly and one side was machined. The PEEK was then flipped in its mounting fixture and the other side machined. Small misalignments in the mounting fixture were magnified near the model nosetip region and resulted deviations from the design model shape. The resulting model had a noticeably sharper nosetip. Small ridges were present near the model nosetip, along the model attachment lines.

This error in alignment was not quantified and without advanced scanning of the model deviations from the designed shape are uncertain. The errors were however noticeable enough that it was decided to attempt to machine an improved model. This cone was used as a test dummy to prepare and perfect the IR techniques and test procedures. Several IR videos of this model exist

and could potentially be used as a secondary study case if desired.

4.1.4 Improved Cone

A second PEEK model was machined utilizing a 4-axis CNC milling machine. This machine included the ability for the model to be rotated about its central axis. A mounting block and shaft were machined from stainless steel. A 178 mm diameter rod of PEEK was procured and the sensor cavities and dowel holes were machined into one face of the rod. Dowel rods were pressed into the mounting cavities and secured with epoxy. The mounting block was then pressed onto the dowel rods. To reduce the amount of machining time necessary on the 4-axis machine, the rod and mounting block were attached to a CNC lathe and the rod was reduced into an oversized cone. The model was then machined using a ball end mill on the 4 axis machine. The machine was programmed to perform passes from the nosetip, along the streamwise direction down the cone surface. The model was then rotated by the machine and another pass made. The result of this machining was a much improved geometry as can be seen in the Fig. 4.6 photographs of the nosetips of the initial and improved attempt. The machining process used resulted in periodic peaks and valleys extending from the model nosetip along rays of the cone. The ridges are imperceptible over the first 100 mm of the cone. The depth and spacing between ridges are quite small roughly 150 mm along the cone but expand with distance along the cone. Initially the model was machined by stepping in 1° increments. This resulted in pronounced peaks and valleys and so the machinists were asked to reduce the increments to half a degree and make another pass. This roughly doubled the machining time but resulted in a much smoother model surface. Further reducing the rotation increment would have further smoothed the surface but also increased machining time by the factor of the reduction. This machining roughness was deemed acceptable and characterized

as discussed in Subsection 4.1.6. A machining error during the machining process resulted in the ball mill impacting the model surface. This produced a divot in the model surface roughly 238 mm downstream of the model nosetip and 10 mm from the model centerline. This divot was not observed to have an impact in the local heating as measured with IR thermography and is also discussed in Subsection 4.1.6. Small holes were included at the rear of the cone along the model centerlines and attachment lines. These holes were originally intended to serve as pressure taps for incidence angle determination. These holes were left unplugged throughout the testing presented here.

This cone was utilized throughout the present study.

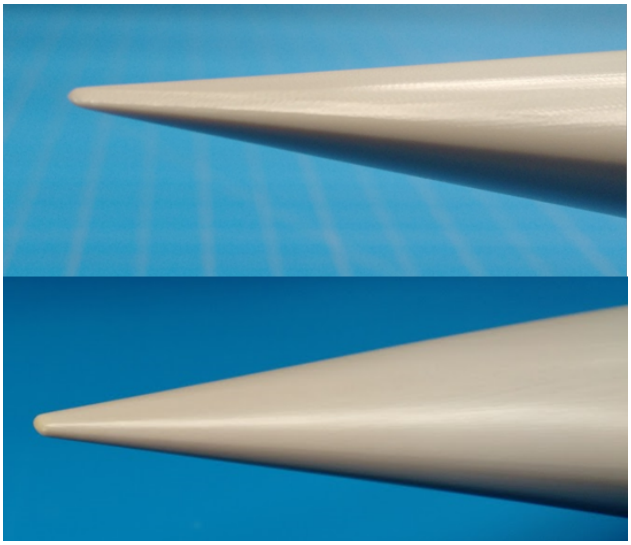

Figure 4.6: Nosetip machining comparison. Above: Initial manufacturing attempt. Below: Improved cone.

4.1.5 Elliptic Nose Tip

The model nosetip geometry was altered from the HIFiRE-5 and ground test model design. The semicircular arc which defines the nosetip results in at a discontinuity in curvature at the junction between the nosetip and the elliptic cone frustum (Choudhari *et al.*, 2009). Such discontinuity has

been shown to be a source of receptivity in low-speed flows (Lin *et al.*, 1992; Saric *et al.*, 2002; Reed & Saric, 2015). Instead of a circular arc, the nosetip of the model constructed and utilized in this campaign is defined by a modified super ellipse which eliminates this discontinuity. In the finished model the shape change vs a semicircular arc is likely within the dimensional tolerance of the machining process but was made as a "best practice" design choice. The super ellipse equation utilized is given as Eq. 4.1.

$$y = B_0 \left[B \left[1 - \left(\frac{A-x}{A} \right)^{2+(\frac{x}{A})^2} \right] + CM\frac{x}{A} \right] \tag{4.1}$$

x is distance in the streamwise direction, B is the nosetip height, A is the nosetip length, M is the slope of the minor axis and C is a tuned parameter and B_0 is a scaling parameter. A MATLAB script originally written by Daniel Charles Mullen was edited by the author to determine B_0 and C via a shooting method. This equation and its coefficients, given in Table 4.1 were input directly into SolidWorks CAD software to define the nosetip geometry.

Table 4.1: Elliptic nosetip parameters.

Parameter	Value
B0	0.891
B	.9454 mm
A	.8364 mm
C	9.45E-4
M	0.1227

4.1.6 As Machined Model Geometry and Surface Roughness Characterization

The model was machined on a 4-axis mill using commercially available Computer Aided Machining software to generate the machining paths. This software takes and translates the CAD model into code usable on the mill. This conversion was performed by the machinists and any loss

in fidelity of the model shape is unknown to the author. Knowing that the model geometry and surface roughness play key roles in the receptivity process and development of disturbances on the model surface, the model was characterized using surface profilometry and micro-CT scans as described in Subsection 3.3.6 and App. B. Table 4.2 highlights RMS and Peak to Peak roughness at several streamwise locations as measured with the laser surface profilometer. Table B.3 in App. B provides a similar table for all locations measured.

Table 4.2: Surface roughness at various streamwise locations.

X Location (mm)	RMS Roughness, R_q (μm)	Average Peak to Peak Roughness R_z (μm)
60	1.7	6.7
120	1.6	7.1
180	2.0	9.2
240	2.3	10
300	2.8	11.4

The general trend observed is consistent with the machining techniques used. The RMS roughness values vary from below 2 μm near the model nosetip to near 3 μm near the rear of the cone with peak to peak roughness from 5 to 12 μm. As discussed in Subsection 4.1.4, the machining process utilized produces peaks and valleys aligned with rays of the cone along its surface. This roughness potentially impacts the transition process on the surface of the cone and thus is important to characterize. These peaks and valleys are imperceptible over the first 100 mm off the cone. The ridges become more visible near 150 mm downstream of the nosetip and are discernible in profilometer scans in this area. The spacing between neighboring ridges is small, less than 0.5 mm initially and 0.8 mm near the base of the cone. Fig. 4.7 is a photograph of the rear of the cone with lighting set up to highlight the roughness present. Visible in the left-hand side of the image is PCB 3D with the center PCB locations near the center. Laser and stylus profilometer scans show that

the ridges are roughly 11 μm peak to peak.

Figure 4.7: Image of rear of cone, lit to highlight machining roughness present.

A machining error resulted in a small hemispherical divot in the surface of the cone. The divot is located 238 mm downstream of the model nosetip and 10 mm off the model centerline. The divot was scanned using the laser profilometer and found to be 80 microns in depth and 3.5 mm in diameter. It is visible in some cases in the ACE IR thermography results of Chapter 6 in the top half of the images. At this downstream location on the cone it is not believed to significantly impact the development of disturbances on the cone. It does not visibly alter the heating observed in the IR data.

The author's experience has shown that the roughness reported by machine shops typically underestimates the actual roughness as measured with the laser profilometer. The laser profilometer has also been seen to have a noise floor; scans of material polished below a certain roughness still return measurements of higher roughness. This noise floor appears to vary with material tested and is likely a function of the spot size of the laser coupled with motion introduced by the traverse stages. Unpublished measurements have shown the noise floor to be higher for PEEK than for

aluminum. By 60 mm downstream the measurements are above the laser profilometer noise floor and confidence in the measurements is improved. Scans near 300 mm downstream were used to compare the laser profilometer to a more accurate contact profilometer. The scans are shown in Fig. 4.8. The scans are not at identical locations and so the roughness line plots are not expected to be identical but should show the same statistical properties. The stylus profilometer gives a more clean signal with the PSD of the roughness showing a distinct peak at 0.8 mm. The laser profilometer is more noisy but shows similar spectral content. Computed roughness properties are shown in Table 4.3. Given the good agreement further profilometer measurements were not made due to their time consuming nature and inherent risk of damaging the measured surface.

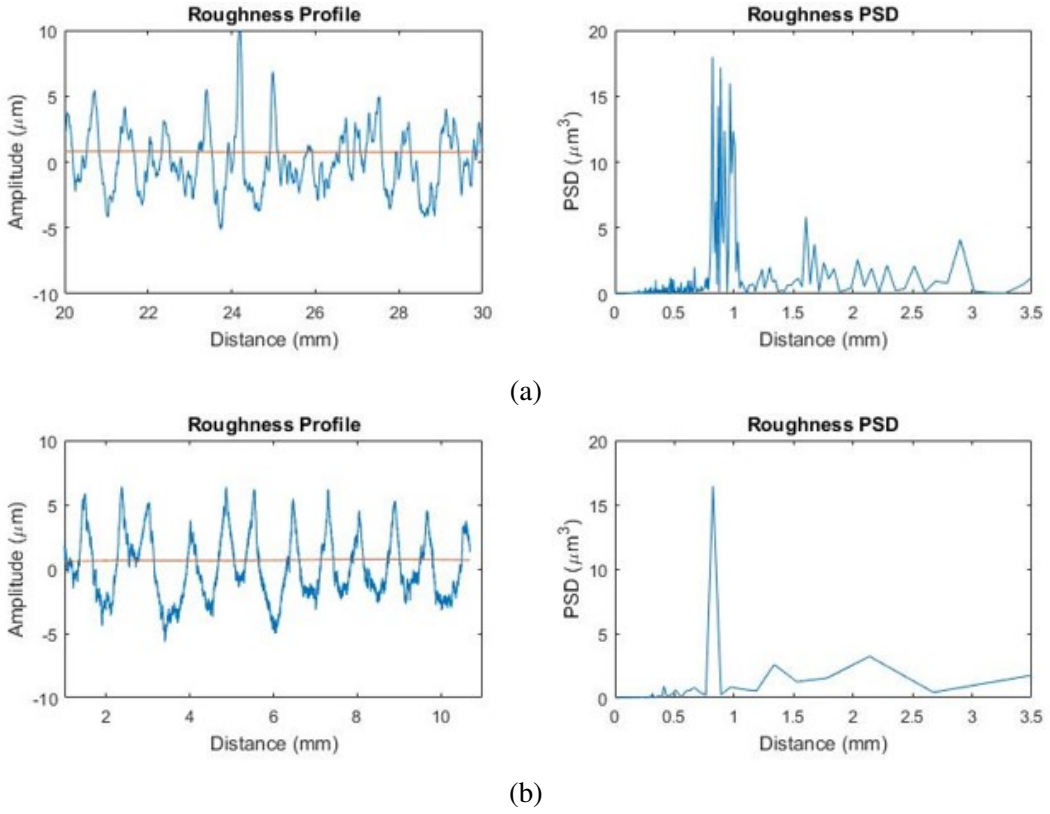

Figure 4.8: Comparison of profilometer systems: sample scan near 300 mm downstream of model nosetip. (a) Laser Profilometer (b) Contact profilometer.

Shown in Fig. 4.9 are the 3-D CAD model and the Micro-CT scan of the model nosetip. Qual-

Table 4.3: Surface roughness statistic comparison between laser and contact profilometer. Improved PEEK model near 300 mm downstream.

Roughness Parameter	Contact Profilometer	Laser Profilometer
R_a	2.2 µm	2.2 µm
R_q	2.6 µm	2.7 µm
R_z	10.8 µm	11.4 µm

itatively the nosetip is very similar to the as designed geometry but it not perfect. At the time of writing analysis of these scans is underway to provide qualitative comparison.

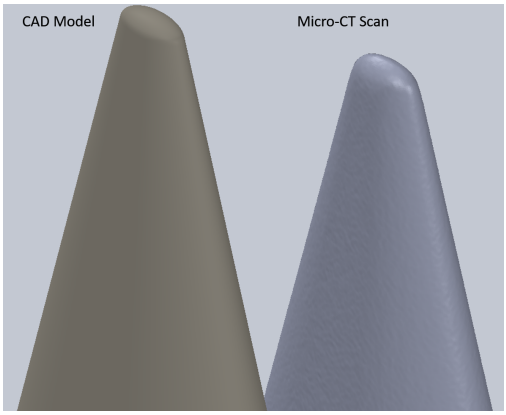

Figure 4.9: Comparison between CAD model (left) and micro-CT scan of PEEK model (right)

4.1.7 Surface Pressure Transducers

As described in Subsection 3.3.2, the model was instrumented with surface pressure transducers to characterize fluctuations within the boundary layer. As will be discussed in Chapter 6, initial IR-only runs were conducted and revealed streaks of increased heating leading into a large lobe of increased heating near the model shoulder in the expected region of dominant crossflow instability. To examine this instability two sensor array patterns were installed in the model. The first was an array of three Kulite pressure transducers. This array was arranged to allow the measurement of

wave angle and speed of any potential traveling crossflow instabilities. This technique follows the work of Poggie *et al.* (2000), and spacing was chosen to mimic Borg & Kimmel (2017*b*)'s successful investigation of travelling crossflow under quiet flow in the Purdue BAM6QT. The array's position on the model was chosen to place it within the region of observed elevated heat flux on the model under noisy flow in the ACE facility. Three PCB transducers were placed on the model to align with three of the streaks observed in the initial IR runs. These transducers were selected due to their high frequency response. Back of the envelope scaling arguments ($U_e/2\delta$ (see Craig & Saric, 2016, for example)) reveal expected frequencies in the 100's of kHz. CFD analysis such as those presented in Kocian *et al.* (2017) confirm that there is expected content outside of the Kulite's 100 kHz linear frequency response range.

As explained in Sec. 6.5, following runs of this configuration of transducers, additional PCB transducers were installed 25 mm directly upstream of the initial set. This allows for a streamwise comparison of disturbance magnitude. The placement was chosen to be directly upstream due to the observed position of the streaks in IR in ACE. The forward position of these transducers was forward of the pocket machined in the back of the model. This required holes to be drilled through the bottom surface of the model. This increased the difficulty of mounting and sealing the pressure transducers. A Kulite transducer was also added directly behind PCB 2D to examine low frequency content in this position. The mounting holes on the bottom of the cone are shown in Fig. 4.10.

Pressure transducers were additionally placed to examine the centerline transition front. A PCB transducer was placed at the model centerline and at 5 mm on either side. The resulting locations of all sensors are presented in Table 4.4 and Fig. 4.11.

All transducer holes were drilled at the diameter of the transducer and hand reamed one size larger to be a tight fit to the transducers. Transducers were held into the model using fast drying

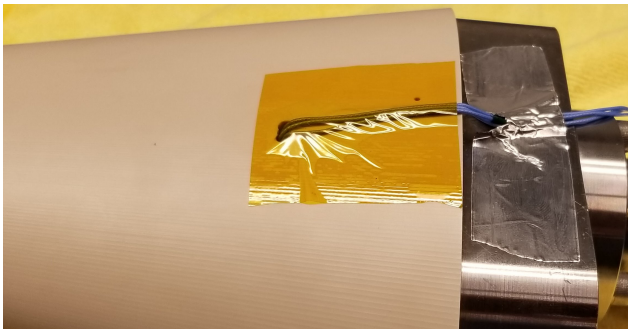

Figure 4.10: Photograph of upstream mounting holes with transducers installed and cables secured using Kapton tape.

Table 4.4: Sensor mounting locations. X is distance along streamwise direction from nosetip and Y is distance from model centerline plane.

Transducer	X (mm)	Y (mm)	Transducer	X (mm)	Y (mm)
Kulite 1	297.6	-25.3	Kulite 2	300	-25.3
Kulite 3	302.4	-23.8	Kulite 4	305	23.4
PCB 1D	300	28.4	PCB 1U	275	28.4
PCB 2D	300	23.4	PCB 2U	275	23.4
PCB 3D	300	18.4	PCB 3U	275	18.4
PCB 4	310	5	PCB 5	310	0
PCB 6	310	-5			

nail polish. Nail polish was placed slightly inside the back side of the mounting hole and at the base of the transducer. Vacuum was pulled with a manual pump on each potted transducer to insure a proper seal. The nail polish proved to be strong enough to withstand repeated runs in the tunnels and still be easily removed with the application of acetone. An example of the nail polish seal is shown in Fig. 3.6.

4.1.8 Instrumented Model DAQ

The M6QTDAQ setup described in Subsection 3.2.4 was utilized for all instrumented model runs. All channels were acquired at 2 MS/s per channel for 100 ms sample lengths. PCB signals were passed through 1 MHz, 8-pole, Bessel low-pass filters with unity gain for anti-aliasing.

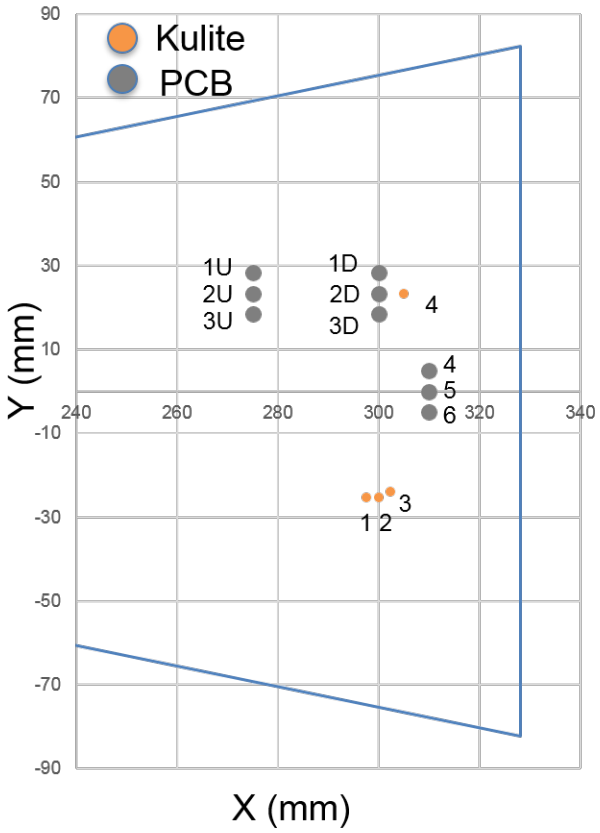

Figure 4.11: Diagram of sensor locations.

Similarly Kulite signals were passed through 8-pole, Bessel, 200 KHz low-pass filters with unity gain. The filtering units were housed within four 2-channel Krohn-Hite FMB3002 chassis. In tests within the ACE facility, Kulite 3 was filtered using a 100 kHz, 12 dB/octave unity gain low-pass filter on a Stanford Research Systems SR-560 preamplifier.

The low passed signals of each PCB as well as the low passed DC coupled Kulite signals were acquired and written to a binary file during the run. These signals were acquired as uncalibrated voltages. This file was then unpacked and processed using a series of MATLAB scripts. Sample processing scripts are included in App. E. In both facilities settling chamber pressure and temperature as well as static pressure were acquired. Tunnel conditions were down sampled by averaging over the sample length.

Frequency response of the filters used was examined using an NI oscilloscope card and high frequency signal generator. A square wave was split from the signal generator directly into the oscilloscope and through the filter into the oscilloscope. The response is then computed and averaged over 100 pulses and the frequency response output. The Bessel filters utilized have a very flat response in their passbands and very gradual roll off reaching -3 dB attenuation at their respective 200 kHz and 1 MHz cutoff frequencies. The filters also exhibit a linear phase response across this range.

4.2 Tunnel Configuration and Run Procedures

4.2.1 ACE: Model Mounting

Typical run procedure in both facilities is to preheat the tunnel by blowing heated air through the facility subsonically. In previous campaigns, test articles were mounted within the tunnel from run to run. This exposes the model to the typical facility preheat, elevating the model surface temperature to near adiabatic wall conditions. New procedures for tunnel runs were designed around the desire to run models at a near room temperature wall condition to allow direct comparison with results from the Purdue BAM6QT and other impulse facilities. The ACE facility test section was equipped with removable aluminum doors allowing for fast access to the test section. The model was mounted to a sting secured to the removable tunnel door. This mounting also had provisions for model wiring which was passed through a single element Conax split compression seal fitting. The bundle of wires was pressure sealed using adhesive wax, which was found to adhere well to the Conax fitting and conform to the wire bundle preventing any leaks. A photograph of the improved PEEK model mounted with in the tunnel is shown in Fig. 4.12. This setup allowed the tunnel to be preheated with a blank door in place and the model to be quickly installed with minimal cooling

of the tunnel.

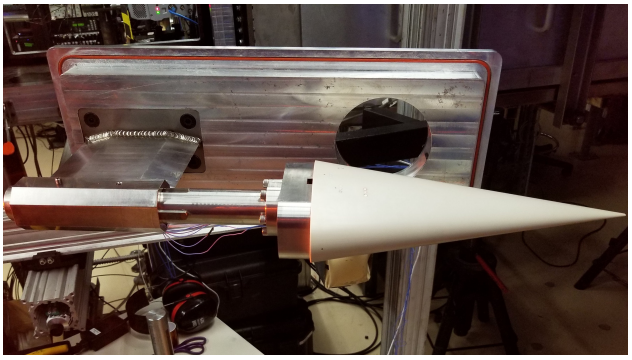

Figure 4.12: ACE mounting example.

4.2.2 ACE: IR Camera Positioning

For all runs in the ACE facility the IR camera was oriented to view the model from above through a 152 mm diameter 9.5 mm thick IR transmissive zinc selenide (ZnSe) window purchased from II-VI Infrared. The camera was rigidly mounted to a cage above the test section constructed of XT-95 optical rail. Images were acquired through the center and upstream windows of the roof depending on the model position within the tunnel. Fig. 4.13 shows a CAD render of the model within the ACE test section and a cartoon diagramming the position of the IR camera relative to the model.

4.2.3 M6QT: Model Mounting

Models in the M6QT were mounted to a motion stage capable of translating in the tunnel flow direction allowing precise placement of models relative to the nozzle exit plane. During previous efforts, models were aligned and secured in place for the duration of a test campaign of several dozen runs. This minimized run to run variation of model alignment. Previous tests have revealed boundary layer instabilities to be very sensitive to model alignment with small changes in angle of attack resulting in large changes to the observed second mode frequency on a sharp cone: as much

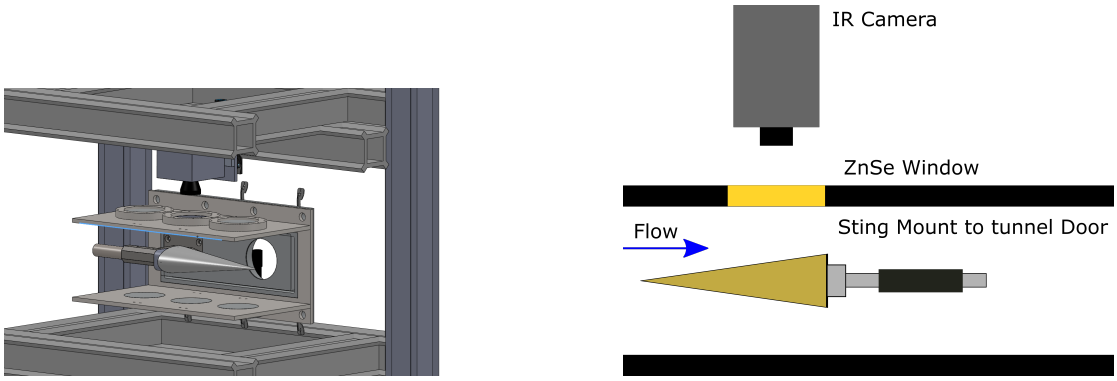

(a) (b)

Figure 4.13: ACE model and IR camera mounting setup. (a) CAD model (b) Cartoon.

as 8.4 kHz-per-0.1° misalignment in the case of Hofferth (2013). Because of the desire to run the model at a close to room temperature wall, runs for this campaign were conducted by inserting the model after a tunnel preheat. In comparison to the ACE facility, the M6QT's enclosed free jet design makes installing the model a somewhat more difficult process. The mounting provisions in the facility are visible in Fig. 4.14. The model and shaft were withheld from the tunnel during the preheat. The bolts visible at the top of the sting were removed and the sting left in place during a preheat. Immediately after a preheat and closing the manual tunnel supply valve, the tunnel doors were removed and two operators (the author and a lab mate) carefully placed the model into the tunnel and secured it to the sting. Care was taken to avoid contacting the nozzle with the model and protective gloves were worn to avoid burns from contact with the hot tunnel interior. The model yaw and roll relative to the tunnel floor was measured using a digital inclinometer with a factory stated accuracy of $\pm$ 0.05°. Due to the difficulty and time constraint involved, alignment was deemed satisfactory if the absolute yaw angle was less than 0.1°. This procedure also required that sensor power supply and signal cables be reconnected before each run. Sensor connectors were color coded and labeled to improve the accuracy and speed of this process. Transducer power supplies were activated similarly to in the ACE facility to avoid heating of the model surface by the

transducers. The doors to the facility were then replaced, allowing positioning of the IR camera for optimal viewing.

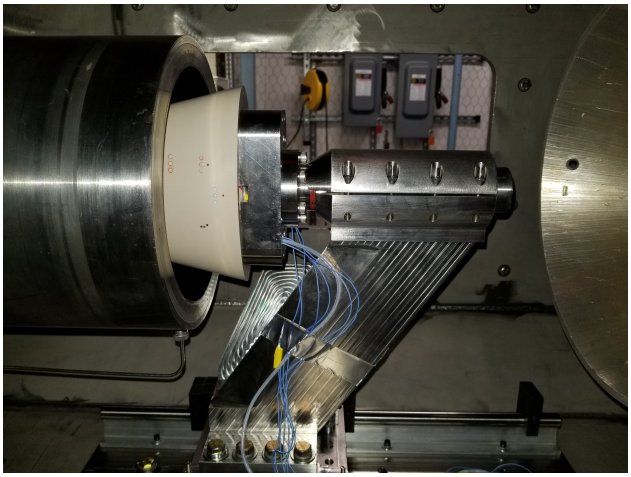

Figure 4.14: Photograph of model mounted in M6QT. Sting traverse is partially visible at the bottom of the figure.

4.2.4 M6QT: Model Positioning

The model position within the M6QT was restricted by several factors. The enclosed jet design of the test section means that the flow exits the nozzle as an over-expanded jet. Test articles must be placed within the facility so as to avoid the impingement of the nozzle exit shockwaves on the model. The other constraint is that shockwaves generated by the model should not impinge on the nozzle wall. The resulting shockwave boundary layer interaction could result in a separated region and tunnel unstart. The large size and half angle of the elliptic cone geometry limited its positioning within the tunnel. The model was positioned so that the base of the cone extended 38 mm past the nozzle exit. Schlieren photography was used to confirm that the nozzle shockwave did not impinge on the model surface. Fig. 4.15 is a sample schlieren image showing the nozzle exit on the left hand side and the end of the model toward the right. The model shock is clearly visible and was not observed to impinge on the model surface for any Reynolds number tested. Fig. 4.16 is a rendering

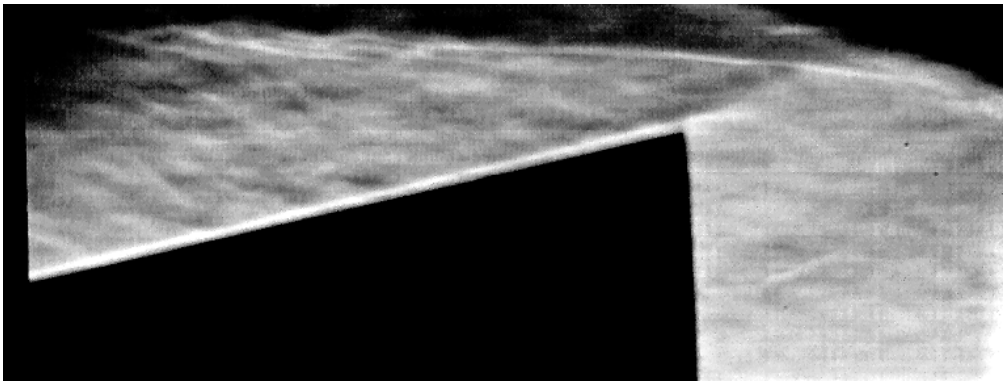

Figure 4.15: Schlieren image of PEEK HF-5 Model in M6QT.

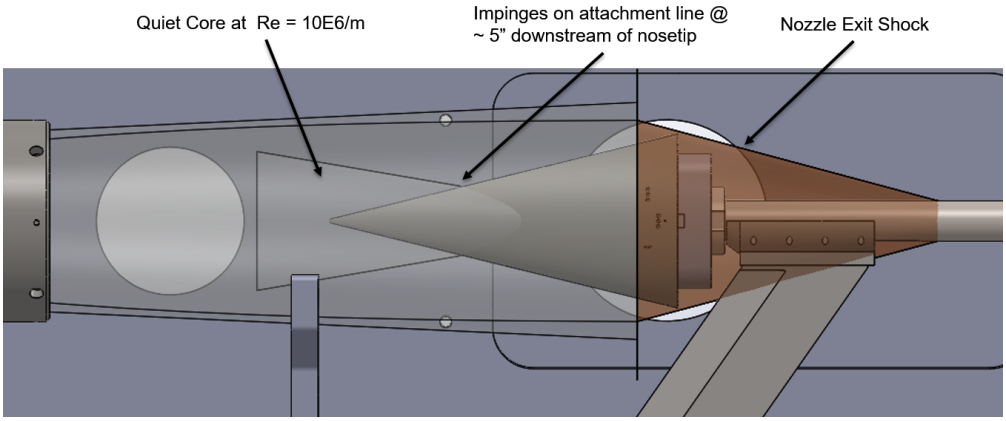

Figure 4.16: CAD model of the elliptic cone model within the M6QT nozzle and test section. Quiet core and nozzle exit shock are indicated.

of the model within the M6QT with the edge of the tunnel quiet core and nozzle exit shockwave highlighted. The quiet core is approximated from the freestream disturbance characterization of Hofferth (2013) and represents the location in the flow at which pitot fluctuations reach $\sim 1\%$. At Re = 10×10^6/m the quiet core is estimated to impinge on the model roughly 127 mm downstream of the model nosetip.

4.2.5 M6QT: IR Camera Positioning

The positioning of the model so far within the nozzle presented a challenge in terms of viewing the model with the IR camera. The M6QT is provisioned with one 203 mm window in each of its doors. This window allows the nozzle exit and several inches downstream to be viewed. This

would have limited the view of model to the 38 mm region downstream of the nozzle exit. To view more of the image the tunnel door was rotated 180 degrees placing the window further aft in the tunnel and allowing the IR camera to be angled through the window to allow approximately 75 mm of the model to be visible. The angle between the normal to the major axis plane and the IR camera was roughly 20°. This setup is shown in Fig. 4.17.

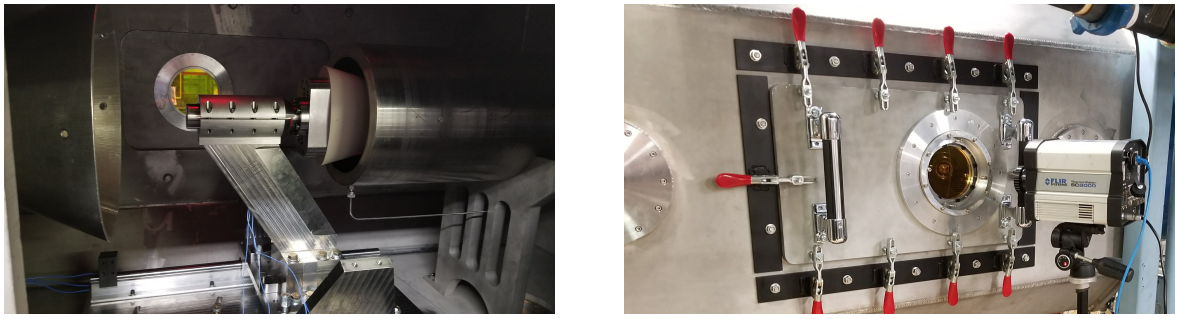

(a) Photograph of model mounted in M6QT with IR window installed.

(b) Tripod mounted IR camera in typical position outside the tunnel.

Figure 4.17: M6QT IR mounting setup

4.3 Uncertainty Analysis

4.3.1 Freestream Properties

Tunnel freestream conditions are computed using settling chamber total pressure and temperature as well as static pressure measured at the wall of the facility nozzle downstream of the limiting characteristic. Temperature is measured directly in both facilities using type-K thermocouples which have a typical accuracy given as the greater of $\pm$ 2.2 K or 2% of the measured temperature. In ACE total pressure is measured with an Endevco 8540-200 pressure transducer with factory stated combined uncertainty (temperature, hysteresis, repeatably and non-linearity) of 2.4% of full-scale output (FSO). The static pressure is measured with a Baratron 631C-10 with a manufacturer stated uncertainty of 0.5% of its reading. The uncertainty is assumed to be 5% to account

for the uncertainty due to the static pressure orifice and tubing. In the M6QT the static pressure is measured by a MKS 902 vacuum transducer with stated uncertainty of $\pm$ 1% of the reading. Total pressure is measured using a MKS Baratron 615A high-accuracy capacitance manometer with factory stated accuracy of $\pm$ 0.12% of its reading.

Mach number and Reynolds number are properties derived from these measured quantities. The ACE facility standard error propagation calculations are provided by Leidy (2019). For Re = 5×10^6/m the propagated uncertainty in Mach number and Reynolds number are 1.5% and 7% respectively. Both uncertainties increase with decreasing Reynolds number. In the M6QT the facility Reynolds number is based on the assumption of a core Mach number of 5.9. This value was experimentally measured by Hofferth (2013). The resulting uncertainty in Re is assumed to be 10%.

4.3.2 Pitot Pressure Measurements

Pitot pressure measurements were made using the probe detailed in Subsection 3.3.2. The stated uncertainty is $\pm$ 0.1% of its 34.5 kPa full scale output. At standard ACE run conditions this results in uncertainties in the measured pressure of between 1% at the lowest Re condition to 0.2% at higher Re conditions. An additional source of uncertainty is in the calibration of the pressure transducer. The sensor was calibrated at room temperature using a calibrated vacuum gauge. During a typical run the probe experienced temperatures as high as 430 K during a typical run. This is within the factory temperature compensated range but may result in a thermal zero offset shift of 3% and thermal sensitivity shift of 3%. Data were acquired at 400 kHz for 100 ms. PSD estimates were performed with 390 averages resulting an in random error uncertainty of 5.1% at a given PSD value. RMS values reported were created by integrating under the PSD using the

trapezoid rule which tends to overestimate the RMS values obtained.

4.3.3 Hotwire Anemometry

A major contributor to hotwire uncertainty is the calibration performed. The hotwires in this study were calibrated in the freestream of the ACE tunnel by sweeping through the mass flux range. Initial calibrations are reported by Leidy *et al.* (2018). The calibrations show temperature dependence which seen to be correctable by Leidy *et al.* (2018) but was not available for the data presented here at the time of writing. Uncertainties in the mass flux RMS and spectral data are a result of the PSD estimated used in their computation. Data were acquired at 2 MHz for 100 ms. PSDs were computed using 390 averages again resulting in 5.1% random error in amplitude at a given frequency. Positional accuracy within the tunnel is similar to that of the freestream pitot probe measurements with an estimated uncertainty of 1 mm.

4.3.4 Surface Pressure Transducers

The Kulite XCE-062-15A transducers utilized have similar error and temperature shift characteristics as the freestream pitot probe with factory stated uncertainty of $\pm$ 0.1% of its 103.5 kPa range. These probes were calibrated at room temperature and based on IR measured surface temperature, experience a maximum 50 K increase in temperature during a run. This results in a $\pm$ 1% thermal zero and sensitivity shift. PCB 132B38 transducers are provided with a single point factory calibration. Work has shown that these factory calibrations vary in accuracy and work is underway at Purdue university to provide better calibrations (Gray *et al.*, 2017). PSDs were computed using 390 averages resulting in 5.1% random error in amplitude at a given frequency.

4.3.5 IR Thermography

A discussion of the IR camera calibration process and assumptions made in processing of the IR images is given in Subsection 3.3.1. The 1-D heat conduction equations utilized to calculate heat flux rely on the surface temperature measured and the thermal properties of the PEEK. The properties utilized here were provided by the manufacturer and are believed to represent room temperature properties. Guelhan *et al.* (2008) observed that these material properties vary with temperature. For the range of temperatures observed in the present study (300-350 K), the variance in density and thermal conductivity is small but C_P & thermal diffusivity vary by up to 10%. Guelhan *et al.* accounted for this variation in their measurements. They also performed a sensitivity study and estimated that for their test environment the worst-case scenario uncertainty in the St measured was $\pm$ 15%. Despite the narrow range of PEEK temperatures observed in the present work, this would seem to indicate that the heat flux observed in the present study is likely more uncertain as the variation of PEEK properties with temperature was not considered. A major contributor to error in the surface temperature measurements is the assumption of the calibration that the matte black aluminum and the model PEEK surface have similar emissivity. The emissivity assumed in the FLIR ResearchIR calibration tool is 0.98. This is likely higher than the emissivity of PEEK which has been estimated as between 0.88 and 0.93 (Borg & Kimmel, 2016). This overestimation of emissivity would lead to an underestimation of the measured temperature of the PEEK surface.

5. RESULTS: ACE FACILITY FREESTREAM CHARACTERIZATION

5.1 Freestream Measurement Overview and Data Acquisition Settings

Previous pitot measurements indicated that freestream pitot pressure fluctuations were reduced as measurements were made upstream of the nozzle exit (see Borg *et al.*, 2015*a*, for example). The present instrumented model was tested with its nosetip at three different stations to take advantage of this variation in tunnel freestream noise. To quantify the noise levels present at each of the three model nosetip positions, freestream pitot and hotwire measurements were made. Pitot runs were conducted by continuously varying the total pressure of the tunnel, effectively sweeping through the tunnel operating Reynolds number range. Pitot pressure data were obtained with a Kulite XCEL-100-5A transducer mounted in pitot configuration. This probe is described in Subsection 3.3.2. Both the DC and AC coupled signals were acquired. Results presented here were computed using the AC coupled signal. The AC coupled (high-pass filtering at 842 Hz) output signal from the transducer was filtered using an 8-pole 100 kHz low pass Bessel filter. Pitot Pressure data were acquired during a Re sweep at 400 kHz for 100 ms per acquisition. Power spectral density estimates were made using Welch's method with a Hann window of 1024 points with 50% overlap. This gives a frequency resolution of approximately 390 Hz. RMS fluctuation levels were computed by integrating under the PSD from 0-100 kHz and taking the square root. Hotwire data were acquired at 500 kHz and PSDs were similarly estimated using a Hann window of 1024 points. The resulting frequency resolution is approximately 488 Hz. RMS fluctuation levels were computed by integrating under the PSD from 9-100 kHz and taking the square root. Freestream measurements at the tunnel centerline were made at the three nosetip position stations as well as

the nozzle exit plane. These positions and the nomenclature used throughout the experiments is given as Table 5.1.

Table 5.1: ACE model nosetip test stations.

Station	Position of probe face relative to nozzle exit
DS (Downstream)	63.5 mm downstream
Nozzle Exit Plane	At nozzle exit plane
Mid (Midstream)	12.7 mm upstream
US (Upstream)	152.4 mm upstream

5.2 Freestream Pitot Measurements

5.2.1 Centerline Nosetip Location Measurements

Pitot pressure RMS fluctuations, normalized by average pitot pressure, are given as Fig. 5.1. The fluctuation levels begin at relatively low values ($\leq$0.6%) for Re $< 3 \times 10^6$/m. These levels are an order of magnitude higher than the standard definition of quiet flow ($P'_{t2} <= 0.05\%$ (Schneider, 2001)) but below what is typical of comparable conventional facilities. As Re/m is increased, fluctuation levels rapidly increase between 3-3.5 $\times 10^6$/m and then decrease above 4.5×10^6/m. The fluctuation levels were comparable at the MID, nozzle exit and DS stations at all freestream Re tested. However, at 152.4 mm forward of the nozzle exit, the RMS fluctuations were about 2.5$\times$ lower the level of those at the downstream stations for Re $< 3 \times 10^6$. This ratio subsequently decreases from about 1.5 to 1.1 as Re/m increases from 3.5×10^6 to 7×10^6. Plotted in Fig. 5.2 are PSDs of the freestream pitot fluctuations at the DS station for several Reynolds number conditions. The peak visible in Fig. 5.4 at roughly 10 kHz below Re/m = 3×10^6, was not seen in the hotwire data obtained at the same location and is seen in all the pitot probe PSDs. It is believed to be electronic noise. The PSDs show that the increase in fluctuation level in Fig. 5.1 above is due initially to frequencies in a band below 10 kHz. Across the freestream noise jump this band grows

and then is followed by broader spectrum noise with content present above the sensor noise floor from 0-100 kHz. This content and trend is similar in profile at each station with the magnitudes lower at the furthest upstream location as seen in Fig. 5.3 and Fig. 5.4.

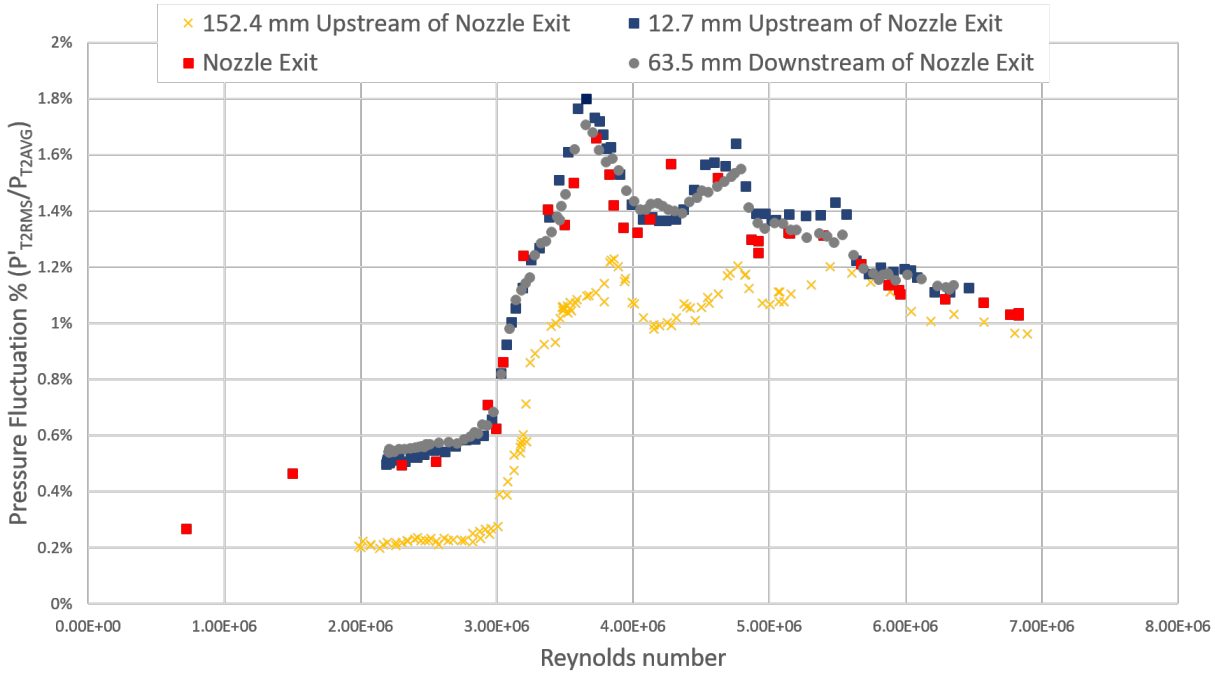

Figure 5.1: Freestream pitot pressure fluctuation levels. ACE tunnel.

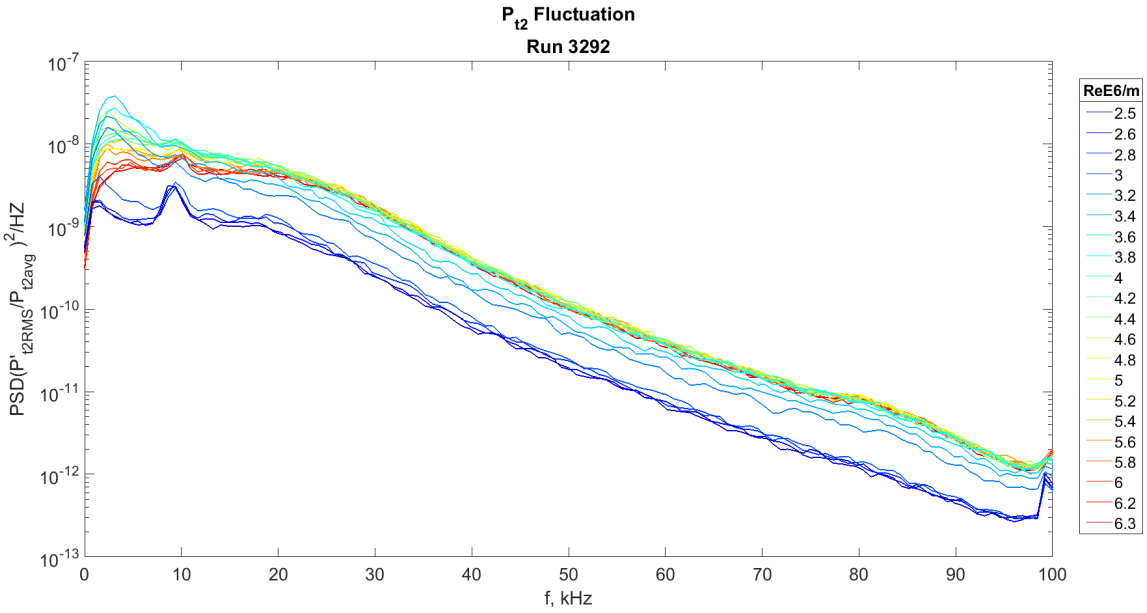

Figure 5.2: PSD of freestream pitot pressure fluctuation DS station.

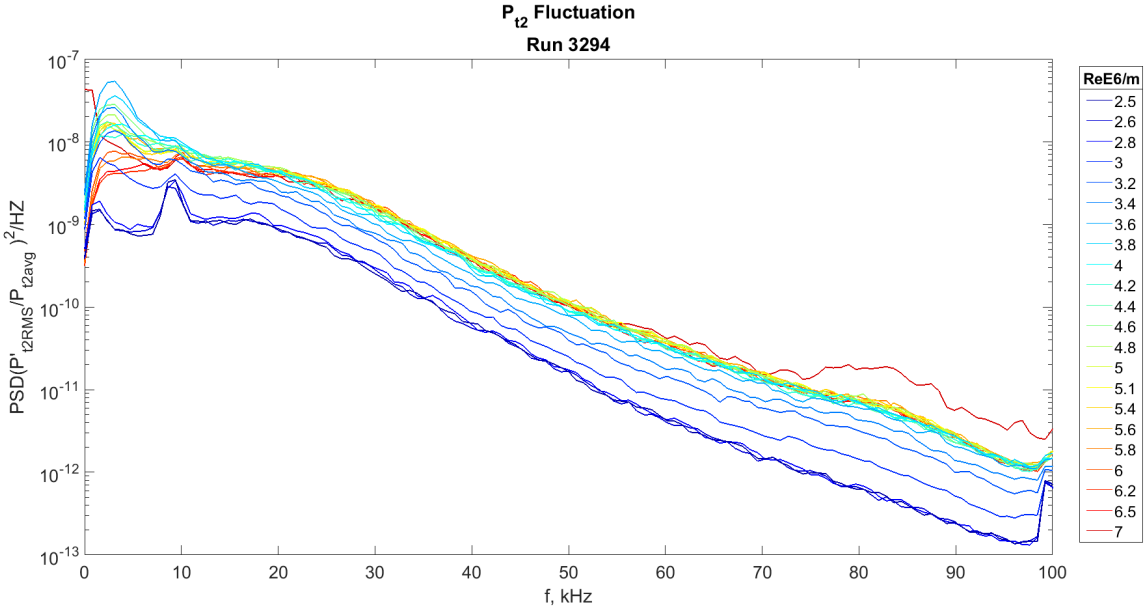

Figure 5.3: PSD of freestream pitot pressure fluctuation MID station.

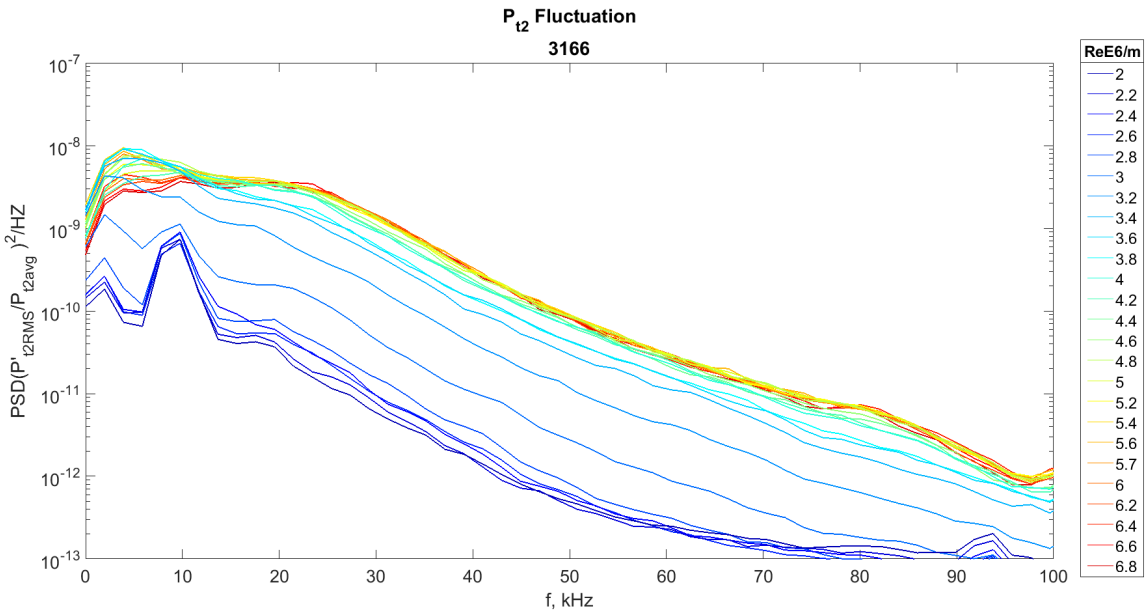

Figure 5.4: PSD of freestream pitot pressure fluctuation US station.

5.2.2 Spanwise Uniformity

Traverses of the tunnel were made in the direction normal to the tunnel floor at centerspan. The facility was held at a constant Reynolds number while the probe was traversed. The probe acquired 100 ms of data at each position. The probe orientation and traverse direction are given in Fig. 5.5. Pitot pressure fluctuations measured vs position for the series of Reynolds numbers tested is given in Fig. 5.6. At the lowest Reynolds numbers, fluctuation levels are uniform from top to bottom of the scan range near 0.5%. As Re is increased, the region of low disturbance flow at the core of the facility shrinks with fluctuation levels off the centerline increasing notably on either side of the centerline. At Re 3×10^6 levels are elevated immediately off the centerline and at 3.5×10^6 the fluctuation levels have snapped to a higher level between 1.5 and 2%. This is in line with the centerline pitot measurements of the previous section. The wedge-shaped rise in fluctuation levels reminiscent of the quiet core seen in the TAMU M6QT supports the theory that

this increase in freestream noise is due, at least in part, to transition on the walls of the facility nozzle. The traverses also show uniformity in average pitot pressure which is in line with previous experiments by Mai (2014) which showed excellent spanwise and top to bottom uniformity at this Mach number.

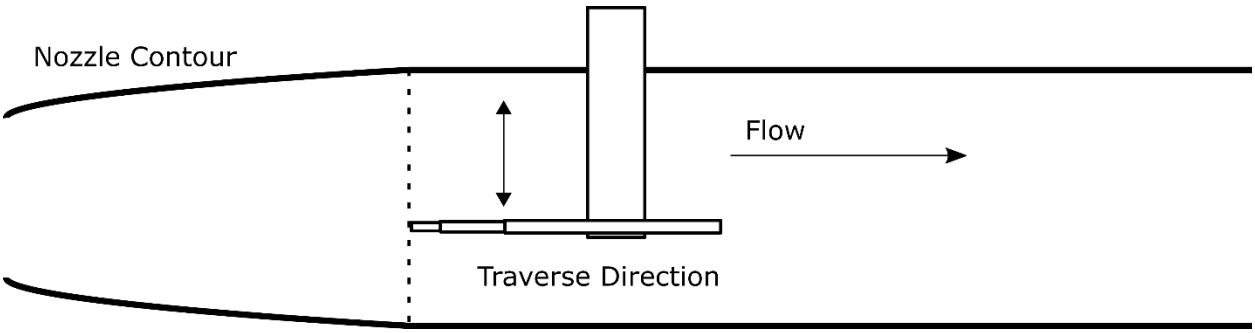

Figure 5.5: Cartoon of freestream pitot probe traverse orientation.

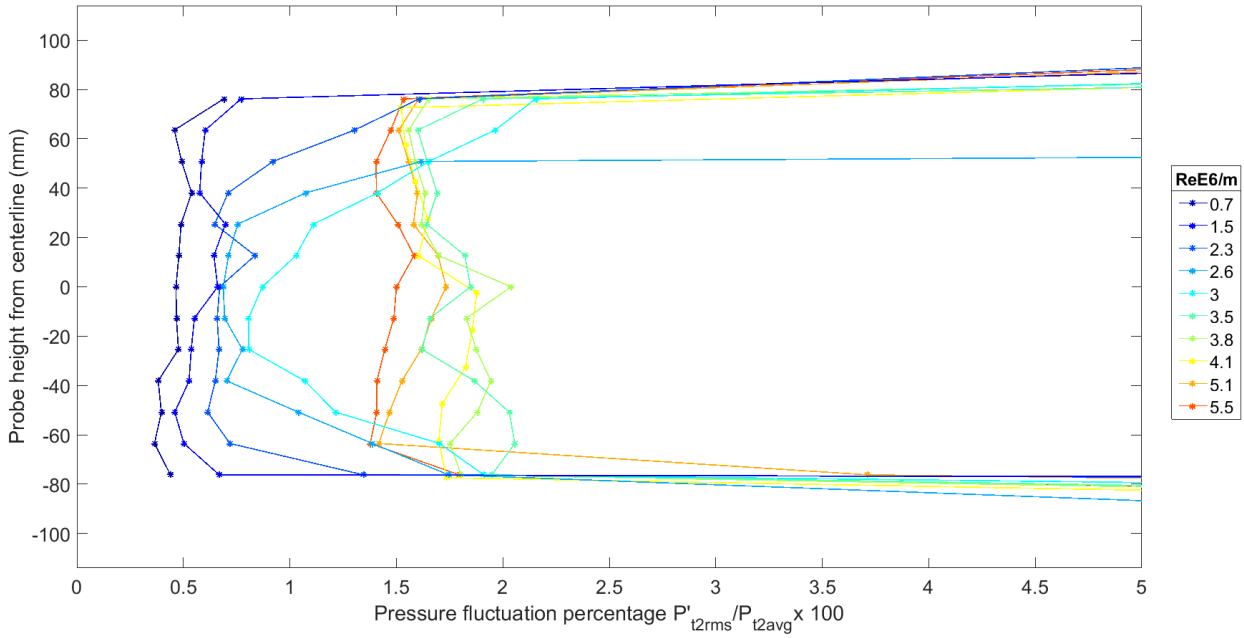

Figure 5.6: Pitot pressure fluctuation levels at nozzle exit.

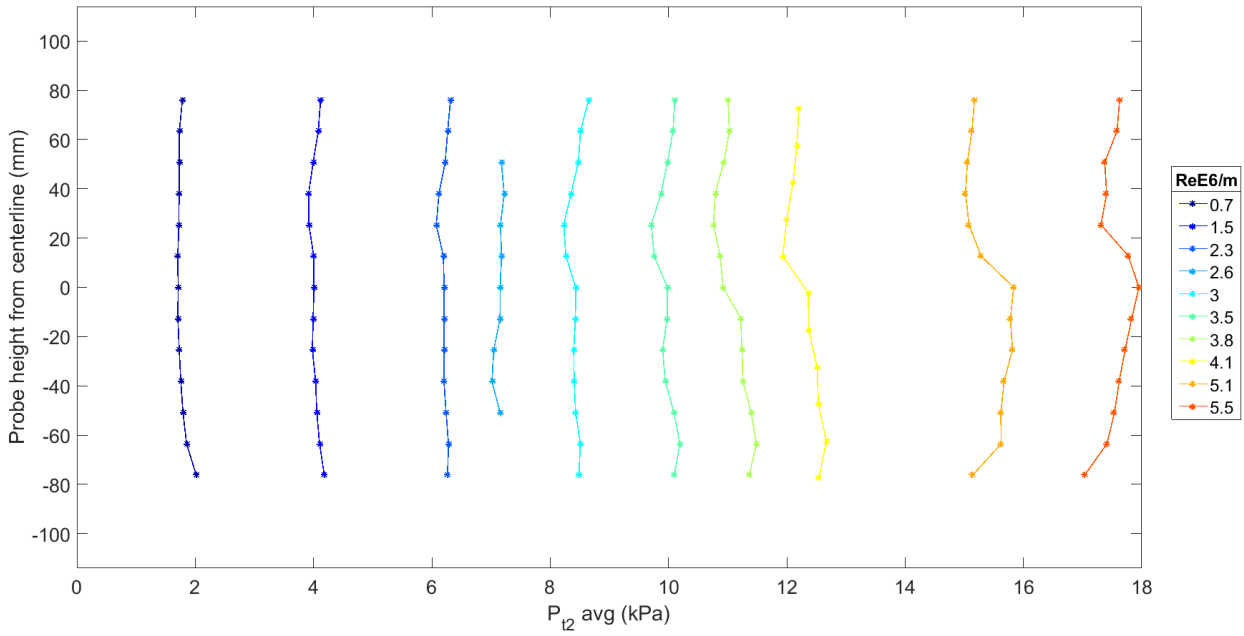

Figure 5.7: Pitot pressure P_{t2} at nozzle exit.

5.3 Freestream Hotwire Measurements

Freestream hotwire measurements were conducted at the tunnel centerline at the 3 streamwise stations. The hotwire was operated using an overheat ratio of $\tau = 0.8$ meaning it is mostly sensitive to mass flux. The normalized RMS mass flux fluctuations are plotted in Fig. 5.8. The same trends observed in the pitot RMS fluctuations are present. There is a $\sim 2\times$ increase in the levels between Re = 3 & 3.5×10^6/m at the MID, and DS stations. There is a roughly $5\times$ increase in fluctuation percentage at the upstream location. As with the pitot data, the large increase in noise occurs at the same unit Reynolds number despite streamwise position within the tunnel.

Waterfall style plots of the PSD of mass flux fluctuations are presented in Fig. 5.9[1]. These plots display frequency on the X-axis and Reynolds number on the Y-axis and are colored by the

[1]The colormap utilized here is the diverging colormap 'balance' from the cmocean package (Thyng, K.M., C.A. Greene, R.D. Hetland, H.M. Zimmerle, and S.F. DiMarco. 2016. True colors of oceanography: Guidelines for effective and accurate colormap selection. Oceanography 29(3):913. http://dx.doi.org/10.5670/oceanog.2016.66). The colormap is divergent with the center representing the median between the lowest and highest observed amplitude.

log of the amplitude of the PSD at a given frequency and Reynolds number. They are useful for at-a-glance examination of the relative changes in the spectra across a range of Re. Below Re = 3×10^6/m, the bulk of the signal is below 10 kHz and is appreciably more narrow at the upstream station. Near 3.5×10^6/m the spectral content broadens and increases in magnitude and remains relatively consistent to the highest Re tested. The narrow spikes near 10 kHz and 25 kHz appear to be due to non-physical electronic sources.

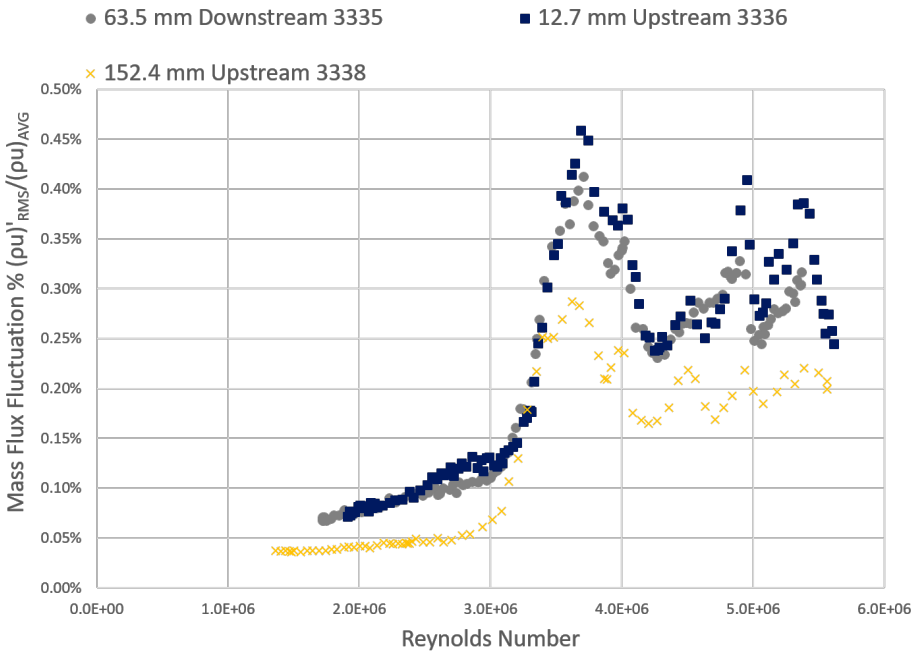

Figure 5.8: Freestream mass flux spectra. Left: DS station, Middle: MID station, Right: US station

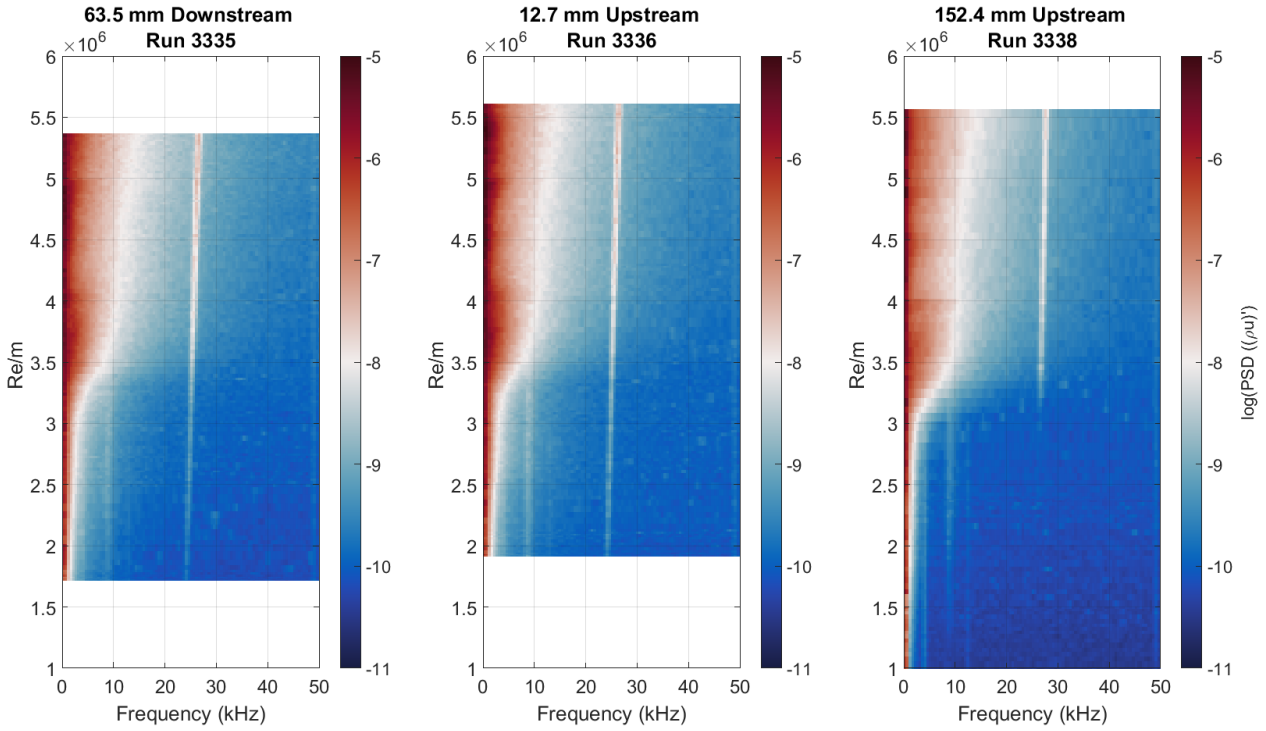

Figure 5.9: Freestream mass flux fluctuation level waterfall plots. From left to right, US station, MID station, DS station.

5.4 Hotwire Measurements Across the Model Shockwave

Freestream disturbances pass through the elliptic model shockwave before interacting with the boundary layer. The effect of the shockwave on the disturbances is complex and is an active research topic in its own right. To gain insight into this effect for the current geometry, hotwire mass flux data were obtained directly above the semi-minor axis 124 mm downstream of the model nosetip, where the probe was traversed across the shockwave. A schlieren image of this configuration during a run is shown in Fig. 5.10 with the model surface, boundary layer and model shockwave visible. Traverses were performed at two Reynolds numbers on either side of the freestream disturbance increase at 3×10^6/m shown in Fig. 5.1 and Fig. 5.8. The results are plotted in Fig. 5.11 and Fig. 5.12 for Re = 2.2×10^6/m and 5×10^6/m respectively. The Y-axis represents

distance relative to the shock position, positive is above the shockwave and negative below towards the surface. As the probe was traversed across the shockwave, there was a large jump in the mean mass flux (left hand side of Fig. 5.11 and Fig. 5.12). The observed increase is a result of the hotwire being sensitive to mass flux normal to its cylindrical sensing element. As a basic control volume analysis shows, the mass flux normal to the oblique body shock is conserved. Additionally, the velocity component parallel to the shockwave is conserved. The density increase across the shock-wave means that this parallel component of velocity leads to higher mass flux which is measured by the hotwire. The hotwire was calibrated in the freestream up to 22 $\mathrm{kg\,m^{-2}\,s^{-1}}$. The mass flux levels below the model shockwave for the Re = 5×10^6/m case were outside of this calibration. The values plotted are extrapolations assuming the calibration held to this elevated flux level. The RMS fluctuations (right hand side of Fig. 5.11 and Fig. 5.12) are seen to have increased in magnitude across the shock-wave for both Re cases. This effect is more pronounced for the 2.2×10^6/m condition with an increase by roughly a factor of 2.

Spectra across the model shockwave for the Re = 2.2×10^6/m condition are given as Fig. 5.13 and the Re= 5×10^6/m condition as Fig. 5.14. In both cases the majority of content is observed below 20 kHz. Across the model shockwave the PSD magnitude increases broadly across the entire frequency range with the spectra maintaining their shape.

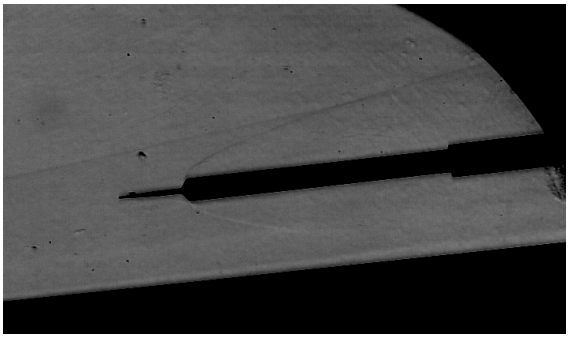

Figure 5.10: Schlieren photograph indicating across the shockwave hotwire positioning. Dark region in the bottom of the image is the model surface.

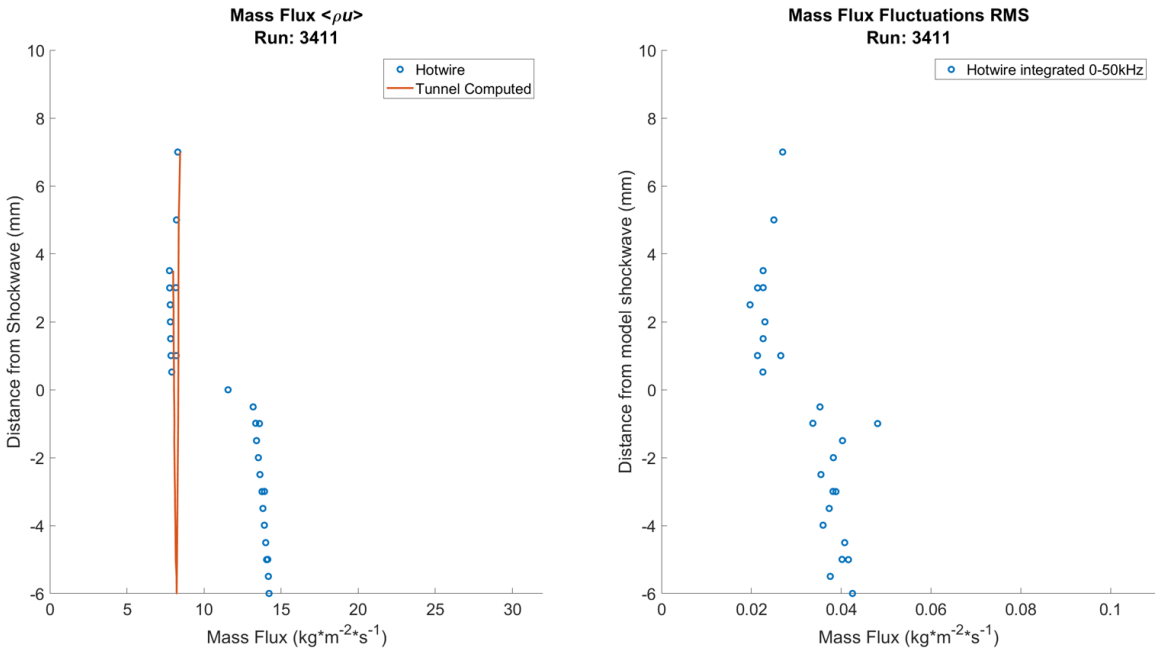

Figure 5.11: Mass flux fluctuation levels across the model shockwave. Re= 2.2×10^6/m

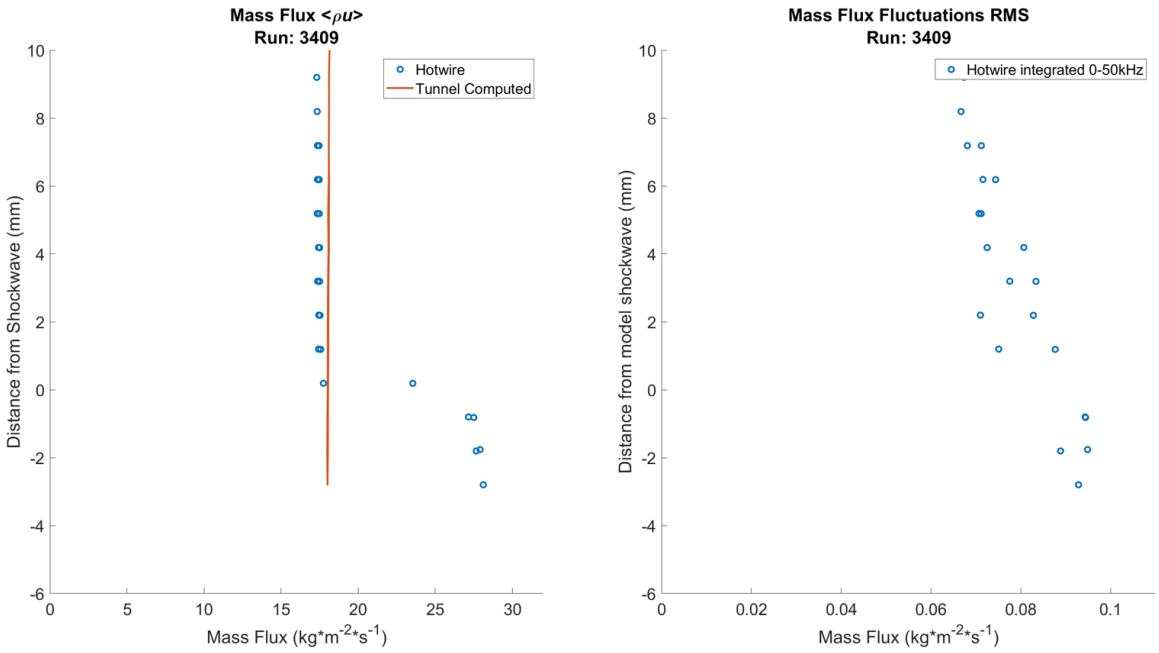

Figure 5.12: Mass flux fluctuation levels across the model shockwave. Re= 5×10^6/m

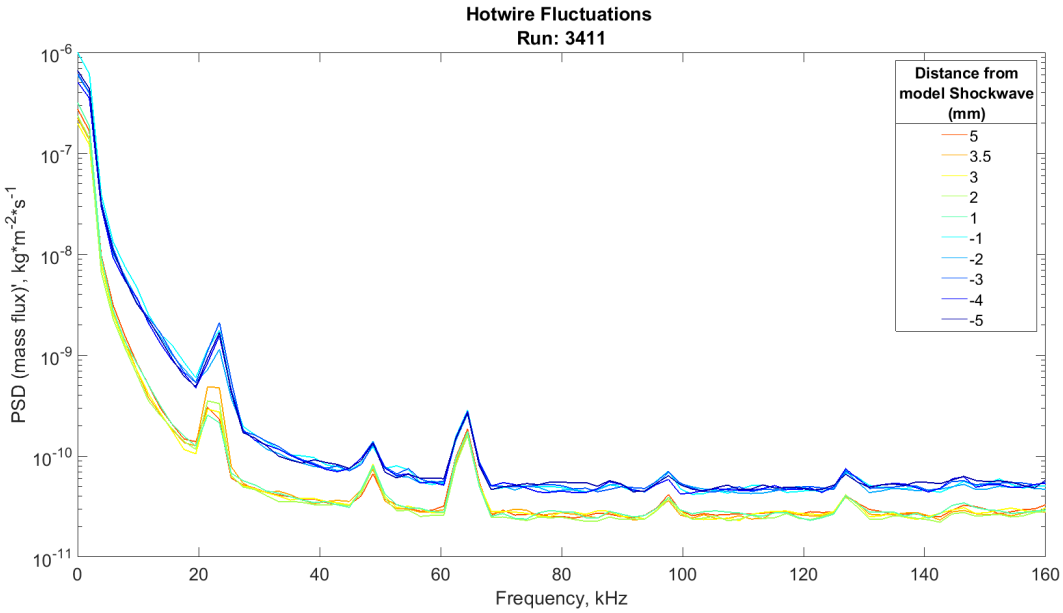

Figure 5.13: PSD of mass flux fluctuations across the model shockwave. Re= 2.2×10^6/m

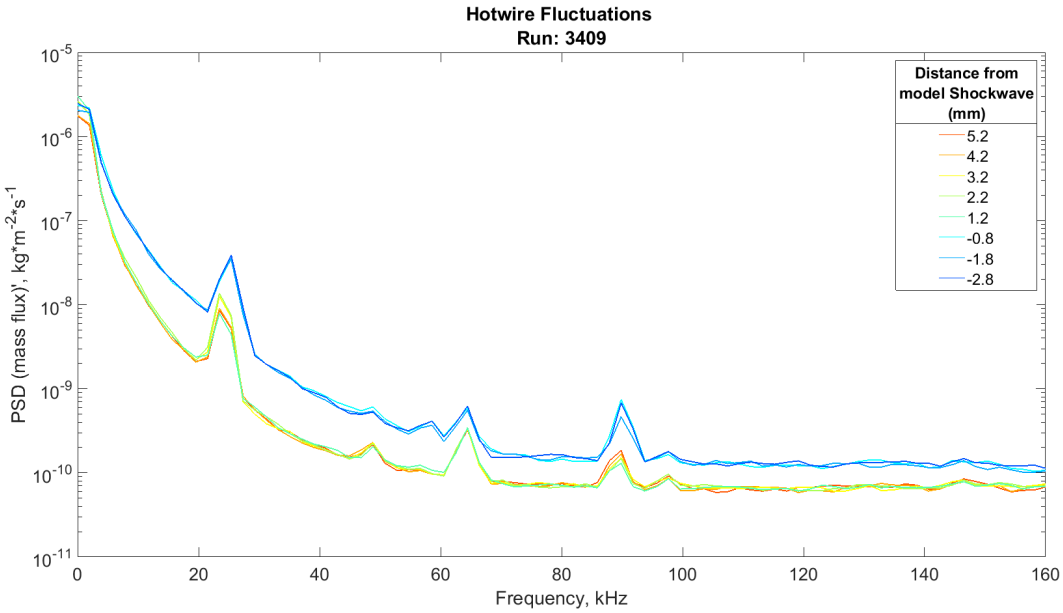

Figure 5.14: PSD of mass flux fluctuations across the model shockwave. Re= 5×10^6/m

5.5 Summary and Discussion of Characterization Results

Freestream disturbances were investigated in the ACE tunnel with both high frequency response pressure transducer and CTA hotwire surveys. These surveys agree well with previous characterizations of the freestream in the ACE facility. They confirm the lower fluctuation levels present upstream of the nozzle exit at the US station. The model nosetip positioned at the US location experiences nearly half the disturbances that it does at the MID and DS locations. Below Re = 3×10^6/m the fluctuations are roughly an order of magnitude higher than those accepted as quiet flow and provide to the opportunity to allow testing of the HIFiRE-5 model at freestream disturbance levels in-between those of a conventional facility and a quiet facility. The observed increase in freestream noise occurred at the same Re = 3×10^6/m at the 3 stations tested and fluctuations increase rapidly over relatively short Re. Based on the decomposition work of Kovasznay (1953) and measurements of Laufer (1961), as well as modern analysis summarized in Duan *et al.* (2018),

the disturbances are believed to consist mainly of acoustic disturbances radiated from turbulent boundary layers on the tunnel nozzle contours and sidewalls. Further characterization especially of spatial extent and evolution would allow for the determination of the exact nature of the disturbances. The source of the transition and consequent freestream noise increase at 3×10^6/m is under investigation at the time of writing.

Measurements across the model shockwave show a modest increase in the mass flux fluctuations within the shock layer with an observed increase in amplitude of the fluctuation spectra across a broad frequency range. As with the freestream measurements the bulk of the spectral content observed is below 20 kHz. Collectively, these measurements provide freestream spectral information as well as across-the-shock disturbance information. These data are useful in contextualizing the observed evolution of disturbances on the elliptic cone and are available for incorporation into future CFD modeling or direct simulation investigations into the effect these disturbances have on the transition process.

6. RESULTS: ACE HIFiRE-5 CAMPAIGN

6.1 ACE Campaign Overview and Data Acquisition Settings

The ACE facility campaign was conducted in three stages. In the first stage IR runs were conducted using the improved PEEK model with no transducers. In the second stage the model was instrumented with pressure transducers and run at 3 stations within the tunnel. In the third stage the model was instrumented with additional PCB transducers to examine growth of instabilities on the model. In this third stage additional hotwire and schlieren measurements were conducted. Experiments were conducted in a methodical manner to gain insight into the effect of instrumenting the model. Initial mounting and blockage tests were run using the aluminum model and initial manufacturing attempt described in 4.1.3. These tests determined the operating range of ACE possible with the model at each of the stations and allowed the diffuser throat height to be optimized for the blockage present. Early measurements were made on the initial PEEK manufacturing attempt and proved useful for practice of the tunnel run procedures minimizing the time between preheat and model run.

The fully instrumented improved model was tested at 3 different freestream stations. Table 6.1 presents the model test conditions. 31xx series runs are runs instrumented with shoulder Kulites 1-3, downstream shoulder PCBs 1-3 DS and centerline PCBs 4-6. 34xx series runs were instrumented with upstream and downstream shoulder PCBs 1-3 DS and US as well as Kulite 4. The sensor locations in model coordinates are given and shown in Table 4.4 and Fig. 4.11. Simultaneous IR and pressure transducer measurements were conducted at the US, MID, and DS locations. At each location, at least two runs were conducted to examine run repeatability. At the US stations

Table 6.1: Nominal ACE test conditions and stations.

Run Number	T_0 (K)	T_w (K)	Re $x10^6$/m	Position Relative to Nozzle Exit
ACE-3126	430	300	2 - 7	DS - Model nosetip 63.5 mm downstream
ACE-3413	430	300	2 - 7	DS - Model nosetip 63.5 mm downstream
ACE-3127	430	300	2 - 7	MID - Model nosetip 12.7 mm upstream
ACE-3415	430	300	2 - 7	MID - Model nosetip 12.7 mm upstream
ACE-3135	430	300	2 - 7	US - Model nosetip 152.4 mm upstream
ACE-3416	430	300	2 - 7	US - Model nosetip 152.4 mm upstream

additional IR measurements were made on the uninstrumented side of the model for further comparison. Additional data and discussion including plots of run conditions as well as IR and spectra plots for each of the runs conducted are given in App. C & App. D. All Stanton number images in this and the results section are presented on the same color scale to allow direct comparison.

Data were acquired using the NI DAQ and LabVIEW VI described in Subsection 3.2.4. Signals were acquired at 2MS/s for 100 ms. The tunnel freestream pressure was varied continuously to sweep through Reynolds number. 100 ms samples were acquired roughly 300 ms apart, an increment determined by execution time of the VI and believed to be limited by write speed to the DAQ computer. Data were saved as a binary file and extracted and processed in MATLAB. PSDs were computed using Welch's method using a Hann window of 512 points with 50% overlap. This resulted in a frequency resolution of 3.9 kHz. IR images were acquired at 15 Hz at two integration times, 8 & 4 ms. The Stanton number plots in this section were created using the 4 ms integration time. The processing techniques used were described in Subsection 3.3.1.

PCBs were all low-pass filtered using 1 Mhz, 8-pole, Bessel filters. Kulites 1 & 2 were low-pass filtered using 200 kHz, 8-pole, Bessel filters and Kulite 3 was low-pass filtered using a 100 kHz, 12 dB/octave, unity gain low-pass filter on a Stanford Research Systems SR-560 preamplifier.

Reynolds number sweeps were conducted by varying the tunnel total pressure. For a nom-

inal run, the tunnel was started at a pressure of 245 kPa corresponding to a Reynolds number of 3×10^6/m. The pressure was then swept down to 2×10^6/m and continuously swept from 2×10^6/m to 7×10^6/m or tunnel unstart. This process was repeated for the majority of the runs with a few runs conducted by starting the tunnel at a higher pressure and sweeping downwards to examine the effect of tunnel run procedure on the measured heat flux. The effect of sweeping the tunnel through these conditions was determined to be minimal by comparison with constant Re runs and the downward swept runs. In each case the same Reynolds number-based trends were observed. This gave confidence that the trends observed from runs conducted in this manner were valid and would allow comparison with other facilities. Appendix C presents a description and comparison of the facility run conditions.

6.2 A Note on Pressure Transducer Response, Filtering, and Interpretation

The Kulite XCE-062-15A pressure transducers utilized have a resonant frequency in the range of 250 kHz. While the signals were filtered at 200 kHz, the roll off of the filter at 250 kHz is small compared to the magnitude of the resonant frequency peak observed. Fig. 6.1 shows an example of a pressure trace obtained during a run in the ACE Facility. The center and left series of traces are Kulites filtered at 200 kHz with an 8-pole Bessel filter. The right trace is from a Kulite low-pass filtered at 100 kHz, using a 12 dB/octave, unity gain low-pass filter on a Stanford Research Systems SR-560 preamplifier. The very large resonant frequency peak is visible in the spectra of all rising above the smaller signal of the instabilities developing on the cone. At higher Re it appears that this peak grows and results in spill over to the frequencies around it effectively raising the tail of the PSDs. This effect coupled with the expected linear range of the transducers limits the confidence in observations above $\sim$ 100 kHz. Results will be presented from 0-200 kHz to

highlight the instability growth.

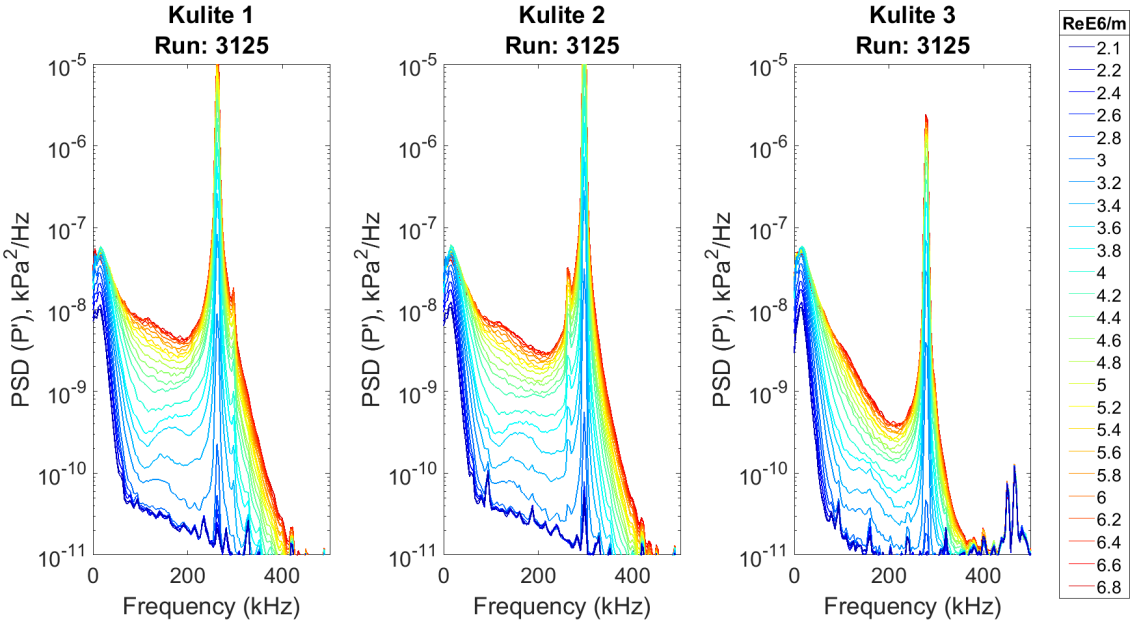

Figure 6.1: PSD of Fluctuating Pressure for Kulite transducer cluster. Run 3125; ACE Tunnel; DS station.

The PCBs utilized are inherently high-pass filtered at $\sim$ 11 kHz. As a result, any signals below this range or slightly above it are difficult to interpret. Plots of PSDs from these transducers are presented on a scale from 10-500 kHz and 10-350 kHz where appropriate to highlight the signal observed. The spectra from several of the transducers utilized exhibit a dogleg feature at $\sim$ 350 kHz visible in the PSD plots in the 0-1 MHz plots of Fig. 6.2. This feature appears regardless of sensor location and persists as the spectra broadens even into regions believed to be fully turbulent. This is believed to be the result of some property of the PCBs or their signal conditioning and not a feature of the flowfield. This feature casts suspicion on any content observed in the 300-400 kHz region, despite the fact that content is expected in this range based on prior CFD analysis.

Both types of transducer were acquired with the DAQ set to -1 to 1 V-DC range to utilize the maximum DAQ resolution. Transducers were acquired before the facility ejector started allowing

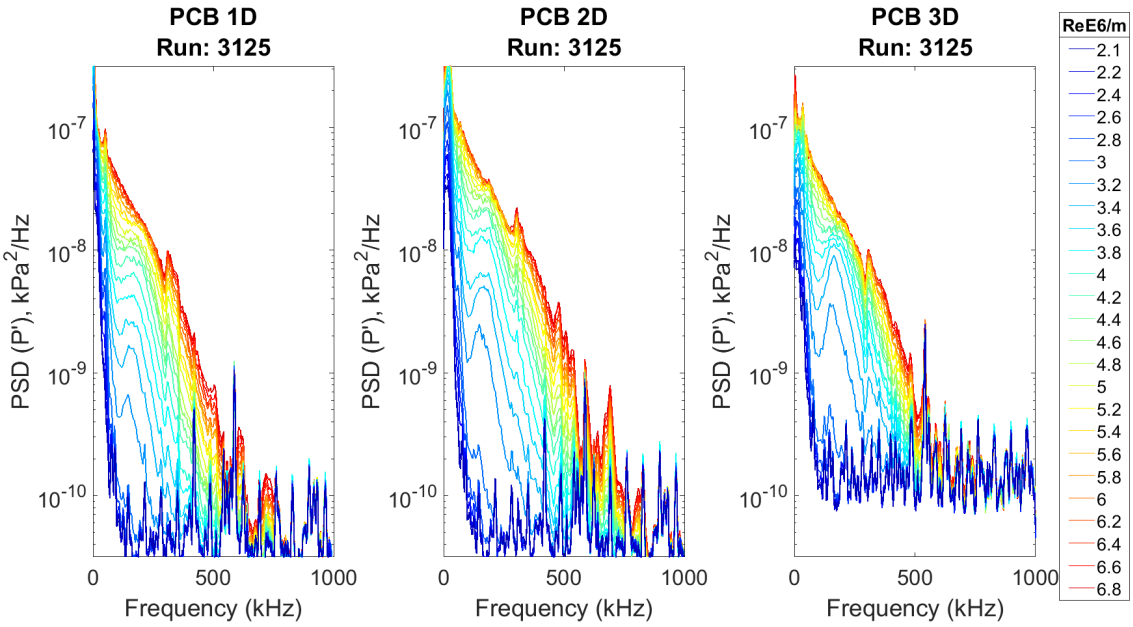

Figure 6.2: PSD of fluctuating pressure for PCB transducer cluster. Run 3125; ACE Tunnel; DS station

for a quiescent air noise floor measurement. PCB power spectral density estimates are presented with this pre-run noise floor. The Kulites in quiescent air register a voltage much higher than one volt and are outside of the DAQ measurement range making a pre-run noise floor measurement impossible.

6.3 Initial IR thermography Runs

Initial experiments on the improved model were conducted prior to expanding the instrumentation cavities and drilling sensor mounting holes on the model surface. These runs served as the baseline to examine any impact caused by the reduction of the thickness of the PEEK material, the effect of installing the transducers, and to help identify regions of interest on the model surface. An example of images from these initial runs is presented in Fig. 6.3. These results were previously reported in Neel *et al.* (2017) and show good agreement with previous results of Borg & Kimmel (2016) & Juliano *et al.* (2015). This comparison is discussed further in Chapter 8.

Comparison of temperature and computed heat flux between the regions on the model with and without cavities showed good agreement giving confidence that the cavities were not significantly affecting the surface temperature or heat flux calculations. Present in these runs was evidence of streaks of increased heat flux leading into the lobes of higher heat flux which dominate the shoulder region of the cone. The observed position of these streaks was utilized in selecting sensor locations. Meetings and discussion with TAMU Computational Stability & Transition lab lead to the selection of PCB transducers due to the high expected frequencies of the secondary crossflow and Mack mode instabilities.

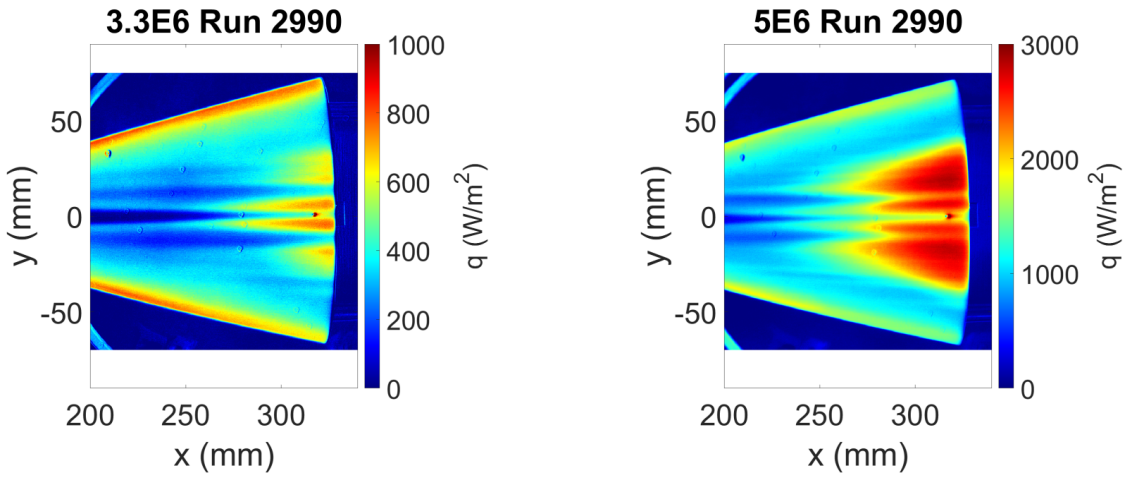

Figure 6.3: Initial IR campaign examples. Left: Re = 3.3×10^6, Right:Re = 5×10^6.

6.4 Instrumented Model Runs - ACE

There are two main regions of interest on the elliptic cone for the current study. The cone shoulder, as described previously, is expected to be a region of dominant growth of the crossflow instability. The centerline region is dominated by the mushroom shaped upwelling of the boundary layer. Heat flux values in both regions were observed to vary with freestream Reynolds number and nosetip position.

6.4.1 DS Station IR

The evolution of Stanton number with freestream Reynolds number at the DS station is shown in Fig. 6.4. Bulk features of the heat flux, observed in the initial IR and as will be shown at all streamwise testing stations, are present. At the lowest Re shown, there is fairly uniform heating across the model shoulder with no discernible front or elevated heating region. Between Re = 3×10^6 - 3.6×10^6/m there is increased heating on both shoulders of the cone. This heating moves forward as Re is increased and evolves into the characteristic lobes of increased heating observed in previous noisy flow experiments on this model geometry. By 5×10^6/m all transducers $\geq$ 300 mm downstream of the model nosetip were engulfed in the higher heat transfer regions. For Re $\geq 4 \times 10^6$/m faint, nearly streamwise streaks are visible. These streaks are somewhat difficult to discern depending on the colormap chosen for the images. Shown in Fig. 6.5 is a higher resolution greyscale image of the Re = 5×10^6/m image of Fig. 6.4. The streaks are clearly visible on the higher contrast colormap on both the top and bottom shoulders of the cone. These streaks were present in the initial IR runs of the previous section. It is important to note that the positioning of the PCB transducers along the cone shoulder was chosen to lie beneath the previously observed streaks. Comparing the heat flux maps here with the uninstrumented runs shows that the streaks are not introduced or seen to be modified by the placements of the sensors on the model surface. As Re is increased above Re = 4×10^6/m the elevated heating front pushes forward on the model surface. The lobes extend from roughly 15 mm on either side of the model surface. Streaks remain visible leading into this region. Increasing Re further extends the lobes farther forward on the cone surface.

Along the model centerline there is a region of low heat flux. This is the signature of the

mushroom shaped upwelling structure created by the model-geometry-induced pressure gradient directing flow towards the centerline. This structure and its influence on surface heating is clearly shown in CFD studies of the geometry (see Dinzl & Candler, 2017). As Re increases, the low heat flux region is narrowed by the growth of two distinct streaks of elevated heating on either side of the model centerline. At 3.6×10^6/m the heating is higher and extends further upstream on the model surface, past 300 mm downstream of the nosetip, and the Stanton number reaches a value close to its eventual maximum at higher Re. As Re increases further the streaks continue to move upstream on the cone. The streaks show excellent symmetry and straddle the centerline of the cone. This indicates that any yaw angle present in the mounting of the cone is small enough as to not effect bulk flow of the centerline mushroom.

6.4.2 DS Station Spectra

PSDs of the fluctuating pressure measured by Kulite sensors with the model at DS station are shown in Fig. 6.6a and waterfall plots in Fig. 6.7a. These show a broad peak centered near the 15-20 kHz range. This disturbance was previously observed in noisy runs in the BAM6QT as well as ACE Borg *et al.* (2015*a*). Near the 3×10^6/m noise jump there is evidence of a peak near 150 kHz. This is outside of the sensors' expected linear frequency range response but may indicate content in this frequency band. As Re increases the 20 kHz peak grows in amplitude reaching a maximum near Re = 4×10^6/m. This aligns with the freestream pitot data where the maximum fluctuation percentages were seen near 4×10^6/m. The peak shifts slightly to the right at higher Re, broadening with the spectra increasing across the measured frequency range. Above 5.4×10^6 no evidence of the 20 kHz peak is visible and the spectra has reached a broad profile indicative of turbulent flow. This broadening and transition to a turbulent spectrum coincides with the sensor

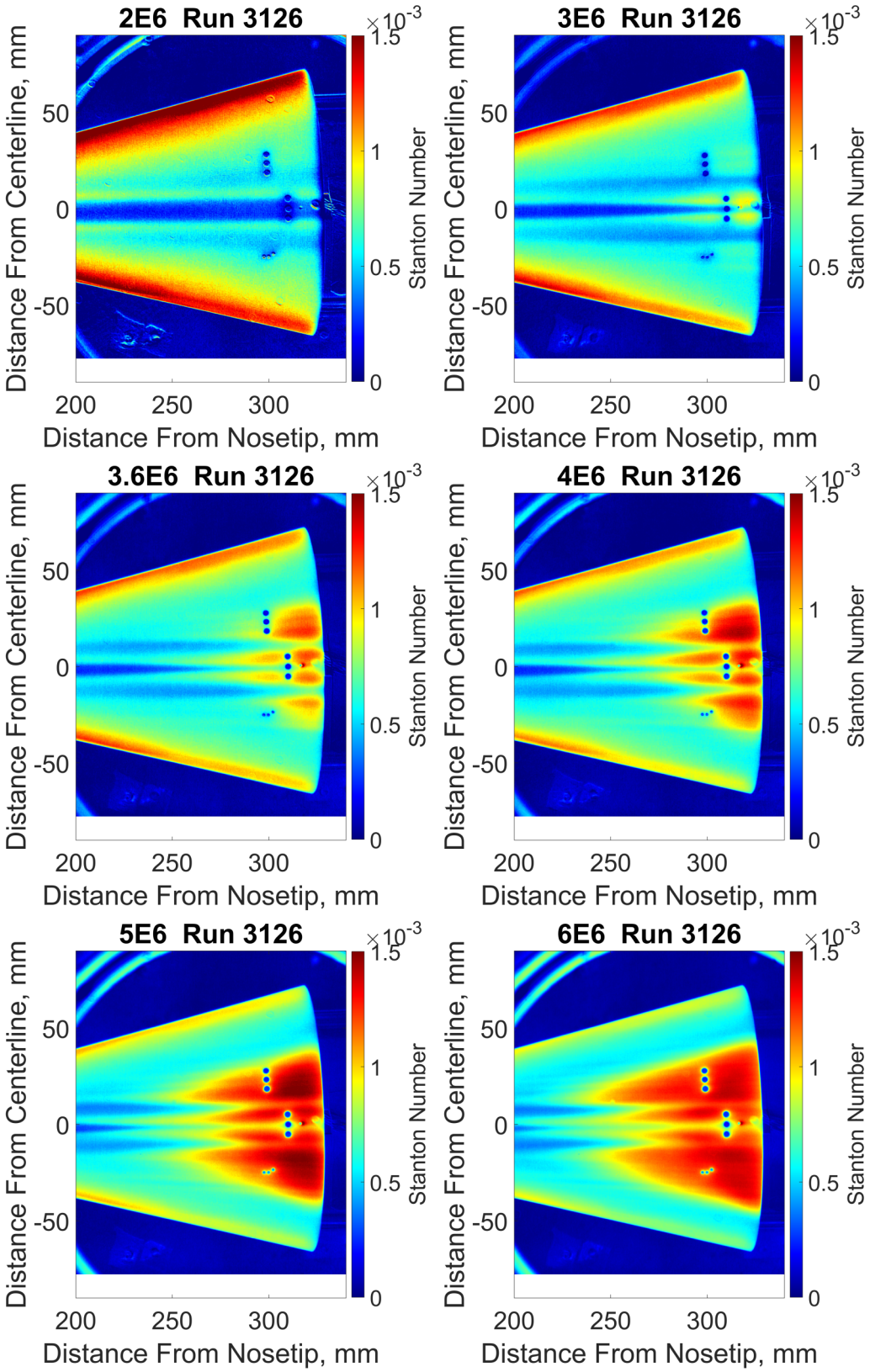

Figure 6.4: Stanton number maps, Re sweep ACE tunnel DS station; initial instrumentation.

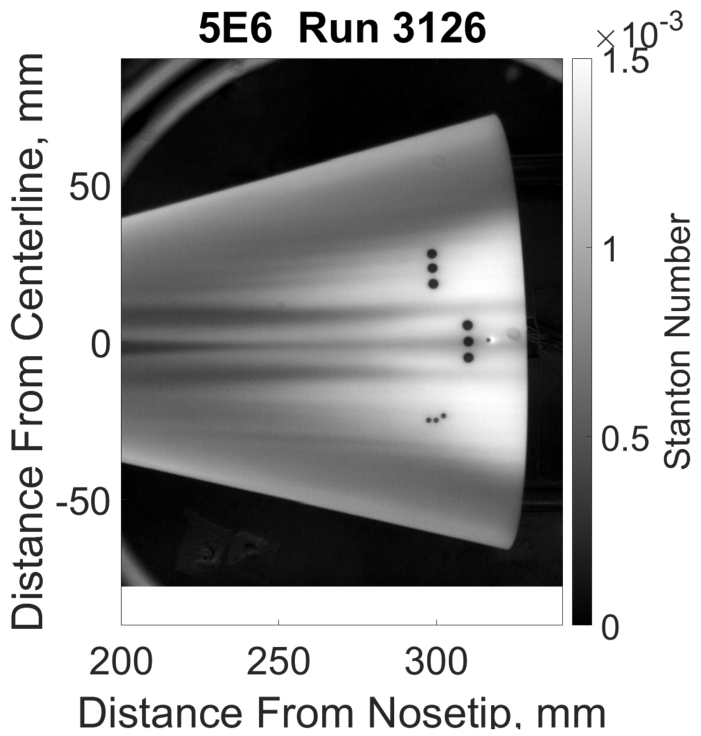

Figure 6.5: Greyscale St map, Re = 5×10^6/m, ACE tunnel DS station.

locations being engulfed by the elevated heating region on the cone shoulder. It is again important to note that a large resonant peak exists at roughly 250 kHz for all Kulites utilized. This resonant peak may account for the rise of the tails of the spectra. Each of the Kulites show the same trend as might be expected due to their relatively close spacing.

The three shoulder-located PCB PSD traces are shown in Fig. 6.6b and waterfall plots in Fig. 6.7b. Below Re = 3×10^6/m, no content is visible above the sensor noise floor for any of the transducers. Focusing on PCB 1D, as freestream Re increases a fairly broad peak from 100-180 kHz rises above the noise floor at each of the sensor locations. Its amplitude increases quickly across the tunnel freestream disturbance increase. Its growth slows near Re = 3.8×10^6/m and it begins to broaden. As this disturbance grows its peak frequency shifts towards higher frequencies. This is the trend expected of an instability which is scaling with boundary layer thickness, shift-

ing higher in frequency as the boundary layer thins with increased Re. This peak broadens and increases in amplitude eventually reaching a broad full profile indicative of turbulent flow. This is observed at all three PCB stations. The development of the disturbances observed varies in a pattern similar to the heating observed in the IR images; the transducer closest to the centerline, PCB 3D the furthest right in Fig. 6.6b, shows the largest initial amplitude and develops to a turbulent profile more quickly than the other two locations. This sensor is the first to be engulfed by the elevated heating region in the IR images. Broadband turbulence occurred at the downstream sensor locations for freestream Re greater than 5×10^6/m, corresponding with the sensors being engulfed by the high heat flux regions observed in the Stanton number maps.

Again, it is worthwhile to note that the sensor position was chosen to lie underneath the streaks observed in the initial IR thermography runs. These streaks are believed to be stationary crossflow vortices and this position corresponds with the trough of the stationary crossflow vortices where Edelman & Schneider (2018) observed the growth of what is believed to be a secondary instability. This evidence, coupled with CFD stability results, points to the 100-200 kHz frequency band observed in the PCB traces being a secondary instability of the stationary crossflow vortices. All three PCBs show this band growing and broadening, eventually to the point of a broad spectrum indicative of turbulent flow. Although not fully conclusive, this secondary instability growth was significant and appears to have led to transition, which is consistent with low-speed experiments Saric *et al.* (2003).

Centerline region PSDs and waterfall plots are presented in Fig. 6.6c & Fig. 6.7c. In this region the centerline instabilities related to the mushroom structure are expected to dominate. The spectra on either side of the centerline show good symmetry. At the lowest freestream Re content is present centered at 50 kHz. Multiple peaks are present in this region, which may be due to poor

PCB response at these low frequencies. The spectra broaden and increase in amplitude quickly reaching a broad turbulent profile. At the model centerline, a large initial peak is present centered near 43 kHz. This peak grows and shifts to higher frequencies as Re is increased. Across the tunnel freestream disturbance jump the peak broadens and decreases in amplitude, eventually being replaced by a peak at a frequency similar to that of the off-centerline sensors and broadens to become fully turbulent. The development and replacement of this frequency are most visible in the waterfall plot of figure Fig. 6.7c where the peak frequency band is visible as a dark red region. Past 4×10^6/m the spectra at each location is very similar. This corresponds well with the IR which shows that at the 310 mm streamwise location of the sensors, the off-centerline streaks move forward and broaden, encroaching on the center PCB.

The interpretation of these centerline PCBs is complicated by the presence of peaks of similar frequencies present in the flow off quiescent air spectra shown as a dashed line in the PSD plots. PCB 5 shows a noise peak at 43 kHz, the initial frequency present and eventual frequency seen at higher Re. The shift in frequency observed makes this trace unlike any of the noise seen at other frequencies, bolstering the theory that it is due to an actual flow feature and not simply electronic noise.

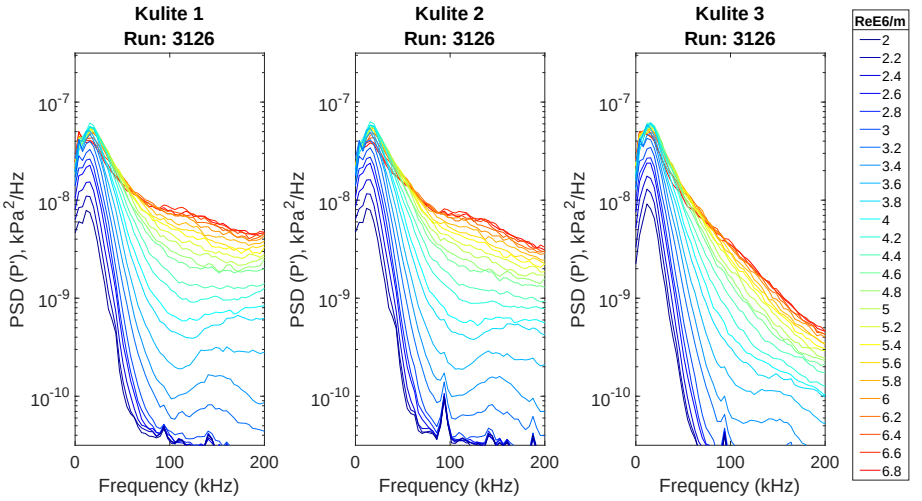

(a)

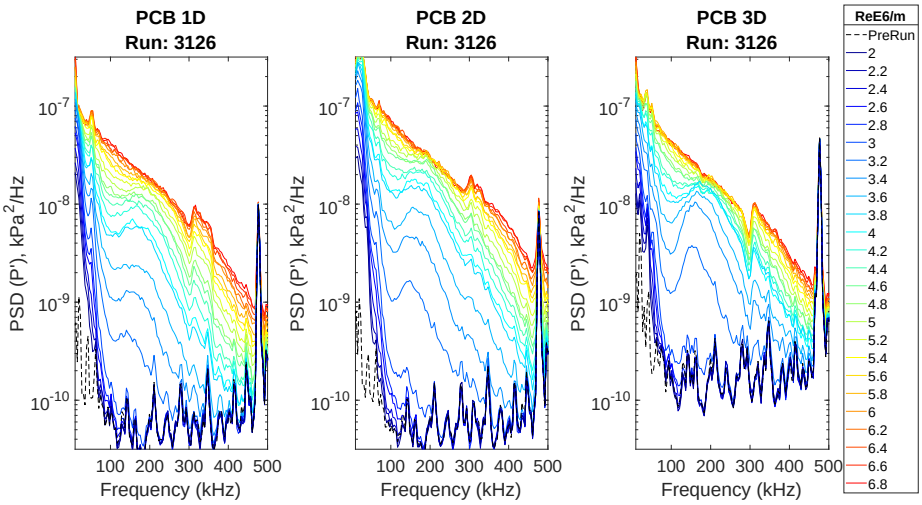

(b)

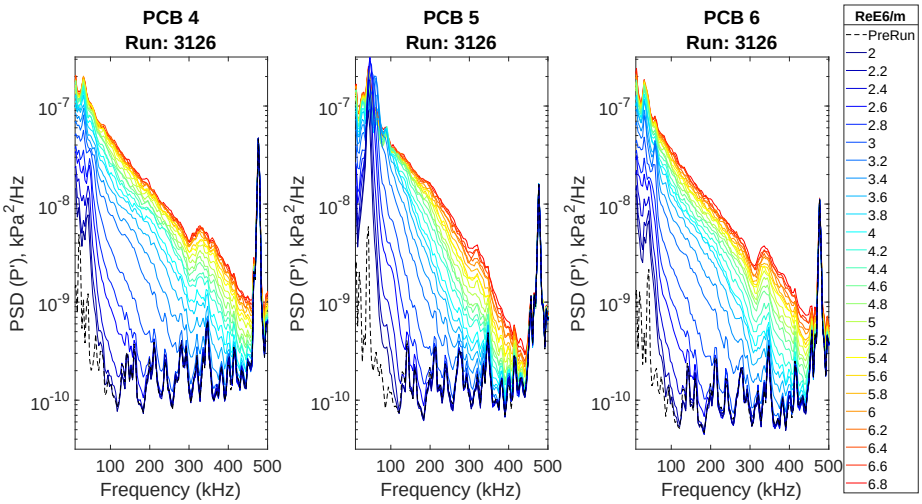

(c)

Figure 6.6: PSD of fluctuating pressure for each transducer cluster. Run 3126; ACE Tunnel; DS station. (a) Kulites, (b) Downstream shoulder PCB, (c) Centerline PCB

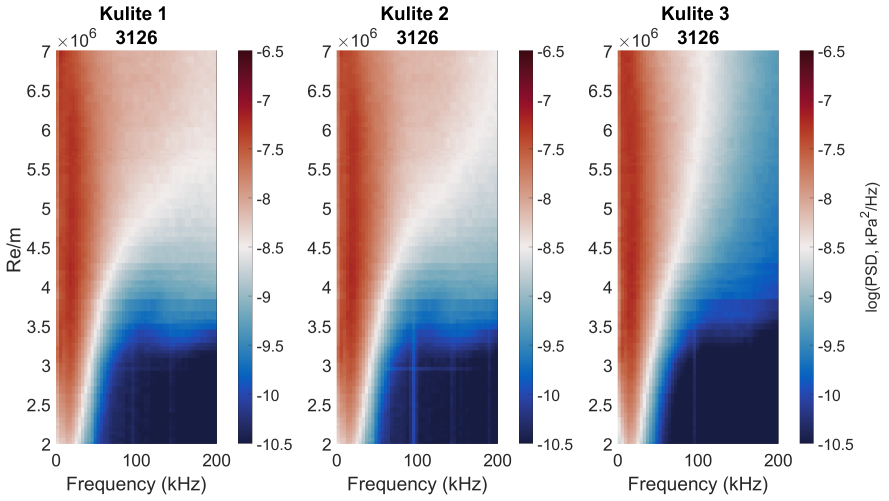

(a)

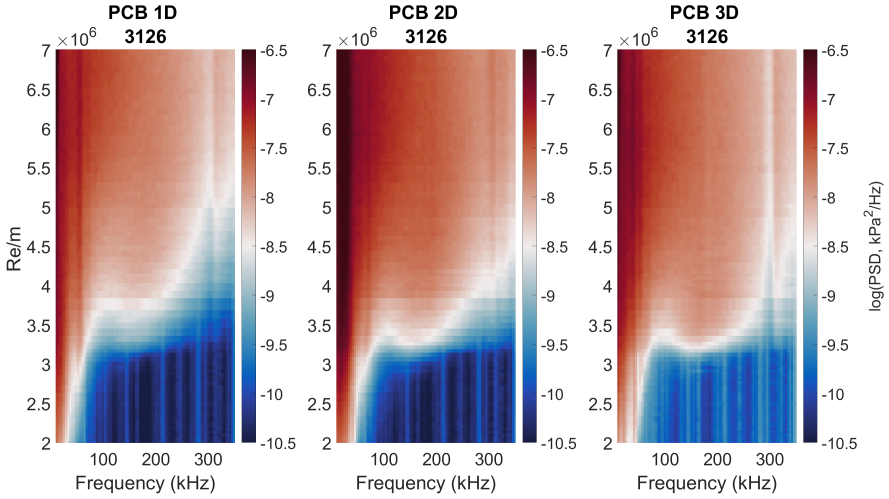

(b)

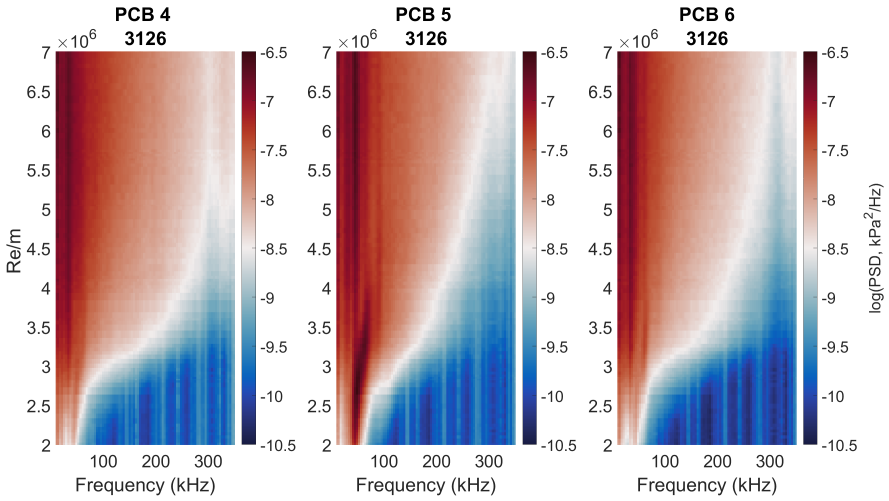

(c)

Figure 6.7: Waterfall PSD of fluctuating pressure for each transducer cluster. Run 3126; ACE tunnel; DS station. (a) Kulites, (b) Downstream shoulder PCB, (c) Centerline PCB

6.4.3 MID Station IR

The freestream characterization of Chapter 5 revealed that the disturbances present at the MID location were very similar to those at the DS location. This is evident in the Stanton number maps presented in Fig. 6.8. The placement of the model relative to the top windows in the ACE tunnel makes the visible area of the cone smaller at this station. The maps show the same trends as at the DS station. The higher heating lobes become evident near Re = 3.6×10^6 and move forward with increasing Re. Streaks are again visible leading into the regions of elevated heating. The similarities are a positive indication that the observed heating on the model surface is a result of the tunnel flow conditions and not the result of reflections or any localized imperfections (weak reflected shocks, small leaks, etc.) in the tunnel flow field.

6.4.4 MID Station Spectra

As with the IR measurements, the spectra for all transducers are in agreement with those at the DS station. Fig. 6.9 & Fig. 6.10 show waterfall plots for each sensor cluster at this station. On the shoulder the same frequency peaks are present in the Kulites and PCBs. The centerline transducers show the same symmetry they did at the DS station with the centerline peak and frequency shift apparent. Again, noise is present in the pre-run noise floor of the centerline PCBs near the dominant frequency and subsequent shift. The peaks present in PCBs 4 & 5 even at the highest Re are at a slightly lower frequency than at the DS station, 39 kHz vs 43 kHz, but the PSDs have only a 4 kHz resolution. Again the shift in frequency indicates that the spectral content present is due to the flow field and not only electronic noise.

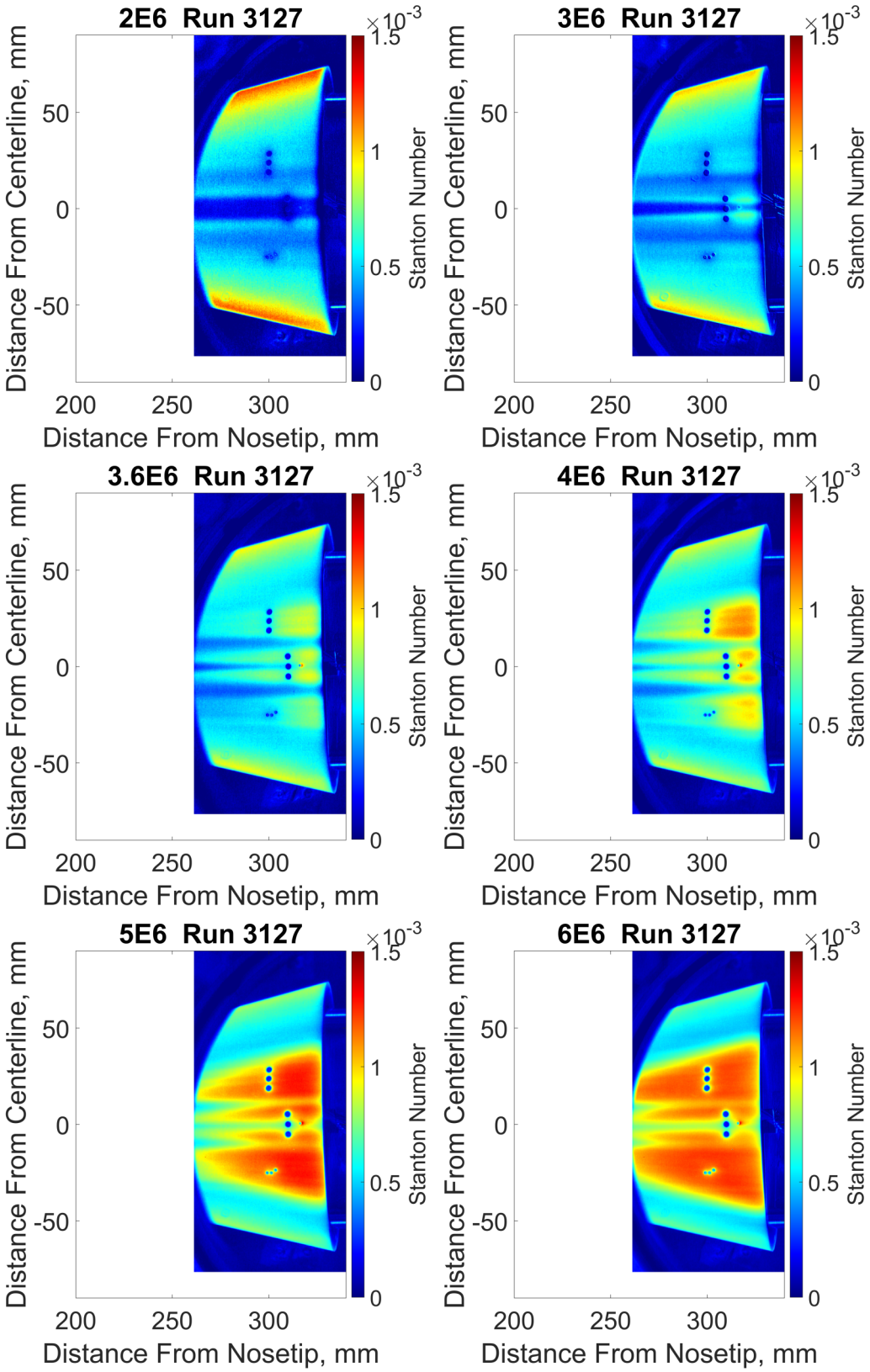

Figure 6.8: Stanton number maps, Re sweep ACE tunnel MID station; initial instrumentation.

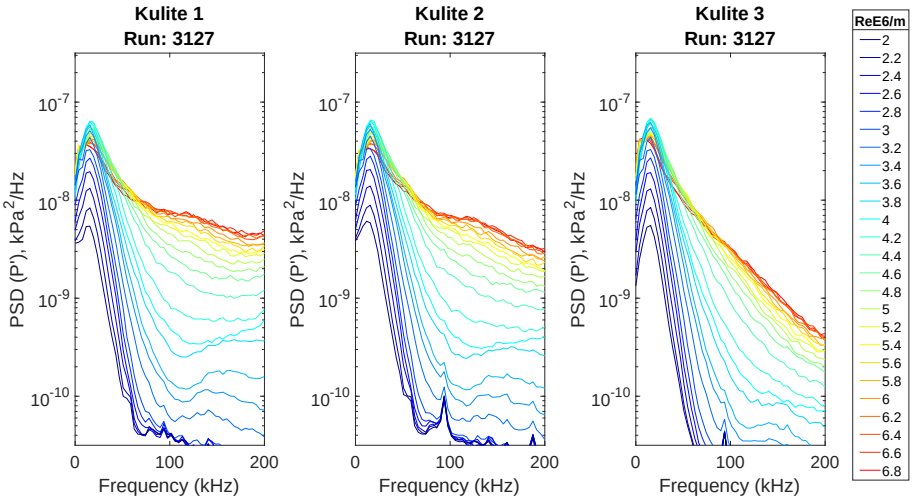

(a)

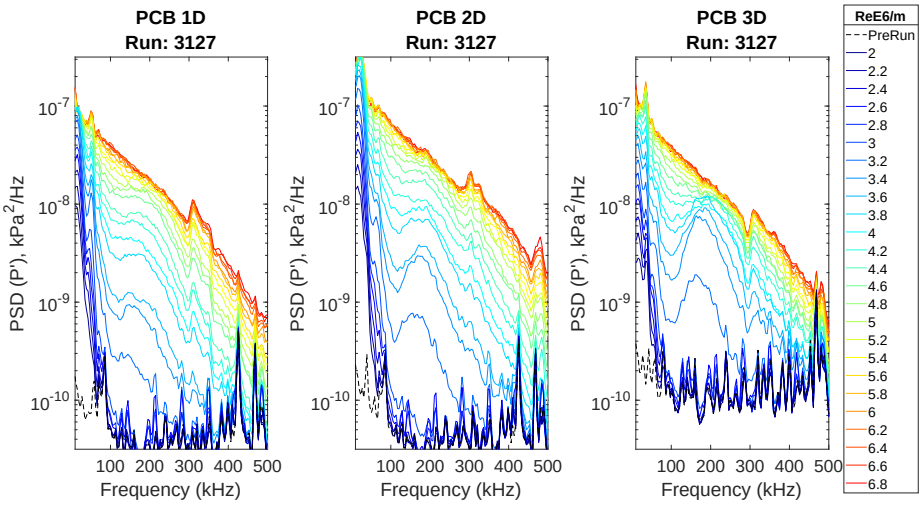

(b)

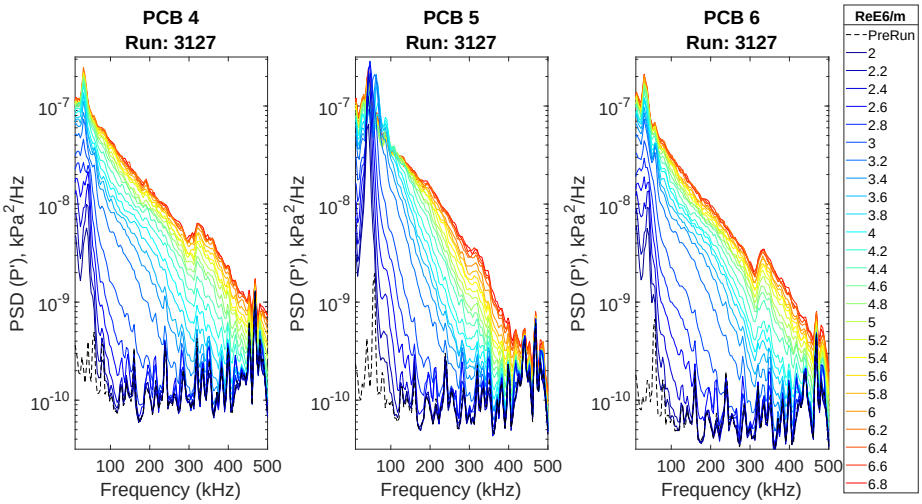

(c)

Figure 6.9: PSD of fluctuating pressure for each transducer cluster. Run 3127; ACE Tunnel; MID station. (a) Kulites, (b) Downstream Shoulder PCB, (c) Centerline PCB

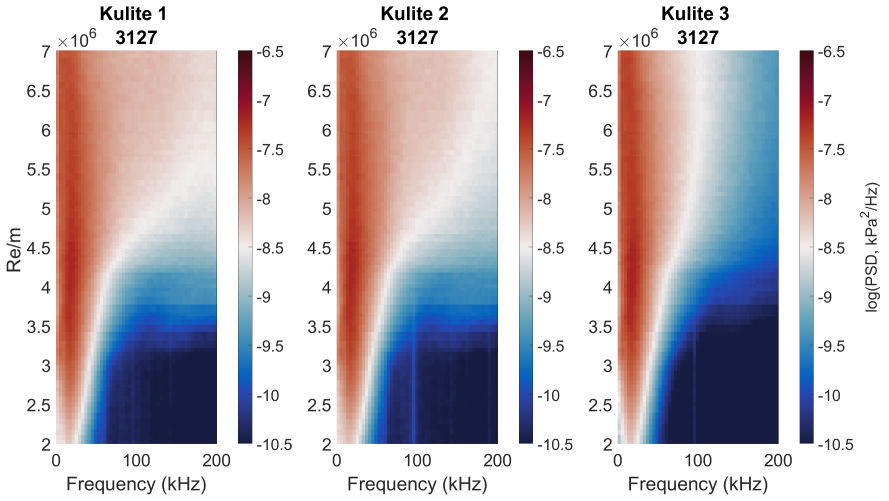

(a)

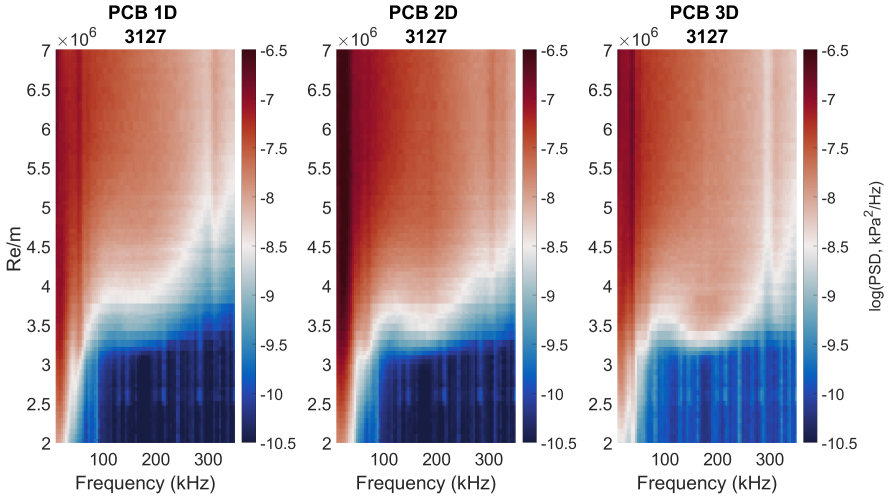

(b)

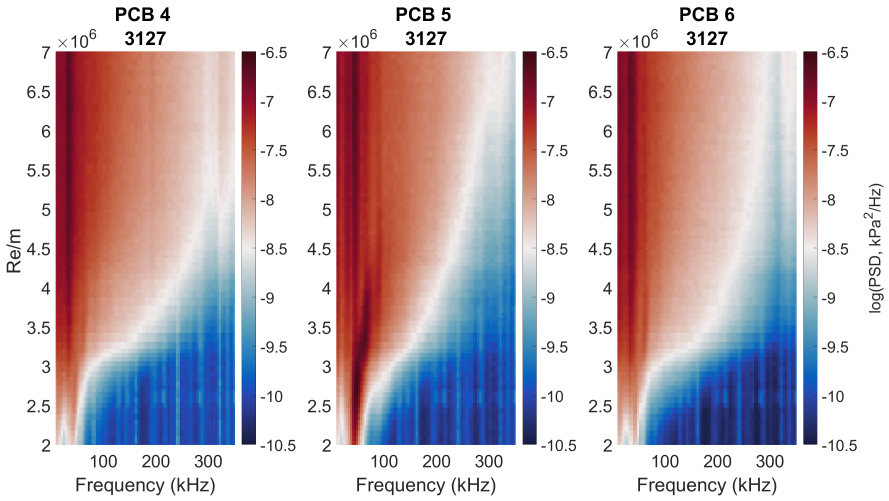

(c)

Figure 6.10: Waterfall PSD of fluctuating pressure for each transducer cluster. Run 3127; ACE Tunnel; MID station. (a) Kulites, (b) Downstream Shoulder PCB, (c) Centerline PCB

6.4.5 US Station IR

Stanton number maps for the lower disturbance level US station are shown in Fig. 6.11. At 2×10^6/m the heating is largely the same as observed at the DS station. Moving to higher Re however, changes in the heat flux are apparent. At Re = 3×10^6/m, the centerline structure has begun to narrow towards the aft end of the cone but the streaks on either side of the model do not show the level or extent of heating present in the DS case. Heating on the cone shoulder is delayed, not appearing until the 4×10^6/m map. The streaks present in this region are much more defined. Clearly visible on the top side of the cone are streaks downstream of the shoulder PCB transducers. These streaks advance upstream on the model covering the transducers by 5×10^6/m. At 6×10^6/m the apparent transition front is similar to that of the DS station. This makes intuitive sense as at and above this Reynolds number the fluctuation levels present are similar at both stations.

6.4.6 US Station Spectra

PSDs and waterfall plots of fluctuating pressure for US station run 3135 are given as Fig. 6.12 & Fig. 6.13. The structure of the peaks observed is similar to those at the DS and MID stations. In the Kulite PSDs peaks are again visible near 20 kHz. The peaks are consistently lower in amplitude for a given Re vs those at the US station. These peaks grow reaching their maximum amplitude near Re = 4.8×10^6/m with the spectra broadening as Re is increased further. Spectral content near 100-200 kHz is again present appearing above the noise floor near 3.6×10^6 for all three sensors. The shoulder PCBs show similar content as at the DS station. There is little content visible below 3×10^6/m. A peak appears from the noise floor at all transducer locations. It is initially sharper and lower in amplitude than at the DS station. It grows rapidly with the peak shifting to higher frequency. Its growth is slower than at the DS station. Near 5×10^6/m the peak has broadened and

is approaching an fully turbulent profile. This occurs at roughly the same Re as at the DS station. At this Re the freestream fluctuation environment is similar at both stations. The centerline PCB again shows growth near 43 kHz. The initial amplitude is again lower than that at the DS station. Noise is present in the pre-run flow-off noise floor near 55 kHz. The peak again shifts to higher frequency reaching 62 kHz by 3.6×10^6/m. This shift is well visualized in the waterfall plots of Fig. 6.13. PCBs 4 & 5 show good symmetry off the centerline, again with lower amplitude for a given Re than at the DS station.

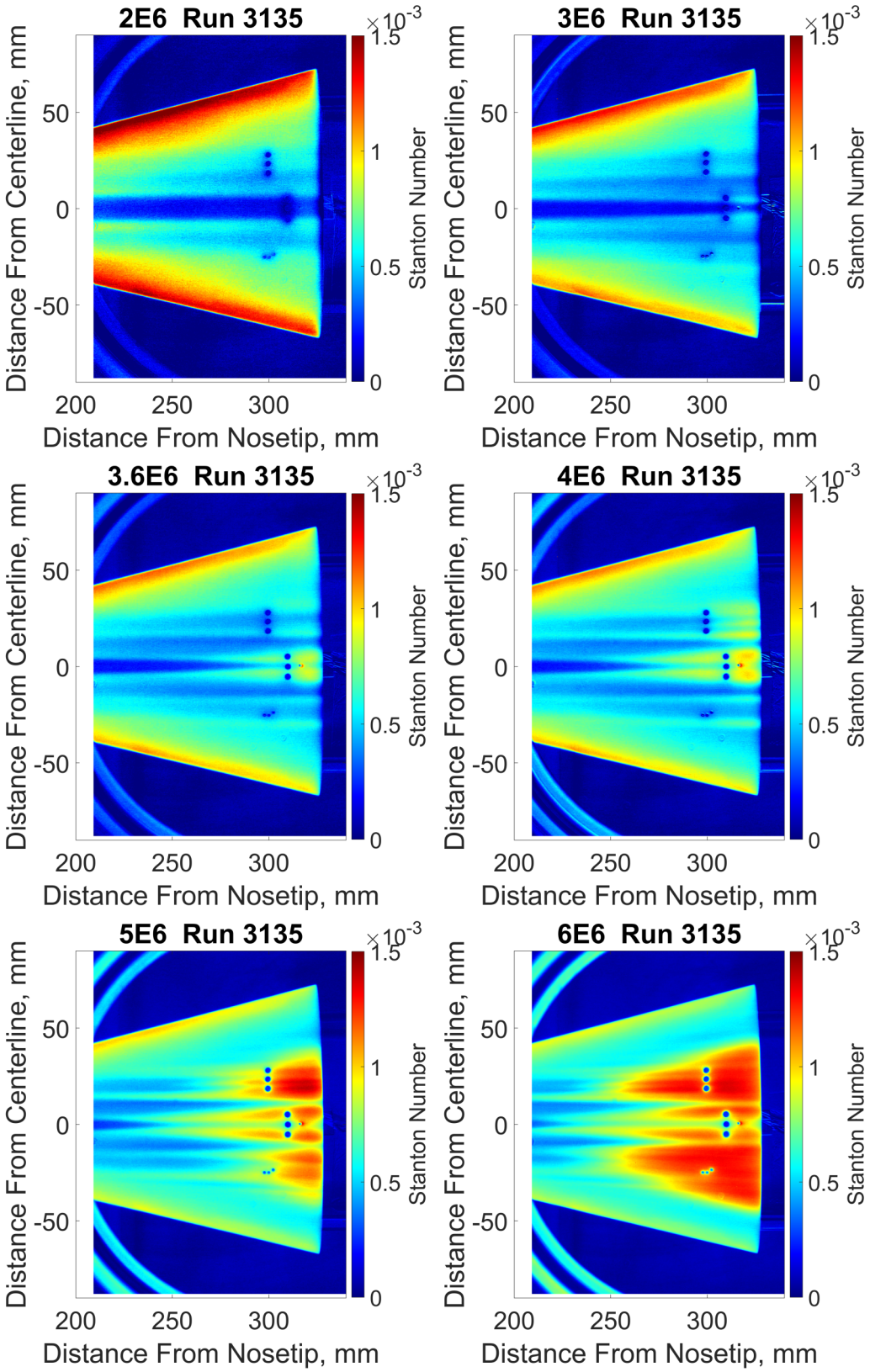

Figure 6.11: Stanton number maps, Re sweep ACE tunnel US station; initial instrumentation.

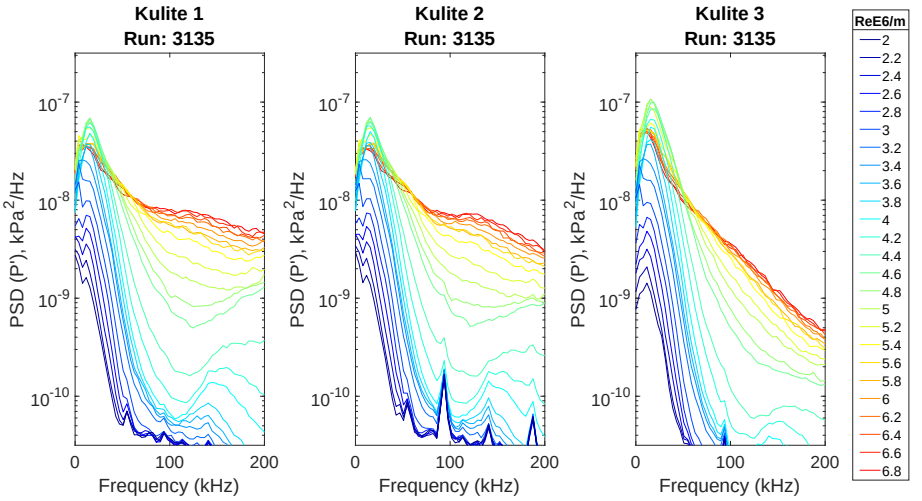

(a)

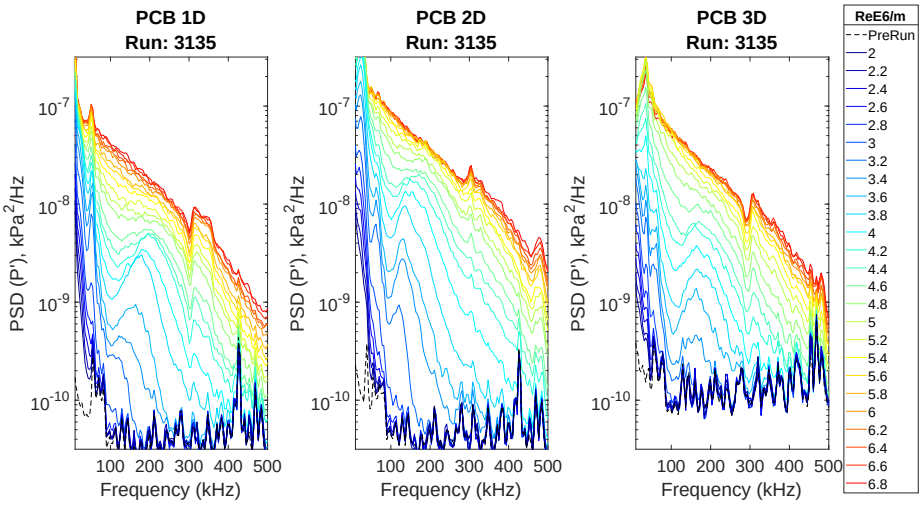

(b)

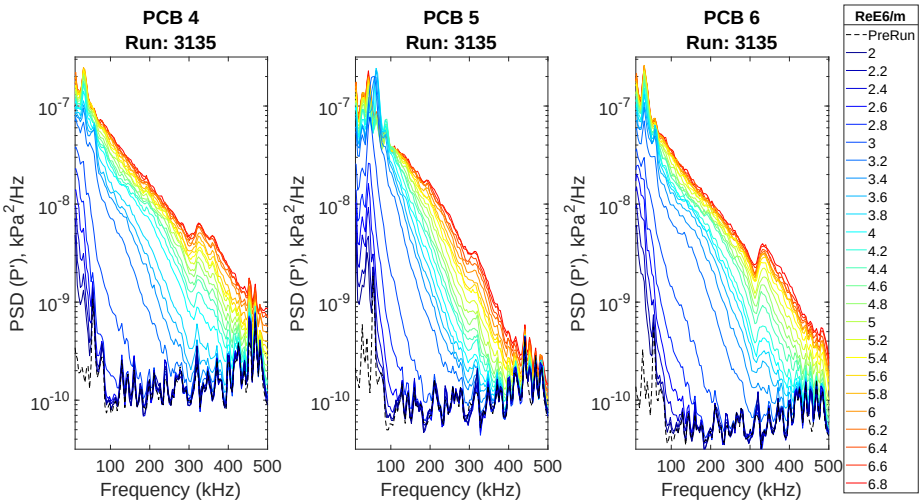

(c)

Figure 6.12: PSD of fluctuating pressure for each transducer cluster. Run 3135; ACE Tunnel; US station. (a) Kulites, (b) Downstream Shoulder PCBs, (c) Centerline PCBs

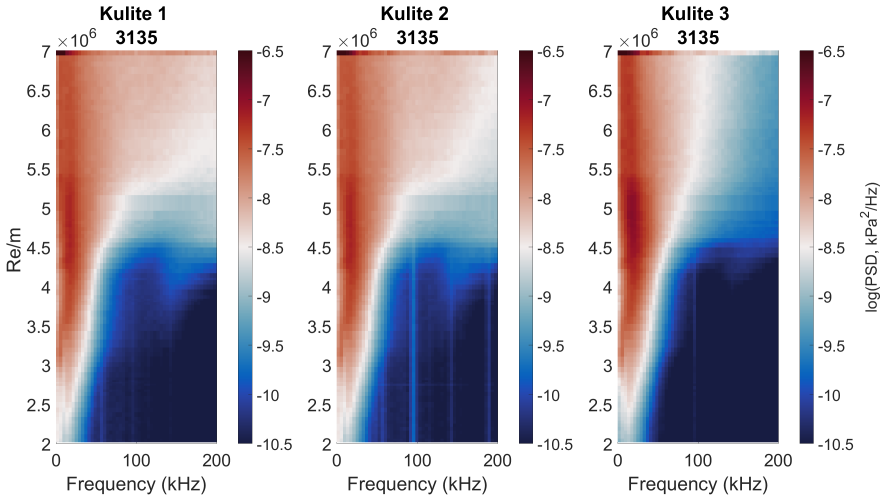

(a)

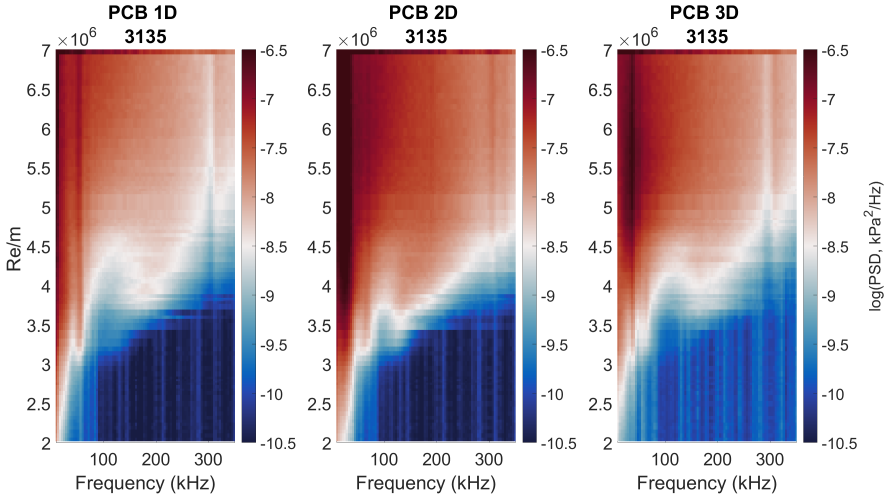

(b)

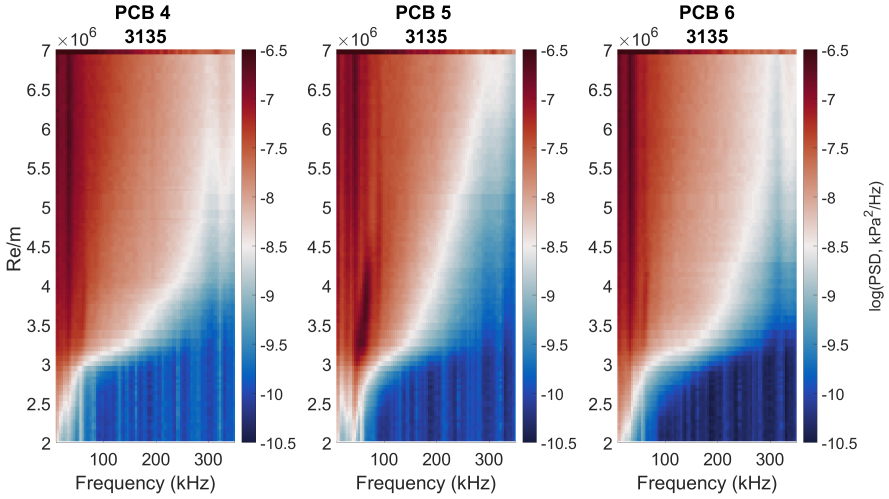

(c)

Figure 6.13: Waterfall PSD of fluctuating pressure for each transducer cluster. Run 3135; ACE Tunnel; US Station. (a) Kulites, (b) Downstream shoulder PCBs, (c) Centerline PCBs

6.4.7 US Station IR - Uninstumented Side of Model

The uninstrumented side of the model was imaged during US station run 3137. This side of the model is solid providing an opportunity to examine any impact the cavities have on the IR results. Stanton number maps are shown in Fig. 6.14. Across the Re range tested the patterns and magnitude of St observed are nearly identical to those measured on the instrumented side of the model. The streamwise streaks apparent in the Re = 3.6×10^6/m and 4×10^6/m show the same spatial extent and St level. This demonstrates that the streaks are not created or strengthened by the pressure transducers mounted on the instrumented side.

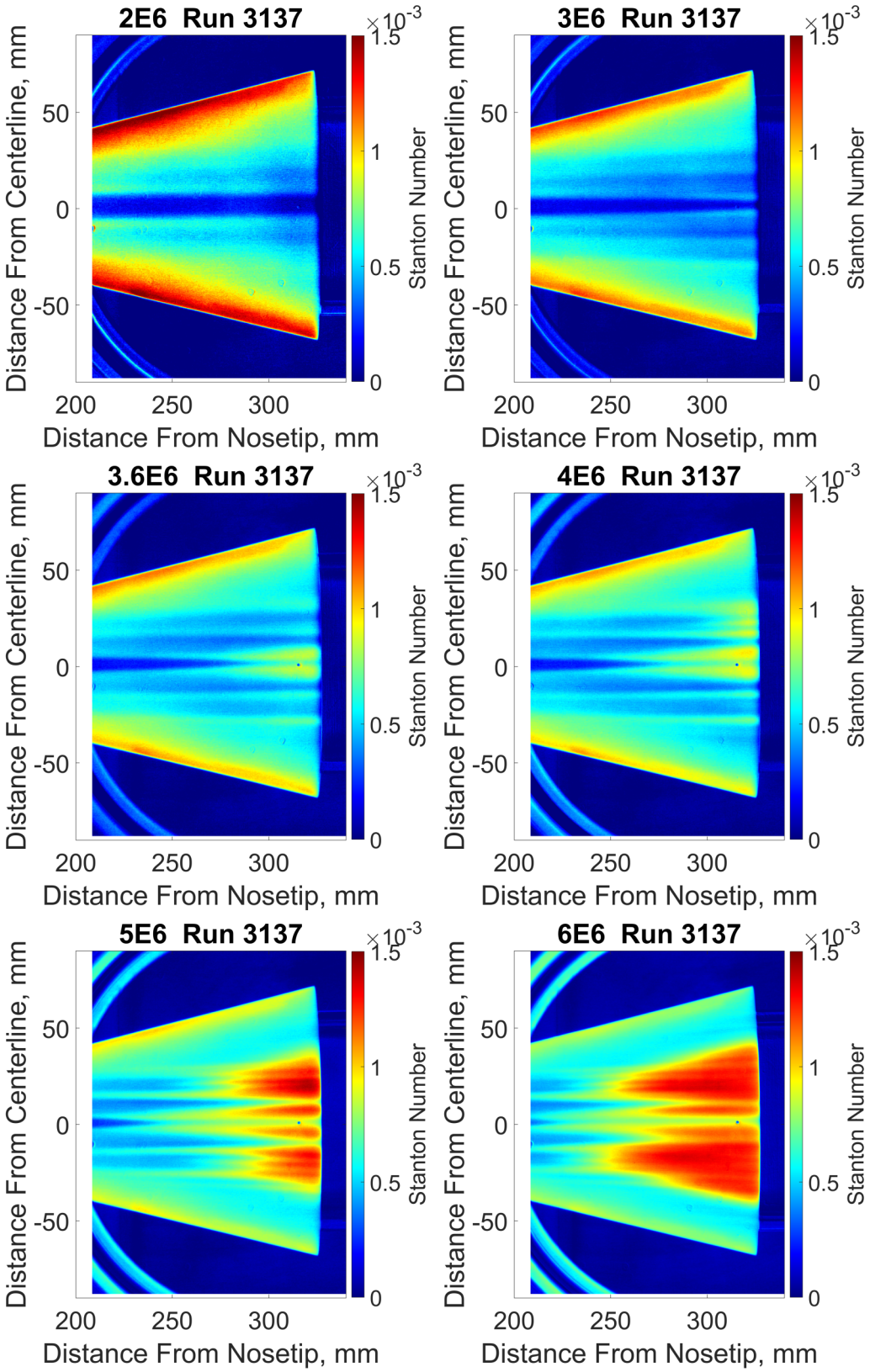

Figure 6.14: Stanton number maps, Re sweep ACE tunnel US station; uninstrumented side.

6.5 Upstream PCB Instrumented Runs

Following the previous campaign, runs were conducted with newly installed PCBs mounted 25 mm upstream of those at 300 mm. Due to the size of the sensors, the observed alignment of the streaks present in ACE, and the relatively small shift in location observed in computed crossflow paths from stability computations provided by the TAMU computational stability group, the transducers were placed directly upstream of the downstream transducers. Placement of these sensors this far forward on the model proved difficult. As documented in Subsection 4.1.7, holes for the transducers were machined through the underside of the model to allow flush mounting at this forward location. This added to the uncertainty of the mounting and sealing of these transducers. In the runs reported here no evidence was observed of leaks or excrescence of the transducers above or below the surface.

6.5.1 IR maps

Stanton number maps for Re sweeps with this instrumentation at the DS and US stations are shown in Fig. 6.15 and Fig. 6.16 respectively. These maps show good agreement with the maps from the previous instrumentation campaign. Of note is that these images were acquired nearly 8 months and 300 ACE tunnel runs apart. In this time the ACE facility nozzle exit Mach number was increased to Mach 7 and then returned to 5.9. The agreement between the tunnel conditions and model heat flux show the repeatability of the facility operating conditions and performance.

6.5.2 DS Station Spectra

PSDs of fluctuating pressure from each of the transducers is shown in Fig. 6.17. PSDs of Kulite 4, downstream of PCB 2D, reveal the same trends as seen in the Kulite data on the other

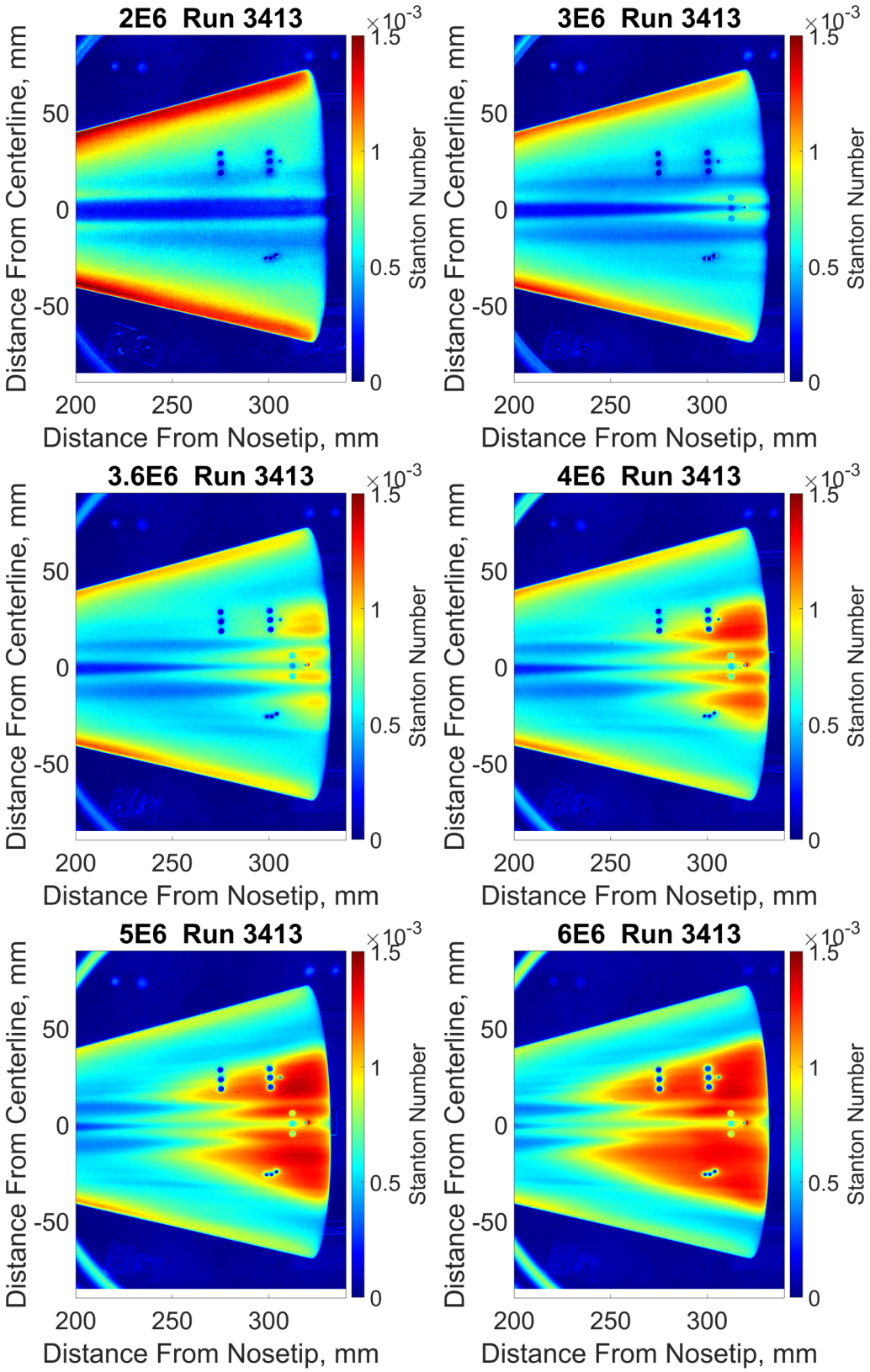

Figure 6.15: Stanton number maps, Re sweep ACE tunnel DS station; upstream instrumentation.

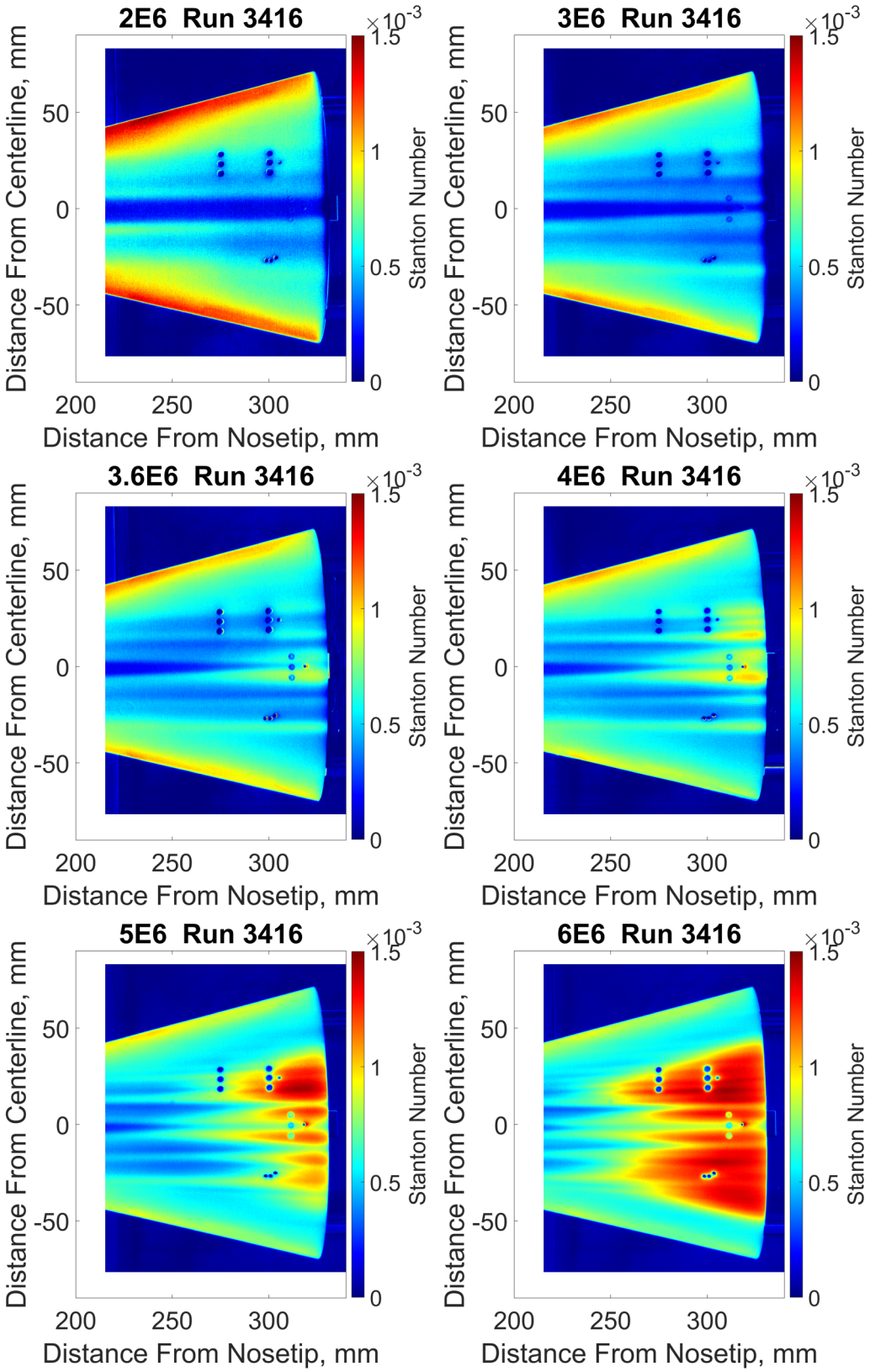

Figure 6.16: Stanton number maps, Re sweep ACE tunnel US station; Upstream instrumentation.

cone shoulder. That is, a peak centered near 20 kHz is visible and grows with increasing Re. Content past the linear response range of the Kulite is seen with a peak near 150 kHz. The traces at the downstream PCBs are in good agreement with those of run 3126 shown in Fig. 6.6b. Peaks are visible in the 100-250 kHz range. These peaks grow in amplitude and shift to higher frequency as Re is increased. There is nothing in the data to indicate that the installation of the upstream transducers has influenced the pressure fluctuations observed at this location. The upstream PCBs show disturbances in the same frequency bands present at the downstream PCBs. As one might expect, the disturbances appear above the noise floor at a higher Re than seen in the downstream PCB cluster. Content is not present in any transducer until 3.2×10^6/m and grows from there reaching a broad, turbulent profile near 5.4×10^6/m at sensors 2U and 3U. Sensor 1U does not converge to what appears to be a turbulent profile as the other transducers do. Looking to the IR data, sensor 1U is never fully engulfed by the elevated heating region as the other transducers are.

6.5.3 US Station Spectra

Trends visible in the PSDs of Fig. 6.18 are similar to those seen at the US station run 3135. The exact frequencies and initial disturbance onset seem to vary somewhat. The exact cause of these differences is unknown. It may be that the alignment of the model is such that the transducers do not lie in the same positions under the narrow streaks. The upstream sensors again show the same development as their downstream counterparts albeit at a higher Re. Small run to run variation was observed in the ACE campaign runs and is briefly discussed in App. D.

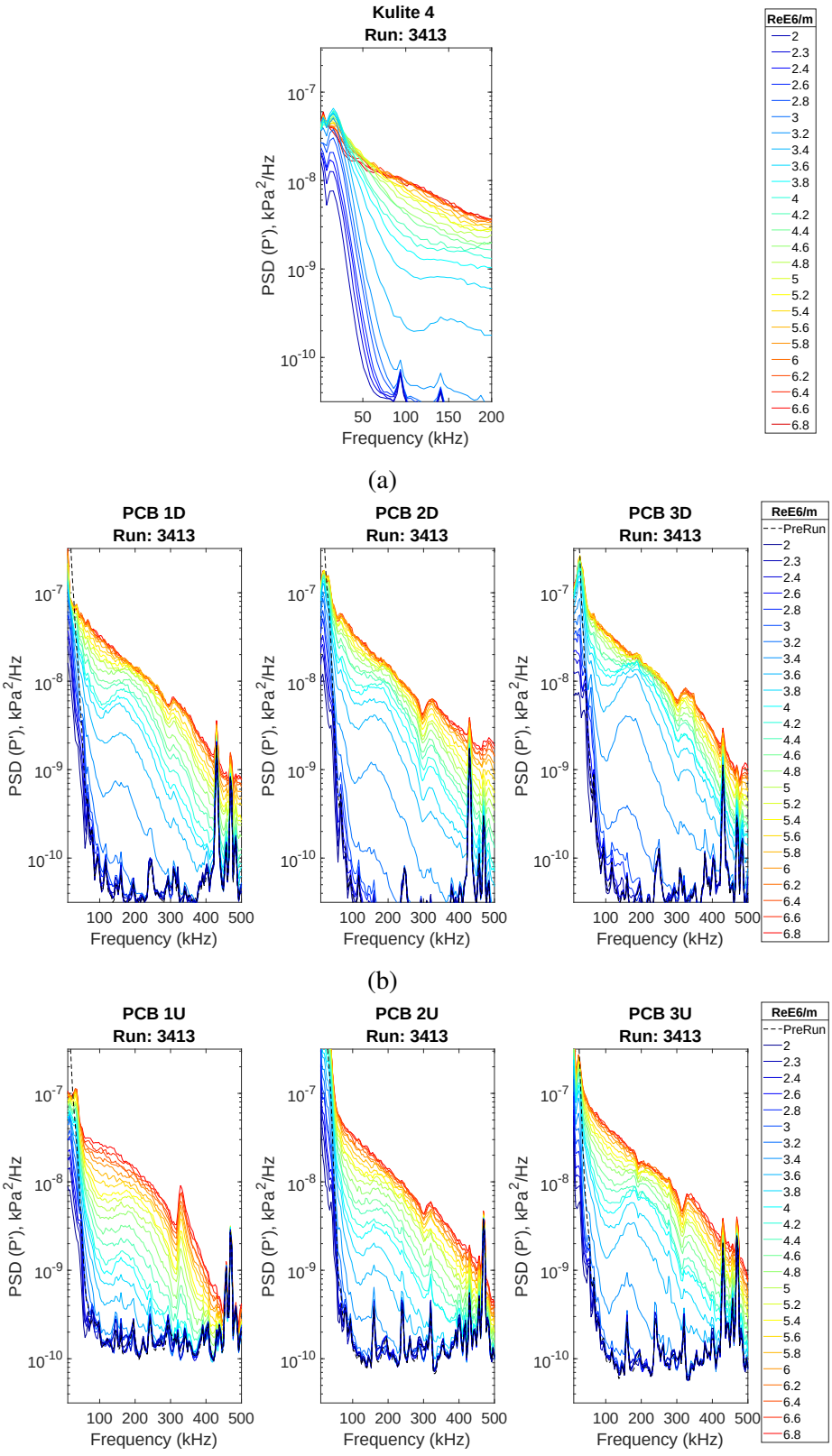

(a)

(b)

(c)

Figure 6.17: PSD of fluctuating pressure for each transducer cluster. Run 3413; ACE Tunnel; DS station. (a) Kulite 4, (b) Downstream shoulder PCBs, (c) Upstream shoulder PCBs

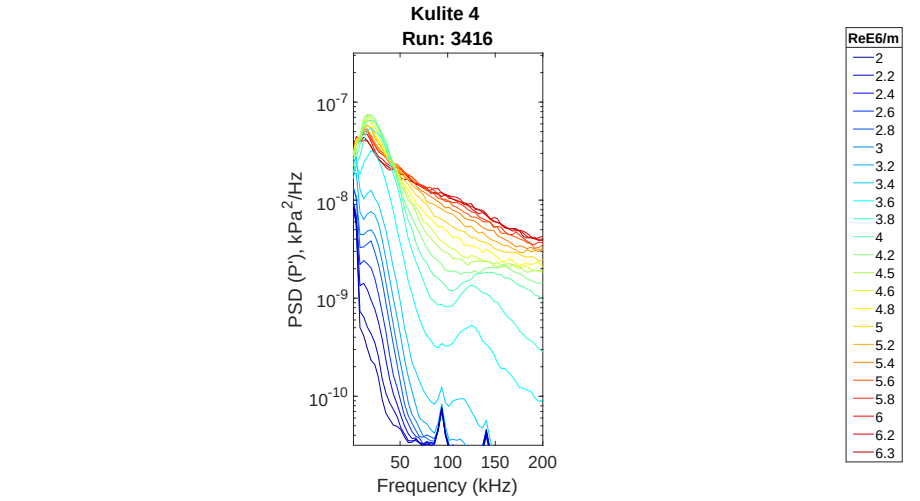

(a)

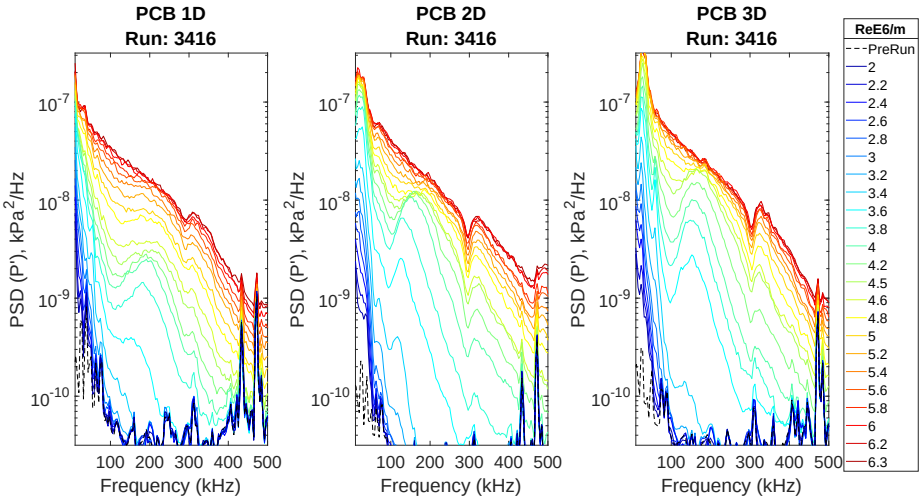

(b)

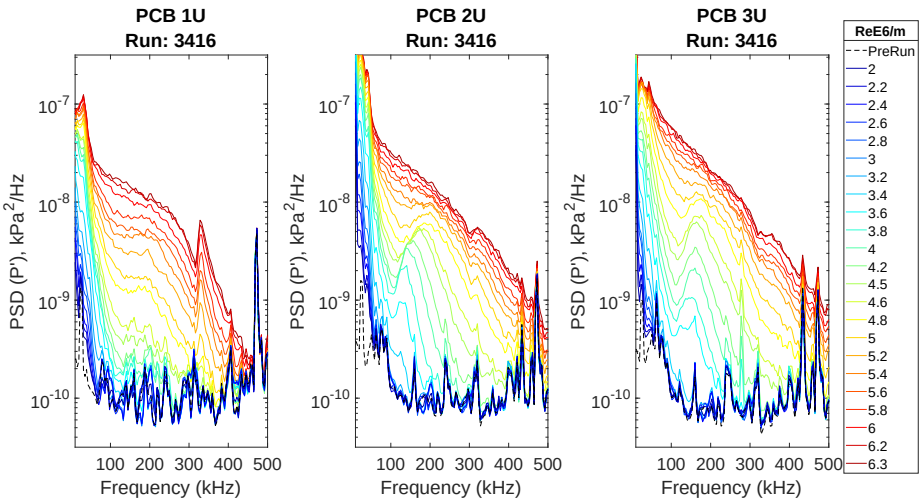

(c)

Figure 6.18: PSD of fluctuating pressure for each transducer cluster. Run 3416; ACE Tunnel; US station. (a) Kulite 4, (b) Downstream shoulder PCBs, (c) Upstream shoulder PCBs

6.6 Centerline Schlieren Images

A campaign of centerline schlieren videos was conducted in conjunction with the upstream instrumented runs of the previous section. High-speed schlieren photography allowed for the visualization of the boundary layer development along the model surface. The Z-type schlieren system described in Subsection 3.3.3 was utilized. The camera frame frequency was set to 60 kHz, with a shutter speed of 159 n sec and a resolution of 952 px x 256 px giving a spatial resolution of 8.2 px/mm. The camera was triggered at the center of each 100 ms NALDAQ acquisition block and acquired 150 frames. Figure 6.19 shows a instantaneous raw frame from the schlieren video and the same frame with a 150 frame average subtracted on the right. These images have been rotated to align with the model surface along the centerline of the model. These images were acquired normal to the model minor axis plane during run 3415 at the MID station. Visible in the image are two light streaks, one near the model surface and one offset at a higher position. This is a result of the mushroom shaped upwelling in the centerline region. At the left-hand side of the figure the streaks are straight lines parallel to the model surface, indicating a laminar boundary layer. Near 200 mm along the surface indications of deviations are present in both the top and bottom streaks. Moving further along the surface, significant distortions are visible. The top streak becomes wavy in character. Along the surface, long inclined structures are present. These features are somewhat more easily visible in the average subtracted image.

Figure 6.21 shows the evolution of the boundary layer with Reynolds number. Here, as expected from the IR and spectral data, the streaks at the top of the mushroom structure and close to the wall are both laminar at low Re. As Re is increased the incoming boundary layer thins and disturbances move forward on the model. These changes are in good agreement with the observa-

tions in the simultaneous IR images. They are also in agreement with spectra from MID station run 3127 shown in Fig. 6.20.

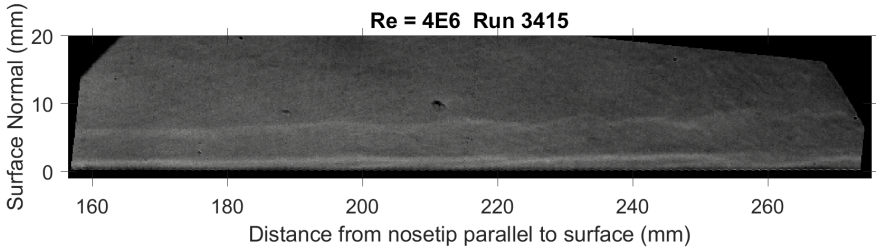

(a)

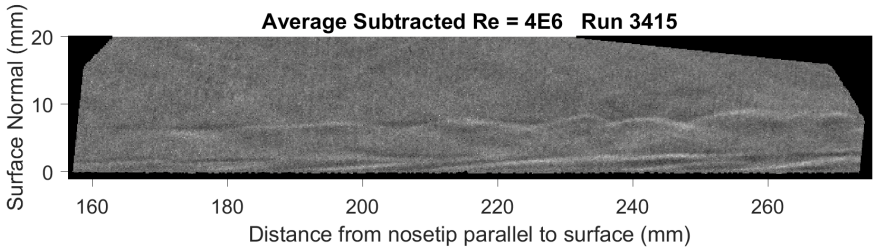

(b)

Figure 6.19: High-speed schlieren of model centerline. (a) Raw instantaneous schlieren image, (b) Average subtracted image.

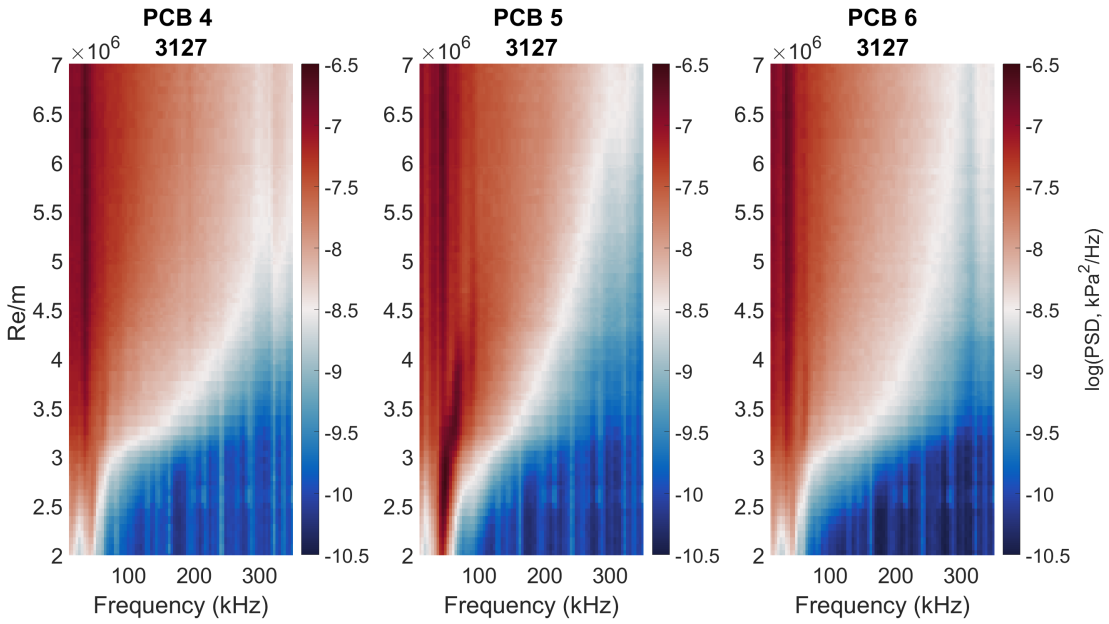

Figure 6.20: Waterfall plots of centerline PCB cluster. Run 3127; ACE tunnel; MID station.

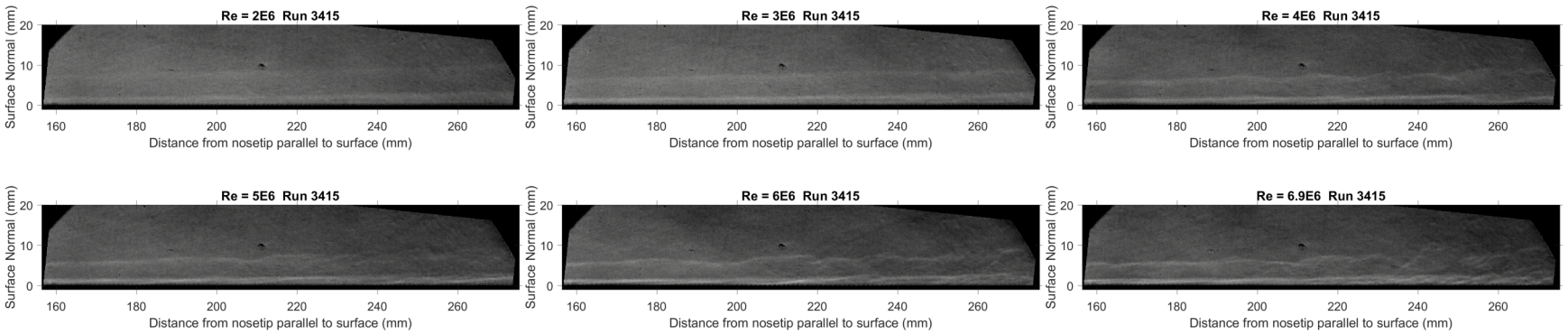

(a)

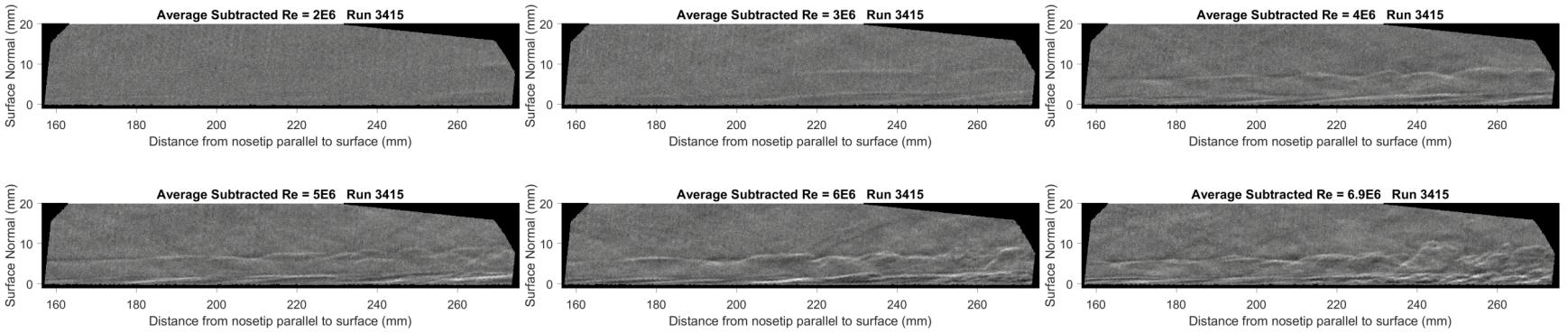

(b)

Figure 6.21: Schlieren images Re sweep Run 3115 ACE; MID station.

6.7 Summary and Discussion of ACE Campaign Results

Runs in ACE were conducted with an uninstrumented model, a model instrumented with Kulites and PCBs at the cone shoulder and PCBs at and straddling the centerline, and finally with PCB transducers mounted on the shoulder with 2 rows of sensors displaced 25 mm apart in the streamwise direction. IR measurements were made of the model's PEEK surface and utilized to compute the heat flux which was then nondimensionalized using freestream conditions into Stanton number. Pressure transducer data was simultaneously recorded allowing examination of pressure fluctuations at the model surface and their evolution. For a subset of runs in the ACE tunnel, high speed schlieren video was acquired surveying the development of the structure near the model centerline. The model was tested at three model nosetip positions previously characterized in Chapter 5, exposing the model to different freestream disturbance environments.

IR results were consistent between campaigns indicating good repeatability in model alignment and showing no evidence that instrumenting the model effected the distribution or evolution of features in the heating fronts. At the DS station, disturbances first appeared as regions of elevated St on either side of the model centerline. These streaks move forward engulfing the centerline PCBs after which PSDs of fluctuating pressure at these transducer locations shows broadband content indicative of a turbulent profile. This is further indication that the elevated heating lobes represent a transition front on the model surface. On the cone shoulder, the development of streaks of elevated heating leading into a more diffuse lobe of elevated heating are observed. This is evidence of the stationary crossflow vortices that are expected to develop in this region. Fig. 6.22 shows a comparison of heating at the three test stations for a series of Reynolds numbers. This figure clearly illustrates the trends observed with lower freestream disturbances. At the MID station,

results are very similar to at the DS station. The freestream characterization revealed very similar pressure and mass flux fluctuations at the two locations. Differences present may be due to small differences in model alignment and differences in disturbance field off the tunnel centerline.

At the US station the heating front appeared at a higher Reynolds number in comparison with the DS station. Transition onset was delayed at the lower disturbance US location. Furthermore, elevated heating streaks, believed to be evidence of stationary crossflow instability, were apparent at each station leading into the more diffuse region of elevated heating. At the US station the streaks were much more apparent.

An interesting feature of the St maps is the elevated St near the leading edges of the model. Here we must be careful to note that the viewing angle as we approach the edges is rapidly increasing, likely altering the emissivity and other assumptions used in calculating the heat flux in this region. One might assume that the the trend of elevated St here is due to the run procedure: Starting at a low Reynolds number with a nominally room temperature wall and sweeping upward. However, the same trend was observed in runs conducted in the opposite manner. It appears that this trend is a result of the nondimensionalization of heat flux to St. The dimensional heat flux plots show that heat transfer is higher in the leading edge region in comparison to farther inboard on the cone surface. As Re increases the heat flux near the leading edge increases. When nondimensionalized by the freestream conditions this trend reverses with highest St at the lower Re. Transition along the model attachment lines was not observed in Borg *et al.* (2011) where direct measurements were made of the attachment line of a similar model using TSP. Experiments including direct viewing of the attachment line as well as wall mounted pressure transducers would allow for investigation of the instabilities along the model leading edges.

Similar frequencies and trends were seen in the pressure transducer data at each of the stations.

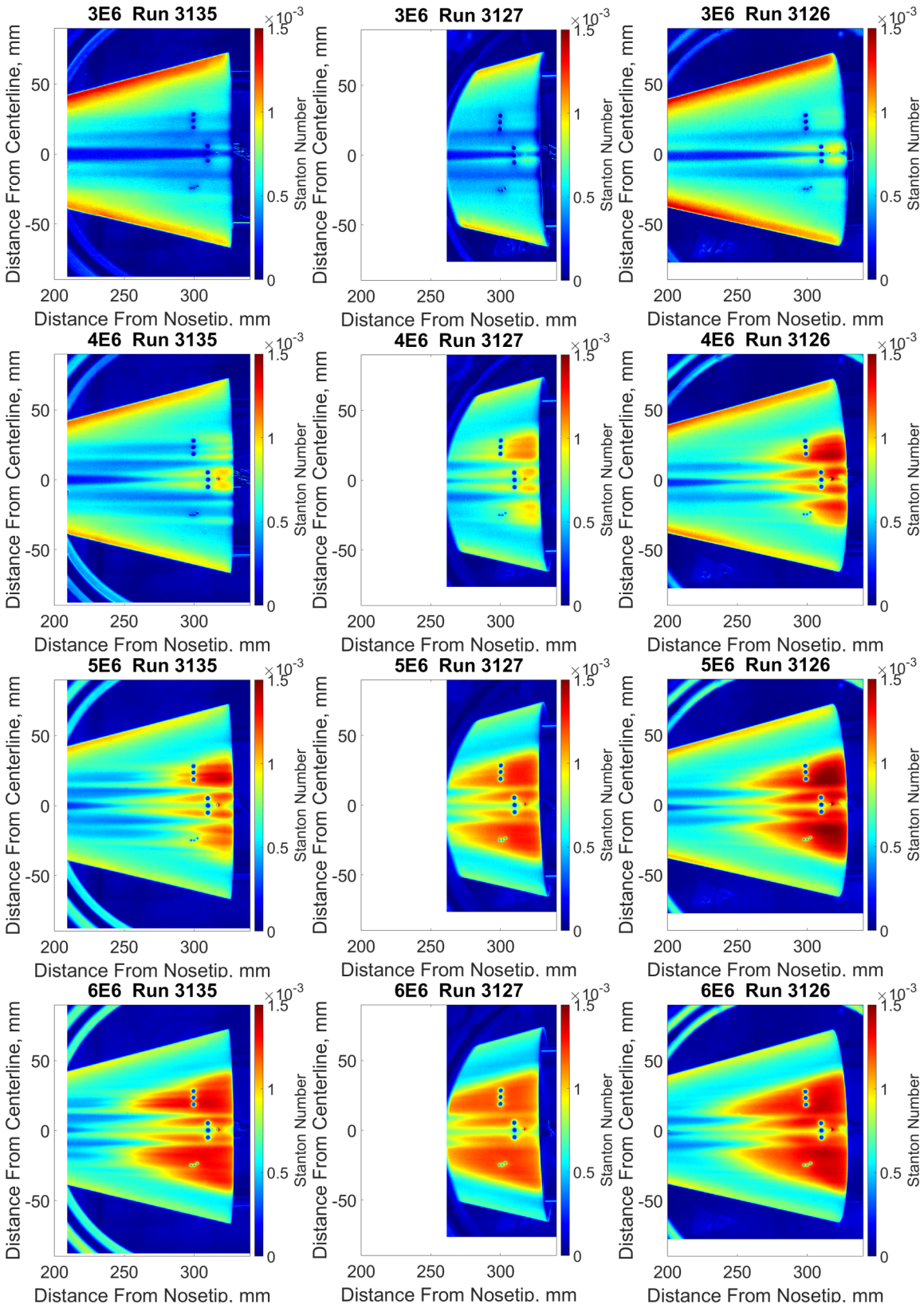

Figure 6.22: Comparison of heating upstream (left) midstream (center) and downstream (right) stations; ACE tunnel.

Table 6.2 summarizes the spectral bands observed on the model surface. The table also presents the possible sources of the spectral band observed which are compared and discussed in more detail in Chapter 8. The Kulite PSDs show disturbances near 20 kHz which grow and peak after the tunnel jump in freestream disturbances. There is also content which appears in the region of 150 kHz. Although this is outside the linear frequency response band of the Kulites, this content is similar to that observed in the PCBs. Shoulder PCBs show some low frequency content but interpretation is made difficult by electronic noise and the sensors response at low frequency. Frequencies in the range of 10-80 kHz appear to be present but don't appear to shift in frequency and are present in the turbulent spectra at the highest Re tested. The centerline PCBs show spectral peaks at low frequencies present on either side of the model centerline. PCB 5 at the centerline shows an initial peak at a similar frequency to that on either side of the model centerline, this frequency then shifts higher as the freestream noise increases and then broadens and is surpassed by content at the original frequency. This content is again in a region where electronic noise seems to be present but its consistent shift in frequency between all of the stations seems to indicate that it is physical content present in the flow.

Table 6.2: Observed excited spectral bands: ACE facility, noisy flow.

Frequency	TAMU ACE (all locations)	Possible Modes
0	IR Therm; Re/m 3.0-8.2$x10^6$	Stationary
10-20 kHz	Kulites 1-3; Re/m=2.0-6.0$x10^6$	Unknown
100-300 kHz	PCB 1-3; Re/m 2.0-5.0$x10^6$	Traveling, Type I & II Secondary Instability, 2nd mode
20-45 kHz	PCB 4,6; Re/m 2.4-6.8$x10^6$	Centerline
45-70 kHz	PCB 5; Re/m 2.0-4.0$x10^6$	Centerline

High-speed schlieren photography of the model centerline revealed the growth and eventual breakdown of structures withing the large centerline mushroom boundary layer. The incoming laminar boundary layer is seen to grow with disturbances at the top edge of the mushroom as well as closer to the model wall. Initial large scale structures are observed appearing as wavelike distortions. Eventually at the higher Re tested, the large scale structures break down into smaller scale structures distributed throughout the boundary layer appearing turbulent. The location of this breakdown coincides with the region of increased St observed along the model centerline in the IR images.

7. RESULTS: TAMU M6QT HIFiRE-5 CAMPAIGN

7.1 M6QT Campaign Overview and Data Acquisition Settings

Following the ACE facility campaign, the instrumented model was run in the M6QT to provide data at a quiet freestream disturbance level. Due to the large base diameter and major axis half angle, it was initially uncertain if the model would fit within the M6QT nozzle exit shock and flow would remain started. Initial runs were conducted with the aluminum blockage model and revealed that the tunnel would indeed start and operate through its nominal quiet Re range without the exit shock impinging on the model surface. A schlieren image and description of the model position within the facility is given in Subsection 4.2.4. The model was positioned with its base extending 38 mm from the nozzle exit plane. The cone of disturbances radiated from the nozzle sidewall is estimated to impinge on the model attachment line at approximately 127 mm downstream of the nosetip at Re = 10×10^6/m.

The physical layout of the M6QT's enclosed-free-jet test section made insertion and alignment more difficult than in the ACE facility. This meant that the model spent more time within the facility before each run resulting in an elevated initial wall temperatures and increased variability in observed heat flux between runs. Data were acquired using the same NALDAQ VI and instrumentation as in the ACE runs. The IR camera was again manually triggered upon opening of the 4" ejector supply ball valve and synced in post processing with the tunnel static pressure. Pressure transducer data were acquired at 2 MHz for 100 ms sampling lengths. Due to a maintenance issue, the Stanford Research filter utilized during the ACE campaign was unavailable. During the initial instrumentation runs, Kulite transducers were all low-pass filtered at 200 kHz using 8-pole Bessel

filters. PCBs 1U-3U and 4-5 were low-pass filtered using 1 MHz filters. PCB 6 was unfiltered and no discernible impact of the lack of filtering was observed in its spectra. Runs with upstream PCB instrumentation were conducted with all PCBs low-pass filtered at 1 MHz and Kulite 4 low-pass filtered at 200 kHz using Khron-Hite 8-pole Bessel filters. Runs were conducted by sweeping settling chamber pressure, effectively sweeping through the Reynolds number operation range of the facility. Re was swept from roughly 7×10^6/m to 12×10^6/m and then down until tunnel unstart. Test conditions for the runs presented are given in Table 7.1 and an example of tunnel conditions is shown in Fig. 7.1. Orange markers in Fig. 7.1 indicate 0.2×10^6/m increments in Re from 7×10^6-11×10^6/m.

Table 7.1: M6QT test conditions.

Run Number	T_0 (K)	T_w (K)	Re $x10^6$/m	Angle of Attack
M6QT-3181	430	319	7-11.6	0°
M6QT-3182	430	317	6.9-12	0°
M6QT-3420	430	319	6.1-11.3	0°
M6QT-3184	430	323	6.9-12	1°

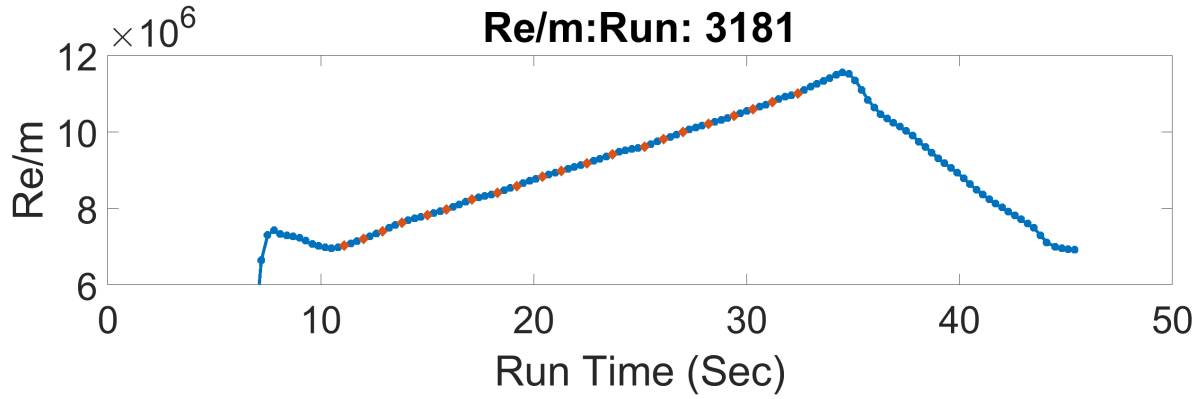

Figure 7.1: Example Re time history of a M6QT run.

7.2 Instrumented Model Runs - M6QT

7.2.1 M6QT IR

Stanton number maps for the range of Reynolds number tested in the M6QT are shown in Fig. 7.2. The maps are presented here on the same scale as the previous ACE results. Immediately obvious is the fact that the heat flux is much lower overall than observed within the ACE tunnel. At Re = 7×10^6/m, nearly streamwise streaks that extend over a large portion of the model surface are clearly visible. These are similar in position and structure as expected from CFD and BAM6QT quiet results. These streaks are believed to be due to stationary crossflow vortices anchored to surface roughness upstream on the cone. Based on the CFD analysis of Kocian *et al.* (2017), the neutral stability points of stationary crossflow instability and corresponding vortices which would coincide with the streaks observed is upstream of the intersection of the nozzle quiet core boundary and the leading edge of the cone. This limits the effect of the radiated disturbances, at least in determining initial amplitudes of disturbances within the model boundary layer.

As Re is increased to 8×10^6/m, elevated heating appears along the streaks towards the rear of the model and are much more pronounced by 9×10^6/m. The most prominent streaks are located at roughly 25 mm from the attachment line on both halves of the cone. These elevated heating regions move forward and expand as Re is increased further. Following one of the streaks in the Re = 10×10^6/m map downstream, the heat flux increases and broadens into a narrow wedge. The pattern of heating within these wedges is discussed further in Sec. 7.5. The streamwise extent of these wedges varies with spanwise position creating a jagged front. As Re increases, some neighboring wedges meet but appear to persist downstream.

The observed heating is roughly symmetrical about the model centerline. A region of elevated

heating appears near the cone shoulder on the bottom half of the model. Streamlines which pass through this region likely originate downstream of where the turbulent nozzle boundary layer radiates noise onto the model surface. This could cause the initial amplitudes of disturbances to be much higher hastening the onset of transition. The discrepancy in the outboard shoulder regions between the top and bottom halves of the maps may be due to variations in machining roughness.

Along the model centerline, evidence of the mushroom structure is present and similar to what was observed in the conventional ACE facility. At Re = 7×10^6/m, on either side of the centerline from 5-7 mm a wide band of heating is visible bordering a lower heat flux flow at the centerline. Unlike in the ACE facility, a streak directly along the model centerline is visible. As freestream Re is increased, slight narrowing between the outer streaks and the centerline is visible near the end of the cone. By Re = 9×10^6/m very limited elevated heating is present near the rear of the cone on either side of the centerline. With further Re increase the elevated heating moves forward with the streaks on either side of the centerline drawing together and impinging on the centerline. At all Re tested, the heating along the centerline is lower than that observed further outboard on the cone shoulder and the streamwise onset of the heating is farther downstream.

7.2.2 M6QT Spectra

The PSD estimates of the fluctuating pressures measured by Kulite sensors on the cone shoulder are shown in Fig. 7.4a and waterfall plots of Fig. 7.5a. The M6QT data are qualitatively different than those measured in the ACE tunnel. In particular, the 10-20 kHz band of content is absent, and instead there is a clear disturbance band in the 20-80 kHz range. A peak near 45-50 kHz is visible in Kulites 1 and 2, but not 3. This peak is the expected frequency band of the traveling crossflow mode on this geometry (Borg *et al.*, 2015*b*). This content appears near Re = 8.5×10^6/m

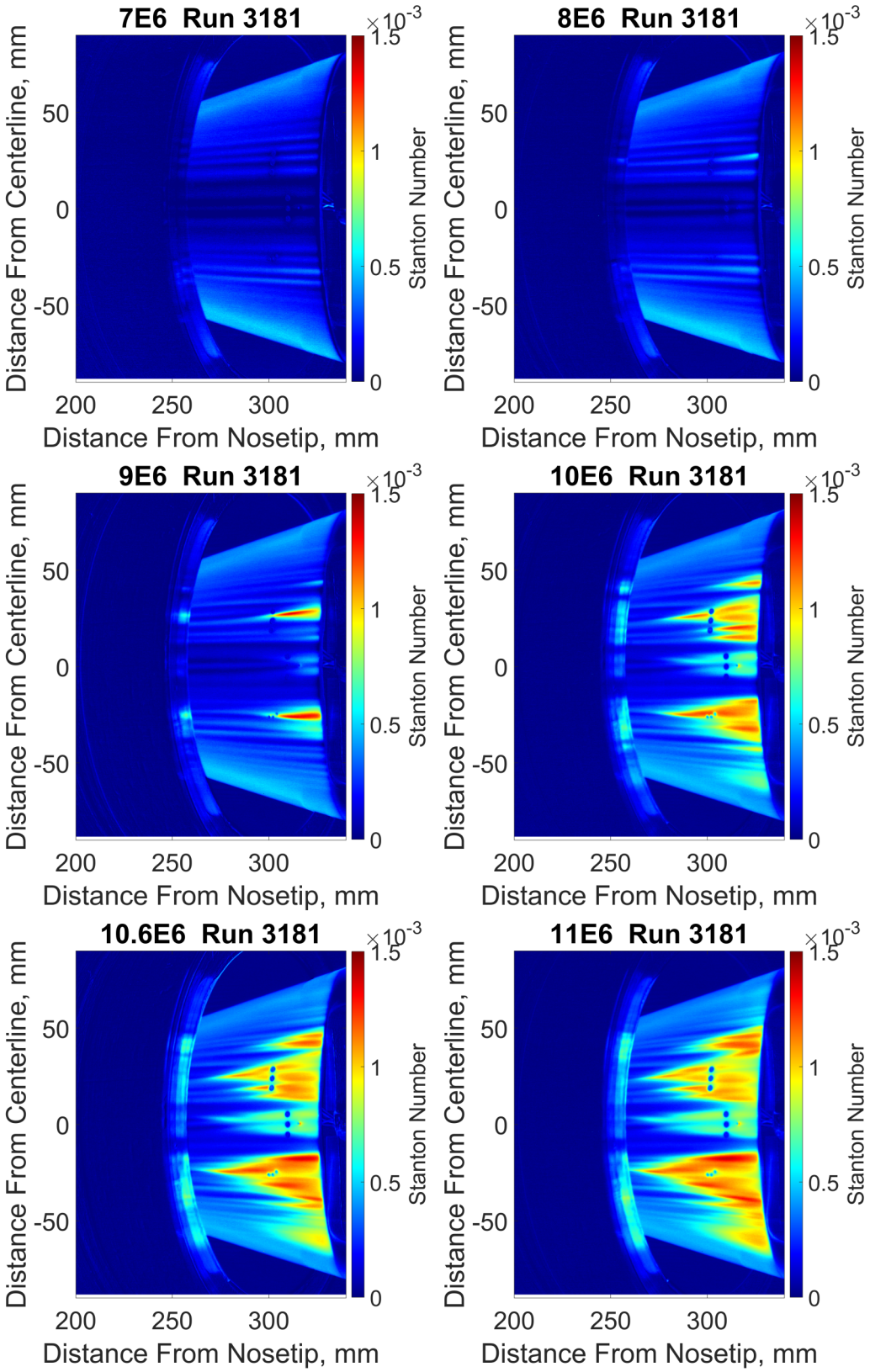

Figure 7.2: Stanton number maps, Re sweep M6QT; Initial instrumentation.

and grows until 9.4×10^6/m where it begins to broaden and is surpassed by broadband noise. This corresponds well with the transducers being engulfed by the heating along the dominant streak on the cone shoulder. Each Kulite eventually collapses to a similar broad profile above 9.8×10^6/m. The elevated lobe between 150 and 200 kHz at these highest Reynolds numbers is believed to be the result of the resonant frequency of the transducers (see Sec. 6.2). The lack of a measured 45 kHz band in Kulite 3 may be because of the positioning of the sensors relative to the heating streaks. Shown in figure Fig. 7.3, at Re = 7×10^6/m Kulites 1 & 2 are beneath the center of the streak while Kulite 3 is towards the outside. By 9×10^6/m the transducers are in slightly different positions with Kulites 1 & 2 near the bottom edge and Kulite 3 near the top edge. The CFD of Moyes *et al.* (2017); Kocian *et al.* (2017) and experiments of Edelman & Schneider (2018) show clear bands of excited frequencies which vary in position with respect to stationary crossflow vortices. The lack of the 45 kHz band in Kulite 3 may indicate interaction of this band with the higher frequency disturbance observed in the PCB spectra. Corke *et al.* (2018) report measurements which show evidence that such an interaction occured on a circular cone at angle of attack under noisy flow with crossflow vortices generated with discrete roughness elements near the nosetip.

The PSD estimates of the fluctuating pressures measured by downstream shoulder PCB sensors are shown in Fig. 7.4b and Fig. 7.5b. Visible in the PCB 1 data is a broad region of growth with an accompanying sharp peak near 200 kHz. This band grows rapidly from Re = 7.2 to roughly 9.4×10^6/m. With increasing Re the peak broadens and decays in amplitude eventually being replaced by a broadband profile indicative of a turbulent boundary layer. This peak is visible to a lesser extent in the spectra from PCB 2. Apparent in the spectra for both PCB 2 and 3 is a band of frequencies centered near 300 kHz. This is the region where the PCB sensors typically show a kink in the spectra that appears to be nonphysical. Flow content may be present at these

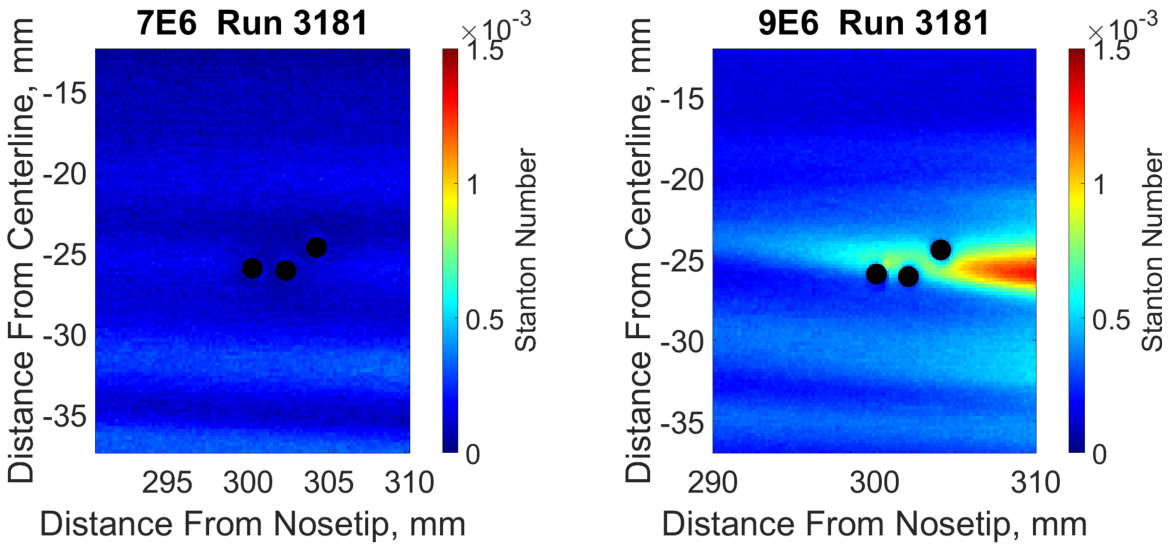

(a) (b)

Figure 7.3: Position of Kulite Cluster Relative to heating streaks, M6QT Run 3181: (a) 7×10^6/m (b) 9×10^6/m. Kulite locations have been indicated with black circles in the figure for visibility.

frequencies, but its interpretation is hampered by this sensor artifact. The variance seen in the transducer spectra is consistent with the expectation that the spectral content varies with location underneath the stationary structures.

The spectra for PCBs 4-6, located along and adjacent to the model centerline, are plotted in Fig. 7.4c and Fig. 7.5c. These data show distinctive behavior on the centerline and 5 mm on either side. PCBs 4 & 6 show three basic excited frequency bands centered near 40, 105 and 210 kHz. The 40 kHz peak appears in the pre-run noise floor spectra and does not appear to shift in frequency during the Reynolds number sweep, both indications that it is some type of sensor noise. The peaks at 105 and 210 kHz are present at the lowest Re tested and are of considerable magnitude. As Re increases the amplitudes grow and shift slightly higher in frequency. Content fills in around these peaks as Re is increased and the peaks are replaced by a broad spectra near 9.4×10^6/m. As Re increases the spectra from PCB 4 broadens to a full apparently turbulent profile. Across the centerline PCB 6 behaves similarly but shows lower amplitude peaks and does

not seem to collapse to a fully turbulent profile. Examining its position underneath the centerline structure in the IR, as Re increases the centerline structure shifts slightly placing the transducer near the outside of the streak. Also visible in the IR is lower Stanton number within the streak than passes over PCB 4. This again illustrates the sensitivity of these measurements to small differences in alignment and resulting position within the structures observed. PCB 5 at the model centerline shows low frequency (<40 kHz) content similar to that seen in PCB 4 and 6. As with those transducers, content at roughly the same position is clear in the noise floor, making analysis of this band uncertain. PCB 5 also has a band of disturbances from 70-120 kHz similar to the transducers on either side of the model centerline. The band has a distinct two peak shape with a small peak at 82 kHz and higher amplitude peak at 105 kHz. These peaks grow and shift to higher frequency, 93 kHz and 120 kHz by Re = 8.4×10^6. The lower frequency peak grows more quickly and surpasses the high frequency peak in amplitude at 8.4×10^6/m. The peak, now at roughly 100 kHz, continues growing, surpassing the eventual amplitude of the broad turbulent spectra of the highest Re tested. The peak reaches its maximum amplitude at 9.6×10^6/m, 113 kHz and quickly broadens, decreasing in amplitude as it does, to a full broad profile.

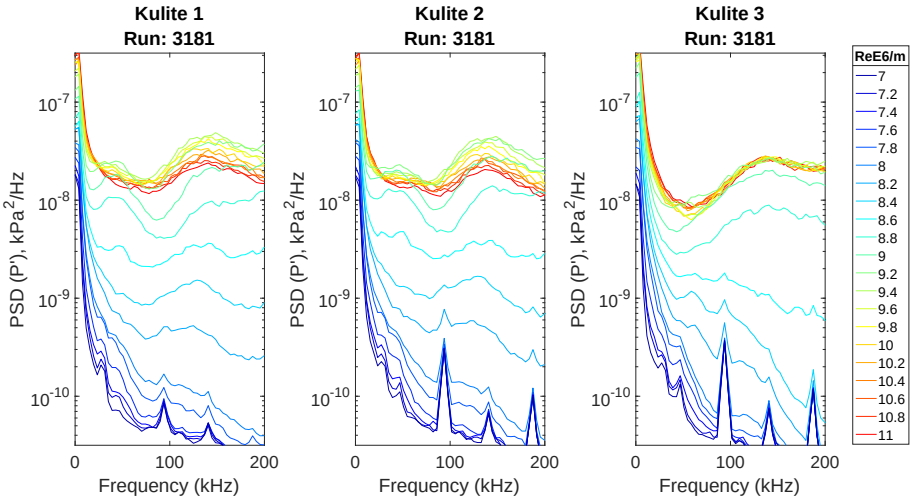

(a)

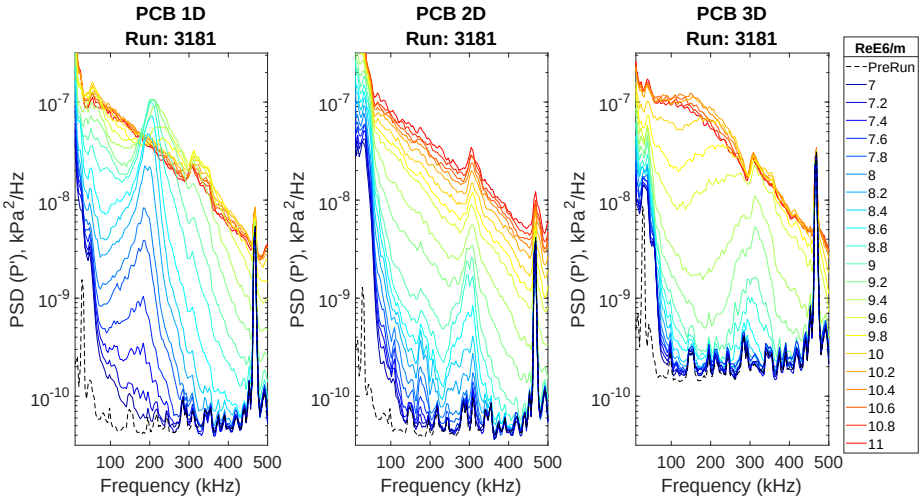

(b)

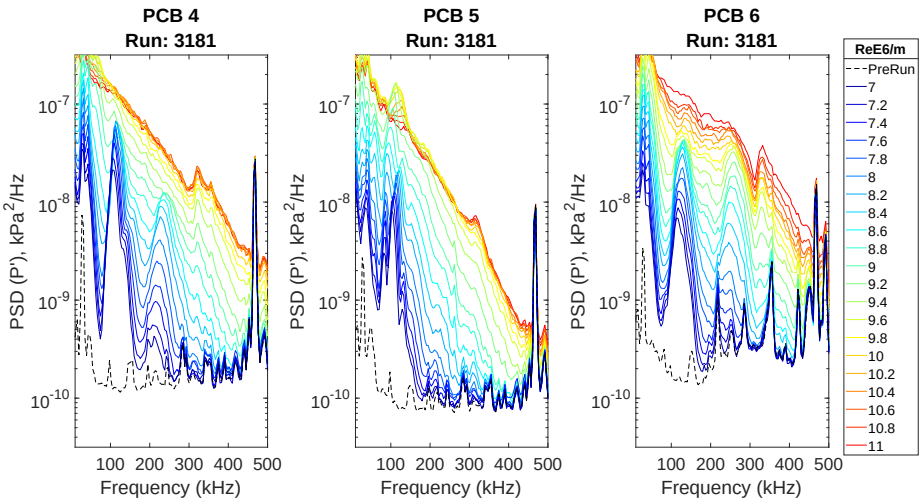

(c)

Figure 7.4: PSD of Fluctuating Pressure for Each transducer cluster Run 3181; M6QT. (a) Kulite, (b) Downstream Shoulder PCB, (c) Centerline PCB

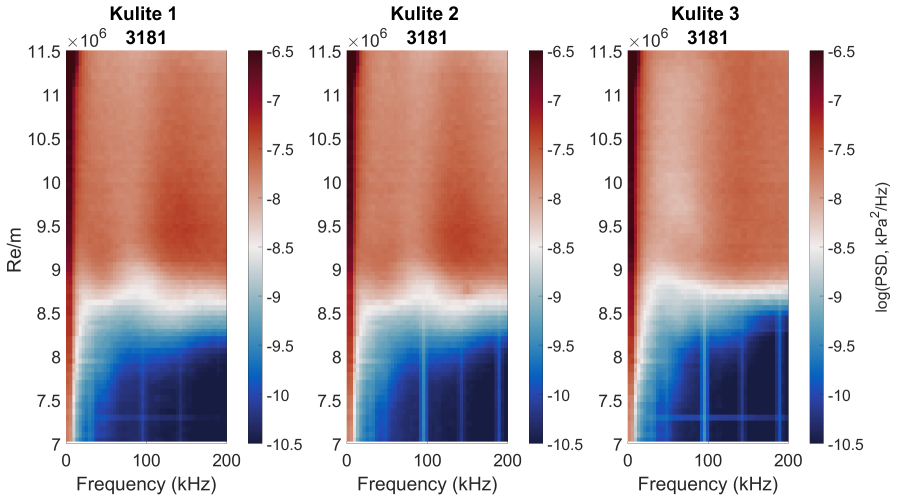

(a)

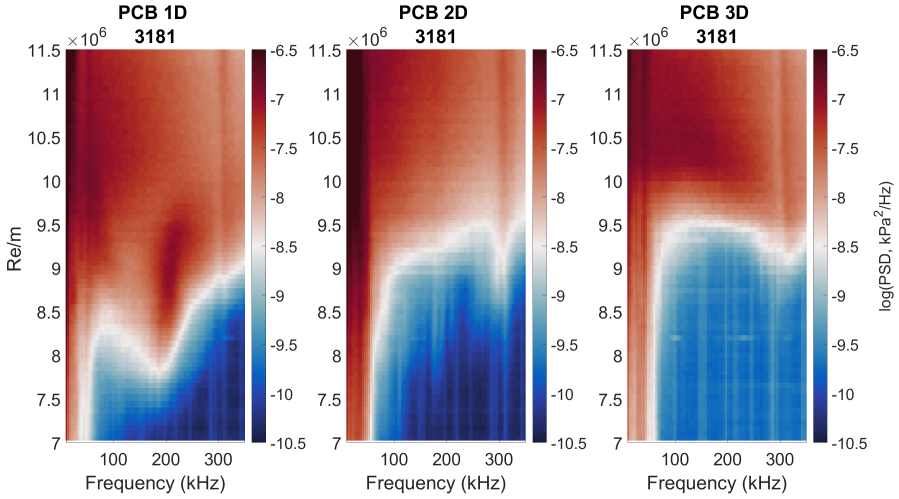

(b)

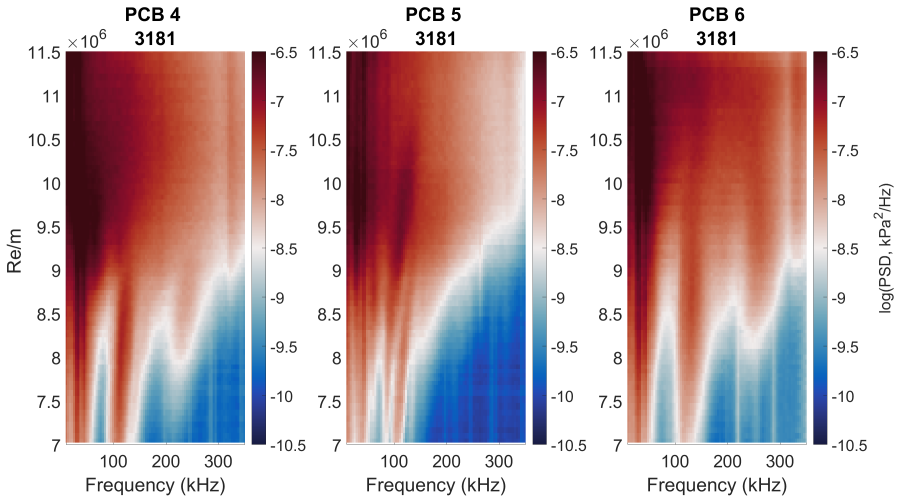

(c)

Figure 7.5: Waterfall PSD of Fluctuating Pressure for Each transducer cluster Run 3181; M6QT. (a) Kulite, (b) Downstream Shoulder PCB, (c) Centerline PCB

7.3 M6QT Upstream Instrumentation Runs

The model instrumented with upstream PCBs was also run in the M6QT to examine spatial growth of instabilities. Stanton number maps from run 3420 in the M6QT under quiet flow are shown in Fig. 7.6. The evolution with freestream unit Reynolds number matches that of run 3181. The upstream transducers do not appear to have altered the heating visible on the model. The Stanton numbers observed are universally higher than during run 3181 despite similar initial conditions, this is believed to be an artifact of the IR camera setup during this run.

PSD estimates for upstream and downstream PCBs 1-3 and Kulite 4 are presented in Fig. 7.7 and Fig. 7.8. In Kulite 4, a slight hump is visible in the spectra near 45 kHz beginning near Re = 9×10^6/m. The peak again broadens and is replaced by broadband content at higher Re. Downstream PCBs 1D-3D show similar content to run 3181 with PCB 1D showing a peak near 200 kHz which grows from 7×10^6/m reaching a maximum amplitude near 9.4×10^6/m and broadening to a turbulent profile. PCB 1U contains some evidence of a 200 kHz peak near 8.8×10^6/m which grows until 9.6×10^6/m and broadens by 9.8×10^6/m. This peak is less dominant a feature than in the spectra of PCB 1D. Examining the IR images of figure Fig. 7.6, the two transducers lie under similar positions within the same elevated temperature streak. Therefore, the difference in the spectra is somewhat unexpected but may indicate the extreme sensitivity of these disturbance measurements to location within the stationary structure. Downstream PCBs 2D and 3D again show content in the 250-350 kHz range, the interpretation of which is complicated by the sensor/noise artifact present at 350 kHz. Upstream transducers PCBs 2U and 3U show growth in a similar band as their downstream counterparts however at a delayed freestream Re as one might expect. As the transition front pushes forward with Reynolds number, PCB 1D is engulfed by the broadening

adjacent streak; this coincides with its broadening to a turbulent profile. PCBs 2D and 3D are also engulfed as the front pushes forward with increasing freestream Re. The upstream PCBs remain outside of this elevated heating region throughout the Re range tested and this is reflected in the spectra not appearing to collapse to broad turbulent profile as their downstream counterparts do.

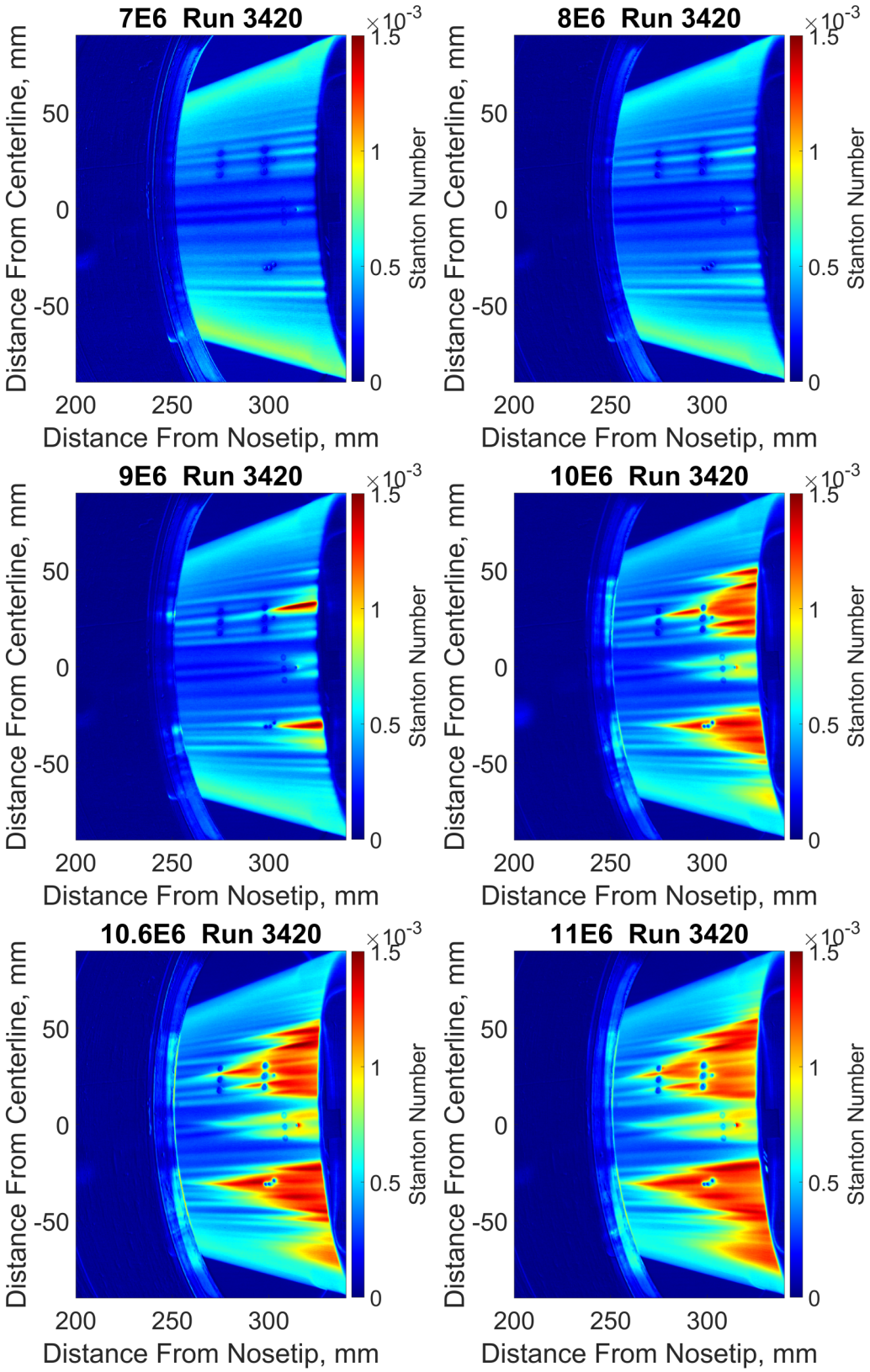

Figure 7.6: Stanton number maps, Re sweep M6QT; Upstream instrumentation.

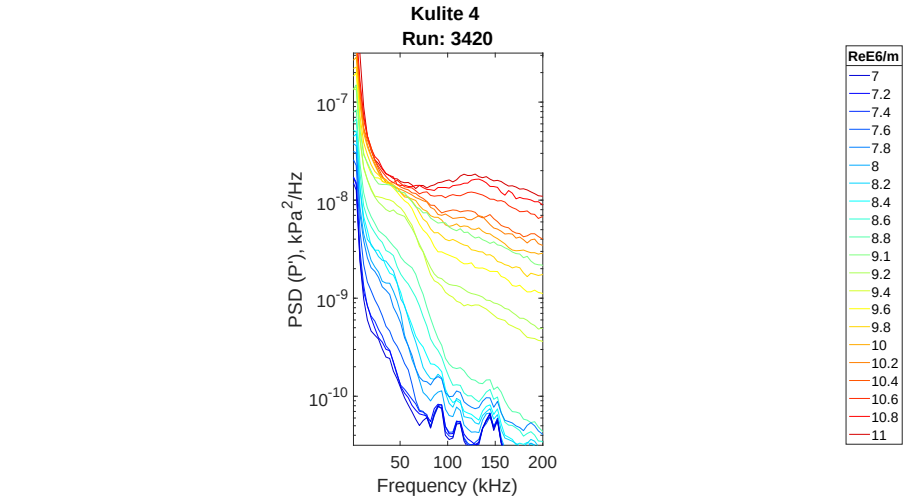

(a)

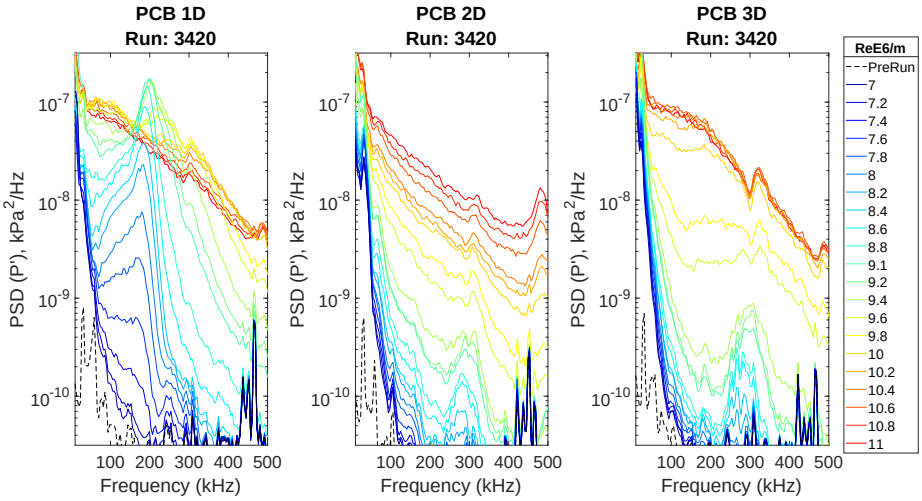

(b)

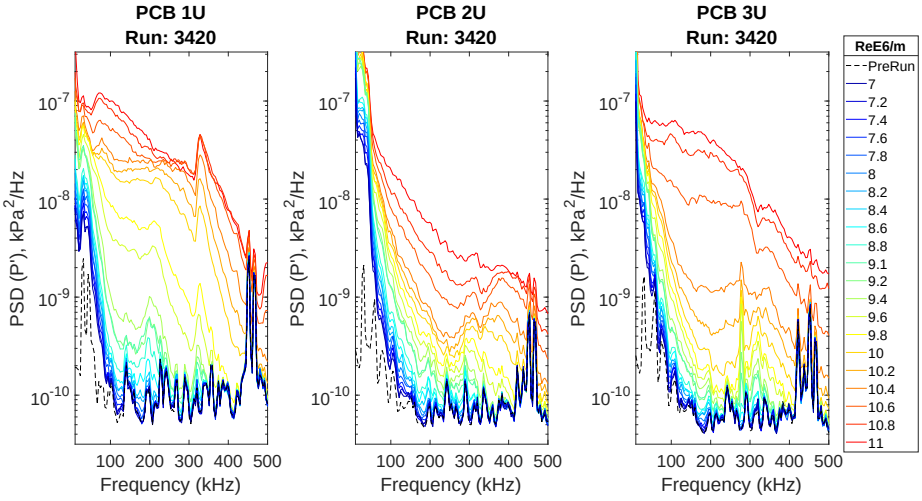

(c)

Figure 7.7: PSD of Fluctuating Pressure for Each transducer cluster Run 3420; ACE Tunnel; DS station. (a) Kulite 4, (b) Downstream shoulder PCBs, (c) Upstream Shoulder PCBs

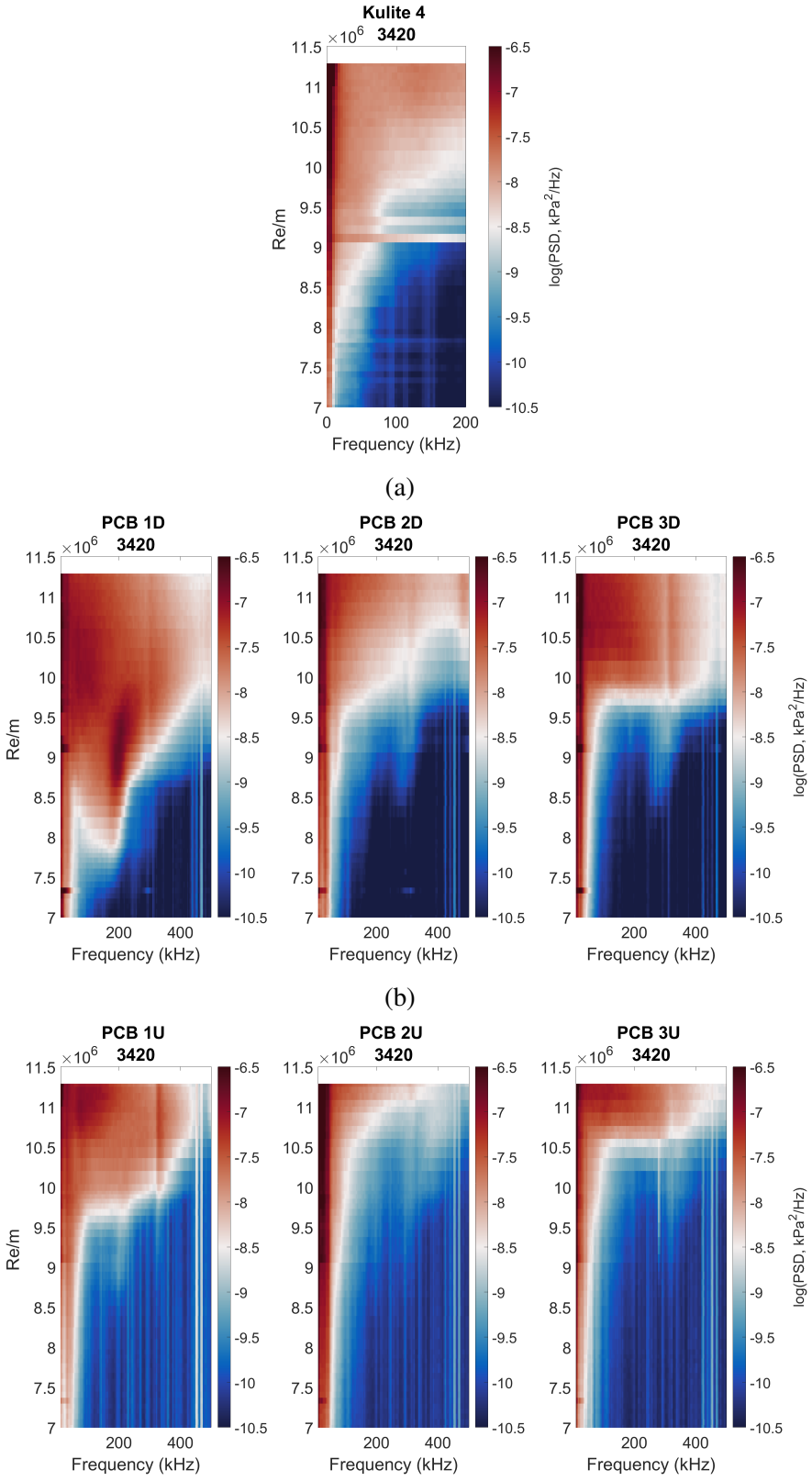

Figure 7.8: Waterfall PSD of Fluctuating Pressure for Each transducer cluster Run 3420; M6QT. (a) Kulite 4, (b) Downstream Shoulder PCBs, (c) Upstream shoulder PCBs

7.4 M6QT Yawed Run

An additional run was conducted with the model nosetip yawed at 1° downward relative to the tunnel floor. This rotation corresponds to the top half of the Stanton number maps as windward. Comparing figures 7.2 and 7.9, the heating on the yawed case is much more asymmetrical with increased heating for a given Reynolds number on the top side and lower heating on the bottom. This is the same trend described in Borg & Kimmel (2017*b*) of yaw angle increasing the strength of the vortices observed on the windward side of the model. With the shift in the location of the vortices due to the yaw angle, the pressure transducers now lie in different positions relative to the vortex structure.

The Kulite transducer data shown in Fig. 7.10a and Fig. 7.11a now all show evidence of spectral content with a peak in the 40-50 kHz range seen only in Kulites 1 & 2 of run 3181 with zero yaw (Fig. 7.4a). In the yawed case Kulite 3 is no longer directly under one of the hot streaks visible in the IR and all three sensors show lower disturbance growth across their spectral range. This indicates that in the zero-incidence case the absence of the 40-50 kHz peak may be due to higher amplitude disturbances directly under a hot streak.

The downstream shoulder PCB data is given in figure 7.10b. Here again the effect of the position of the transducers underneath the crossflow structures is seen. With 1° yaw, PCBs 1 & 3 lie in between hot streaks and show a much stronger growth of the disturbance centered near 220 kHz. PCB 2, which initially lies near the edge of a streak, shows high disturbance levels in a band from 100-230 kHz with a peak near 220 kHz which grows in amplitude rapidly with Re and shifts to a lower frequency before being replaced by a more narrow band centered at 125 kHz near Re/m = 8.6E6. This shift corresponds to the transducer location being overtaken by the region of

increased heating along the streak adjacent to it seen in the IR images for Re/m 8.0E6 and 9.0E6.

An important observation of this yaw study is that spectral traces are sensitive to location with respect to the stationary structures. Hence, some of the differences observed between the two facilities (freestream disturbance environments) may reflect this sensitivity.

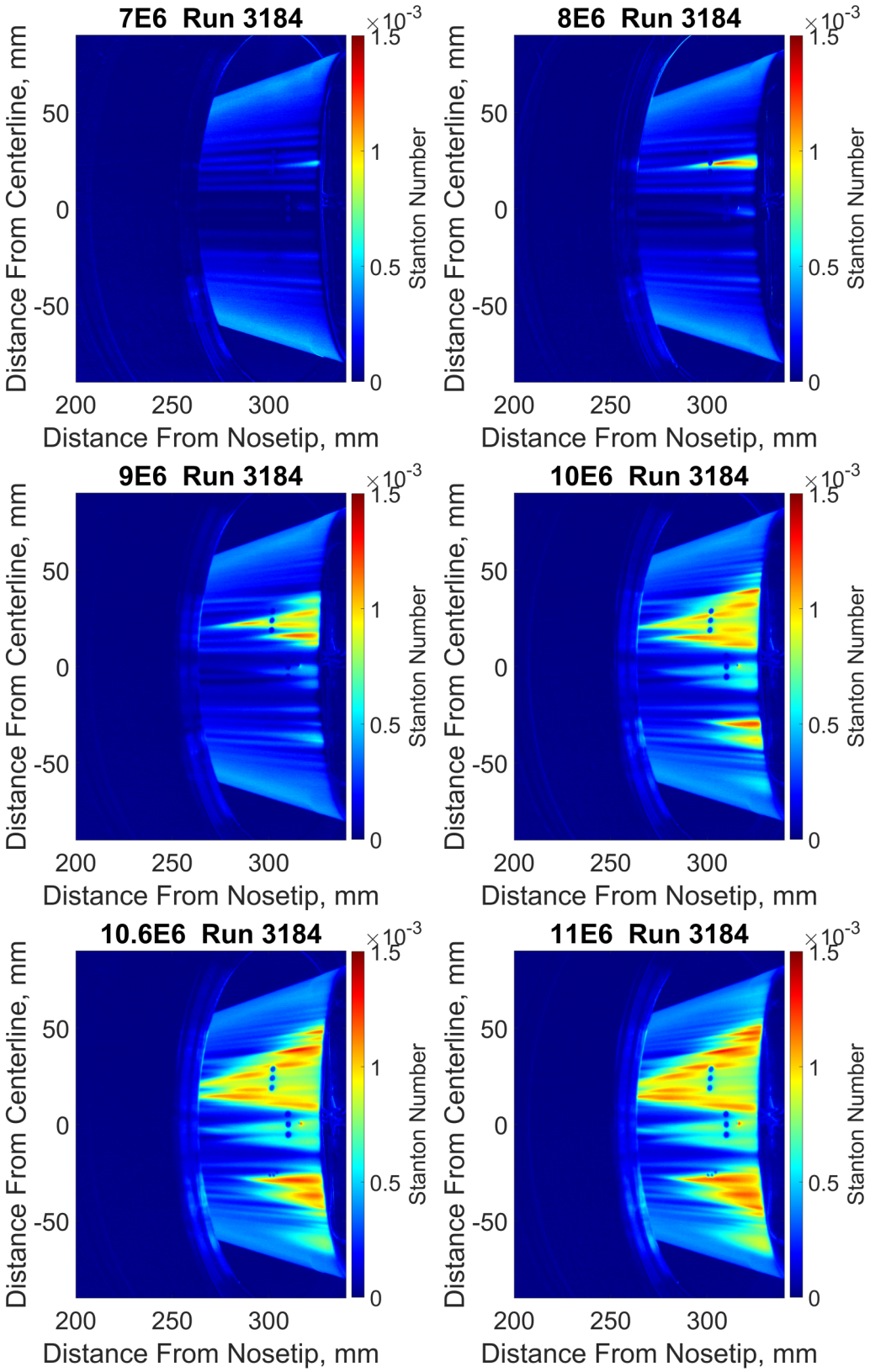

Figure 7.9: Stanton number maps, Re sweep M6QT; Initial instrumentation.

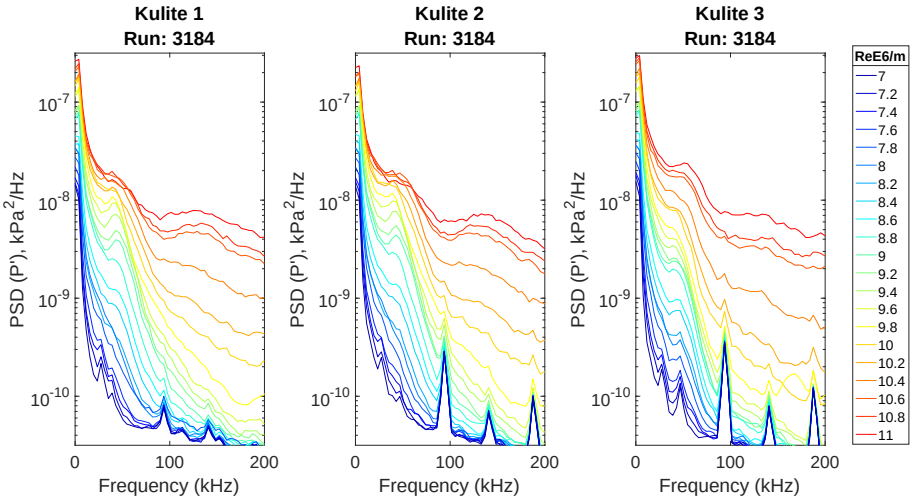

(a)

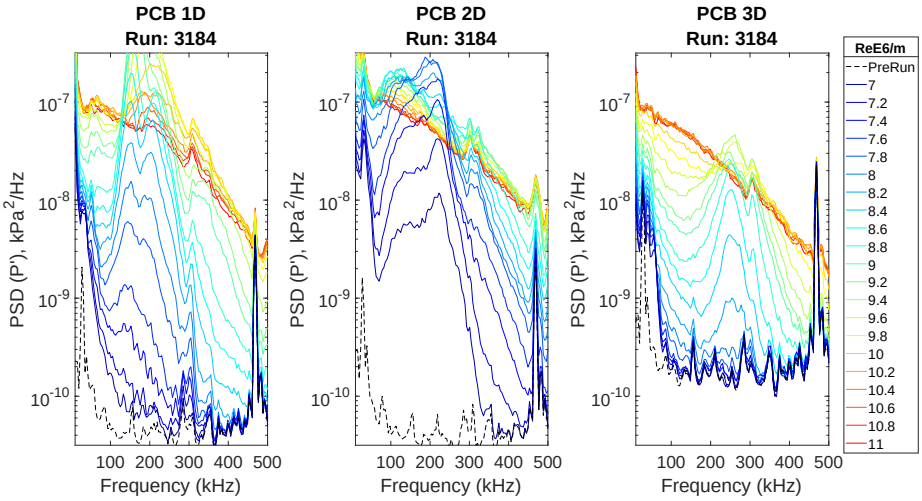

(b)

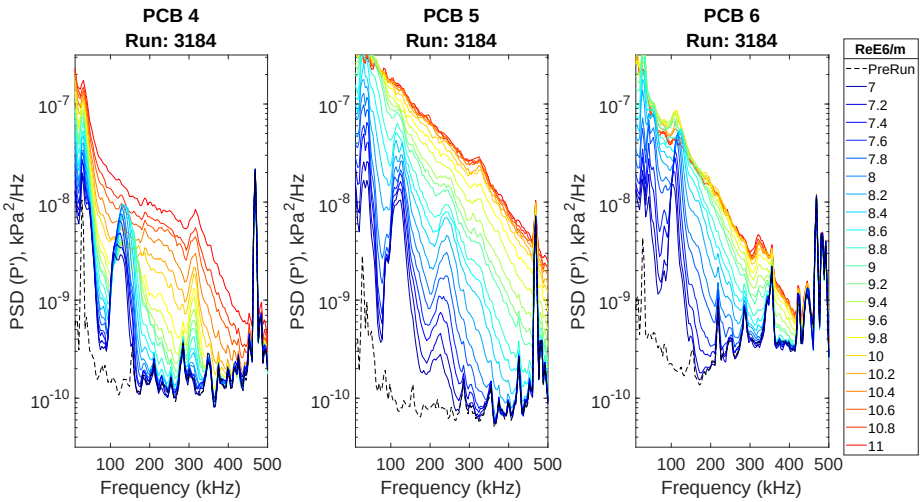

(c)

Figure 7.10: PSD of Fluctuating Pressure for Each transducer cluster Run 3184; M6QT. (a) Kulite, (b) Downstream Shoulder PCB, (c) Centerline PCB

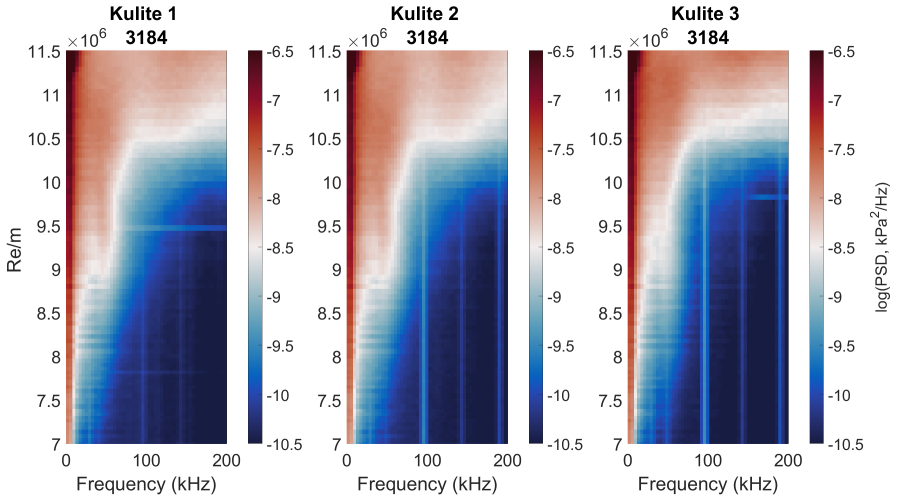

(a)

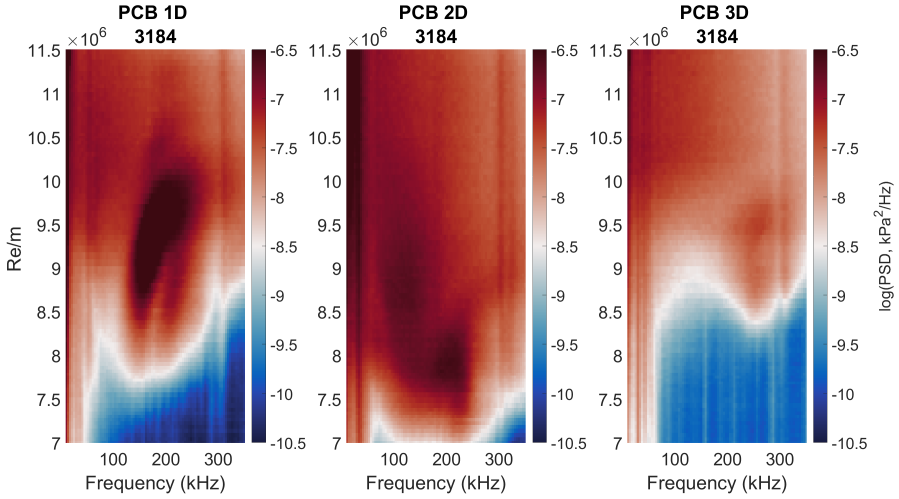

(b)

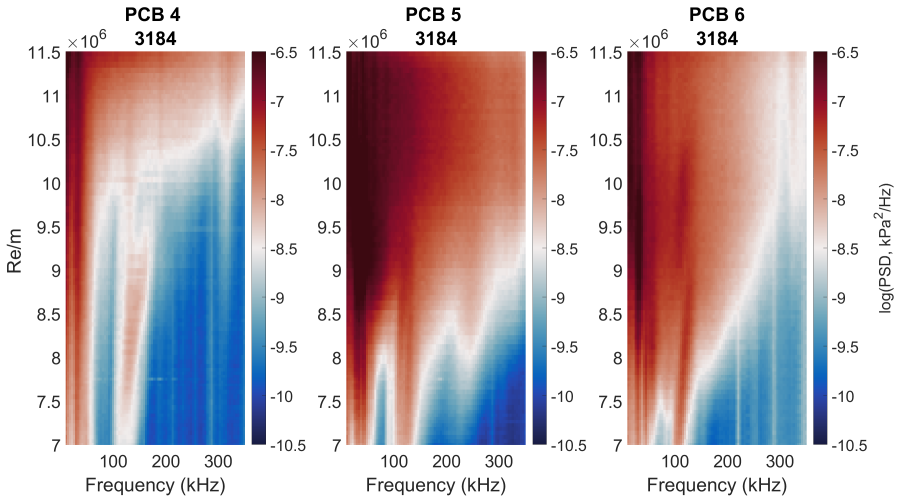

(c)

Figure 7.11: Waterfall PSD of Fluctuating Pressure for Each transducer cluster Run 3184; Mach 6 Quiet Tunnel. (a) Kulite, (b) Downstream Shoulder PCB, (c) Centerline PCB

7.5 Evolution of Heating Within Streaks

An interesting observation of the IR is the location of the elevated heat flux within the streaks present on the model surface. Examining the St maps in Fig. 7.2, the streaks initially visible at low Re show elevated heating near the rear of the cone which moves forward as Re is increased. The peak of this region originates on the outboard (from the centerline) side of the figure and broadens downstream into a lower heat flux region. This is perhaps most apparent in the 9×10^6/m and 10×10^6 maps of Fig. 7.2 and Fig. 7.6. As diagrammed in Fig. 7.12, the elevated heating streaks correspond with the trough of the stationary crossflow vortices. On both sides of the cone, the region within the streak which initially shows elevated heating corresponds with the edge of the trough corresponding to the upwelling region of the adjacent vortex. This is the expected region of type-I secondary instability. This trend appears to be present in the DNS work of Dinzl & Candler (2017). Their figure 11d showing normalized velocity contours from spanwise slices on a region of the cone shoulder overlaid on the heat flux is reproduced here as Fig. 7.13. The authors describe the stationary vortices interacting with the wall surface resulting in elevated heat flux. The DNS shows the crest of the wave rolling over and essentially collapsing on itself before regaining its vortical structure, remaining distinct from the neighboring vortices. The surface heat flux streaks remain distinct and transition is not observed. However, in the St maps of runs in the M6QT and in the previous literature the streaks appear to broaden and coalesce with some spanwise variance still present. Pressure transducer data in these regions indicate that transition has occurred. Dinzl & Candler posit that this difference is caused by presence of freestream acoustic disturbances within the experimental facilities and the lack thereof in the DNS, arguing that the freestream disturbances interact with and provide excitation for the secondary instabilities present in the distorted mean

flow leading to breakdown of the vortices.

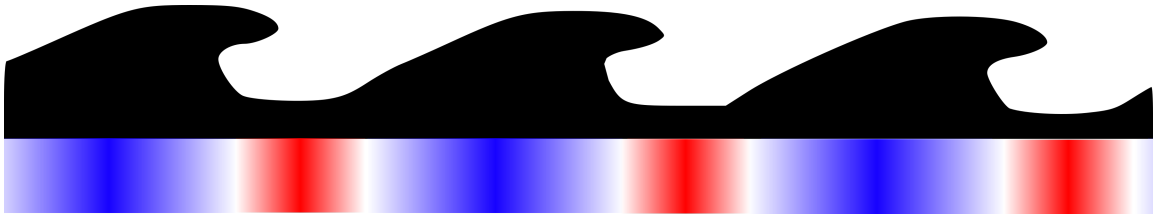

Figure 7.12: Diagram of modified basic state of boundary layer distorted by stationary crossflow vortices.

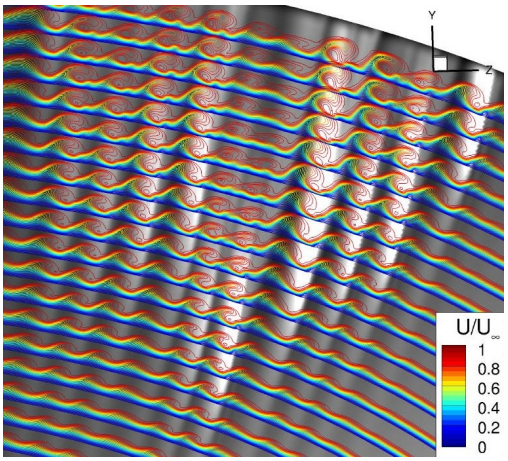

Figure 7.13: Streamwise velocity overlaid on surface heat flux; Reprinted from Dinzl & Candler (2017) Fig. 11.d.

Yawed M6QT run 3184 may provide an example of a case where this wall interaction occurs without the flow transitioning fully as well as potential vortex coalescence observed by Dinzl & Candler. The St maps of Fig. 7.6 show development of a heating streak near PCB 2D between 7×10^6/m and 8×10^6/m. The streak is initially present as a streak of low heat flux. A peak of higher heating appears near the very rear edge of the cone and moves forward with Re. The peak heating appears to occur near the top edge of the heating streak. This peak heating moves forward past the position of PCB 2D. The Re = 9×10^6/m map shows the transducer in a region of heat flux elevated from the baseline level but not as high as the thin region of elevated heating now apparent in the streak. As described in the previous section, the spectra from PCB 2D indicate

that initially there is rapid growth at a frequency band from 50-250 kHz with a narrow peak near 200 kHz. As Re increases the band grows with the 200 kHz peak being replaced by a peak near 125 kHz over a very short Re range, 8.2×10^6/m to 8.6×10^6/m. The 125 kHz peak persists until nearly 10×10^6/m, long after the transducer location has been engulfed by the front of elevated heat flux. The reader is cautioned that interpretation of the heat flux in this region is complicated somewhat by the effects of the PCB mounting in the area, ie. heat transfer from the transducer to the surrounding PEEK surface. However similar regions were observed in an Re sweep of the uninstrumented side of the model, shown in Fig. 7.14. The maps are presented without scale as the transducers, used to scale and map the other images, are absent. These regions could possibly be due to the wall interaction and vortex reformation described by Dinzl & Candler or also a result of vortex coalescence that was also observed to result in a region of elevated heat flux followed by a relatively lower heat flux region. Overall the DNS data seem to offer a compelling explanation of some aspects of the experimental results. Further experiments targeted at examining this region with higher IR resolution and ideally off surface measurements to resolve the vortex development are warranted to provide more conclusive comparison.

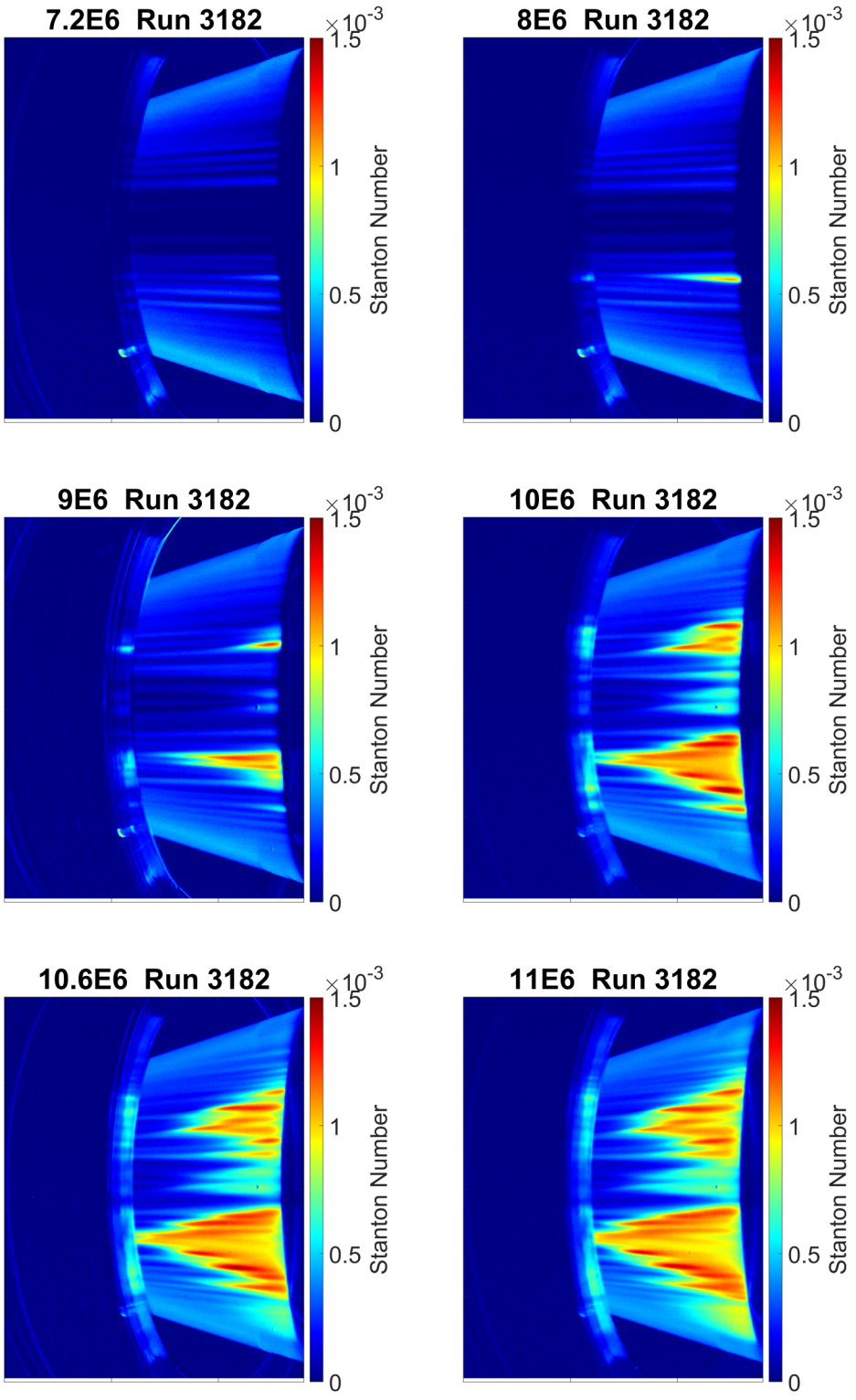

Figure 7.14: Stanton number maps, Re sweep run 3182 M6QT; uninstrumented side of model.

7.6 M6QT Bleed Valves Closed Noisy Runs

Two runs were performed with the M6QT bleed valves closed. Running the tunnel with the bleed valves closed produces noisy flow across the operable Re range with estimated pitot fluctuations on the order of 5%. Stanton number maps are shown in Fig. 7.15. The visible cone surface shows a turbulent heating pattern with similar St to the ACE facility runs. The limited viewing area makes direct comparison of spatial extent difficult. At 7×10^6/m the region of elevated St extends further outboard from the centerline than at the same condition in the ACE facility. These runs were instrumented with shoulder PCBs 1D-3D. At all Re tested the PSD spectra show a broad turbulent profile.

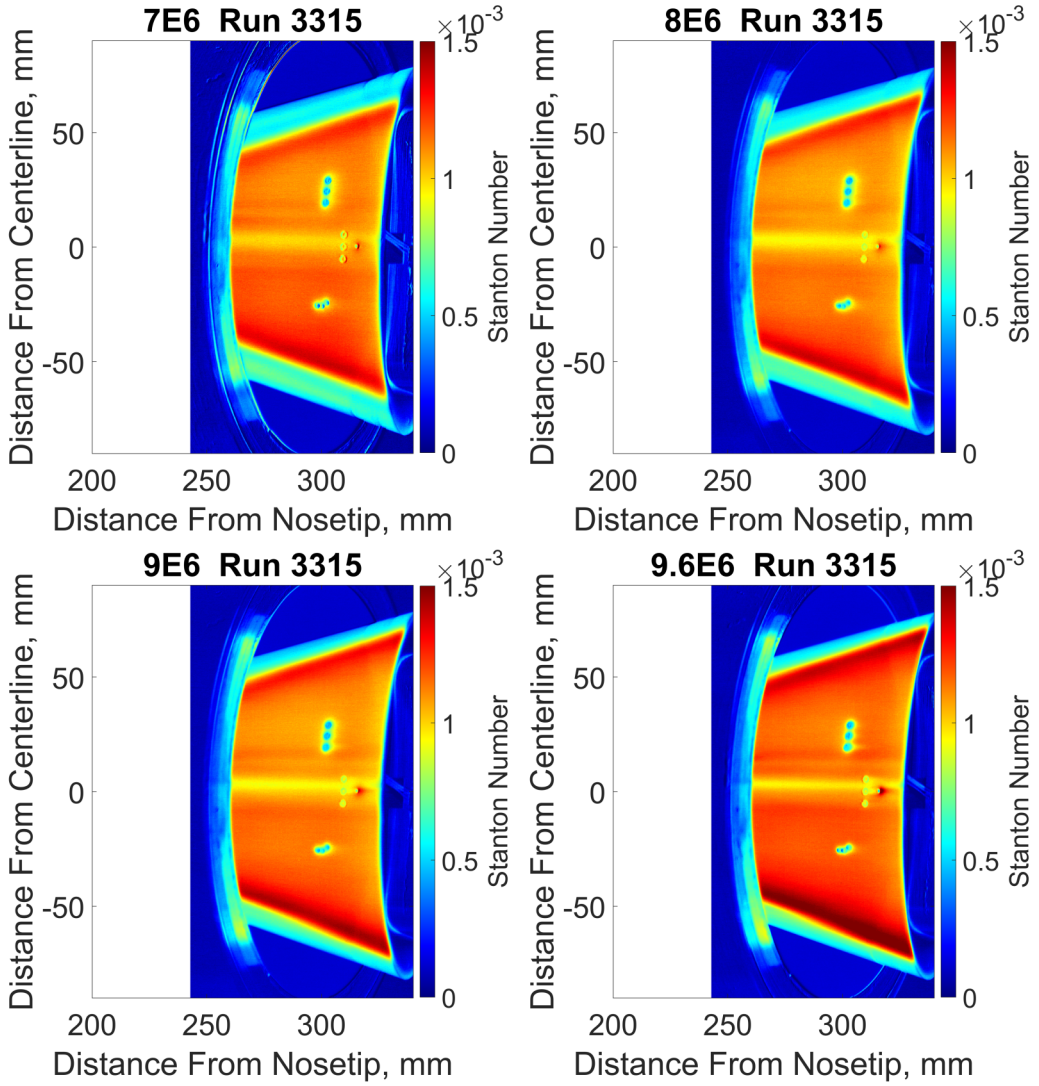

Figure 7.15: Stanton number maps, Re sweep run 3315 M6QT bleed valves closed, noisy; uninstrumented side of model.

7.7 Summary and Discussion of M6QT Campaign Results

Runs of the 2:1 elliptic cone model were performed in the M6QT under noisy and quiet flow. Initial runs were performed to determine optimal placement within the tunnel, avoiding impingement of the nozzle exit shock on the model and model shock impingement on the nozzle wall. Simultaneous IR and pressure transducer measurements were performed with upstream and downstream surface transducer configurations. The majority of runs were performed at a nominal 0° incidence angle. An additional run was performed with the model nosetip yawed 1° downward to provide a data point on the sensitivity of the transition process to incidence angle. Two runs were performed with the facility bleed valves closed, exposing the model to the highest level of freestream disturbances available in the NAL's hypersonic facilities.

Quiet runs reveal distinct heating streaks present on the model. Based on CFD analysis and previous experiments, these streaks are believed to be the result of co-rotating stationary crossflow vortices. These streaks are visible in Stanton number maps at Re = 7×10^6/m the lowest Reynolds number tested. The boundary layer appears laminar at all points along the cone at this condition. With increased Re, the streaks develop regions of further elevated heating which appear near the rear of the cone and progress forward. Depending on their position under the streak structure, shoulder Kulites detect disturbances with a spectral peak near 45 kHz which is the expected travelling crossflow frequency for this geometry and Mach number. Shoulder PCBs detect higher frequencies (200-300 kHz) which are in the range of expected secondary instabilities and second mode disturbances. As the streaks engulf the sensor locations, broad full spectra are observed indicative of turbulent flow. At the model centerline, fluctuating pressure spectra from PCB 5 show the development of content from 70-120 with dual peaks near 82 and 120 kHz. The disturbances

grow in amplitude with freestream Re shifting to higher frequency. The lower disturbance peak appears to dominate and grows until broadening as the two streaks on either side of the centerline are seen to impinge on the sensor. PCBs 4 & 6 show dual bands of frequency centered at 105 and 210 kHz. These peaks grow and remain a factor of two in frequency apart, suggesting they may be harmonics. Frequency bands observed in the 0° AoA M6QT runs and their possible mechanisms are summarized in Table 7.2.

Table 7.2: Observed excited spectral bands M6QT, Run 3181.

Frequency	TAMU M6QT	Possible Mechanism
0	IR Therm; Re/m 7-11.6$x10^6$	Stationary Crossflow
20-80 kHz	Kulites 1D,2D; Re/m 8.5-9.6$x10^6$	Traveling Crossflow
100-400 kHz	PCB 1,2; Re/m 7.2-10.0$x10^6$	Traveling, Type I & II Secondary Instability, 2nd mode
20-70 kHz	PCB 4-6; Re/m 7-10.0$x10^6$	centerline
70-150 kHz	PCB 4-6; Re/m 7-10.0$x10^6$	centerline
150-300 kHz	PCB 4 & 6; Re/m 7-10.0$x10^6$	centerline

Noisy runs were performed in the M6QT by leaving the nozzle throat bleed valves closed. At the minimum operable Re, 7×10^6/m, the visible cone surface revealed a heating pattern similar to that observed in the ACE facility over the visible portion of the cone. Broad heating with no discernible streaks is present for all Re tested with similar Stanton number to turbulent regions on the ACE cone. Shoulder PCB transducers show broad turbulent spectra across all Re tested. The heating observed and yaw angle trends compare well with CFD and previous experiments. The patterns visible in the St maps is largely similar to that observed by Borg & Kimmel (2016) and Juliano & Schneider (2010). Direct comparison and discussion are provided in Sec. 8.1. Heating

within the streaks appears to agree well with the observations of the DNS simulations of Dinzl & Candler (2017) on the same geometry.

8. DISCUSSION

8.1 Comparison with Previous Results

An advantage of testing the 2:1 elliptic HIFiRE-5 geometry is the current interest in the geometry and the availability of CFD and experimental results from previous and concurrent studies. This section discusses the results presented above and places them in the context of available computational and experimental data.

8.1.1 Ground Test Experimental Results

Experiments on this 38.1% scale geometry have been conducted in the Purdue BAM6QT in both quiet and noisy configurations. Early experiments utilized an aluminum cone constructed by Juliano & Schneider (2010). This model was further instrumented and utilized by Borg (Borg *et al.*, 2011, 2012, 2013, 2015*a*,*b*). For later studies, Borg constructed a model with a stainless-steel nose and a PEEK frustum allowing IR thermography based measurements. The nosetip is reported to have an RMS surface roughness of 0.5 μm. Borg & Kimmel (2016), Borg & Kimmel (2018), Juliano *et al.* (2015) and Juliano *et al.* (2019) present heat flux measurements conducted on these models under both quiet and noisy flow at Mach 6 in the Purdue University BAM6QT. Freestream RMS pitot fluctuations in the BAM6QT operated in noisy mode are reported by Borg & Kimmel (2018) as roughly 3% of average pitot pressure.

2:1 Ellipse in "Noisy" Flow

Presented in Fig. 8.1 are heat flux maps from the noisy flow experiments of Borg & Kimmel (2016) and Juliano *et al.* (2015) compared with results from the ACE facility at the DS station.

Borg and Juliano utilized IR thermography and temperature sensitive paint (TSP) respectively to examine the heat flux on the model surface and its evolution with Re. Several features of the heat flux front are present in all three experiments. Streaks bordering a lower heat flux region at the model centerline are visible and similar in streamwise extent and size. On the cone shoulder the position of the lobes of heating are also similar. Heat flux values between the three experiments are comparable. A notable difference is that the ACE tunnel results show smaller spanwise extent of lobes of elevated heating. The distance between the attachment lines and most outboard edge of the heating lobes is smaller in the ACE facility than in the BAM6QT. This trend is also observed in comparison of the ACE and TAMU M6QT noisy mode results, indicating that the heating front differences are the result of freestream disturbance levels.

A major difference between the current experiments and those of the BAM6QT is evidence of streamwise streaks. Unlike the present experiments, neither Borg nor Juliano observed evidence of streamwise streaks, characteristic of stationary crossflow vortices, in heat flux measurements under noisy flow conditions. As previously discussed, runs in the ACE facility at the DS station do show streaks of elevated heating, roughly aligned with the streamwise direction, leading in the lobes of elevated heating at the shoulder. These streaks originate upstream of and persist into the region of higher heat flux. They are more distinct at the lower disturbance US station in ACE.

Borg *et al.* (2012) did observe streamwise streaks in oil flow visualization conducted under noisy and quiet flow in the BAM6QT. As shown in Fig. 8.2 the Borg *et al.* results are qualitatively similar to the present IR in terms of streak position and wavelength. Visible in both images are streaks that appear to originate upstream of the apparent transition front and lead into a more diffuse lobe on the cone shoulder.

Borg & Kimmel (2018) present IR data with heat flux non-dimensionalized to St using freestream

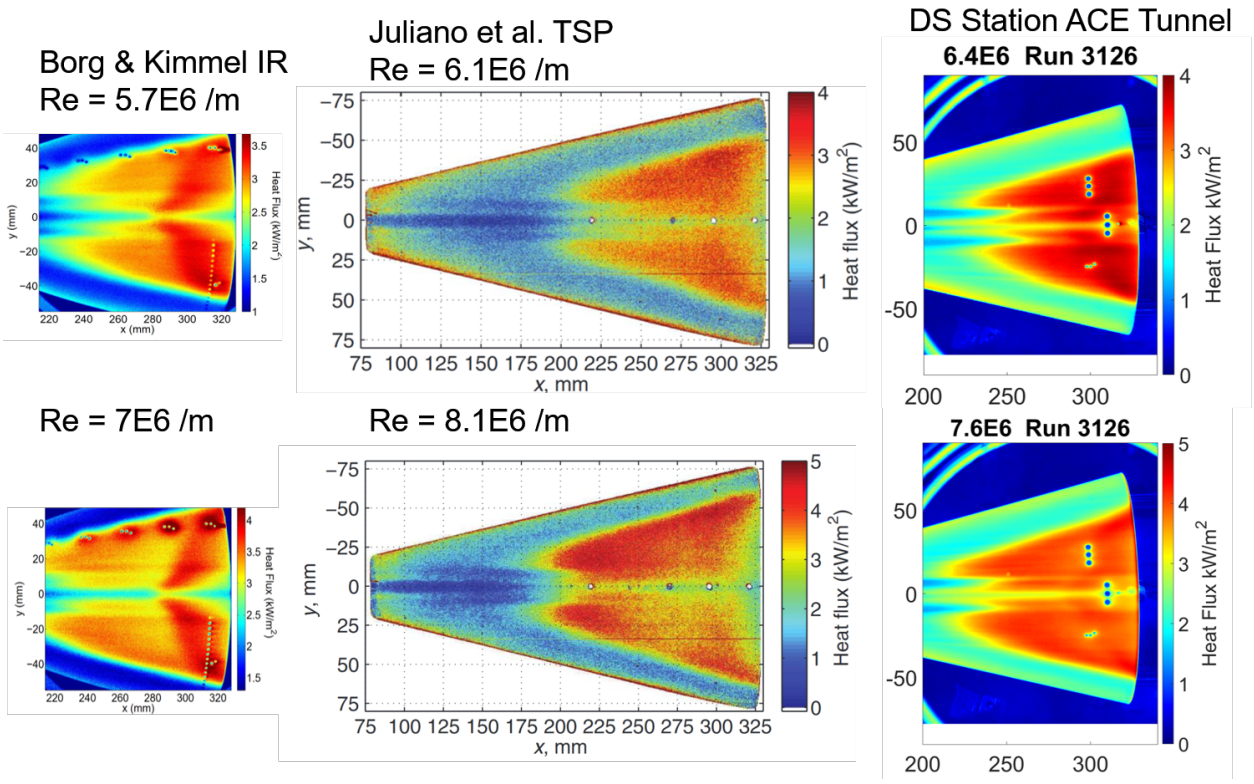

Figure 8.1: Comparison of IR thermography between the present (right) and Purdue University BAM6QT IR results of Borg & Kimmel (2016) (left) and TSP of Juliano *et al.* (2015) (center). Borg results reprinted from Borg & Kimmel (2016). Juliano results reprinted from Juliano *et al.* (2015).

properties, wall temperature, and total temperature in the same manner as the present experiments (Eq. 3.7). This nondimensionalization ideally allows direct comparison between individual runs in different facilities. Fig. 8.3 is such a comparison between the ACE facility runs at the US and DS station and Borg's BAM6QT noisy results. The left column shows a St map for a Re = 3.1×10^6/m reproduced here from Borg & Kimmel (2018) figure 8c. The middle column shows St maps from the ACE DS station at a similar Re = 3.2×10^6/m as well as a higher Re = 3.8×10^6. The right column shows St maps from the lower disturbance ACE US station again at a similar Re = 3.2×10^6/m and elevated Re = 4.8×10^6. The ACE images have been cropped and the colormap chosen to match Borg & Kimmel's. Comparing the first row, there is agreement in the elevated

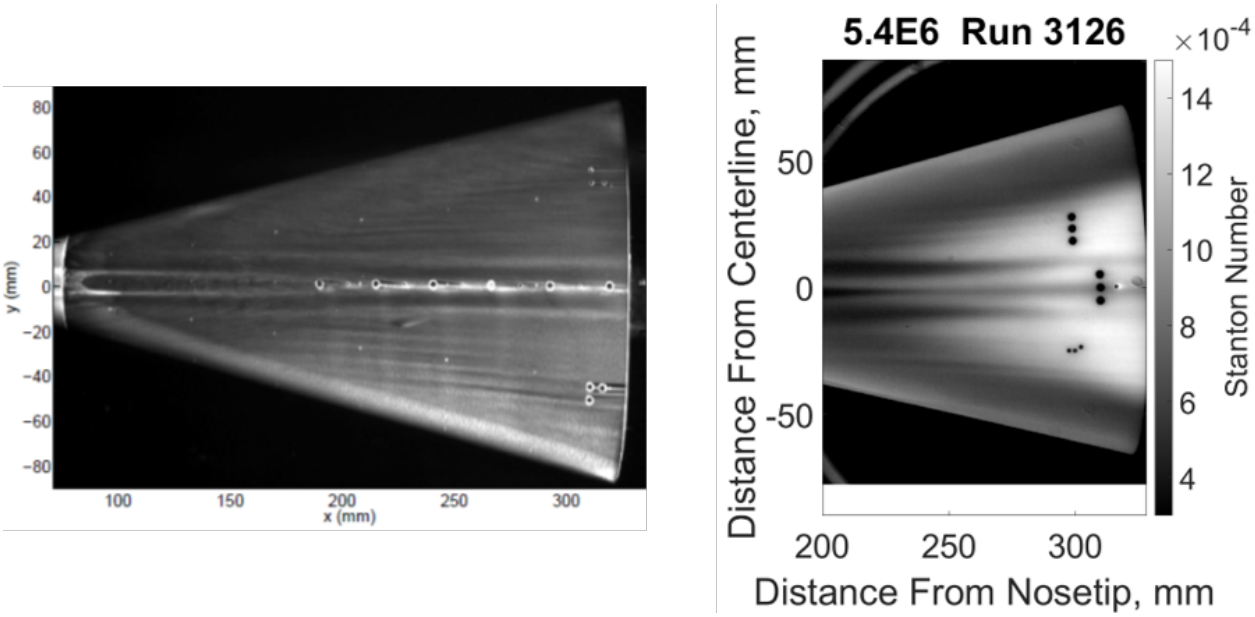

Figure 8.2: Comparison of oil flow and IR thermography, Left: BAM6QT Noisy flow 5.4×10^6/m reprinted from (Borg *et al.*, 2012) Right: ACE DS station.

heating region locations and their spanwise position between the BAM6QT and ACE DS station. The US station map shows minimal heating towards the rear of the cone for the centerline structure. The BAM6QT results show elevated heating along the model centerline and shoulder which is higher than at matched Re at either the DS or US ACE stations. A potential explanation for this is differences in the freestream disturbance environments. In the case of both the ACE US and DS locations this Re is associated with the freestream disturbance increase observed with RMS pitot fluctuation levels near 1% at the DS station and 0.5% at the US station. These levels are significantly lower than the 3% RMS Pitot fluctuation level reported by Borg & Kimmel (2018) for noisy flow in the BAM6QT. The bottom row of Fig. 8.3 shows St maps at Re which show similar heating extent and St magnitude to the Borg results. These St levels and front extent are not seen until Re = 3.8×10^6/m at the DS station and 4.8×10^6/m at the US station.

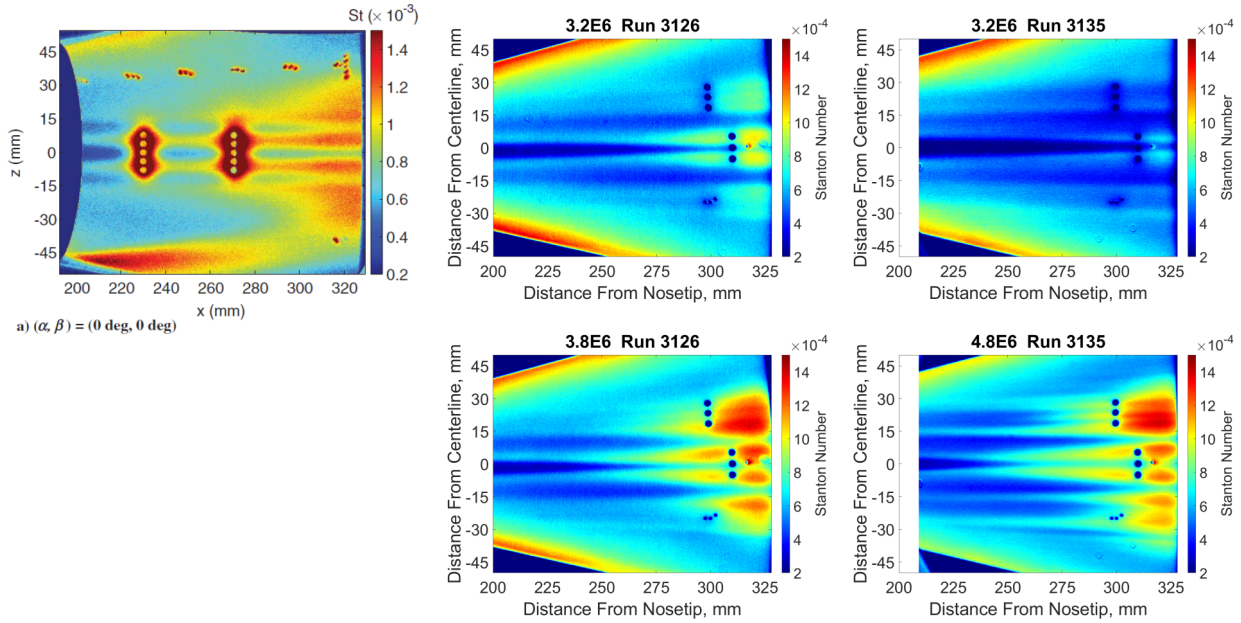

Figure 8.3: St Comparison between Purdue BAM6QT under noisy flow and ACE DS & US stations. Top Row from left to right Borg & Kimmel (2017*b*) BAM6QT noisy Re = 3.1×10^6/m, ACE DS station 3.2×10^6/m, ACE US station 3.2×10^6/m. Bottom row from left to right: ACE DS station 3.8×10^6/m, ACE US station 4.8×10^6/m. Bottom row Re was chosen to maximize similarity to Borg & Kimmel 3.1×10^6 condition.

2:1 Ellipse in "Quiet" Flow

Similar to the noisy ACE results above, the heat flux observed in the M6QT is strikingly similar to the BAM6QT results of Borg & Kimmel (2016). Presented in Fig. 8.4 is a comparison between the present IR and pressure transducer results and those of Borg *et al.* (2015*b*) & Borg & Kimmel (2016) under quiet flow. The top row shows a Re matched pair of heat flux maps with Borg & Kimmel's results on the left and the present results on the right cropped to approximate Borg & Kimmel's field of view. The features present in both maps are qualitatively similar. Clearly visible are streamwise streaks that extend over a large portion of the model surface. As discussed, these are believed to be stationary crossflow vortices anchored to upstream surface roughness. The centerline region in both cases shows an elevated heating streak along the centerline with $\sim$ 5

mm wide outboard streaks on either side. The heat flux scales are similar but not identical. The TAMU M6QT model initial wall temperature was roughly 20 K higher than the room temperature wall of the BAM6QT model. This would tend to result in lower heat flux into the TAMU M6QT model given similar freestream conditions. Near the rear of the cone there is elevated heating in the TAMU M6QT which is not apparent in the BAM6QT map. The second row of Fig. 8.4 shows heat flux at Re = 11.3×10^6/m in the BAM6QT and Re = 10.6×10^6/m in the TAMU M6QT. Heating is comparable in magnitude and position both in the centerline region and shoulders. Streaks in the TAMU M6QT map are in similar positions but broader downstream of the point where their heating increases. The TAMU M6QT results show evidence of vortices coalescing which is not apparent in the BAM6QT results. Streaks of elevated heating are also seen to extend further upstream on the TAMU model than in the Borg results. Comparing the evolution of heat flux vs Re between the results of Chapter 7 with those of Borg & Kimmel, the streaks are observed to break down to higher heating at lower Re in the TAMU M6QT. This difference and the outboard streaks on the TAMU model are potentially due to differences in surface roughness and freestream disturbance environment between the two experiments. The nosetip of the model used in the Borg & Kimmel (2016) experiments has lower surface roughness; 0.5 μm RMS compared to the $\sim$ 1.5 μm RMS of the current experiment's PEEK nosetip. This may result in differences in initial amplitude of instabilities affecting the eventual breakdown location. Further, at elevated Re, the rear portion of the M6QT model lies outside of the quiet core and is impinged upon by the elevated noise radiated from the turbulent nozzle boundary layer. This elevated noise may interact with the secondary instabilities in this region hastening their growth and breakdown.

The final row of Fig. 8.4 shows normalized Kulite pressure fluctuation PSDs at various Reynolds numbers in both facilities. The sensor locations on the cone shoulder are different between the two

cones. The TAMU model Kulite 1 is more inboard and upstream than the Borg *et al.* (2015*b*) sensor whose PSDs are shown. Evident in both traces is a band of frequencies centered near 45 kHz which grows above the sensor noise floor before broadening and being replaced by a more broadband full spectrum. The experimental results of Borg *et al.* (2015*b*) and Borg & Kimmel (2017*a*) as well as the stability analysis of Kocian *et al.* (2017) demonstrate that this frequency band is related to the traveling crossflow instability on this geometry. The PEEK model in the studies of Borg & Kimmel is instrumented with several clusters of 3 Kulite transducers aligned along a ray of the cone. Typically they observe this 45 kHz frequency band in all Kulite transducers of a given cluster and have successfully calculated phase speeds and angles which further agree with predicted traveling crossflow behavior.

Juliano (2010) presents PCB transducer data obtained along the model centerline (also reported in Juliano & Schneider (2010)). Juliano observed content in PCBs stationed on the model centerline at 220, 270, and 320 mm downstream of the nosetip. The authors report difficulty in interpreting the signals observed due to noise believed to be a sensor artifact in the same region of the spectra as the peaks observed. They do however report a few cases in which the location and behavior of the spectral content is very similar to that observed in the TAMU M6QT. In several cases they observed excited frequencies in a band from 80-95 kHz which decay in amplitude and decrease in frequency as the Re is decreased. Juliano presents comparisons with LST results that indicate good agreement with expected second mode frequencies in this region (for example his figure 8.20).

The disturbances measured in this region are interesting and warrant further study. At the time of writing, discussion is underway to preform computations examining this centerline region and the potential mechanisms responsible for the observed spectral content and behavior.

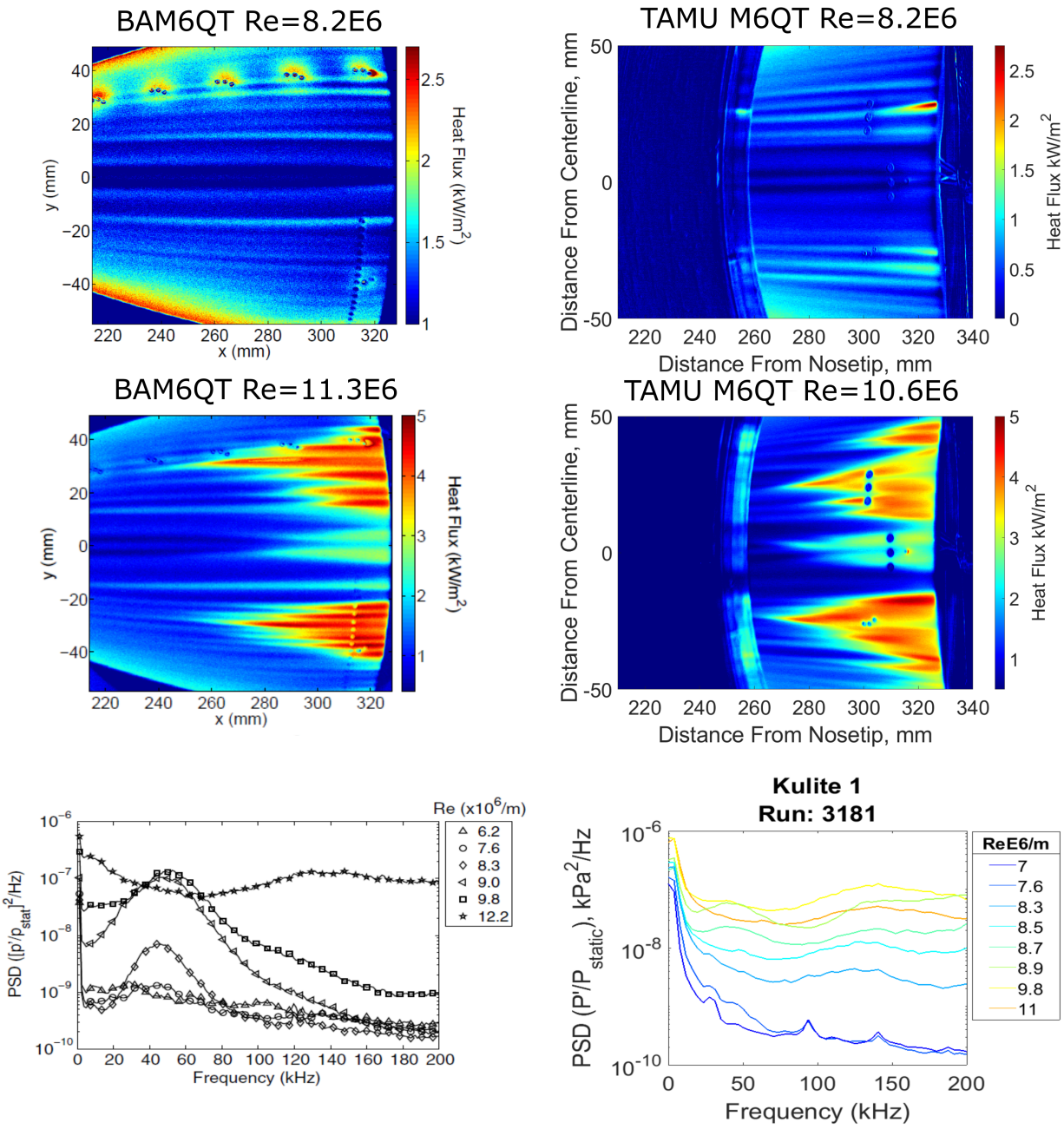

Figure 8.4: Comparison of IR thermography and Kulite sensor results between the present TAMU M6QT (right) and Purdue University Boeing/AFOSR Mach 6 Quiet Tunnel (left). Borg results reprinted from Borg *et al.* (2015*b*) & Borg & Kimmel (2017*a*).

8.1.2 Computational Results

Several computational efforts have examined the 38.1% scale HIFiRE-5 geometry. These efforts were summarized in Chapter 2 and some comparisons drawn in the results chapters (5 6 7). Particular comparison was made to the DNS results of Dinzl & Candler (2017) in Sec. 7.5. The TAMU Computational Stability and Transition Lab has conducted several studies which are relevant for comparison to the present results. In analysis similar to that of Moyes *et al.* (2017) for the right-circular cone under hypersonic conditions, Kocian *et al.* (2016) and Kocian *et al.* (2017) present stability analysis for the crossflow dominated shoulder region of the 2:1 elliptic cone HIFiRE-5 geometry.

Kocian *et al.* (2016) presents linear analysis for two Re conditions examining the expected growth of the crossflow instability. Conditions presented match the 8.3×10^6/m and 11.8×10^6/m conditions of Dinzl & Candler (2015) & Dinzl & Candler (2017). Their linear stability results show good agreement with earlier studies of Choudhari *et al.* (2009) & Li *et al.* (2012) with N-factors of traveling and stationary crossflow peaking on the shoulder of the cone in locations similar to the fronts observed in the present M6QT experiments as well as the BAM6QT experiments. Building on the LST and LPSE analysis, NPSE and spatial biglobal computations were used to provide information on the spatial extent of mean flow distortion as well as frequencies and spatial extent of the various instability modes present in the boundary layer. These analyses were conducted for the 11.8×10^6/m condition. This condition is higher than the maximum quiet Re of the TAMU M6QT but usefull qualitative comparisons can be made.

Kocian *et al.* (2016)'s figure 10 shows the growth rates of various instability modes at several stations along a crossflow vortex path. At the upstream-most stations shown, traveling crossflow

and second mode disturbances show the largest growth rates. This region is where mean flow distortion due to the stationary crossflow instability and nonlinear effects are small. Downstream in further distorted regions the boundary layer thickness varies and the most amplified second mode frequency increases within the now distorted boundary layer. A type I secondary instability is seen to develop at a frequency near that of the originally detected second mode instability. At the downstream most station growth rates of instabilities are elevated and span a very broad frequency range. Kocian *et al.* (2017) indicate that this may explain the behavior of the Kulite signals of Borg & Kimmel (2016), which initially show a narrow peak centered near 45 kHz that grows in amplitude at downstream locations and broadens, eventually reaching a turbulent profile. Borg & Kimmel's spatial observations match the trends observed at a single sensor with increasing Re. As shown before comparable behavior was observed in the TAMU M6QT results.

Another observation of the TAMU M6QT quiet run experiments was variation of observed frequency with position of PCBs relative to stationary streaks. An example of the spatial extent of various modes within the boundary layer is reproduced here as Fig. 8.5 from Kocian *et al.* (2017)'s figure 7. These maps show contours representing distribution of the different modes: traveling, type-I secondary, type-II secondary and second mode. The determination of the nature of these modes follows that of Moyes *et al.* (2017) which showed good agreement with the PCB measurements of Edelman & Schneider (2018). The Kocian *et al.* (2017) analysis helps explain the variance observed in the spectra between shoulder PCB transducers. The frequencies of disturbances are observed to vary with position within the stationary crossflow structures.

Moyes *et al.* (2018) presents a computational study of the effects of initial amplitude on hypersonic crossflow development. The authors varied the initial stationary crossflow disturbance amplitude used to seed computations for a single vortex path. They observed trends similar to low-

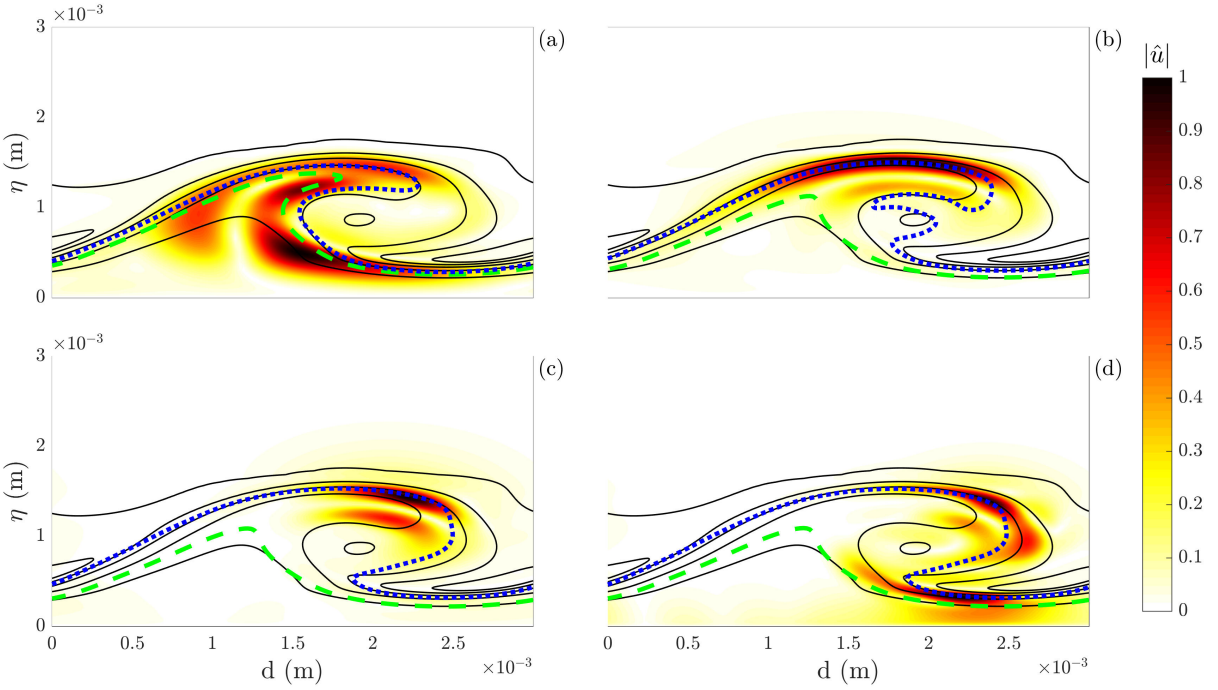

Figure 8.5: Normalized isocontours of $|\hat{u}|$ with five isolines of $\overline{\rho u}^*$ (black lines), critical layer (blue lines), and relative sonic line (green lines). The selected disturbances are (a) traveling crossflow at F = 45 kHz, (b) type-I at F = 200 kHz, (c) type-II at F = 400 kHz, and (d) second mode at F = 575 kHz. (Figure and caption reprinted from Kocian *et al.* (2017))

speed experiments in that increased initial amplitude lead to earlier saturation of stationary waves and decreased the saturation disturbance amplitude. Analysis of instability frequencies showed strong dependence on initial crossflow amplitude as they were impacted by the altered boundary layer thicknesses present.

In conjunction with the TAMU Computational Stability and Transition Lab, analysis similar to those presented by Kocian *et al.* (2017) are being conducted at conditions matched to the present experiment and sensor locations. This will allow a more direct comparison to the experimentally observed stationary crossflow wavelengths as well as frequency bands at the transducer locations of the present model.

8.1.3 Comparison Summary

Overall the current experiment appears to agree well with previous studies and CFD. The trends present are similar both under high freestream disturbance flow in ACE and the M6QT run noisy as well as at low freestream disturbance in the M6QT run quiet. For the present discussion this agreement serves as a sanity check that the model, surface instrumentation and IR thermography are providing reasonable results. Knowing that the transition process on the model of the present study behaves similarly to the available literature gives confidence that the observations of changes with freestream disturbance levels are real and not an artifact of the model or instrumentation.

8.2 Effect of Freestream Disturbances

The effect of environmental disturbances on the crossflow instability and transition was investigated on a 38.1% scale model of the HIFiRE-5 elliptic cone geometry. The model was exposed to varied freestream disturbance levels. In the ACE facility tunnel runs were conducted with the model nosetip at 3 streamwise stations, using the natural variation of freestream disturbances within the facility to expose the model to different levels of freestream disturbance. In the M6QT facility runs were conducted with the facility operating in "quiet" and "noisy" modes, exposing the model to freestream environments with lower disturbances than the ACE facility and much greater than the ACE facility, respectively. The following discussion centers on briefly summarizing the results obtained and presented in the previous chapters and expanding the discussion of the impact the freestream disturbances were observed to have.

8.2.1 Within the ACE Facility

Runs were conducted at the three streamwise stations characterized in Chapter 5. The DS and MID stations were observed to have similar freestream disturbance levels at the model centerline; Pitot pressure fluctuations of approximately 0.55% before the large jump at Re = 3×10^6/m and 1.8-1.2 % thereafter. The US station has pitot fluctuation levels near 0.2% below 3×10^6/m and between 1% and 1.2% at higher Re. The general trend observed between the US and DS stations is that the onset of transition is delayed. The heat flux and pressure data in both the centerline and shoulder regions of the cone show that the heat flux and disturbance amplitude are smaller at the US station for a given Re.

In the shoulder region of the cone the heating pattern is significantly different at the US and DS stations. At the DS station very faint streaks are observed leading into the more diffuse turbulent region which grows in the cone shoulder region. At the lower disturbance US station, these streaks are much more apparent and can be seen to develop and move upstream with increasing Re. The differences between the stations are exemplified by the St maps presented in Fig. 8.6. The spectra from PCB 3D at both stations, Fig. 8.7, show similar frequency instability bands develop, but that development is delayed significantly at the lower disturbance station. In both cases this content develops only after the significant freestream disturbance increase at 3×10^6/m.

IR and pressure transducer data at the MID station showed good agreement with runs at the DS station showing slightly lower heating. Possible causes for this difference include small model alignment differences and differences in the freestream disturbance field off the tunnel centerline. Spanwise pitot pressure scans at the nozzle exit presented in Chapter 5 do show spanwise variation indicating a cone of lower disturbances similar to that observed in the M6QT. These off centerline

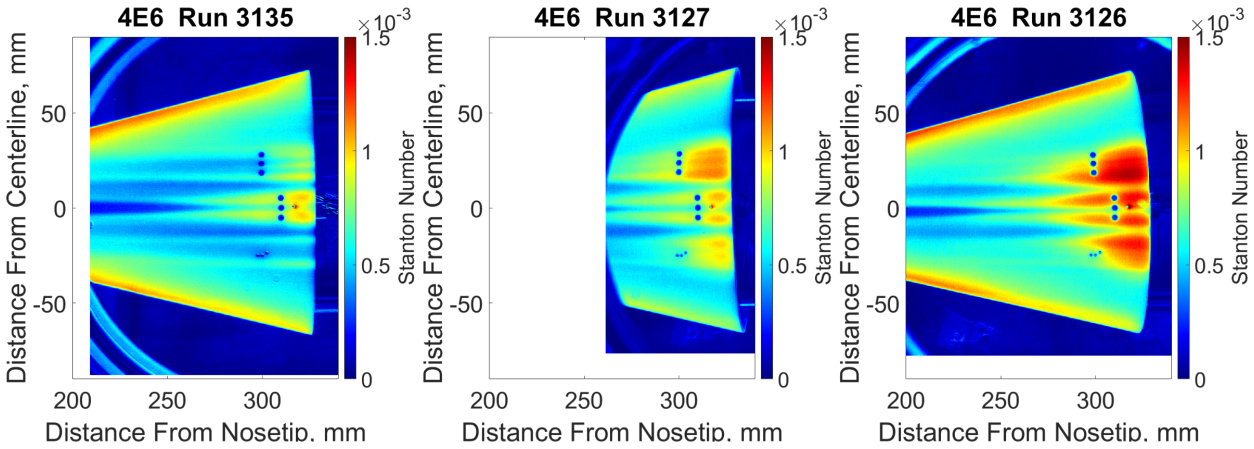

Figure 8.6: Stanton number maps at Re = 4×10^6/m. left: US station, middle: MID station, right: DS station

disturbances would impinge on the model at different locations at MID and DS stations, potentially altering the initial amplitude and development of disturbances within the model boundary layer.

8.2.2 Quiet vs Conventional Facility - ACE vs M6QT

Runs of the 2:1 elliptic cone model were conducted in the M6QT under both noisy and quiet flow for comparison with the ACE campaign results. Under noisy flow, the elevated freestream disturbances resulted in the broad diffuse heating similar in extent and Stanton number to that observed in the ACE facility. Across the Re range of the facility the shoulder PCB transducers were engulfed in the elevated heating region and showed broad full profiles indicative of a turbulent boundary layer.

Under quiet flow the evolution of surface heating was very different. Overall heating on the model surface was much lower. Whereas evidence of transition is observed on the ACE model as early as Re = 3×10^6/m, the heating levels at 7×10^6/m under quiet flow indicate that the flow over the model is fully laminar. Streaks of elevated heating are much more distinct in the M6QT. These trends can be seen in the St maps of Fig. 8.8. The top row shows maps at 9×10^6/m in

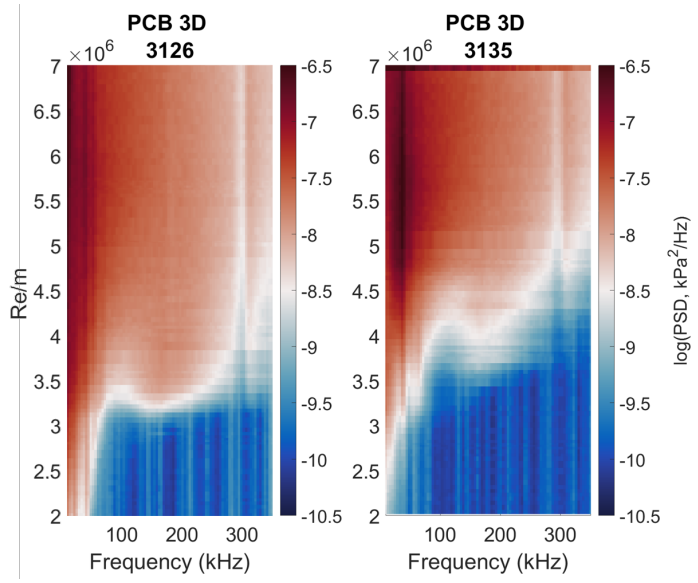

Figure 8.7: Waterfall plots of PCB 3D pressure fluctuation left: DS station Right: US station.

the M6QT and 4×10^6/m at the US (middle column) and DS (right column) stations in the ACE facility. The bottom row shows Re = 10×10^6/m and Re = 5×10^6/m. The location of streaks at and immediately outboard of the centerline are similar between the facilities. Fig. 8.9 shows spanwise slices of the St maps 287 mm downstream of the model nosetip. At these Re freestream disturbances are $\leq$ 0.05% in the M6QT, 1.0 % at the ACE US station and 1.4% at the ACE DS station.

Spectra from one transducer from each cluster are shown in Fig. 8.10. Kulite traces in ACE show a band of disturbances centered near 20 kHz which is absent in the M6QT, instead replaced by a 45 kHz peak. The PCB traces show bands at similar frequency with those in ACE at a lower frequency than in the M6QT. The M6QT frequency band is narrower than in ACE. At the model centerline fluctuation levels are similar between the two facilities despite the large difference in Re. Peaks observed in the ACE US case are lower in frequency than observed in the M6QT. This trend of lower frequencies at the lower Re in ACE is what would be expected with instability frequency increasing as boundary layer height decreases with Re. Eventual turbulent spectra levels

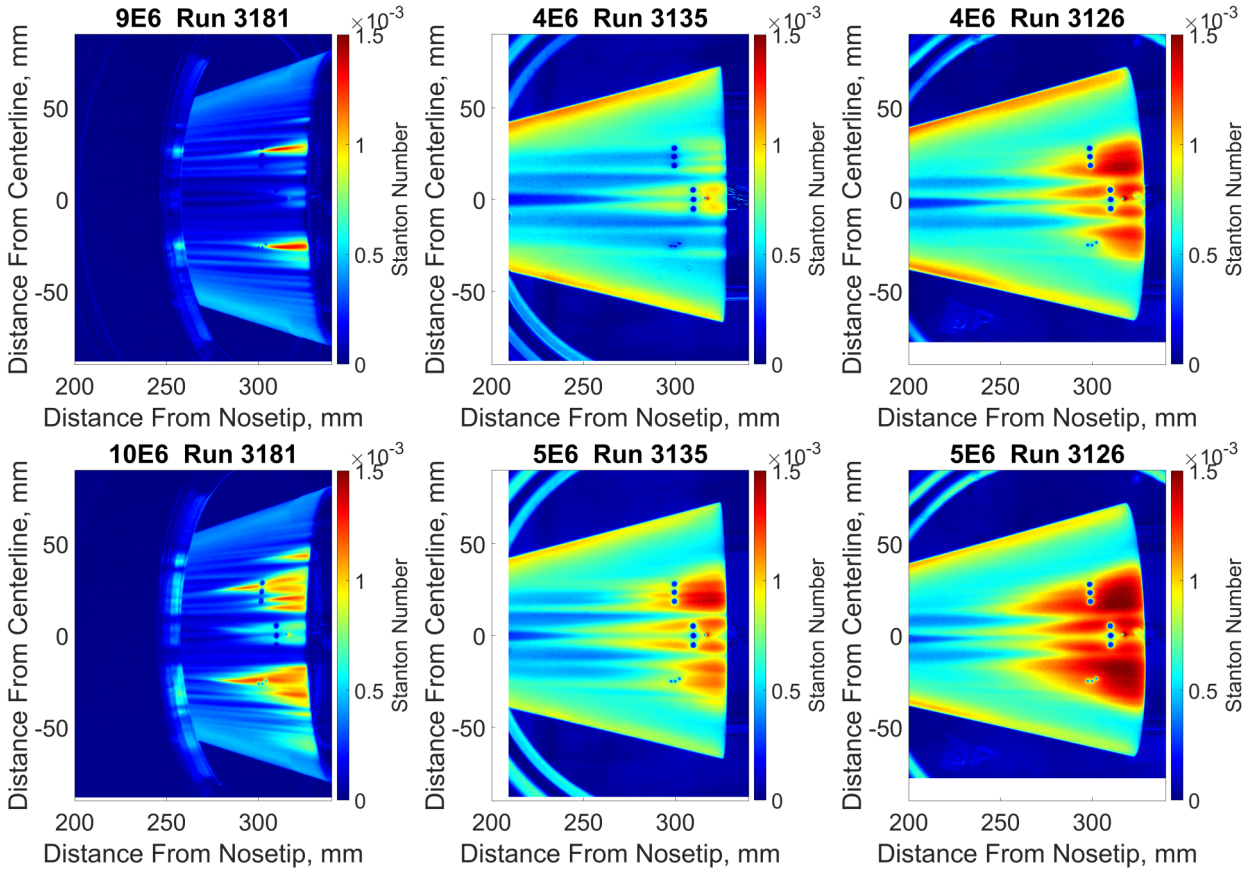

Figure 8.8: St maps comparing M6QT quiet and ACE US and DS stations. left: M6QT, center: ACE US station, right: ACE DS station.

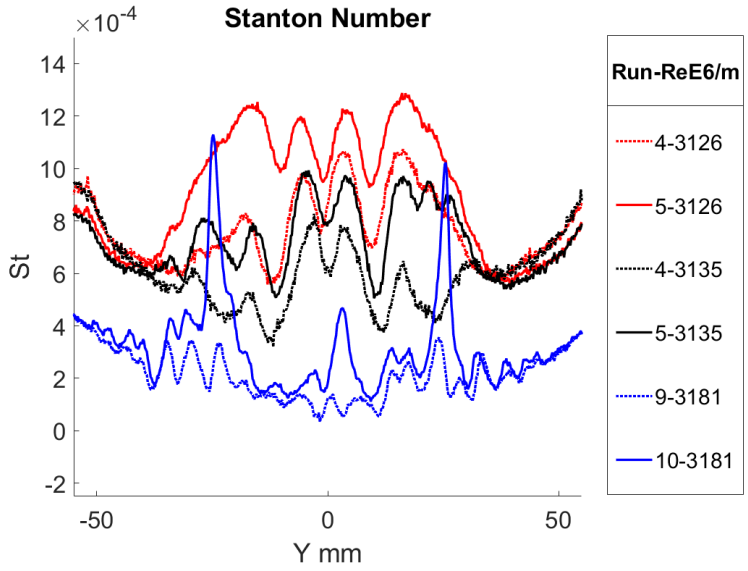

Figure 8.9: Spanwise slices of St at ACE US, ACE DS stations and M6QT, X = 287 mm.

and shapes are similar in both facilities.

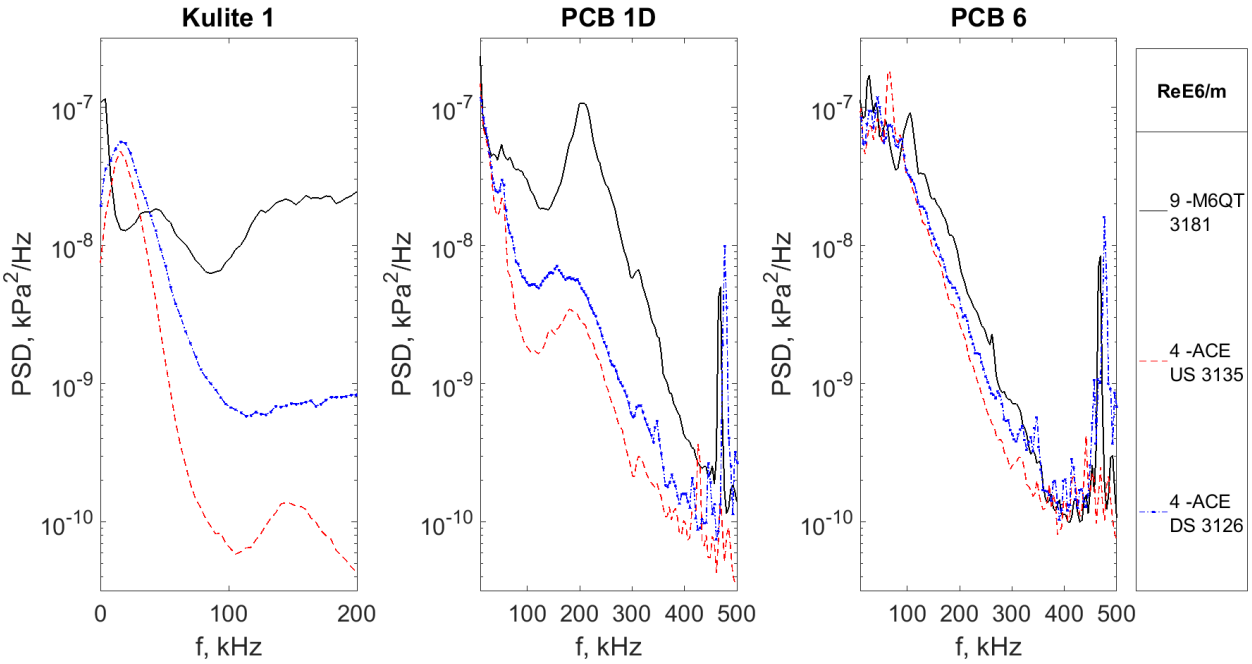

Figure 8.10: Fluctuating pressure PSD from each sensor cluster at ACE US & DS stations and M6QT quiet configuration.

Fig. 8.11 shows St maps at Re = 7×10^6/m at the different freestream disturbance levels tested. In the M6QT quiet flow map, centerline structure and shoulder streaks are visible but appear to show laminar heating levels across the model. In ACE the elevated heating lobes are seen over much of the cone shoulder and the centerline structure shows turbulent heating for nearly the entire visible region of the cone. The M6QT noisy flow map shows elevated heating lobes on the shoulder which are similar in magnitude to those in the ACE maps. The lobes extend further out onto the shoulder of the cone which is similar to the trend observed in the comparison of the ACE and BAM6QT noisy results above.

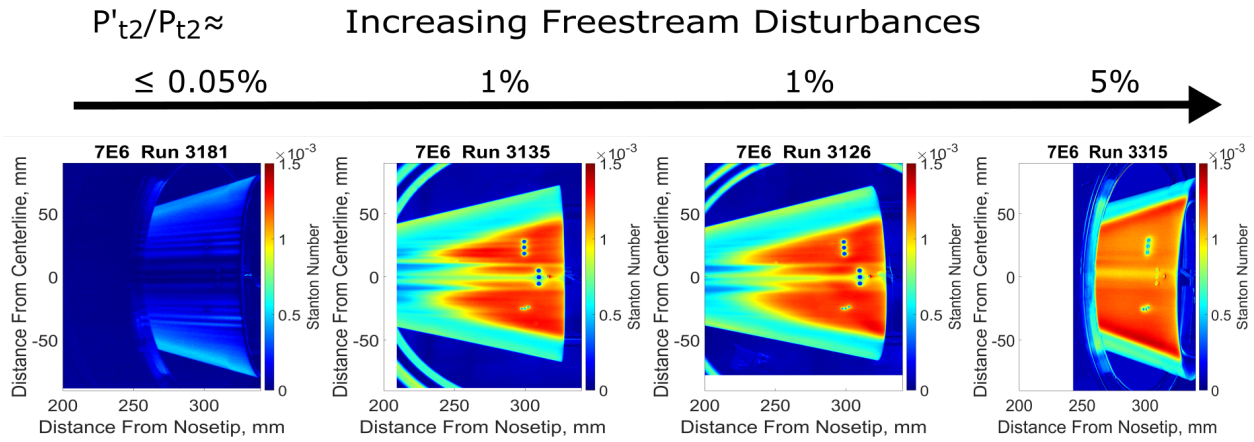

Figure 8.11: Comparison between Re = 7×10^6/m condition, from the left: M6QT quiet flow, ACE US station, ACE DS station, M6QT noisy flow

8.3 Discussion Summary

The data of the previous two chapters provide evidence that the freestream disturbance levels are influencing the transition process on the 2:1 elliptic cone. The question of the exact nature of the changes observed with varied freestream disturbance levels remains. The observations of the present campaign exposing the model to freestream disturbance levels in between those of quiet and conventional noisy facilities show that streamwise streaks in similar positions to those observed in quiet flow do appear but still lead into a more diffuse region on the shoulders with the peak of these lobes more inboard than observed under quiet flow. Several possibilities exist to explain this behavior. Theory and low-speed experiments point to travelling crossflow as becoming the dominant instability with increased freestream vortical disturbances, potentially resulting in the diffuse front observed on the cone shoulder. If the trends at low-speed were seen to hold at high-speed, it might be expected that the large broad transition region seen under noisy flow might be the result of traveling crossflow. It is possible that acoustic freestream disturbances are interacting with the curved shockwave of the elliptic cone model and producing vorticity. This vorticity could

then interact with the model surface roughness to increase the initial amplitudes of the travelling crossflow instability causing the early transition observed. Evidence for this mode of transition has not been found in any of the surface pressure data of experimental studies in ACE or the BAM6QT in noisy mode. The DNS results of Dinzl & Candler (2017) also don't see evidence of this with increasing surface roughness although their calculations do not account for freestream disturbances. Borg & Kimmel (2017*a*) and Borg & Kimmel (2017*b*) report evidence that the transition on the cone shoulder did follow the same trends with incidence angle under noisy and quiet flow indicating that crossflow does play a role. Given the nonlinear nature of crossflow instability development observed in low-speed experiments and CFD, it is possible that interactions are occurring between different modes and behave differently in the presence of elevated freestream disturbance. Second mode has been observed to be particularly sensitive to acoustic freestream disturbances typical of hypersonic facilities. As discussed above, the quiet flow, Re = 11.8×10^6/m computations of Kocian *et al.* (2016) showed initial growth of second mode instabilities that is overtaken by the nonlinear effects of the stationary vortices and their secondary instabilities. It could be that in the presence of elevated freestream disturbances this second mode instability is stronger in its interaction with the developing stationary crossflow leading to this earlier breakdown and diffuse front observed. The similarities in frequencies may also account for the spectral observation of the PCBs in this study. Secondary instabilities of the crossflow vortices and second mode waves are currently impossible to distinguish based on surface pressure measurements alone and are predicted to be very similar in frequency. This study does not provide an obvious answer to the question of what is causing the diffuse front observed but does provide a set of observations and data on the effect and sensitivity of the transition process to these freestream disturbances. The data here underscore the need for further experimental and computational investigation of these effects. The data provided

by this study serve the purpose of establishing a well-characterized dataset allowing computational study of the transition process observed and its variance with the interaction of freestream disturbances and roughness on the model surface.

9. CONCLUSIONS

The objective of the present study was to investigate the effects of freestream disturbances on the crossflow instability and transition process for Mach 6 flow over a 2:1 elliptic cone. To meet this objective, experiments were performed in the the ACE and M6QT hypersonic wind tunnels at Texas A&M University. The role of four freestream inflow conditions on the 3-D crossflow process was examined using the unique characteristics of the two facilities. Within the ACE tunnel the model was positioned with its nosetip at three streamwise stations relative to the nozzle exit plane. The freestream disturbances at each station were characterized using pitot pressure and hotwire mass flux measurements. The M6QT was operated in its low disturbance quiet mode and also its elevated freestream disturbance noisy mode. IR thermography was utilized to measure the spatial variation and extent of surface heating and high frequency surface mount pressure transducers were utilized to examine the magnitude and spectral content of pressure fluctuations within the boundary layer. High speed schlieren photography was used to examine the breakdown of the mushroom shaped upwelling in the centerline region. Experimentally, this work and the concurrent work of Leidy (2019) utilized a broad range of experimental techniques which enhanced the state of the art at the NAL.

Both ACE freestream diagnostics indicated a rapid increase of RMS fluctuation levels with increasing Re near Re = 3×10^6/m. Levels were found to vary with streamwise location relative to the nozzle exit. At the US station, pressure and mass flux fluctuations are roughly half those at the MID and DS locations for Re $\leq 3 \times 10^6$/m. At Re > 6×10^6/m fluctuation percentages at each location are the same. In addition, hotwire data were acquired to quantify how the shockwave gen-

erated by the elliptic cone modified the freestream disturbance in ACE. The general trend observed was that the magnitude of the spectra increased, while maintaining shape, for measurements taken behind the shockwave. This corresponded with higher RMS fluctuation levels behind the shock.

The transition process on the 2:1 elliptic cone was observed to have a strong dependence on the freestream environment. The high heat flux crossflow induced transitional and turbulent fronts were altered in shape and occurred at significantly lower Reynolds numbers under conventional noisy (ACE DS) conditions vs. quiet flow. This result was in good agreement with previous experiments on this geometry performed in the Purdue BAM6QT. A major difference to previous experiments was the detection of streaks of elevated heating leading into the more diffuse heating lobes observed on the cone shoulder under noisy flow. Varying the position of the model upstream of the nozzle exit within the conventional ACE facility exposed the model to lower freestream disturbance levels, resulting in more distinct heating streaks on the model surface and delaying the observed onset of transition. Under quiet flow in the M6QT, similar streamwise streaks, believed to be evidence of stationary crossflow vortices, are observed. The heating levels observed are much lower than in the ACE facility even at much higher Re/m. Several bands of apparent instability growth were identified in pressure fluctuation spectra in both facilities. Reynolds number sweeps allowed the observation of the growth of these bands to eventual breakdown to turbulence. Within the ACE facility the general trend is that the disturbances appear in the transducer spectra at higher Re and disturbance amplitudes are lower at the US vs the DS station. A band of growth at a frequency similar to the expected second mode and type-I secondary instability are seen in both facilities in shoulder PCB spectra although they appear at much lower freestream Re in the higher disturbance ACE environment. In ACE, the frequency is observed in all transducers, whereas it is more location dependent in the M6QT. This is potentially due to the positions of the sensors relative

to the stationary streaks observed in the IR. In ACE, the transducers remain in similar positions relative to three neighboring waves while more variation in relative position is observed in the M6QT. Shoulder Kulite transducers show content which compares well with the observations of Borg *et al.* (2015*a*). Content near the expected traveling crossflow frequency is observed in the M6QT and is replaced by a lower frequency disturbance in the conventional ACE facility. The centerline flow region was seen to be modified by freestream disturbance level as well, showing delayed transition with decreasing freestream disturbance levels. Spectral content observed varies between the ACE and M6QT facilities with higher disturbance frequencies and potential evidence of harmonics present in the M6QT results.

The data obtained and presented here represent a well characterized set of results which will enable further study and comparison with present and future work. The results show that the transition process on this geometry is sensitive to freestream disturbance levels present in conventional hypersonic facilities and suggests that this sensitivity is not a simple binary noisy/quiet feature. Further analysis, both experimentally and computationally, is warranted.

9.1 Future Work and Recommendations

The shear volume of data obtained in this study and the available flight and ground test data for comparison is remarkable. Further data analysis of the current data set is possible and planned. More advanced analysis aimed at looking for interactions between the disturbance frequencies observed is warranted. Bispectral analysis similar to that performed by Craig & Saric (2016) and Corke *et al.* (2018) would be particularly insightful.

Further registration and dewarping of the IR images is warranted. Fiducials, essentially IR reflective markers, have been utilized to great effect for this process. Duncan *et al.* (2013) et al.

placed reflective aluminum tape on a portion of their model outside of the area of interest and had success registering and dewarping their images. Borg & Kimmel (2017*b*) have had success using their Kulite sensor arrays as fiducials. The fiducials should ideally be accounted for in the planning and construction of the models under test. This would reduce noise in the values computed from the temperature maps. Utilizing the available FLIR high speed data recorder to obtain higher frame rate IR would allow further averaging of computed heat flux, also reducing the noise of the final output values. The characterization of both facility should be continued taking into account the suggestions and knowledge of the transition community summarized in Duan *et al.* (2018). Higher frequency measurements using PCB transducers as well as spatial measurements using high frequency probes would be especially useful. The design of the traverse constructed for this campaign should be refined. Currently the traverse is capable of traversing normal to the tunnel wall during a run but has trouble traversing in the spanwise direction. Kulite and PCB transducers used in this study gave good signal but could be improved by improvements in data acquisition and filtering.

Non-invasive off body techniques have the potential to allow visualization of vortices within the model boundary layer. This would help shed light on the development of the boundary layer and any instabilities present. At the time of writing progress is being made in utilizing the vibrationally excited NO monitoring (VENOM) simultaneous velocity and temperature measurement technique. This technique should be investigated for potential use in visualization within model boundary layers.

REFERENCES

Beresh, S. J., Henfling, J. F., Spillers, R. W. & Pruett, B. O. M. 2011 Fluctuating wall pressures measured beneath a supersonic turbulent boundary layer. *Physics of Fluids* **23** (7), 075110, doi:10.1063/1.3609271.

Berger, K., Rufer, S., Kimmel, R. & Adamczak, D. 2009 Aerothermodynamic Characteristics of Boundary Layer Transition and Trip Effectiveness of the HIFiRE Flight 5 Vehicle. In *39th AIAA Fluid Dynamics Conference*. American Institute of Aeronautics and Astronautics, doi:10.2514/6.2009-4055.

Bippes, H. 1999 Basic experiments on transition in three-dimensional boundary layers dominated by crossflow instability. *Progress in Aerospace Sciences* **35** (4), 363–412, doi:10.1016/s0376-0421(99)00002-0.

Borg, M., Kimmel, R. & Stanfield, S. 2011 HIFiRE-5 attachment-line and crossflow instability in a quiet hypersonic wind tunnel. In *41st AIAA Fluid Dynamics Conference and Exhibit*. American Institute of Aeronautics and Astronautics, doi:10.2514/6.2011-3247.

Borg, M., Kimmel, R. & Stanfield, S. 2012 Crossflow Instability for HIFiRE-5 in a Quiet Hypersonic Wind Tunnel. In *42nd AIAA Fluid Dynamics Conference and Exhibit*. American Institute of Aeronautics and Astronautics, doi:10.2514/6.2012-2821.

Borg, M. P. & Kimmel, R. L. 2016 Simultaneous Infrared and Pressure Measurements of Crossflow Instability Modes for HIFiRE-5. In *54th AIAA Aerospace Sciences Meeting*. American Institute of Aeronautics and Astronautics, doi:10.2514/6.2016-0354.

Borg, M. P. & Kimmel, R. L. 2017*a* Ground Test Measurements of Boundary-Layer Instabilities and Transition for HIFiRE-5 at Flight-Relevant Attitudes. In *47th AIAA Fluid Dynamics Conference*. American Institute of Aeronautics and Astronautics, doi:10.2514/6.2017-3135.

Borg, M. P. & Kimmel, R. L. 2017*b* Ground Test Measurements of Boundary-Layer Instabilities and Transition for HIFiRE-5 at Flight-Relevant Attitudes. In *47th AIAA Fluid Dynamics Conference*. American Institute of Aeronautics and Astronautics, doi:10.2514/6.2017-3135.

Borg, M. P. & Kimmel, R. L. 2018 Ground Test of Transition for HIFiRE-5b at Flight-Relevant Attitudes. *Journal of Spacecraft and Rockets* **55** (6), 1329–1340, doi:10.2514/1.a34163.

Borg, M. P., Kimmel, R. L., Hofferth, J. W., Bowersox, R. D. & Mai, C. L. 2015*a* Freestream Effects on Boundary Layer Disturbances for HIFiRE-5. In *53rd AIAA Aerospace Sciences Meeting*. American Institute of Aeronautics and Astronautics, doi:10.2514/6.2015-0278.

Borg, M. P., Kimmel, R. L. & Stanfield, S. 2013 Traveling Crossflow Instability for HIFiRE-5 in a Quiet Hypersonic Wind Tunnel. In *43rd Fluid Dynamics Conference*. American Institute of Aeronautics and Astronautics, doi:10.2514/6.2013-2737.

Borg, M. P., Kimmel, R. L. & Stanfield, S. 2015*b* Traveling Crossflow Instability for the HIFiRE-5 Elliptic Cone. *Journal of Spacecraft and Rockets* **52** (3), 664–673, doi:10.2514/1.a33145.

Bowcutt, K., Paull, A., Dolvin, D. & Smart, M. 2012 HIFiRE: An international collaboration to advance the science and technology of hypersonic flight. In *Proceedings of the 28th International Congress of the Aeronautical Sciences*, pp. 2012–998. ICAS Secretariat RA Leiden, The Netherlands.

Boyd, C. & Howell, A. 1994 Numerical investigation of one-dimensional heat-flux calculations. *Tech. Rep.*. Naval Surface Warfare Center Dahlgren Div. Silver Spring, MD.

Bushnell, D. 1990 Notes on initial disturbance fields for the transition problem. In *Instability and transition*, pp. 217–232. Springer, doi:10.1007/978-1-4612-3430-2_28.

Choudhari, M., Chang, C.-L., Jentink, T., Li, F., Berger, K., Candler, G. & Kimmel, R. 2009 Transition Analysis for the HIFiRE-5 Vehicle. In *39th AIAA Fluid Dynamics Conference*. American Institute of Aeronautics and Astronautics, doi:10.2514/6.2009-4056.

Corke, T., Arndt, A., Matlis, E. & Semper, M. 2018 Control of stationary cross-flow modes in a mach 6 boundary layer using patterned roughness. *Journal of Fluid Mechanics* **856**, 822–849, doi:10.1017/jfm.2018.636.

Craig, S. A. & Saric, W. S. 2016 Crossflow instability in a hypersonic boundary layer. *Journal of Fluid Mechanics* **808**, 224–244, doi:10.1017/jfm.2016.643.

Crawford, B. K., Duncan, G. T., West, D. E. & Saric, W. S. 2014 Large-Span, Non-Contact Surface Profilometry for Laminar-Flow Diagnostics. In *30th AIAA Aerodynamic Measurement Technology and Ground Testing Conference*. American Institute of Aeronautics and Astronautics, doi:10.2514/6.2014-2940.

Deyhle, H. & Bippes, H. 1996 Disturbance growth in an unstable three-dimensional boundary layer and its dependence on environmental conditions. *Journal of Fluid Mechanics* **316** (-1), 73, doi:10.1017/s0022112096000456.

Dinzl, D. J. & Candler, G. V. 2015 Analysis of Crossflow Instability on HIFiRE-5 using Direct Numerical Simulation. In *53rd AIAA Aerospace Sciences Meeting*. American Institute of Aeronautics and Astronautics, doi:doi:10.2514/6.2015-0279.

Dinzl, D. J. & Candler, G. V. 2017 Direct Simulation of Hypersonic Crossflow Instability on an Elliptic Cone. *AIAA Journal* **55** (6), 1769–1782, doi:10.2514/1.j055130.

Duan, L., Choudhari, M. M., Chou, A., Munoz, F., Radespiel, R., Schilden, T., Schröder, W., Marineau, E. C., Casper, K. M., Chaudhry, R. S., Candler, G. V., Gray, K. A. & Schneider, S. P. 2018 Characterization of Freestream Disturbances in Conventional Hypersonic Wind Tunnels. *Journal of Spacecraft and Rockets* pp. 1–12, doi:10.2514/1.a34290.

Duncan, G. T., Crawford, B., Tufts, M. W., Saric, W. S. & Reed, H. L. 2013 Effects of step

excrescences on swept-wing transition. In *31st AIAA Applied Aerodynamics Conference*, pp. 1–18. American Institute of Aeronautics and Astronautics, doi:10.2514/6.2013-2412.

Edelman, J. B. & Schneider, S. P. 2018 Secondary Instabilities of Hypersonic Stationary Crossflow Waves. *AIAA Journal* **56** (1), 182–192, doi:10.2514/1.J056028.

Fedorov, A. 2011 Transition and Stability of High-Speed Boundary Layers. *Annual Review of Fluid Mechanics* **43** (1), 79–95, doi:10.1146/annurev-fluid-122109-160750.

Gray, K. A., Chynoweth, B., Edelman, J., McKiernan, G., Wason, M. P. & Schneider, S. P. 2017 Boundary-Layer Transition Measurements in the Boeing/AFOSR Mach-6 Quiet Tunnel. In *55th AIAA Aerospace Sciences Meeting*. American Institute of Aeronautics and Astronautics, doi:10.2514/6.2017-0068.

Guelhan, A., Schuette, G. & Stahl, B. 2008 Experimental Study on Aerothermal Heating Caused by Jet-Hypersonic Crossflow Interaction. *Journal of Spacecraft and Rockets* **45** (5), 891–899, doi:10.2514/1.35899.

Hofferth, J., Bowersox, R. & Saric, W. 2010 The Mach 6 Quiet Tunnel at Texas A&M: Quiet Flow Performance. In *27th AIAA Aerodynamic Measurement Technology and Ground Testing Conference*. American Institute of Aeronautics and Astronautics, doi:doi:10.2514/6.2010-4794.

Hofferth, J. W. 2013 Boundary-Layer Stability and Transition on a Flared Cone in a Mach 6 Quiet Wind Tunnel. PhD thesis, Texas A&M University.

Juliano, T. & Schneider, S. 2010 Instability and Transition on the HIFiRE-5 in a Mach-6 Quiet Tunnel. *40th Fluid Dynamics Conference and Exhibit* (July), 1–34, doi:10.2514/6.2010-5004.

Juliano, T. J. 2010 Instability and Transition on the HIFiRE-5 in a Mach-6 Quiet Tunnel. PhD thesis, Purdue University.

Juliano, T. J., Borg, M. P. & Schneider, S. P. 2015 Quiet Tunnel Measurements of HIFiRE-5 Boundary-Layer Transition. *AIAA Journal* **53** (4), 832–846, doi:10.2514/1.j053189.

Juliano, T. J., Paquin, L. & Borg, M. P. 2016 Measurement of HIFiRE-5 Boundary-Layer Transition in a Mach-6 Quiet Tunnel with Infrared Thermography. In *54th AIAA Aerospace Sciences Meeting*, , vol. 595. American Institute of Aeronautics and Astronautics, doi:10.2514/6.2016-0595.

Juliano, T. J., Paquin, L. A. & Borg, M. P. 2019 HIFiRE-5 Boundary-Layer Transition Measured in a Mach-6 Quiet Tunnel with Infrared Thermography. *AIAA Journal* pp. 1–10, doi:10.2514/1.j056750.

Kimmel, R. & Adamczak, D. 2012 HIFiRE-1 Background and Lessons Learned. In *50th AIAA Aerospace Sciences Meeting including the New Horizons Forum and Aerospace Exposition*, pp. 1–15. American Institute of Aeronautics and Astronautics, doi:10.2514/6.2012-1088.

Kimmel, R., Adamczak, D., Juliano, T. & Paull, A. 2013 HIFiRE-5 Flight Test Preliminary Results. In *51st AIAA Aerospace Sciences Meeting including the New Horizons Forum and Aerospace Exposition*. American Institute of Aeronautics and Astronautics, doi:10.2514/6.2013-377.

Kimmel, R. L., Adamczak, D. W., Hartley, D., Alesi, H., Frost, M. A., Pietsch, R., Shannon, J. & Silvester, T. 2018 Hypersonic international flight research experimentation-5b flight overview. *Journal of Spacecraft and Rockets* **55** (6), 1303–1314, doi:10.2514/1.a34148.

Kimmel, R. L., Klein, M. A. & Schwoerke, S. N. 1997 Three-Dimensional Hypersonic Laminar Boundary-Layer Computations for Transition Experiment Design. *Journal of Spacecraft and Rockets* **34** (4), 409–415, doi:10.2514/2.3236.

Kocian, T. S., Moyes, A., Mullen, C. D. & Reed, H. L. 2016 PSE and Spatial Biglobal Instability Analysis of HIFiRE-5 Geometry. In *46th AIAA Fluid Dynamics Conference*. American Institute of Aeronautics and Astronautics, doi:10.2514/6.2016-3346.

Kocian, T. S., Moyes, A., Reed, H. L., Craig, S. A., Saric, W. S., Schneider, S. P. & Edelman, J. 2018 Hypersonic Crossflow Instability. In *2018 AIAA Aerospace Sciences Meeting*, pp. 1–25. Reston, Virginia: American Institute of Aeronautics and Astronautics, doi:10.2514/6.2018-0061.

Kocian, T. S., Moyes, A. J., Mullen, D. & Reed, H. L. 2017 PSE and Spatial Biglobal Instability Analysis of Reduced Scale and Flight HIFiRE-5 Geometry. In *55th AIAA Aerospace Sciences Meeting*, p. 0768. American Institute of Aeronautics and Astronautics, doi:10.2514/6.2017-0768.

Kovasznay, L. 1953 Turbulence in Supersonic Flow. *Journal of the Aeronautical Sciences* **20** (10), 657–674, doi:10.2514/8.2793.

Lakebrink, M. T., Paredes, P. & Borg, M. P. 2017 Toward robust prediction of crossflow-wave instability in hypersonic boundary layers. *Computers & Fluids* **144**, 1–9, doi:10.1016/j.compfluid.2016.11.016.

Lau, K. Y. 2008 Hypersonic Boundary-Layer Transition: Application to High-Speed Vehicle Design. *Journal of Spacecraft and Rockets* **45** (2), 176–183, doi:10.2514/1.31134.

Laufer, J. 1961 Aerodynamic Noise in Supersonic Wind Tunnels. *Journal of the Aerospace Sciences* **28** (9), 685–692, doi:10.2514/8.9150.

Leidy, A., Neel, I. T., Tichenor, N. R., Bowersox, R. D. & Schmisseur, J. D. 2018 High-Speed Schlieren Imaging and Hot-wire Characterization of Cylinder-Induced Hypersonic Shock Boundary Layer Interactions. In *2018 Fluid Dynamics Conference*. American Institute of Aeronautics and Astronautics, doi:10.2514/6.2018-3703.

Leidy, A. N. 2019 An Experimental Characterization of 3-D Transitional Shock Wave Boundary Layer Interactions at Mach 6. PhD thesis, Texas A&M University.

Li, F., Choudhari, M., Chang, C.-L., White, J., Kimmel, R., Adamczak, D., Borg, M., Stanfield, S. & Smith, M. 2012 Stability Analysis for HIFiRE Experiments. In *42nd AIAA Fluid Dynamics Conference and Exhibit*. American Institute of Aeronautics and Astronautics, doi:10.2514/6.2012-2961.

Lin, N., Reed, H. L. & Saric, W. S. 1992 Effect of Leading-Edge Geometry on Boundary-Layer Receptivity to Freestream Sound. In *Instability, Transition, and Turbulence*, pp. 421–440. Springer New York, doi:10.1007/978-1-4612-2956-8_42.

Mack, L. 1984 Special course on stability and transition of laminar flow. *AGARD report* **709**.

Mai, C. L. N. 2014 Near-Region Modification of Total Pressure Fluctuations by a Normal Shock Wave in a Low-Density Hypersonic Wind Tunnel. PhD thesis, Texas A&M University.

Marineau, E. C. 2017 Prediction Methodology for Second-Mode-Dominated Boundary-Layer Transition in Wind Tunnels. *AIAA Journal* **55** (2), 484–499, doi:10.2514/1.J055061.

Michael Holden and Timothy Wadhams and Matthew MacLean and Erik Mundy 2009 Reviews of studies of boundary layer transition in hypersonic flows over axisymmetric and elliptic cones conducted in the CUBRC shock tunnels. In *47th AIAA Aerospace Sciences Meeting including The New Horizons Forum and Aerospace Exposition*. American Institute of Aeronautics and Astronautics, doi:10.2514/6.2009-782.

Moyes, A., Kocian, T. S., Mullen, D. & Reed, H. L. 2018 Effects of Initial Disturbance Amplitude on Hypersonic Crossflow Instability. In *2018 AIAA Aerospace Sciences Meeting*. American Institute of Aeronautics and Astronautics, doi:10.2514/6.2018-1820.

Moyes, A. J., Paredes, P., Kocian, T. S. & Reed, H. L. 2017 Secondary instability analysis of crossflow on a hypersonic yawed straight circular cone. *Journal of Fluid Mechanics* **812**, 370–397, doi:10.1017/jfm.2016.793.

Muralikrishnan, B. & Raja, J. 2009 *Computational Surface and Roundness Metrology*. London: Springer London, doi:10.1007/978-1-84800-297-5.

Neel, I. T., Leidy, A. & Bowersox, R. D. 2017 Preliminary Study of the Effect of Environmental Disturbances on Hypersonic Crossflow Instability on the HIFiRE-5 Elliptic Cone. In *55th AIAA Aerospace Sciences Meeting*. American Institute of Aeronautics and Astronautics, doi:10.2514/6.2017-0767.

Neel, I. T., Leidy, A., Tichenor, N. R. & Bowersox, R. 2018*a* Characterization of Environmental Disturbances on Hypersonic Crossflow Instability on the HIFiRE-5 Elliptic Cone. In *22nd AIAA International Space Planes and Hypersonics Systems and Technologies Conference*. American Institute of Aeronautics and Astronautics, doi:doi:10.2514/6.2018-5375.

Neel, I. T., Leidy, A., Tichenor, N. R. & Bowersox, R. 2018*b* Characterization of Environmental Disturbances on Hypersonic Crossflow Instability on the HIFiRE-5 Elliptic Cone. In *22nd AIAA*

International Space Planes and Hypersonics Systems and Technologies Conference. American Institute of Aeronautics and Astronautics, doi:10.2514/6.2018-5375.

Oliviero, N. B., Kocian, T. S., Moyes, A. & Reed, H. L. 2015 EPIC: NPSE Analysis of Hypersonic Crossflow Instability on Yawed Straight Circular Cone. In *45th AIAA Fluid Dynamics Conference*, , vol. 2772, p. 2015. American Institute of Aeronautics and Astronautics, doi:10.2514/6.2015-2772.

Panayotov, I. V., Orti, V., Cuisinier, F. & Yachouh, J. 2016 Polyetheretherketone (PEEK) for medical applications. *Journal of Materials Science: Materials in Medicine* **27** (7), 118, doi:10.1007/s10856-016-5731-4.

Paredes, P., Gosse, R., Theofilis, V. & Kimmel, R. 2016 Linear modal instabilities of hypersonic flow over an elliptic cone. *Journal of Fluid Mechanics* **804**, 442–466, doi:10.1017/jfm.2016.536.

Poggie, J., Kimmel, R. L. & Schwoerke, S. N. 2000 Traveling Instability Waves in a Mach 8 Flow over an Elliptic Cone. *AIAA Journal* **38** (2), 251–258, doi:10.2514/2.979.

Radeztsky, R. H., Reibert, M. S. & Saric, W. S. 1999 Effect of Isolated Micron-Sized Roughness on Transition in Swept-Wing Flows. *AIAA Journal* **37** (11), 1370–1377, doi:10.2514/2.635.

Reed, H., Kimmel, R., Schneider, S. & Arnal, D. 1997 Drag prediction and transition in hypersonic flow. In *28th Fluid Dynamics Conference*. American Institute of Aeronautics and Astronautics, doi:10.2514/6.1997-1818.

Reed, H. L., Kocian, T. S. & Saric, W. 2018 Interactive Computations and Experiments in Stability and Transition Research. In *2018 Applied Aerodynamics Conference*. Atlanta, Georgia: American Institute of Aeronautics and Astronautics, doi:10.2514/6.2018-3320.

Reed, H. L. & Saric, W. S. 2015 Receptivity: The Inspiration of Mark Morkovin (Invited). In *45th AIAA Fluid Dynamics Conference*. American Institute of Aeronautics and Astronautics, doi:10.2514/6.2015-2471.

Reed, H. L., Saric, W. S. & Arnal, D. 1996 Linear Stability Theory Applied to Boundary Layers. *Annual Review of Fluid Mechanics* **28** (1), 389–428, doi:10.1146/annurev.fl.28.010196.002133.

Saric, W., Carrillo, R. & Reibert, M. 1998 Nonlinear stability and transition in 3-D boundary layers. *Meccanica* **33**, 469–487, doi:10.1023/A:1004368526215.

Saric, W. S., Reed, H. L. & Kerschen, E. J. 2002 BOUNDARY-LAYER RECEPTIVITY TO FREESTREAM DISTURBANCES. *Annual Review of Fluid Mechanics* **34** (1), 291–319, doi:10.1146/annurev.fluid.34.082701.161921.

Saric, W. S., Reed, H. L. & White, E. B. 2003 Stability and Transition of Three-Dimensional Boundary Layers. *Annual Review of Fluid Mechanics* **35** (1), 413–440, doi:10.1146/annurev.fluid.35.101101.161045.

Saric, W. S., West, D. E., Tufts, M. W. & Reed, H. L. 2019 Experiments on Discrete Roughness Element Technology for Swept-Wing Laminar Flow Control. *AIAA Journal* **57** (2), 641–654, doi:10.2514/1.j056897.

Schneider, S. P. 2001 Effects of High-Speed Tunnel Noise on Laminar-Turbulent Transition. *Journal of Spacecraft and Rockets* **38** (3), 323–333, doi:10.2514/2.3705.

Semper, M., Pruski, B. & Bowersox, R. 2012 Freestream Turbulence Measurements in a Continuously Variable Hypersonic Wind Tunnel. *AIAA Paper* **732**, 2012, doi:10.2514/6.2012-732.

Shea, J. F. 1988 Report of the Defense Science Board Task Force on the National Aerospace Plane (NASP). *Tech. Rep.*. Office of the Under Secretary of Defense for Acquisition, Washington DC.

Tichenor, N. R. 2010 Characterization of the Influence of a Favorable Pressure Gradient on the Basic Structure of a Mach 5.0 High Reynolds Number Supersonic Turbulent Boundary Layer. PhD thesis, Texas A&M Engineering.

Tufts, M. W., Borg, M. P., Gosse, R. C. & Kimmel, R. L. 2018 Collaboration Between Flight Test, Ground Test, and Computation on HIFiRE-5. In *2018 Applied Aerodynamics Conference*. American Institute of Aeronautics and Astronautics, doi:10.2514/6.2018-3807.

White, E. B. & Saric, W. S. 2005 Secondary instability of crossflow vortices. *Journal of Fluid Mechanics* **525**, 275–308, doi:10.1017/s002211200400268x.

APPENDIX A

IR THERMOGRAPHY & PROCESSING

Infrared thermometry has become a valuable tool for investigating boundary layer transition. Regions of increased heating across a model surface can reveal the development of instabilities as well as the onset of transition. The use of the technique presented in this dissertation leverages experience reported in several previous experiments involving hypersonic flow and boundary layer transition (Guelhan *et al.*, 2008; Borg & Kimmel, 2017*b*; Juliano *et al.*, 2016; Duncan *et al.*, 2013).

The use of this technique relies on the model's ability to radiate heat and preserve spatial differences in heating. A model surface that has high emissivity and low thermal conductivity is required. High emissivity ensures that the model radiates enough infrared radiation to be measurable and does not act as a mirror, reflecting its surroundings as a low emissivity material does. Low thermal conductivity ensures that heating caused by the flow over the model remains spatially isolated and does not diffuse across the model surface.

Many experiments have been conducted utilizing traditional metal models painted with an insulative layer of matte black paint. This technique provides excellent results but does have drawbacks. Painting the model may dramatically alter its surface roughness. Orange peel roughness typical of some painting applications has been shown to introduce distributed roughness causing transition to move forward on a swept wing (Saric *et al.*, 2019). Additionally, the application of the paint can be difficult to control, resulting non-uniform distribution over the model surface.

Several recent studies have utilized high temperature plastics to construct models or inserts for the use of IR thermography. These plastics are characterized by their high glass transition

temperatures and/or melting points, their low thermal conductivity, their high emissivity, and their relative strength. One such plastic is polyether ether keytone (PEEK). PEEK is utilized in several sectors including biomedical engineering. Its inertness, resistance to degradation, and strength make it a useful material for biological implants such as stents, bone replacements and dental implants (see Panayotov *et al.*, 2016). PEEK has a high emissivity, estimated to be between 0.89 and 0.94. FLIR IR cameras utilize a so-called power linear sensor meaning that the voltage output of the sensor is given as

$$V = C\varepsilon W \tag{A.1}$$

where V is the voltage output, C is a sensor based constant, ε is the emissivity and W is the radiant emittance in $\mathrm{W\,m^{-2}}$. From a high level view the radiant emittance observed by the camera can come from several sources. Principle among the sources are the radiation from the object being measured, reflections of the surroundings on the object surface (the power of which go as 1-ε), and emission from the atmosphere between the measurement surface and the camera sensor. In the present experiment radiation from surface reflections and the atmosphere were neglected. For surface reflections, the high emissivity of the PEEK means that it is a poor reflector. In addition the initial frame subtraction process described in Subsection 3.3.1 helps eliminate constant temperature reflections from the images. Atmospheric emittance is relatively low compared to the emittance of the PEEK surface and the distance between the camera and the model is short. The calibration procedure utilized to calibrate the FLIR camera output to temperature is described in detail in Leidy (2019) and the estimated error associated with the technique is discussed in Sec. 4.3. A sample of the heat flux processing code utilized is given in App. E.

APPENDIX B

ROUGHNESS PROCESSING

As discussed in Subsection 3.3.6, a Keyence LK-H022 laser profilometer mounted to a custom made traverse system was utilized to measure the surface roughness of various models. This system was originally designed and constructed by and described in Crawford *et al.* (2014). The system consists of an off the shelf Keyence laser attached to a custom made two-stage traversing system. The system has a 120 mm throw in its Y-axis and 950 mm in its longer X-axis. The laser utilized has a depth resolution of 0.02 μm and a laser spot size of 25 μm. The system is capable of 2 μm steps in the X-axis.

Scans are conducted using a wifi-based control interface. Scans are made in the X direction and recorded to the on-board storage of the traverse control box. The traverse moves continuously through the scanned area. The laser system samples at 10 kHz and is averaged to a value at each position. The raw output of the system is an ASCII file of the measured heights at each of the sampling positions.

For roughness analysis, this data is processed using MATLAB. A roughness processing code was developed following the descriptions and examples given in Muralikrishnan & Raja (2009). The data is first median filtered to remove noise introduced by the traverse and any spurious laser returns. A least squares polynomial fit is then applied to the data and subtracted to remove the form of the measured profile. Next a so-called 0^{th} order Gaussian regression filter is used to fit the waviness of the profile. A fit is generated based on a filter kernel of a user input wavelength. This fit is subtracted from the form subtracted data from the previous step. This results in an

Table B.1: Surface roughness parameter definitions.

Roguhness Parameter	Definition
R_a	Average Roughness
R_q	RMS Roughness
$R_z(i)$	distance between highest peak and lowest valley in a λ_c sized window of the roughness profile.
R_z	Average of $R_z i$ across measured profile

isolated roughness profile fit for examination. This process is depicted in the form of a flowchart and cartoon of measured profiles in Fig. B.1. User inputs to the code include the order of the form removal polynomial and the cutoff wavelength for the 0^{th} order Gaussian filter.

Roughness parameters can be defined in several different ways, and thus it is important to define the parameters used and the method utilized to compute them. Definitions of the parameters utilized are given in Table B.1 and an example of the processing code is presented in Sec. E.2.

Table B.2 shows RMS and average peak to peak roughness for several spanwise locations. Table B.3 shows the results at each of the streamwise locations scanned. Each scan can be further processed for the examination of spatial spectra, examining the wavelengths of roughness content present.

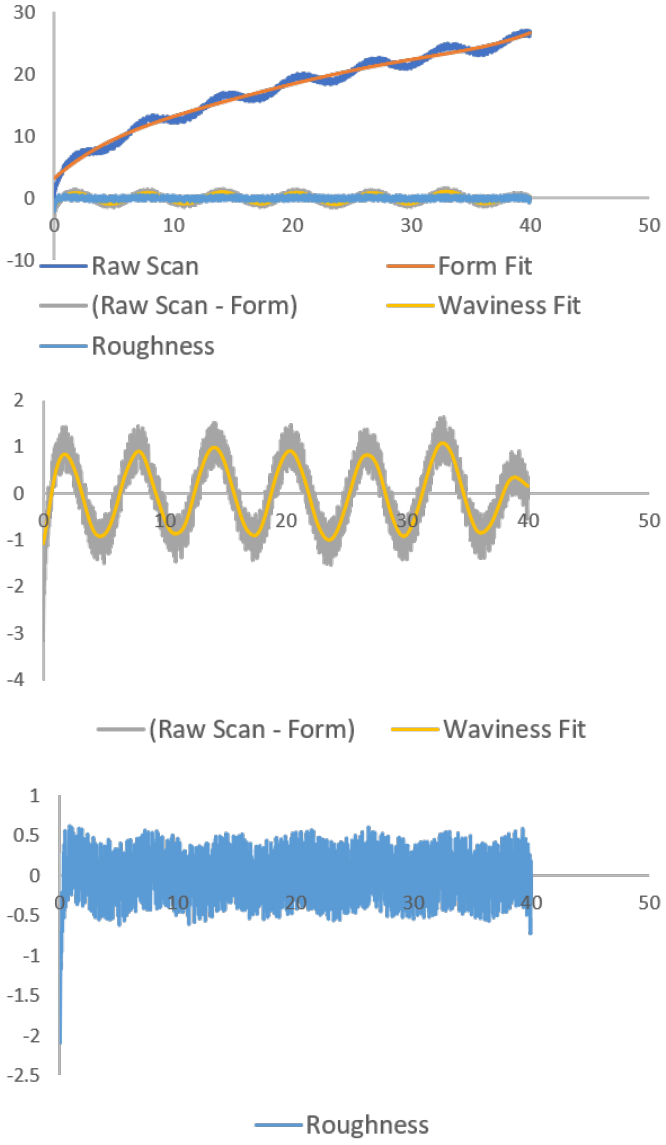

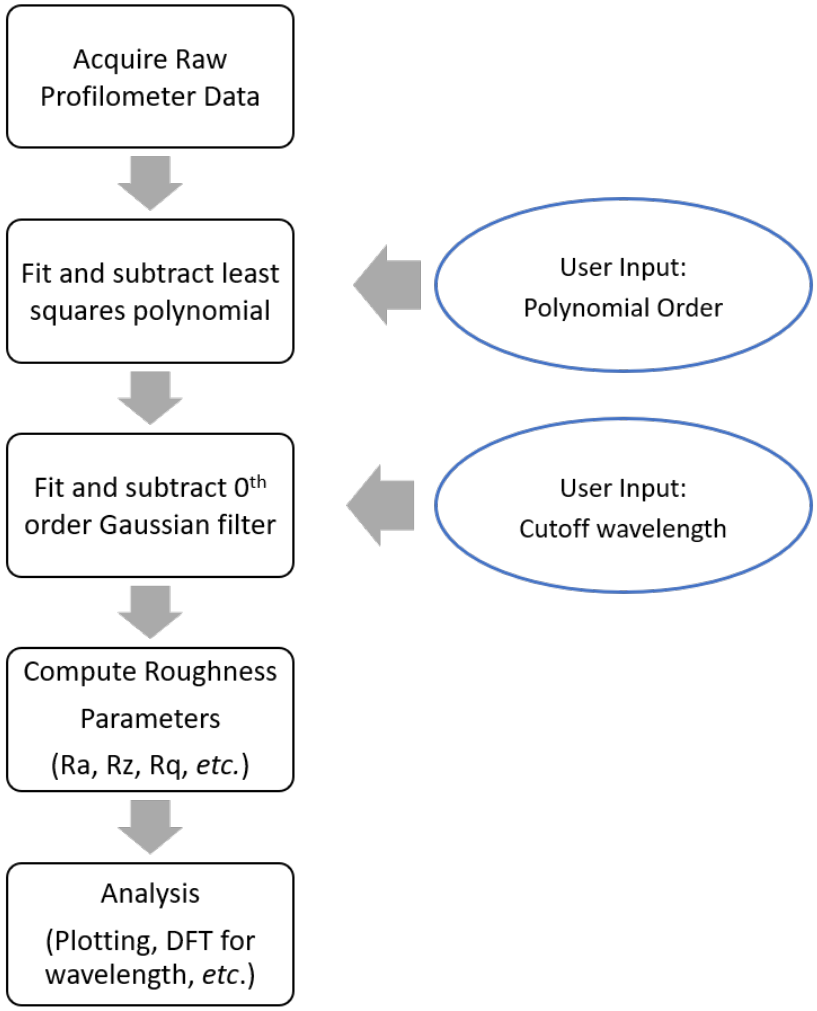

Figure B.1: Roughness processing flow.

Table B.2: Surface roughness parameters at scanned streamwise locations.

X Location (mm)	RMS Roughness, R_q (μm)	Average Peak to Peak Roughness R_z (μm)
60	1.7	6.7
120	1.6	7.1
180	2.0	9.2
240	2.3	10
300	2.8	11.4

Table B.3: Surface roughness at various streamwise locations.

Scan Number	X location (mm)	Average Roughness Ra (μm)	RMS Roughness Rq (μm)	Pk-Pk Average Rz (μm)	Cutoff wavelength (mm)
1	60.5	1.3	1.7	6.9	0.8
2	55.6	1.3	1.6	6.5	
3	50.6	1.4	1.9	7.7	
4	45.7	1.5	1.9	7.7	
5	40.7	1.5	2.0	8.6	
6	35.7	1.5	1.9	8.1	
7	30.8	1.5	1.9	7.4	
8	25.8	1.5	1.9	7.6	
9	20.8	1.7	2.2	8.7	
10	15.9	1.4	1.7	7.2	

Continued: Surface roughness at streamwise locations.

Scan Number	X location (mm)	Average Roughness Ra (μm)	RMS Roughness Rq (μm)	Pk-Pk Average Rz (μm)	Cutoff wavelength (mm)
11	10.9	1.5	1.9	7.4	
12	6.0	1.7	2.2	8.7	
13	1.0	2.0	2.5	9.6	
1	120.1	1.3	1.6	7.1	1.5
2	115.1	1.3	1.6	6.9	
3	110.2	1.3	1.6	6.9	
4	105.2	1.2	1.5	6.5	
5	100.2	1.3	1.6	6.9	
6	95.3	1.7	2.6	10.3	
7	90.3	1.4	1.8	7.6	
8	85.4	1.4	1.7	7.3	
9	80.4	1.5	1.9	7.9	
10	75.4	1.5	1.9	8.4	
11	70.5	1.6	2.1	8.7	
12	65.5	1.5	1.9	8.1	
13	60.5	1.6	2.0	8.9	
1	179.7	1.6	2.0	9.2	2.5

Continued: Surface roughness at streamwise locations.

Scan Number	X location (mm)	Average Roughness Ra (μm)	RMS Roughness Rq (μm)	Pk-Pk Average Rz (μm)	Cutoff wavelength (mm)
2	174.7	1.5	1.9	9.1	
3	169.7	1.5	2.0	8.8	
4	164.8	1.6	2.0	9.1	
5	159.8	1.5	1.9	8.8	
6	154.8	1.5	1.9	8.5	
7	149.9	1.6	2.0	9.0	
8	144.9	1.6	2.0	9.3	
9	139.9	1.5	1.9	8.6	
10	135.0	1.6	2.1	8.7	
11	130.0	1.6	2.0	9.0	
12	125.1	1.5	2.0	8.9	
13	120.1	1.5	1.9	8.4	
1	239.2	1.9	2.3	10.0	2.5
2	234.2	2.0	2.5	10.2	
3	229.3	1.9	2.3	9.7	
4	224.3	Scanning Error			

Continued: Surface roughness at streamwise locations.

Scan Number	X location (mm)	Average Roughness Ra (μm)	RMS Roughness Rq (μm)	Pk-Pk Average Rz (μm)	Cutoff wavelength (mm)
5	219.4	1.9	2.4	10.0	
6	214.4	1.8	2.3	9.9	
7	209.4	1.8	2.2	9.8	
8	204.5	1.8	2.2	9.5	
9	199.5	1.9	2.3	10.3	
10	194.5	1.6	2.0	8.9	
11	189.6	1.6	2.0	9.0	
12	184.6	1.7	2.1	8.8	
13	179.7	1.6	2.1	9.1	
1	298.8	2.3	2.8	11.4	2.5
2	293.8	2.3	2.8	11.4	
3	288.8	2.3	2.8	11.6	
4	283.9	2.2	2.7	12.1	
5	278.9	2.2	2.8	11.3	
6	273.9	2.1	2.6	10.8	
7	269.0	2.0	2.5	10.2	
8	264.0	2.1	2.6	11.2	

Continued: Surface roughness at streamwise locations.

Scan Number	X location (mm)	Average Roughness Ra (μm)	RMS Roughness Rq (μm)	Pk-Pk Average Rz (μm)	Cutoff wavelength (mm)
9	259.1	2.0	2.5	10.5	
10	254.1	2.4	3.4	12.3	
11	249.1	2.0	2.5	10.7	
12	244.2	2.1	2.6	11.3	
13	239.2	2.0	2.4	10.8	
1	328.1	2.6	3.1	12.5	2.5
2	325.6	2.6	3.2	12.8	
3	323.1	2.5	3.0	12.5	
4	320.7	2.6	3.1	12.3	
5	318.2	2.3	2.8	11.5	
6	315.7	2.3	2.7	11.1	
7	313.2	2.3	2.9	11.9	

APPENDIX C

TUNNEL RUN CONDITIONS

This appendix presents the run conditions for each of the instrumented runs conducted and presented in the main text. Table C.1 and Table C.2 present the test conditions including the model temperature as well as tested Reynolds number range. Figures for each run show the measured freestream conditions and model surface temperature during each run. Staring at the top left, plotted are the settling chamber pressure and Mach number. The tunnel total temperature is plotted in the top right figure along with the nozzle static pressure. The nominal 430 K stagnation temperature is shown with a solid black line and dashed lines indicate $\pm$ 2.5% bands. The bottom plot shows the Reynolds number and model surface temperature vs time. Red dots indicate 0.1E6/m steps in Re. Overall the run profiles are very consistent within each facility. This consistency gives confidence that the changes observed between model stations within the ACE tunnel are due to the freestream environment and not an artifact of the tunnel run position.

Table C.1: M6QT Instrumented Run conditions

Run Number	Model initial Temperature K	Re_{min} $x10^6/m$	Re_{max} $x10^6/m$	Notes
3179	312	6.8	11.5	
3180	318	6.9	11.6	
3181	319	7.0	11.6	
3182	317	7.0	11.9	Imaged uninstrumented side of model
3183	336	7.1	11.6	
3184	323	6.9	12.0	Model yawed 1° nosetip down
Upstream PCB Transducers Installed				
3418	316	6.2	11.5	
3419	312	6.1	11.2	
3420	319	6.1	11.3	

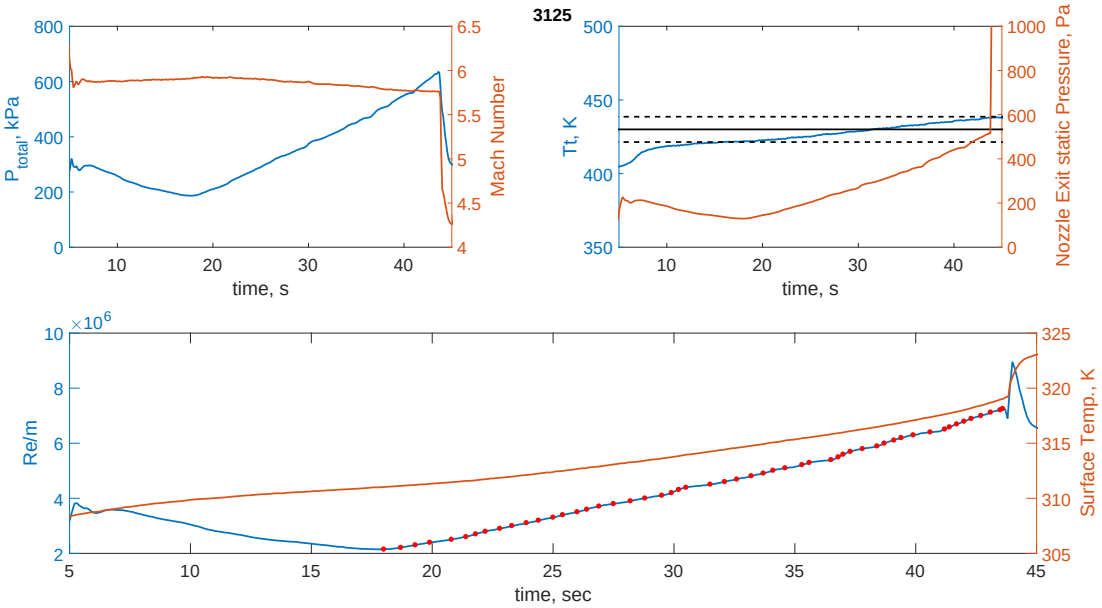

Figure C.1: Run conditions ACE DS Station Run 3125.

Table C.2: ACE Instrumented run conditions.

Run Number	Model initial Temperature K	Re_{min} $x10^6/m$	Re_{max} $x10^6/m$	Model Position	Notes
3115	296	2.4	8.3	2.5" Downstream	
3116	299	3.7	7.5	2.5" Downstream	
3117	297	3.0	5.8	2.5" Downstream	
3119	302	3.5	6.0	2.5" Downstream	Swept down in Re
3124	304	2.1	7.3	2.5" Downstream	
3125	306	2.1	7.3	2.5" Downstream	
3126	296	1.9	7.9	2.5" Downstream	
3127	304	2.0	7.7	0.5" Upstream	
3128	302	1.1	4.1	0.5" Upstream	Swept down in Re
3135	301	2.0	7.1	6" Upstream	
3136	301	2.0	7.2	6" Upstream	Imaged uninstrumented side of model
3137	298	2.0	7.2	6" Upstream	
Upstream PCB Transducers Installed					
3412	302	1.9	7.2	2.5" Downstream	
3413	302	2.0	7.1	2.5" Downstream	
3414	305	1.9	8.6	0.5" Upstream	Schlieren
3415	300	2.0	7.9	0.5" Upstream	Schlieren
3416	300	2.0	6.5	6" Downstream	
3417	301	1.9	7.4	6" Downstream	

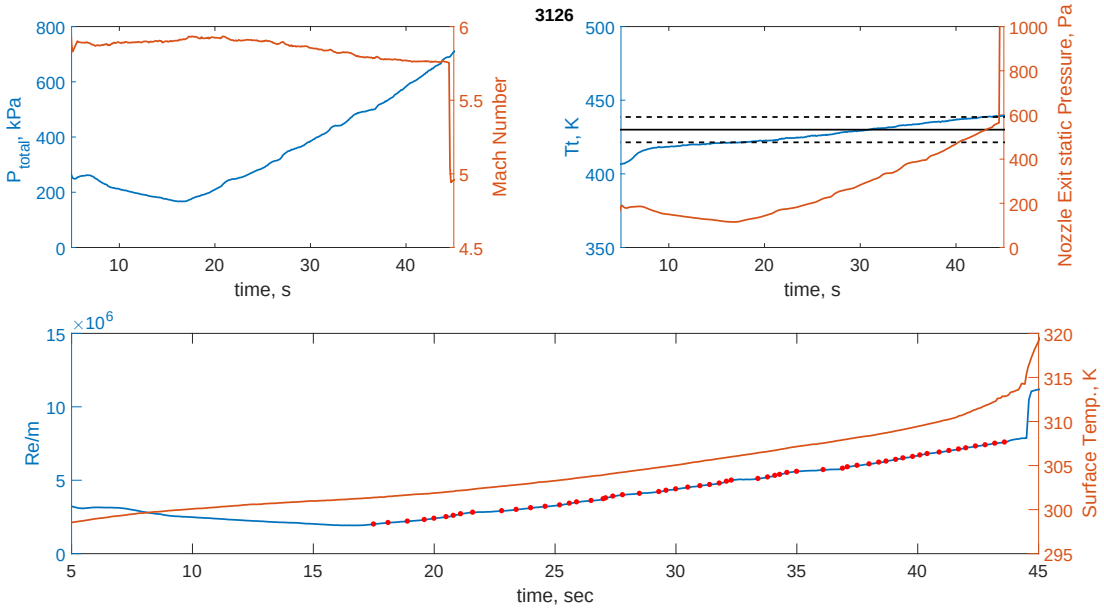

Figure C.2: Run conditions ACE DS Station Run 3126.

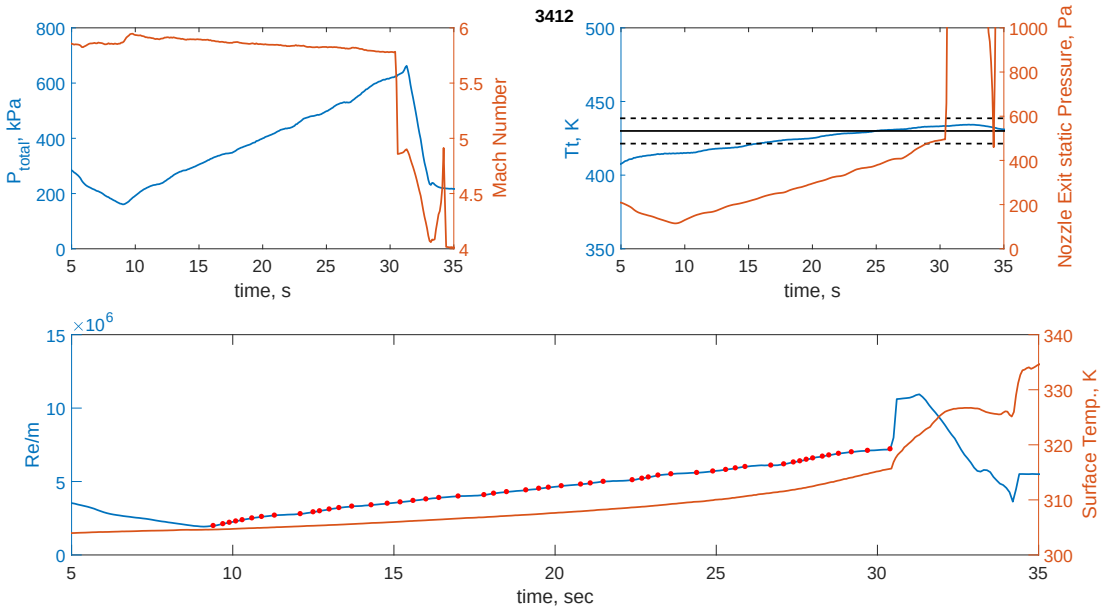

Figure C.3: Run conditions ACE DS Station Run 3412.

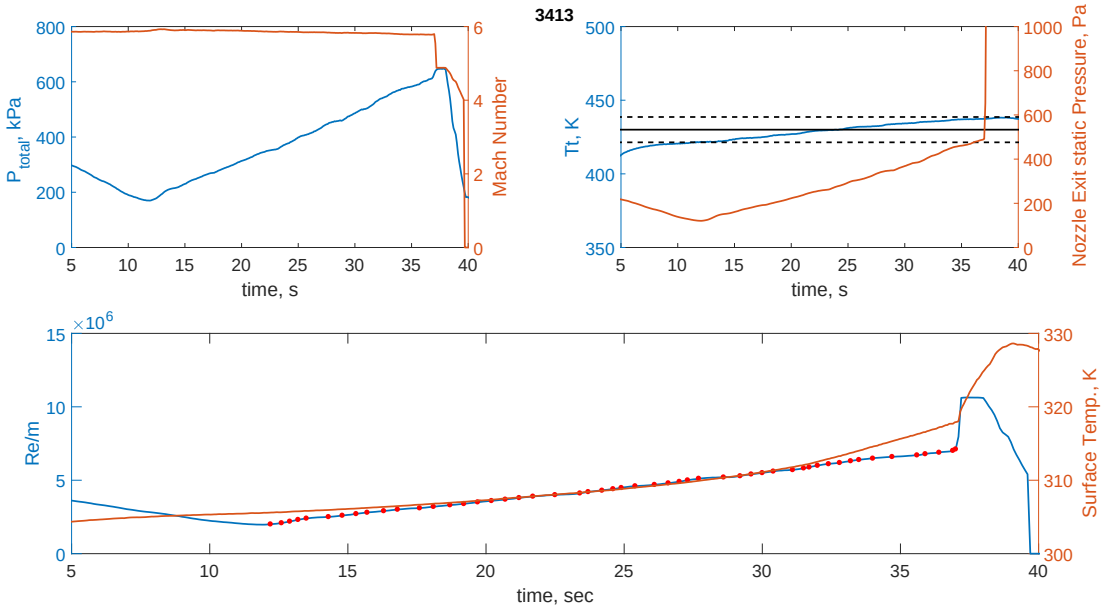

Figure C.4: Run conditions ACE DS Station Run 3413.

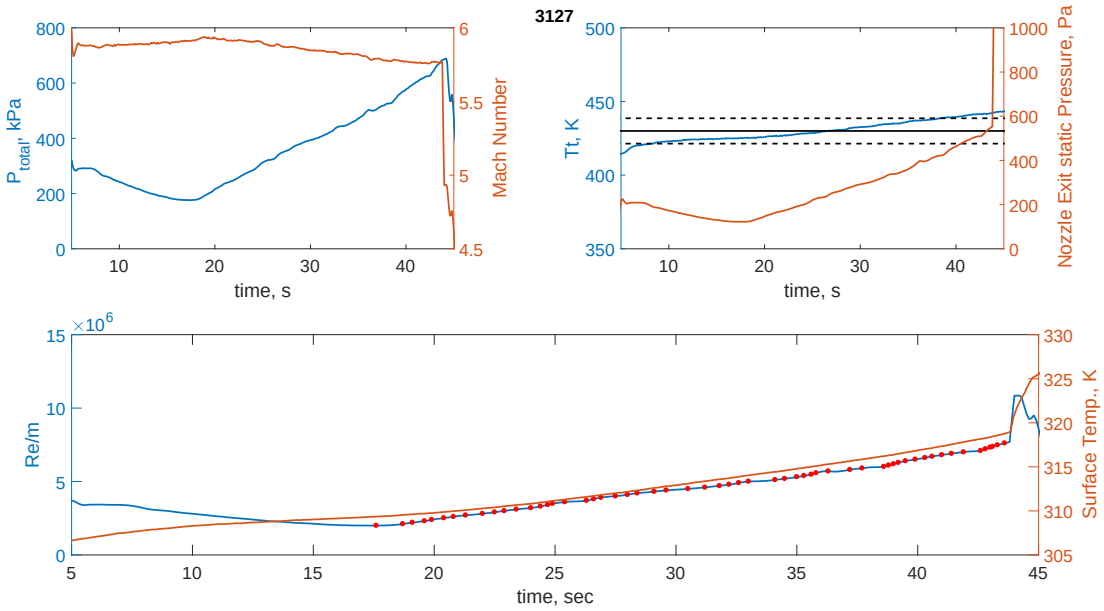

Figure C.5: Run conditions ACE MID Station Run 3127.

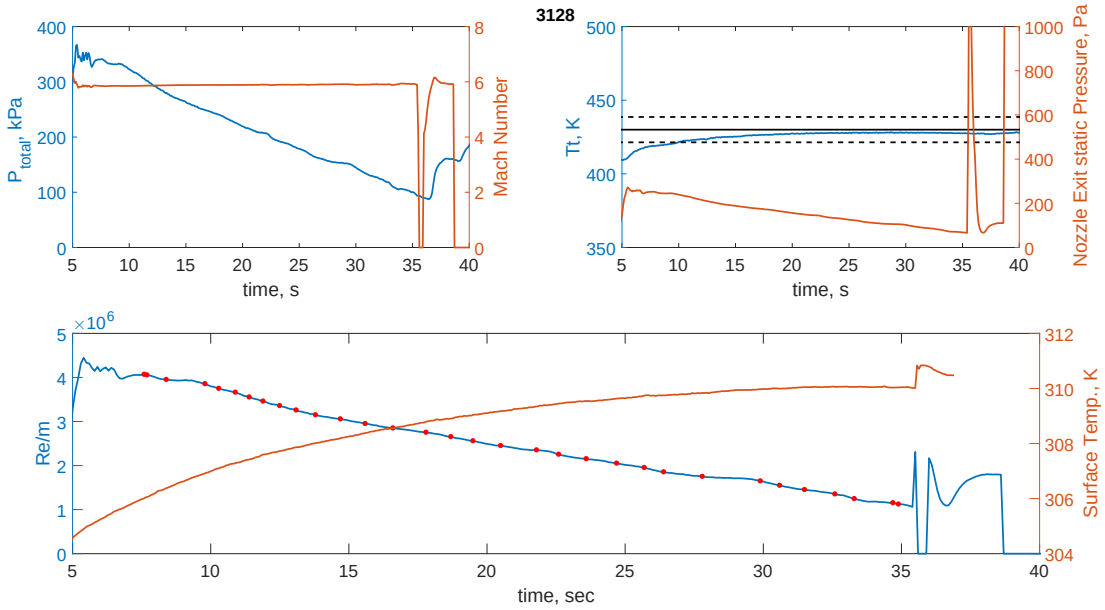

Figure C.6: Run conditions ACE MID Station Run 3127.

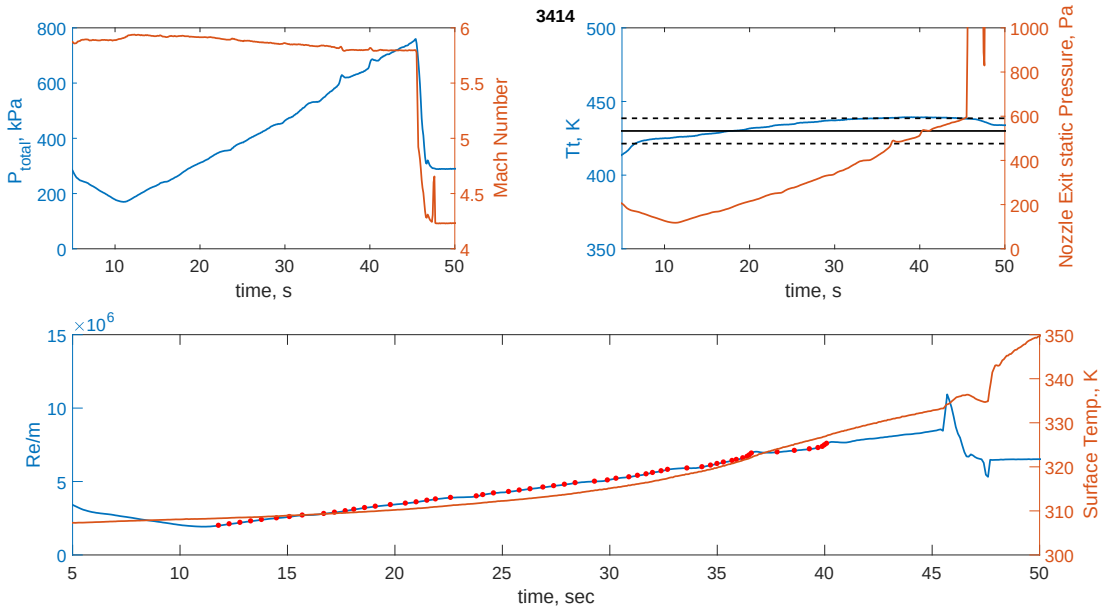

Figure C.7: Run conditions ACE MID Station Run 3414.

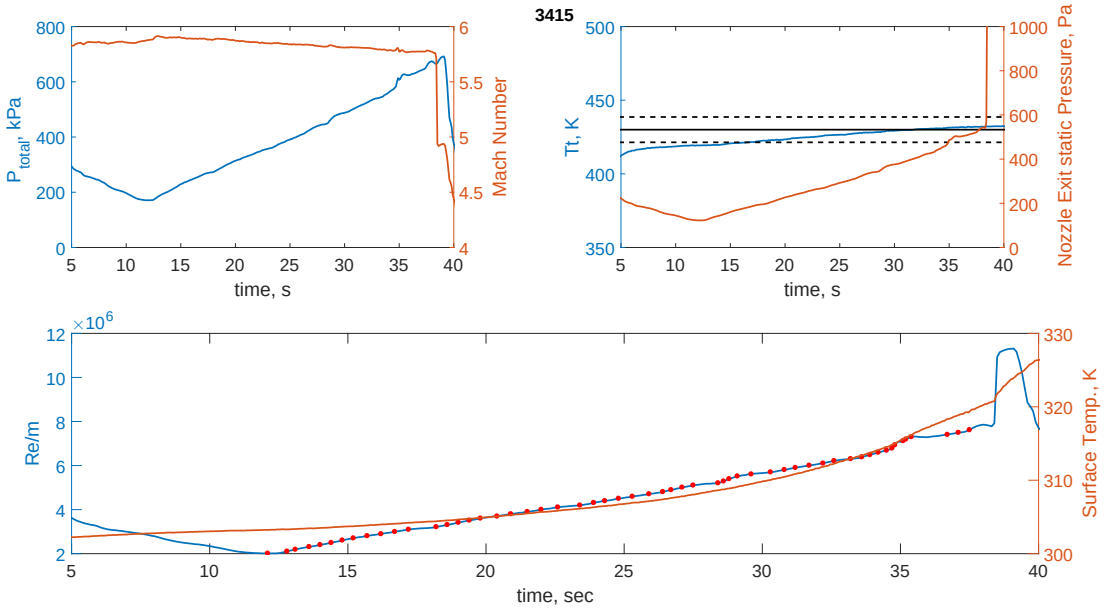

Figure C.8: Run conditions ACE MID Station Run 3415.

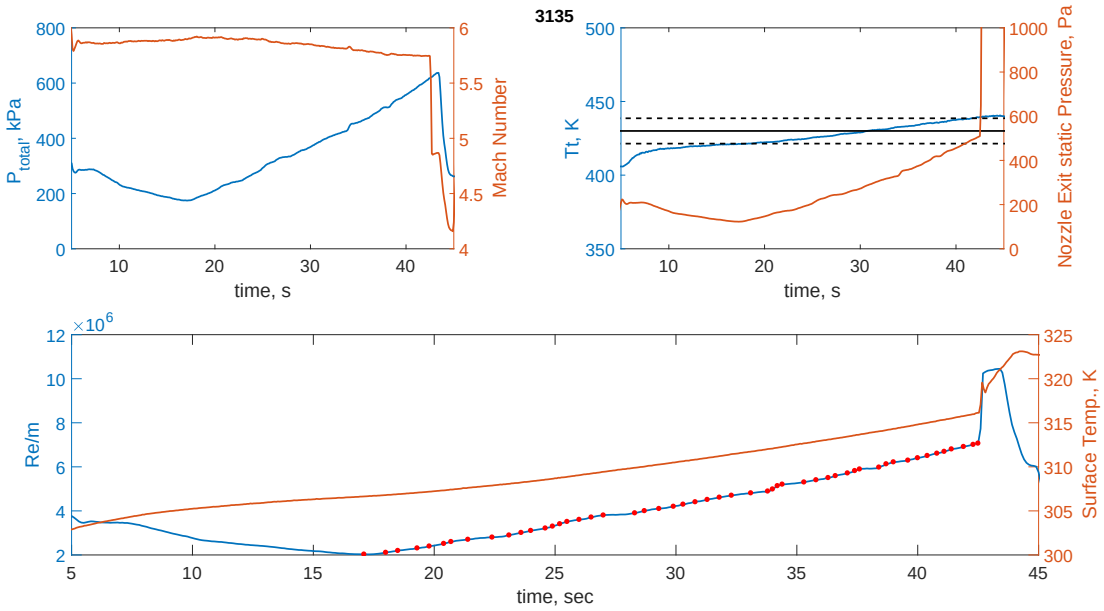

Figure C.9: Run conditions ACE US Station Run 3135.

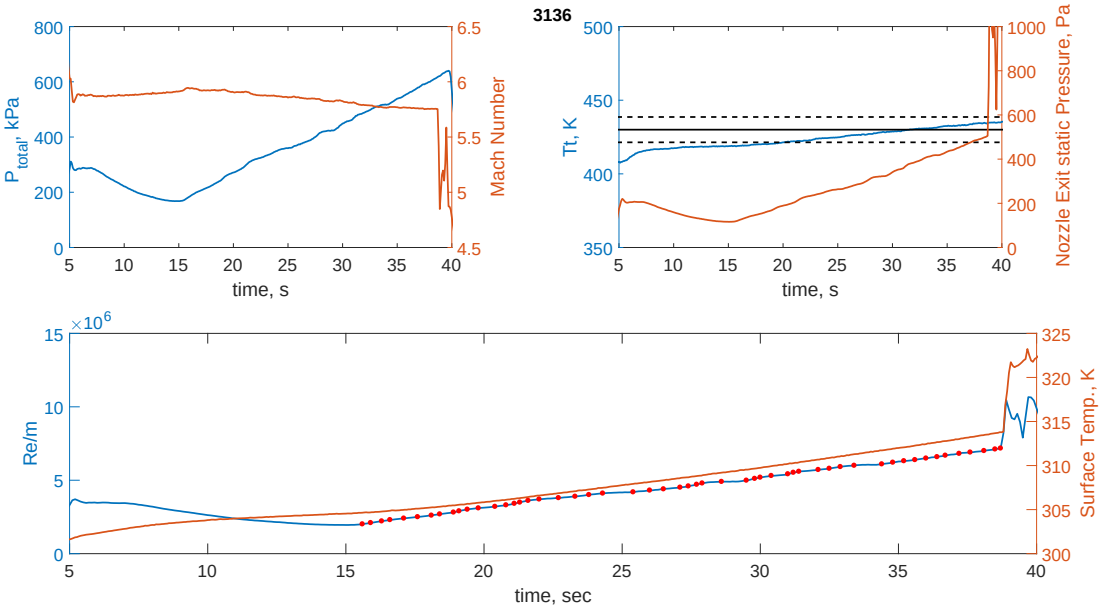

Figure C.10: Run conditions ACE US Station Run 3136.

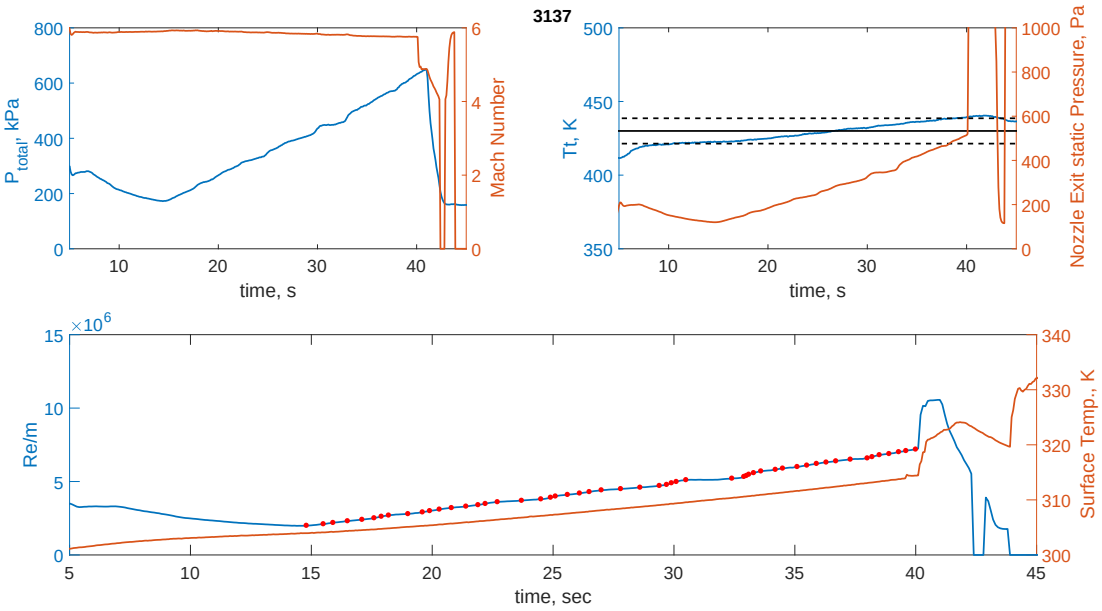

Figure C.11: Run conditions ACE US Station Run 3137.

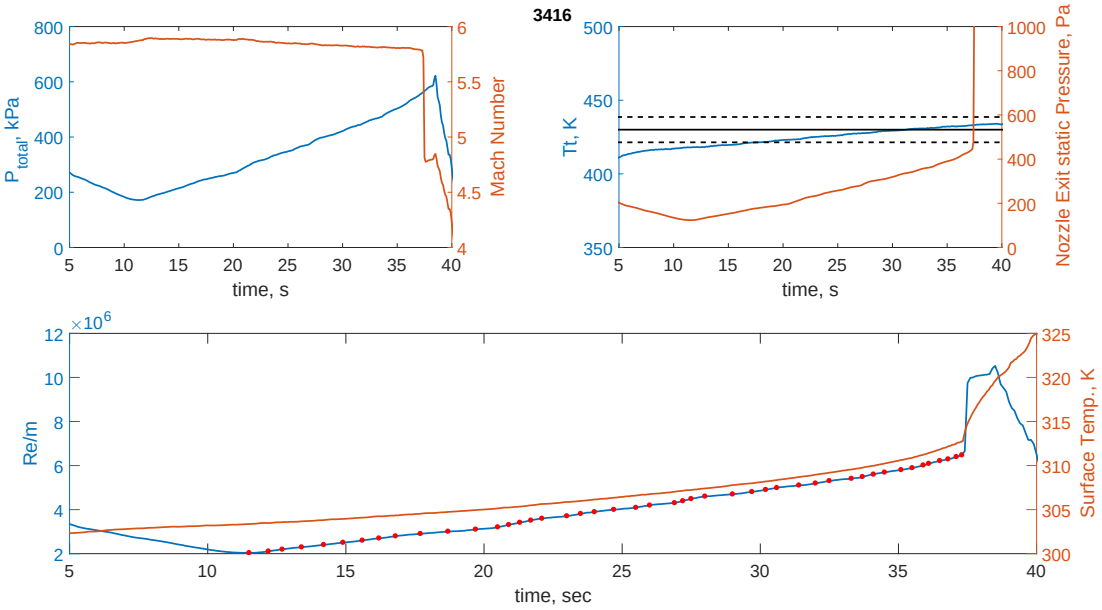

Figure C.12: Run conditions ACE US Station Run 3416.

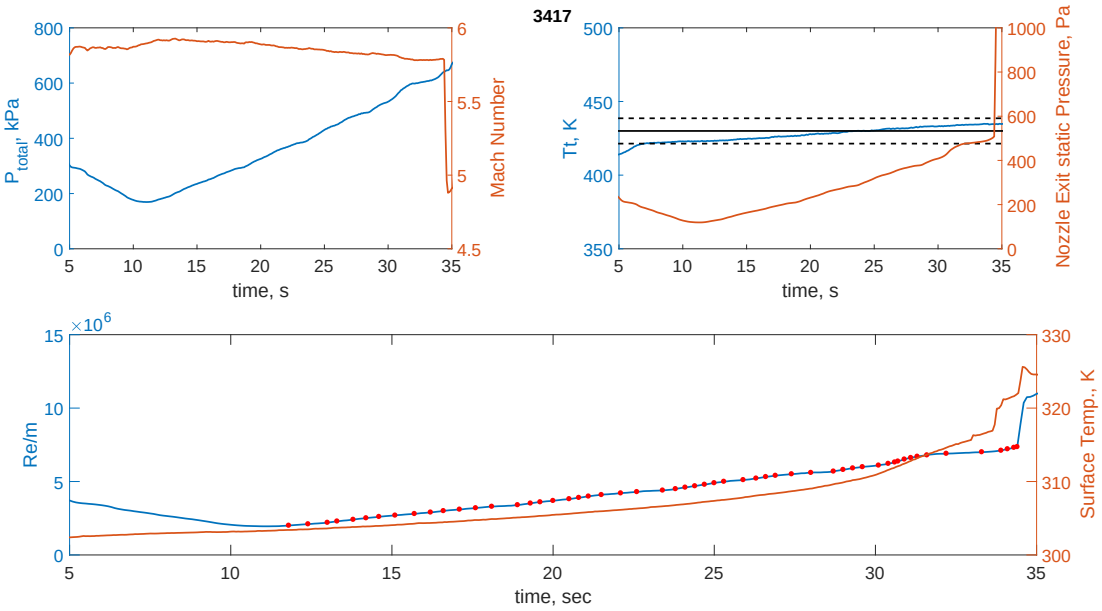

Figure C.13: Run conditions ACE US Station Run 3417.

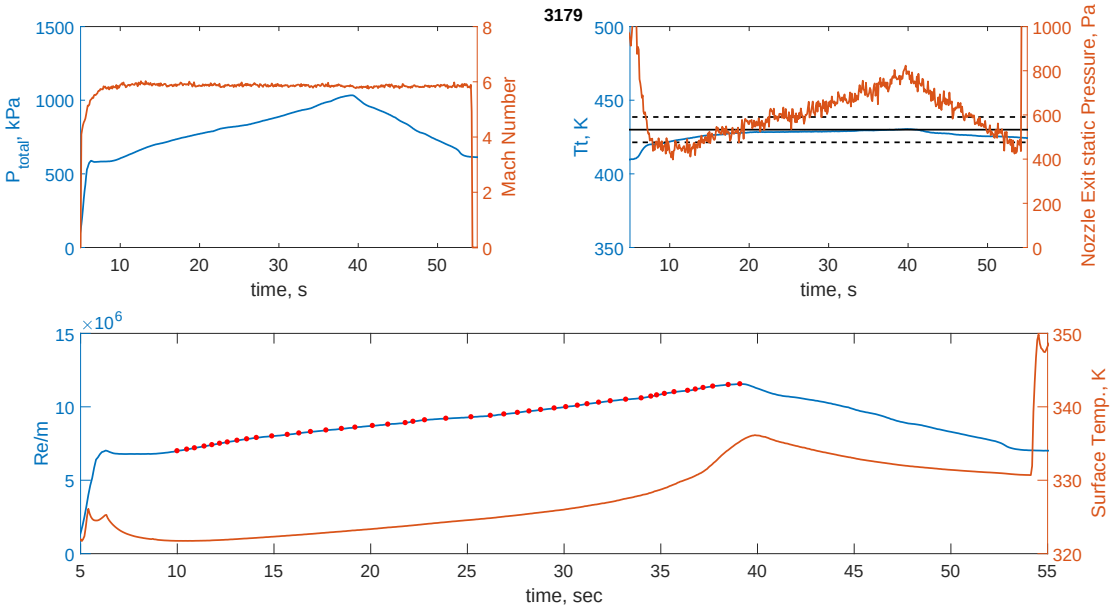

Figure C.14: Run conditions M6QT Run 3179.

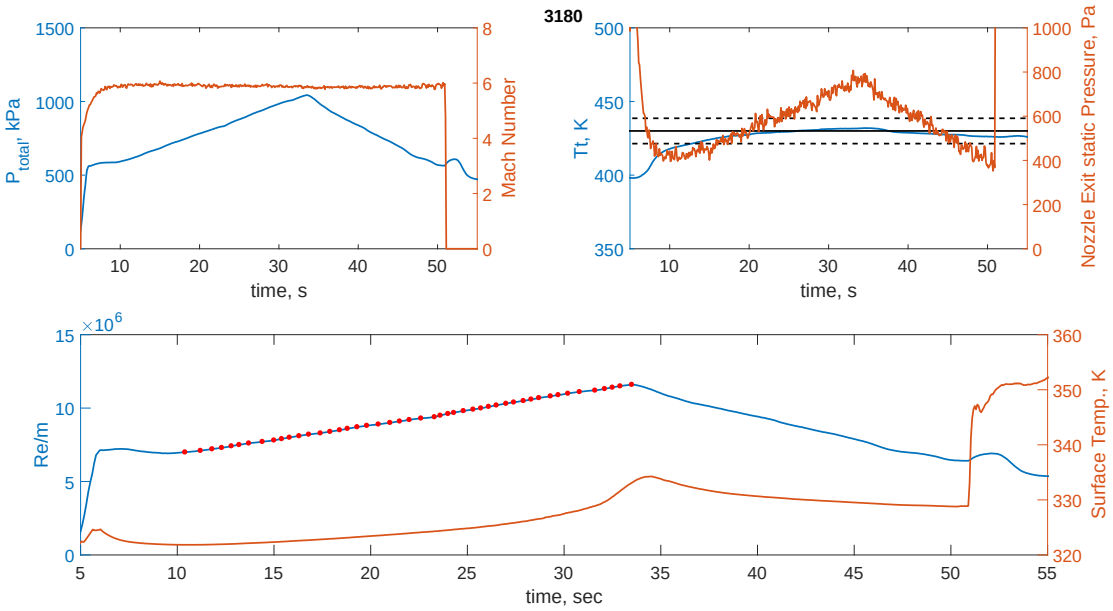

Figure C.15: Run conditions M6QT Run 3180.

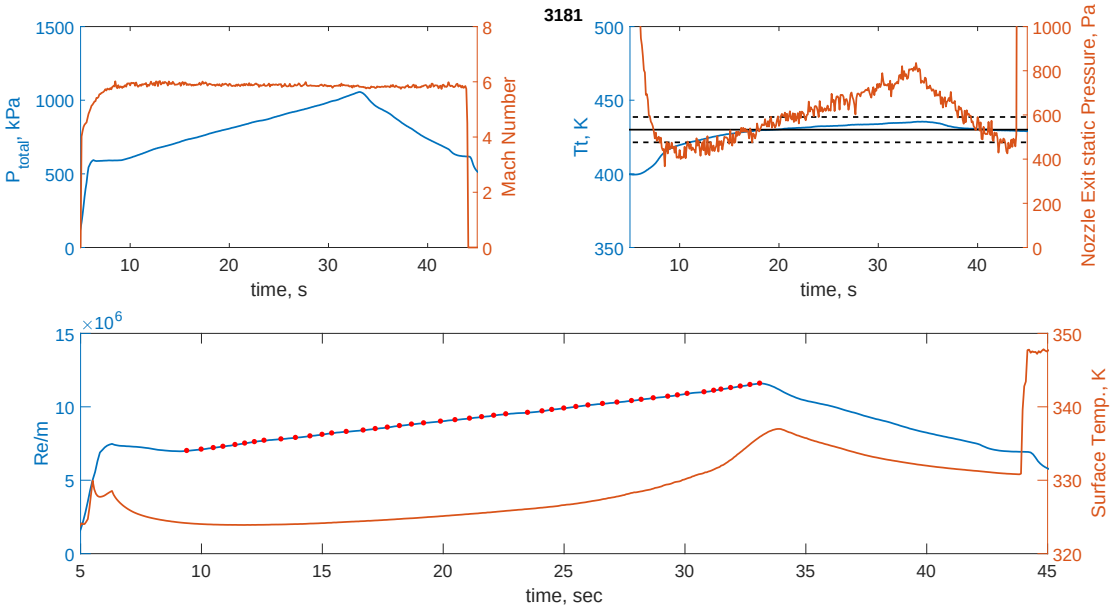

Figure C.16: Run conditions M6QT Run 3181.

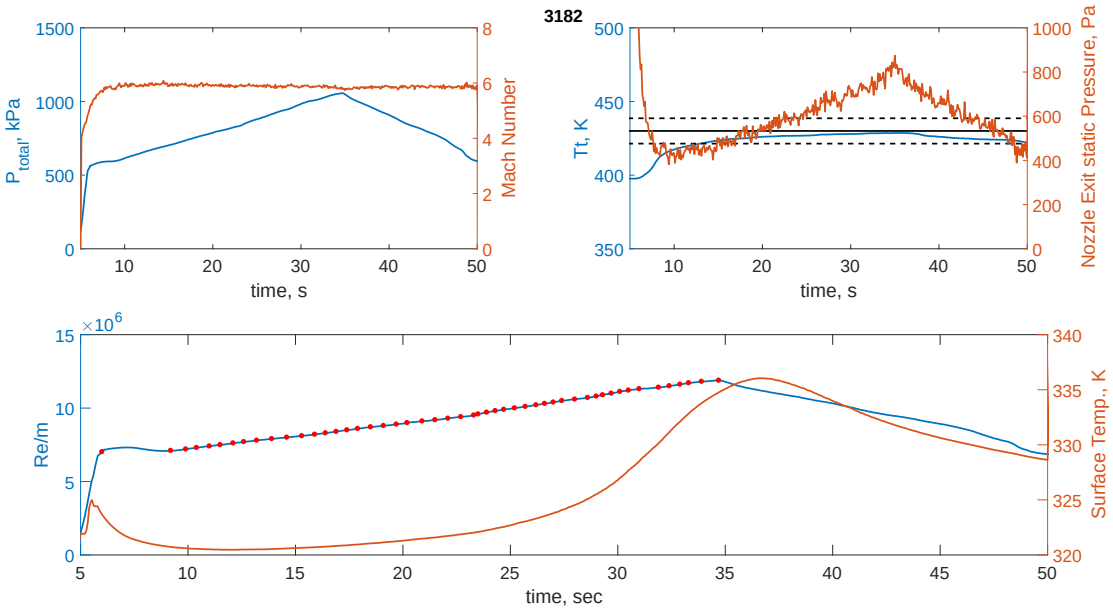

Figure C.17: Run conditions M6QT Run 3182.

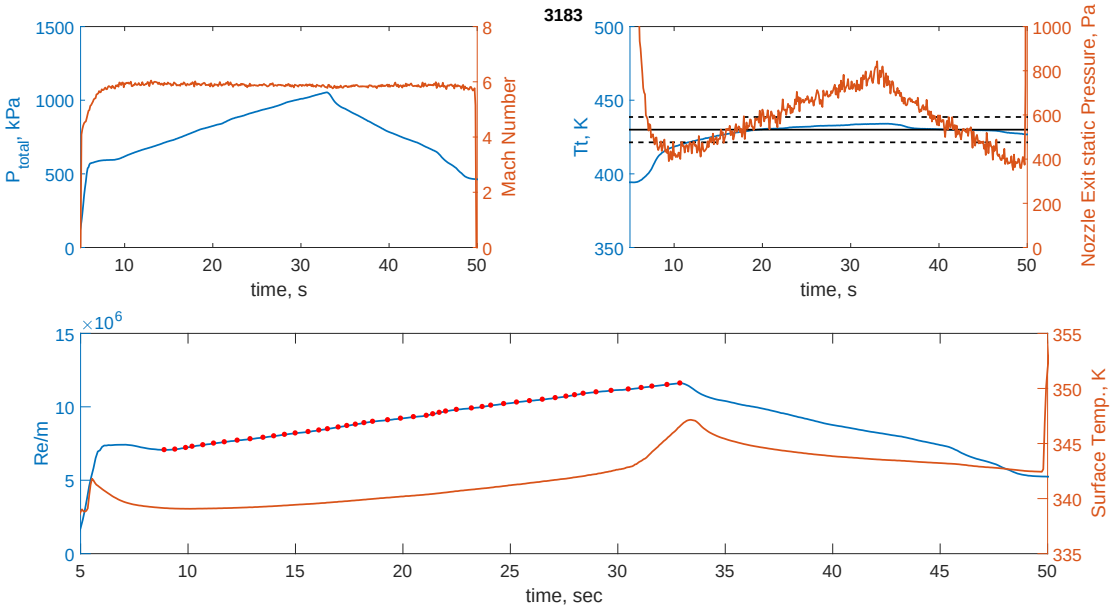

Figure C.18: Run conditions M6QT Run 3183.

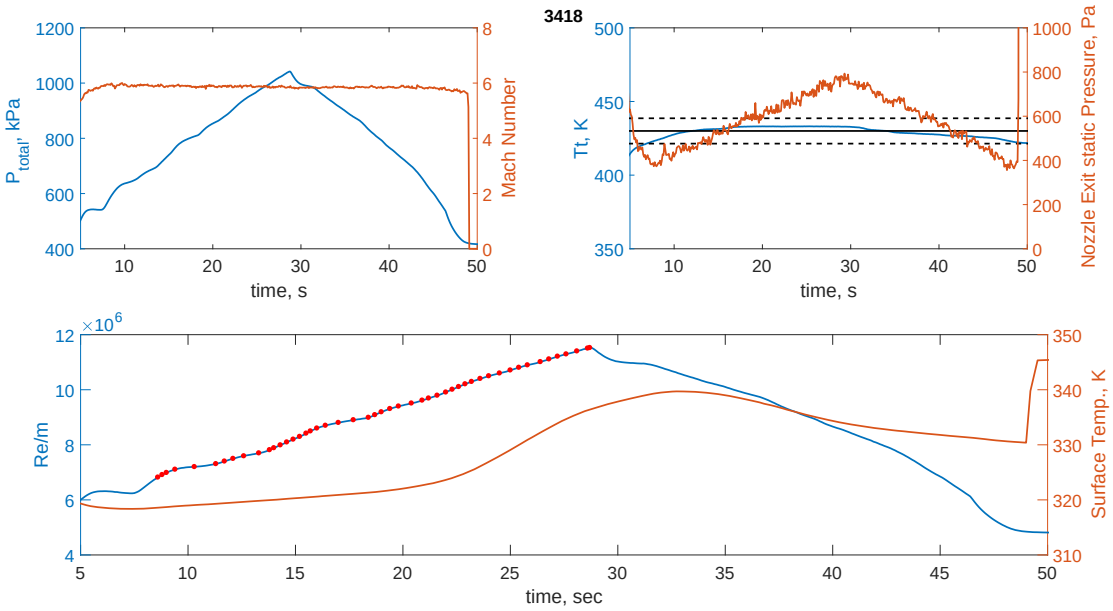

Figure C.19: Run conditions M6QT Run 3418.

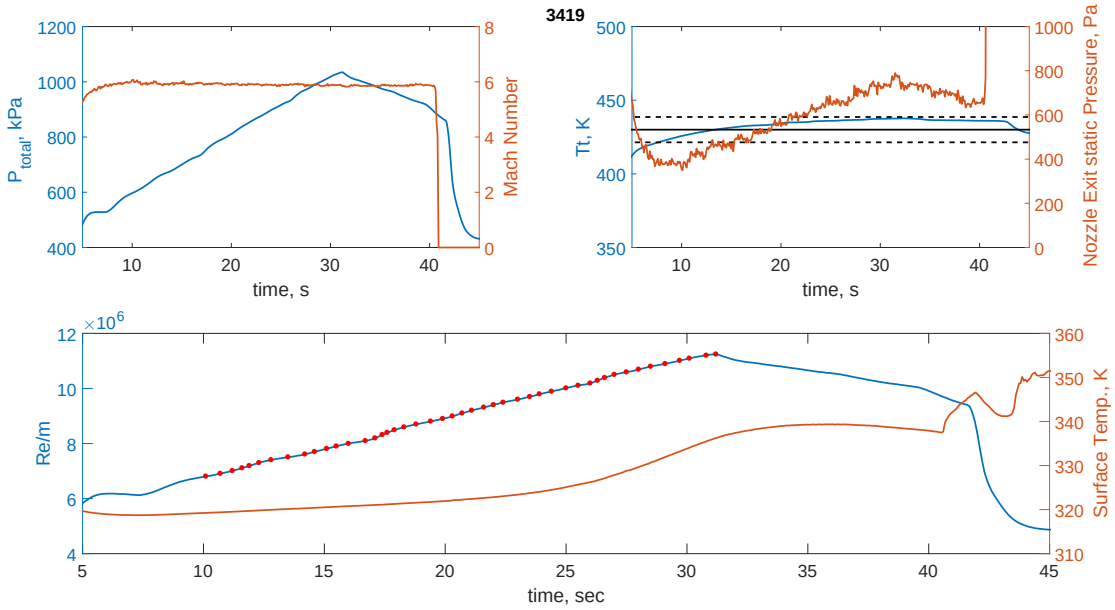

Figure C.20: Run conditions M6QT Run 3419.

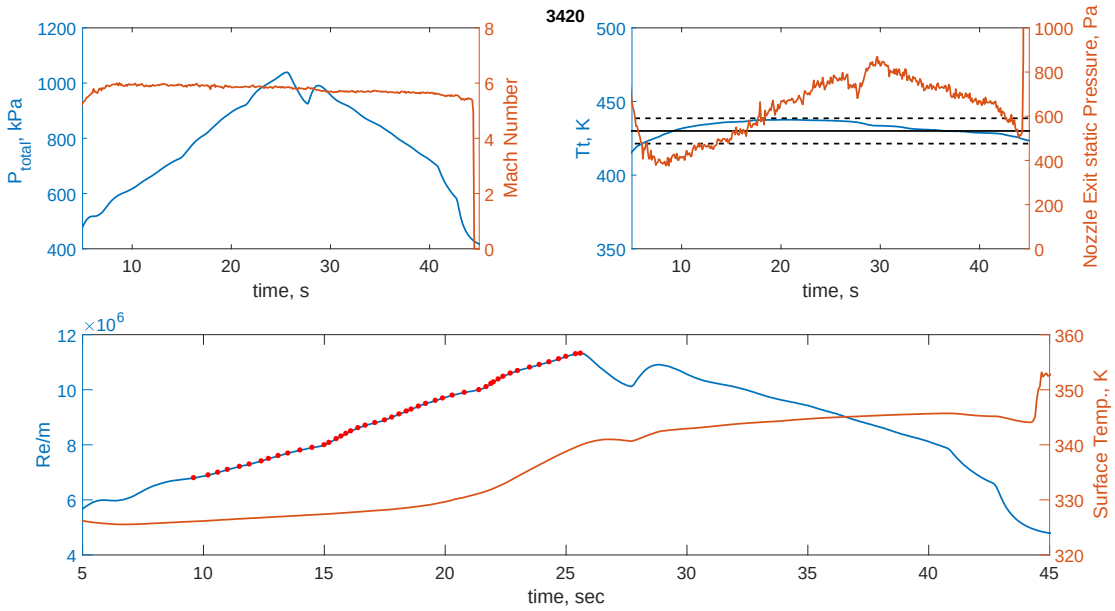

Figure C.21: Run conditions M6QT Run 3420.

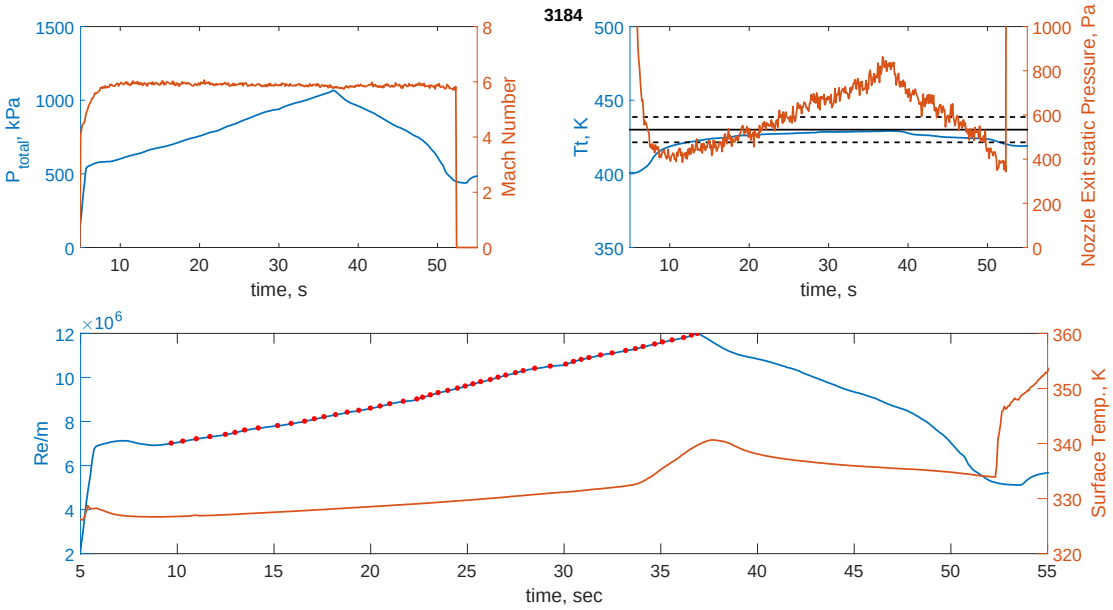

Figure C.22: Run conditions M6QT Run 3184.

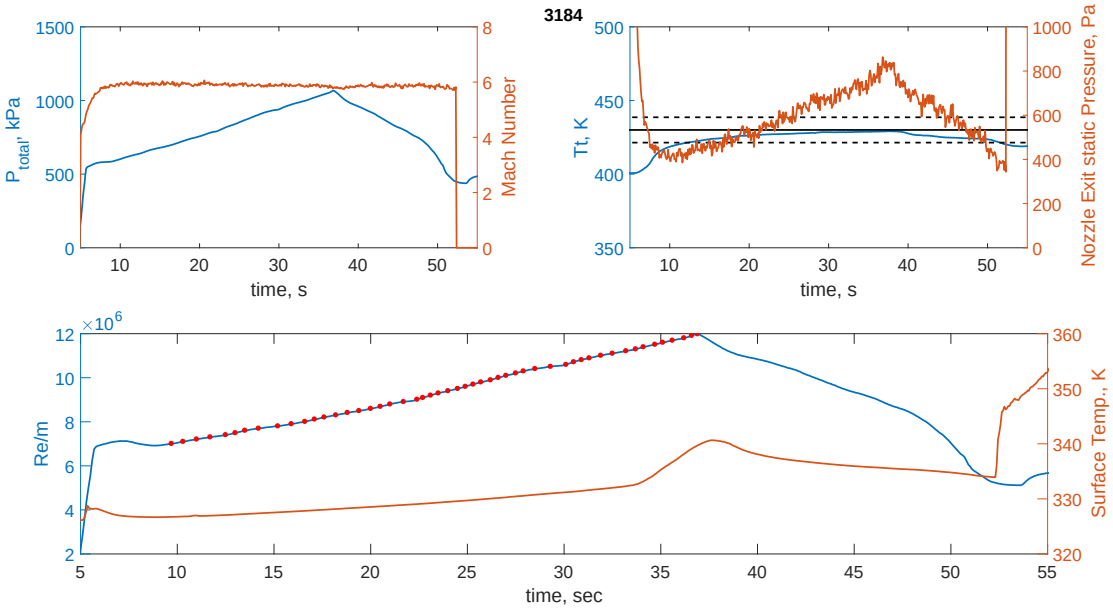

Figure C.23: Run conditions M6QT Run 3315 Noisy.

APPENDIX D

RESULTS GALLERY

This appendix contains IR and pressure transducer data for all instrumented runs conducted in addition to the runs highlighted in the main text. Pressure fluctuation spectra are given as PSD line plots. This appendix helps underscore the breadth of the data obtained. It also provides an example of the repeatability observed between runs. In both facilities the runs show good repeatability both in the extent and magnitude of Stanton number and the frequencies and amplitudes of the power spectra. In the M6QT due to the difficulty in model alignment, more run to run variation is observed. This is due to minor ($< 1°$) variations in the model's yaw. The data of Borg & Kimmel (2017*b*) and IR results of the intentional $1°$ yaw of run 3184 demonstrate the high sensitivity of the flow field to yaw angle.

D.1 Stanton Number Maps & Pressure Transducer Data

Stanton number maps for Re spanning the conditions tested are presented in Fig. D.1-D.22. PSDs of fluctuating pressure for each transducer for all runs are shown in Fig. D.23-D.43.

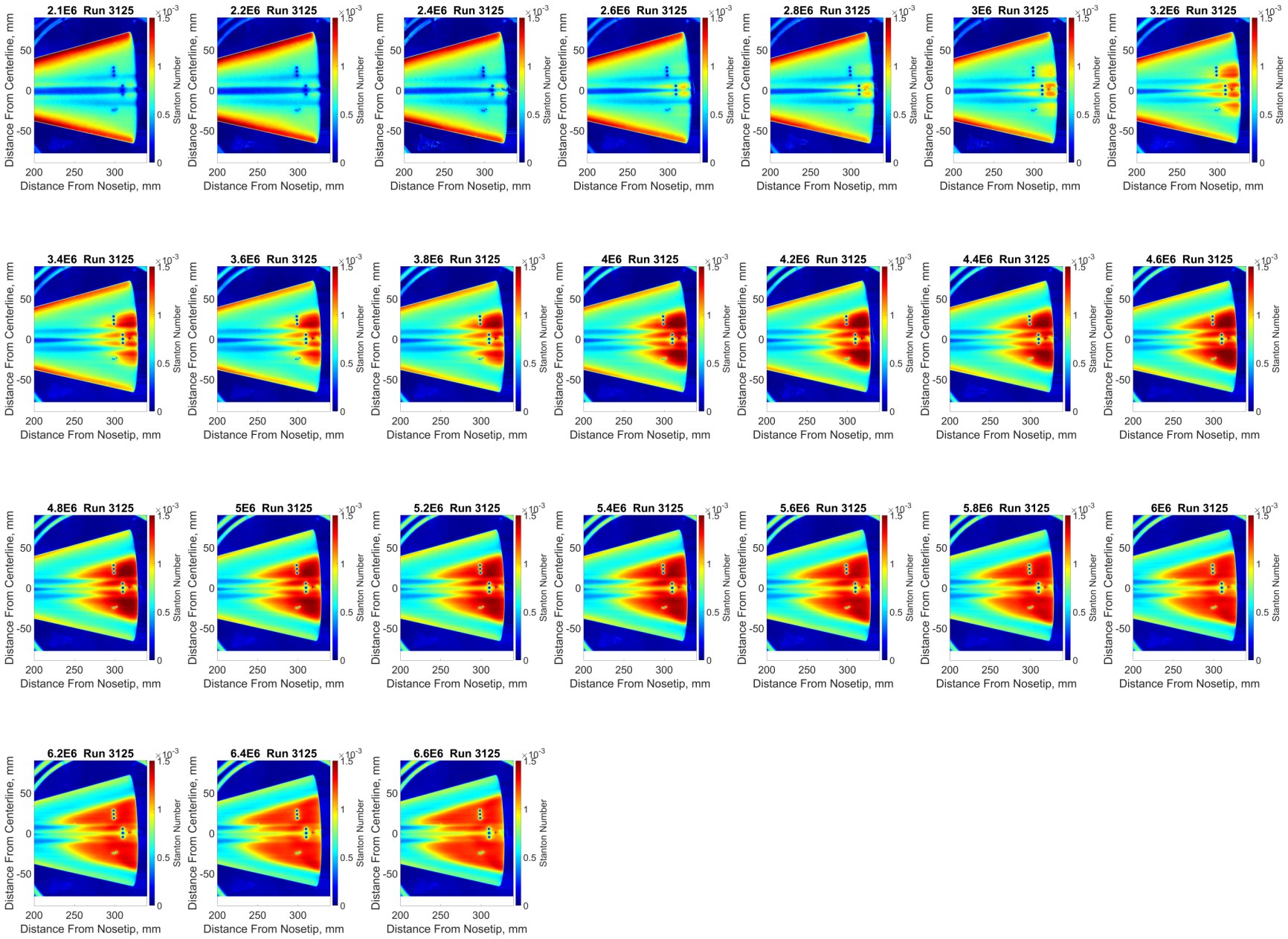

Figure D.1: St maps: ACE DS Station Run 3125.

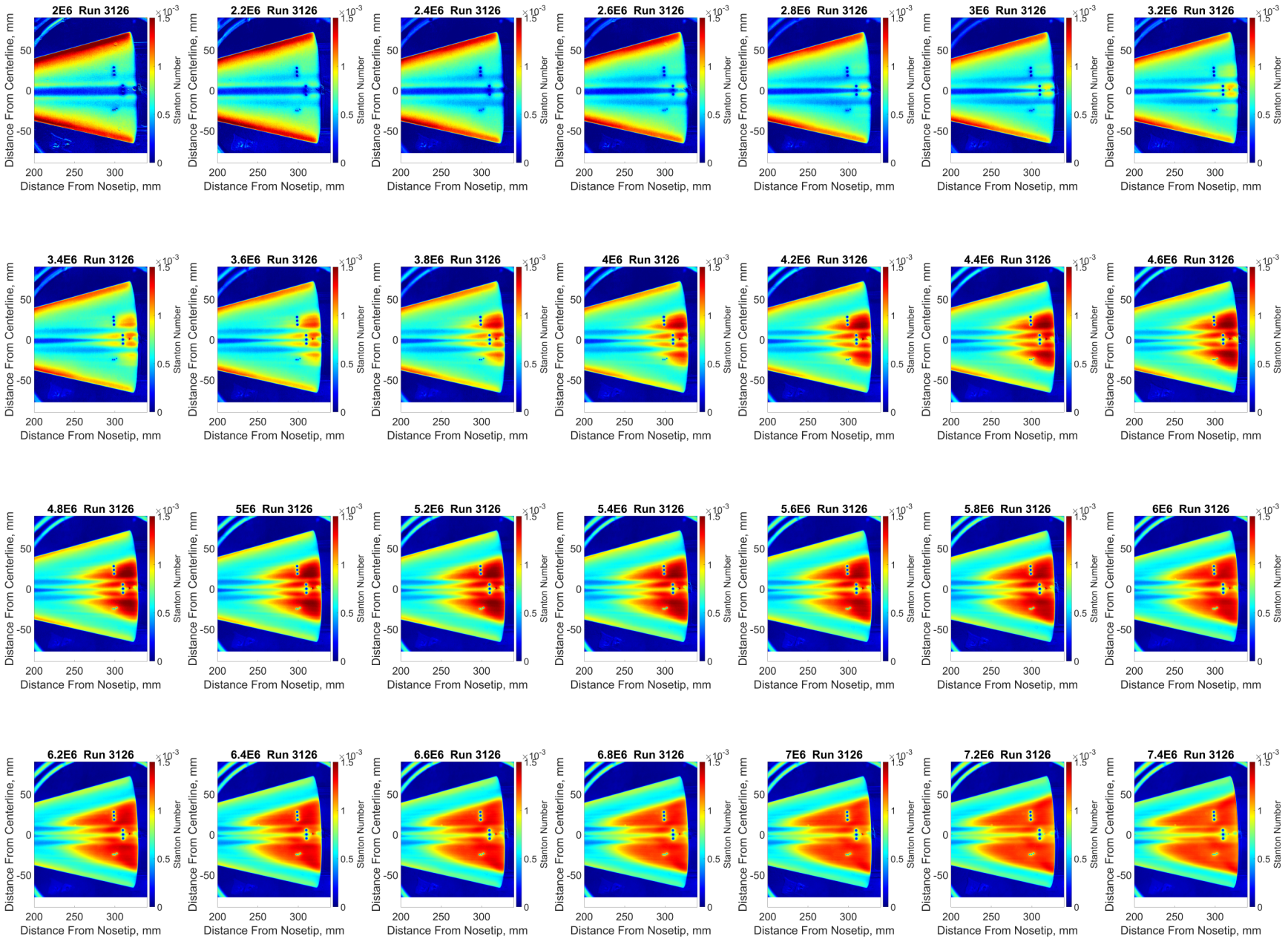

Figure D.2: St maps: ACE DS Station Run 3126.

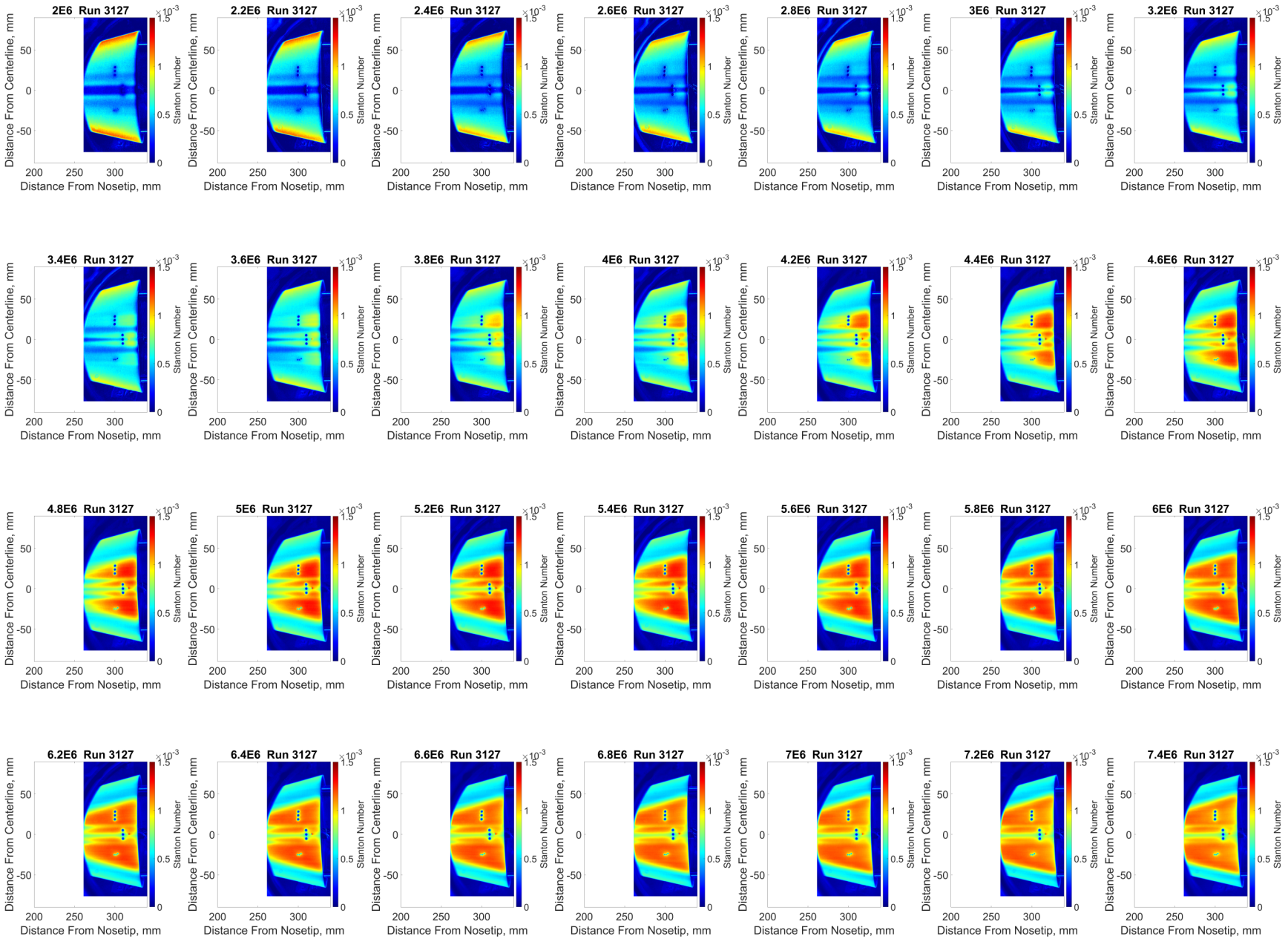

Figure D.3: St maps: ACE MID Station Run 3127.

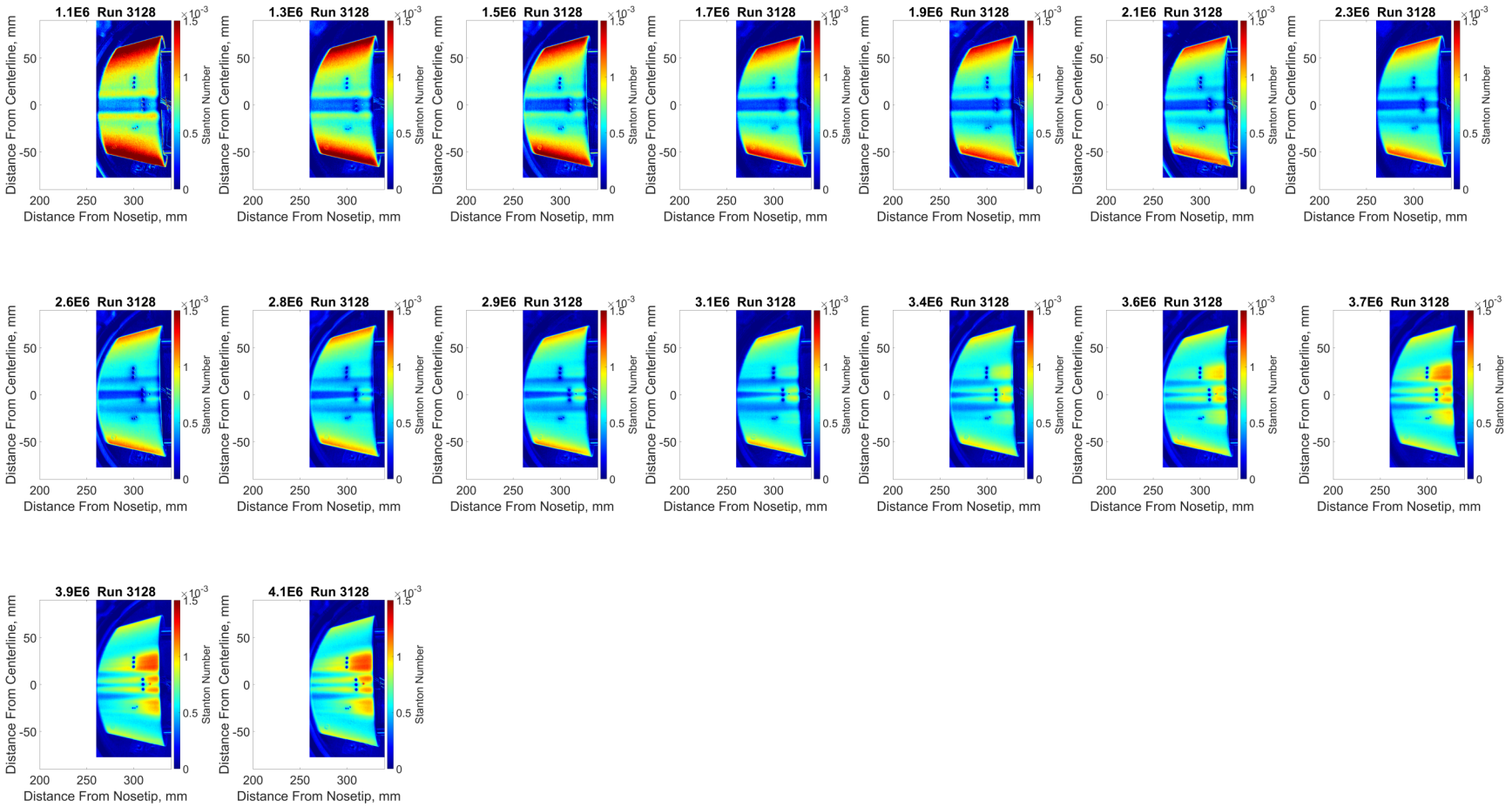

Figure D.4: St maps: ACE MID Station Run 3128.

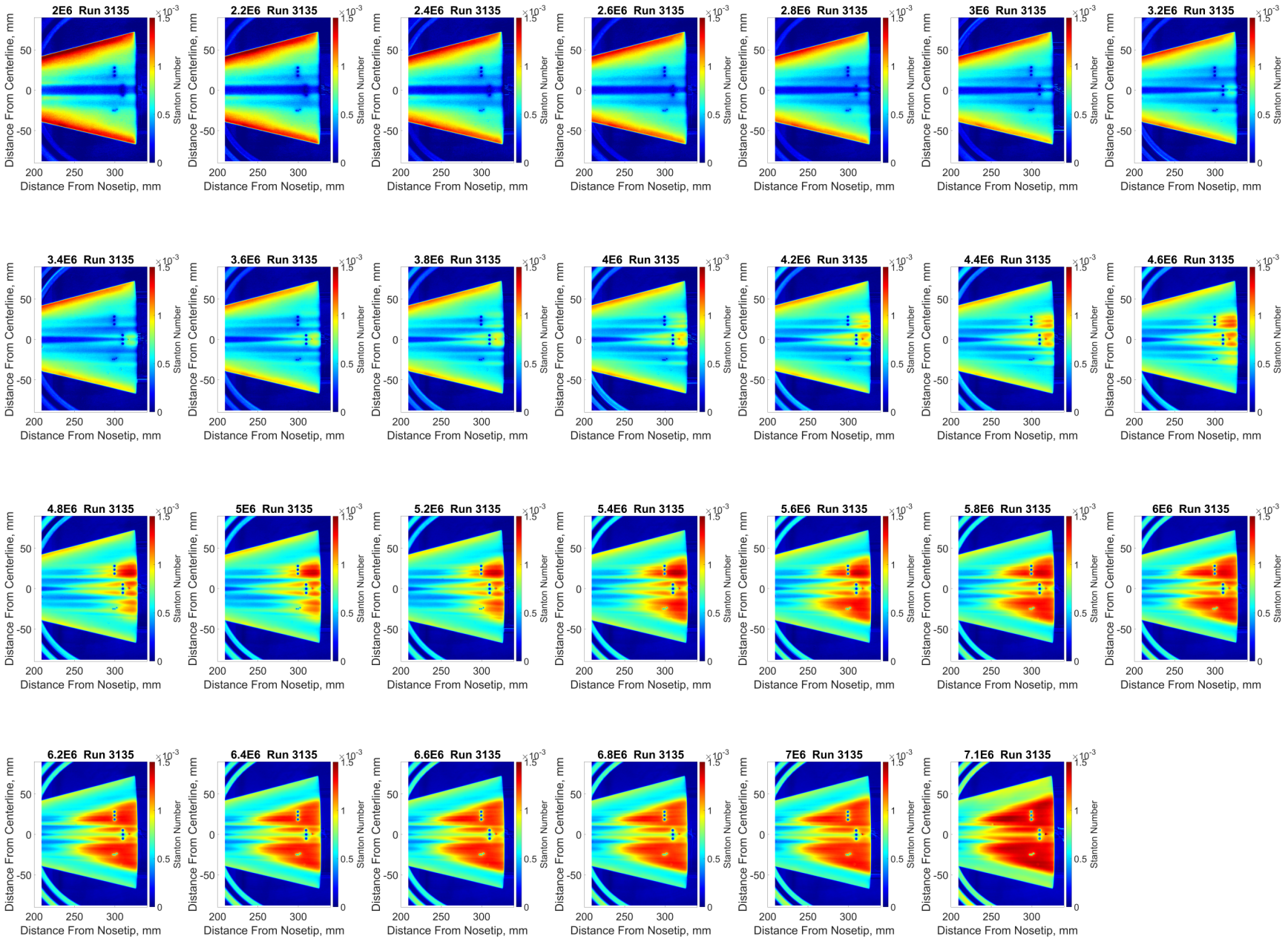

Figure D.5: St maps: ACE US Station Run 3135.

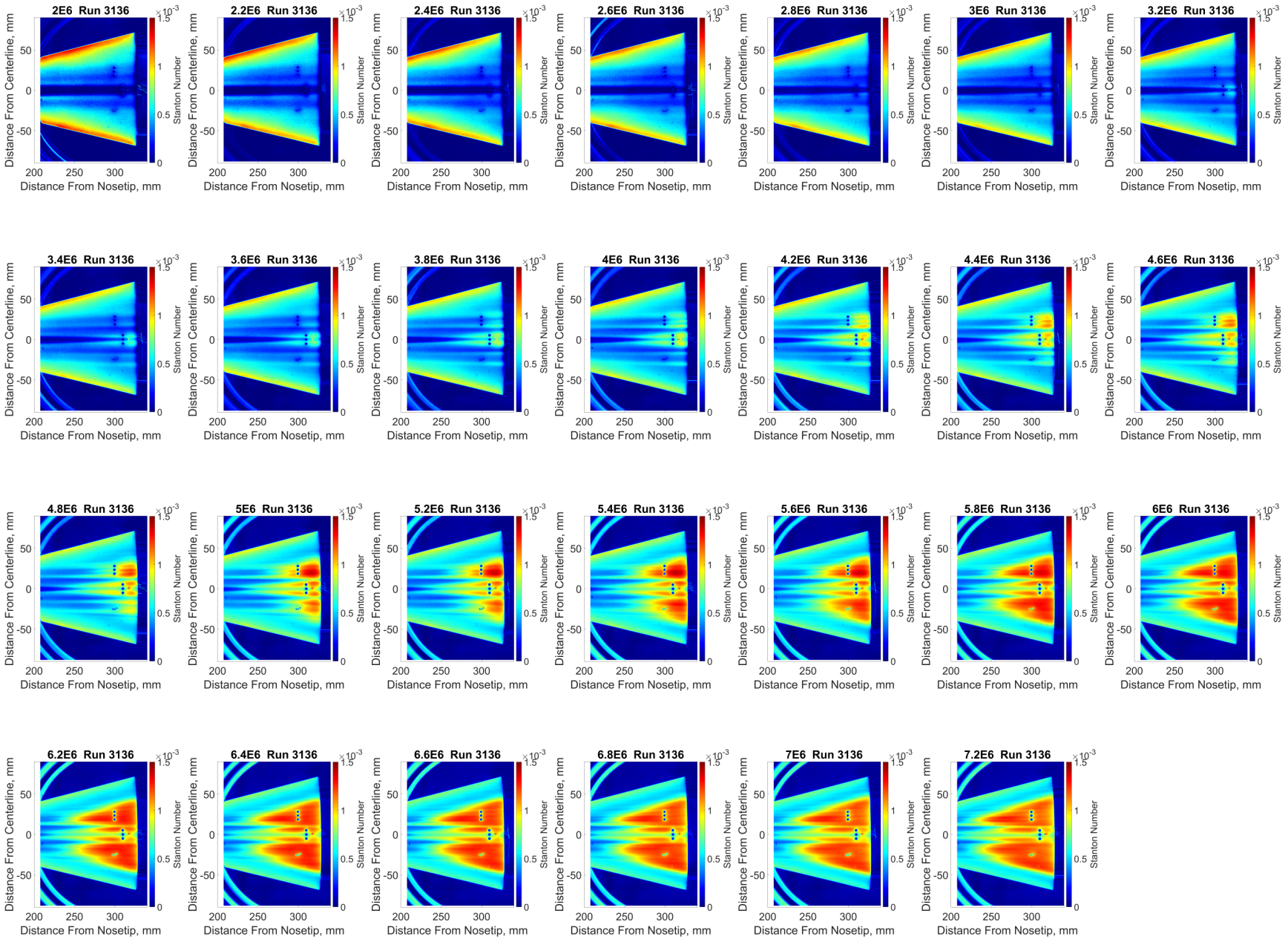

Figure D.6: St maps: ACE US Station Run 3136.

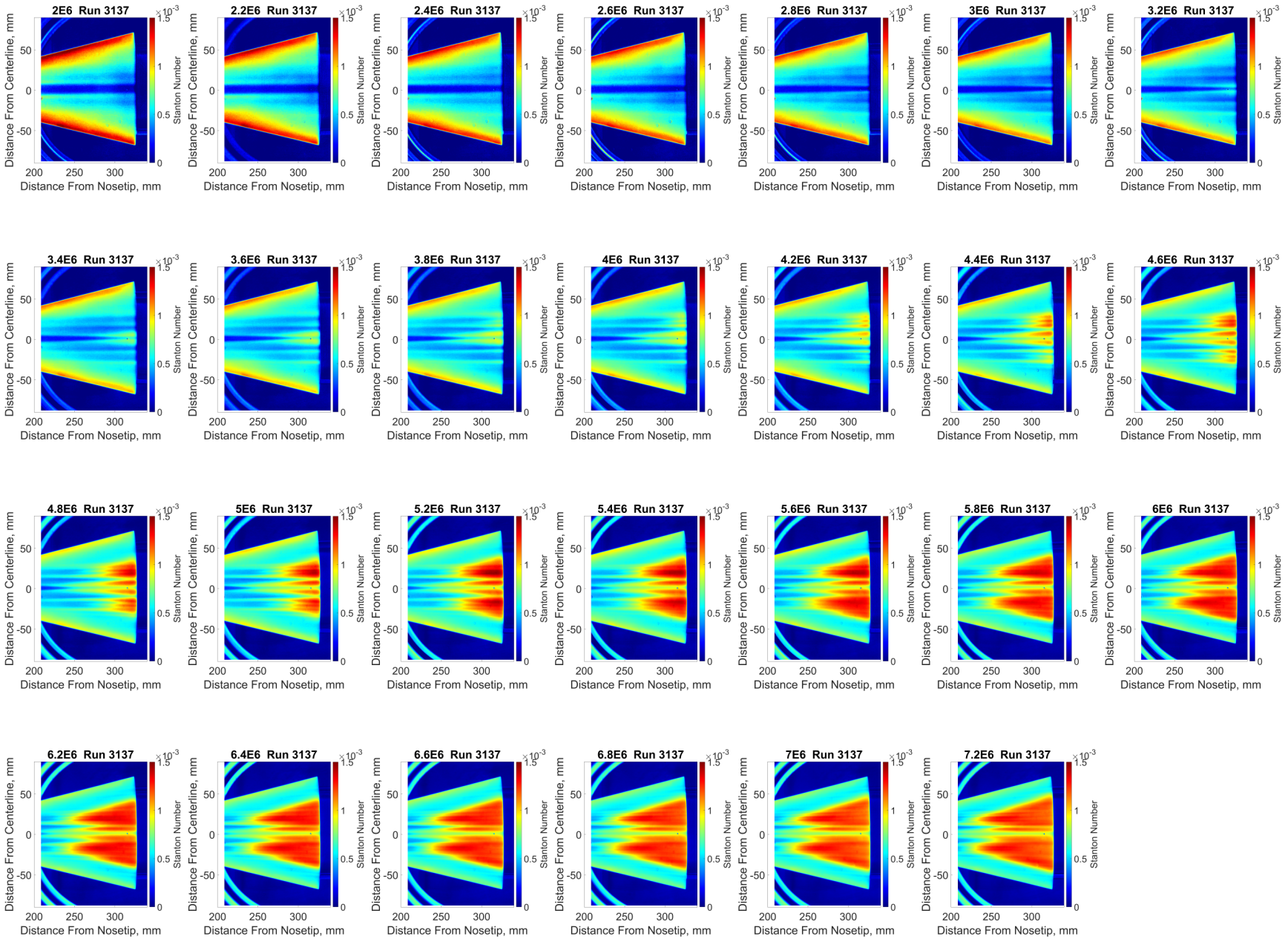

Figure D.7: St maps: ACE US Station Run 3137.

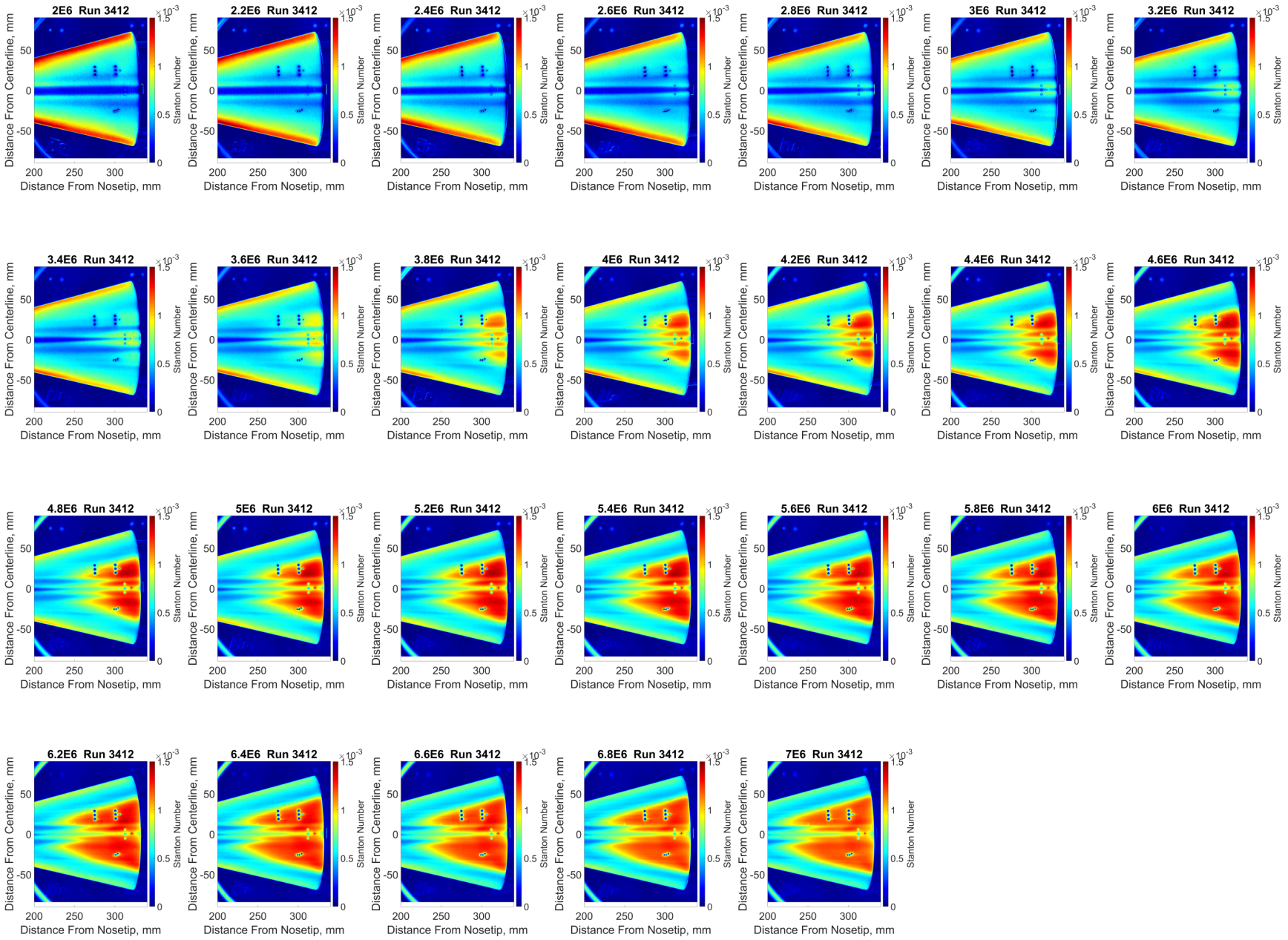

Figure D.8: St maps: ACE DS Station Run 3412.

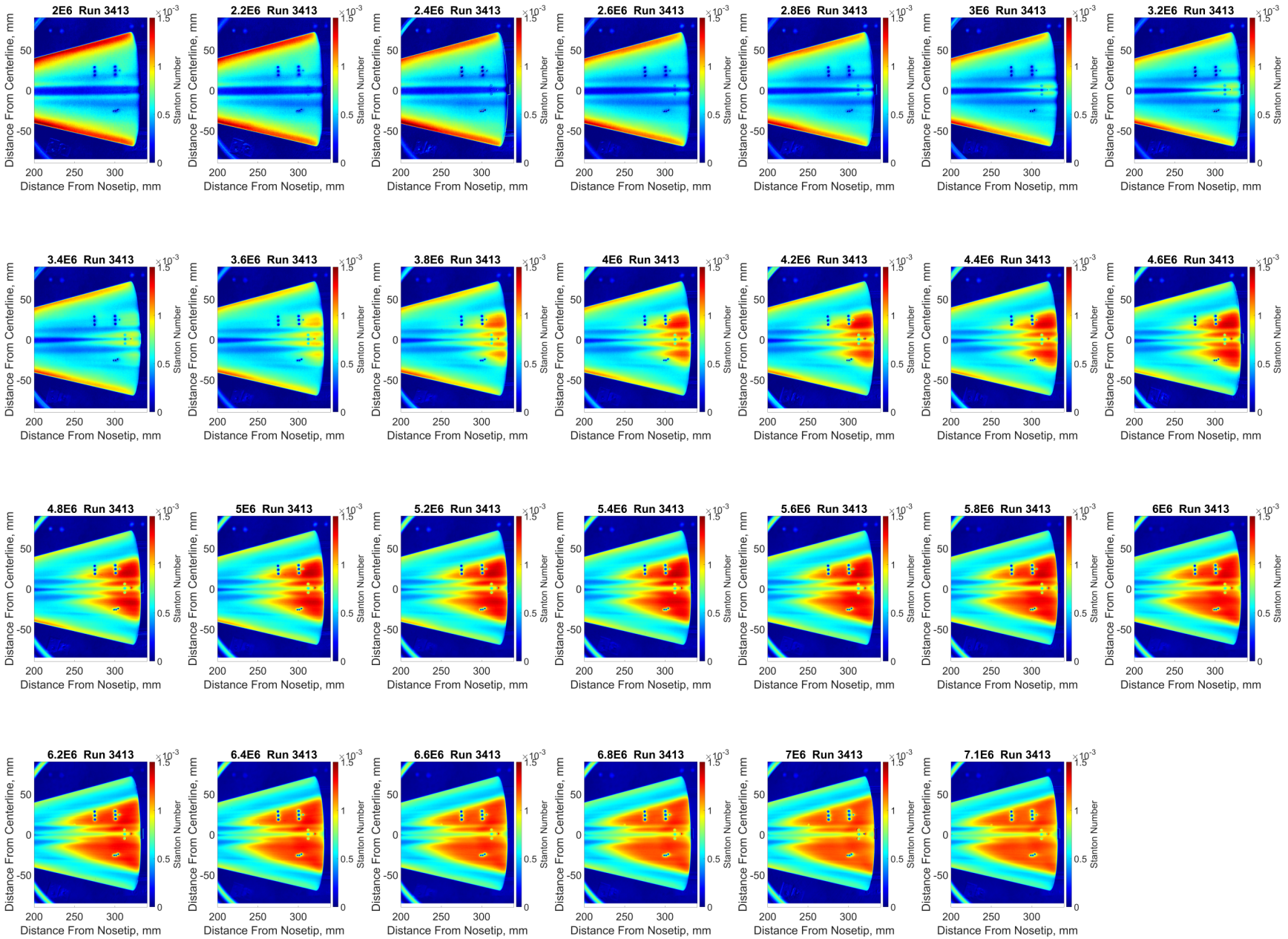

Figure D.9: St maps: ACE DS Station Run 3413.

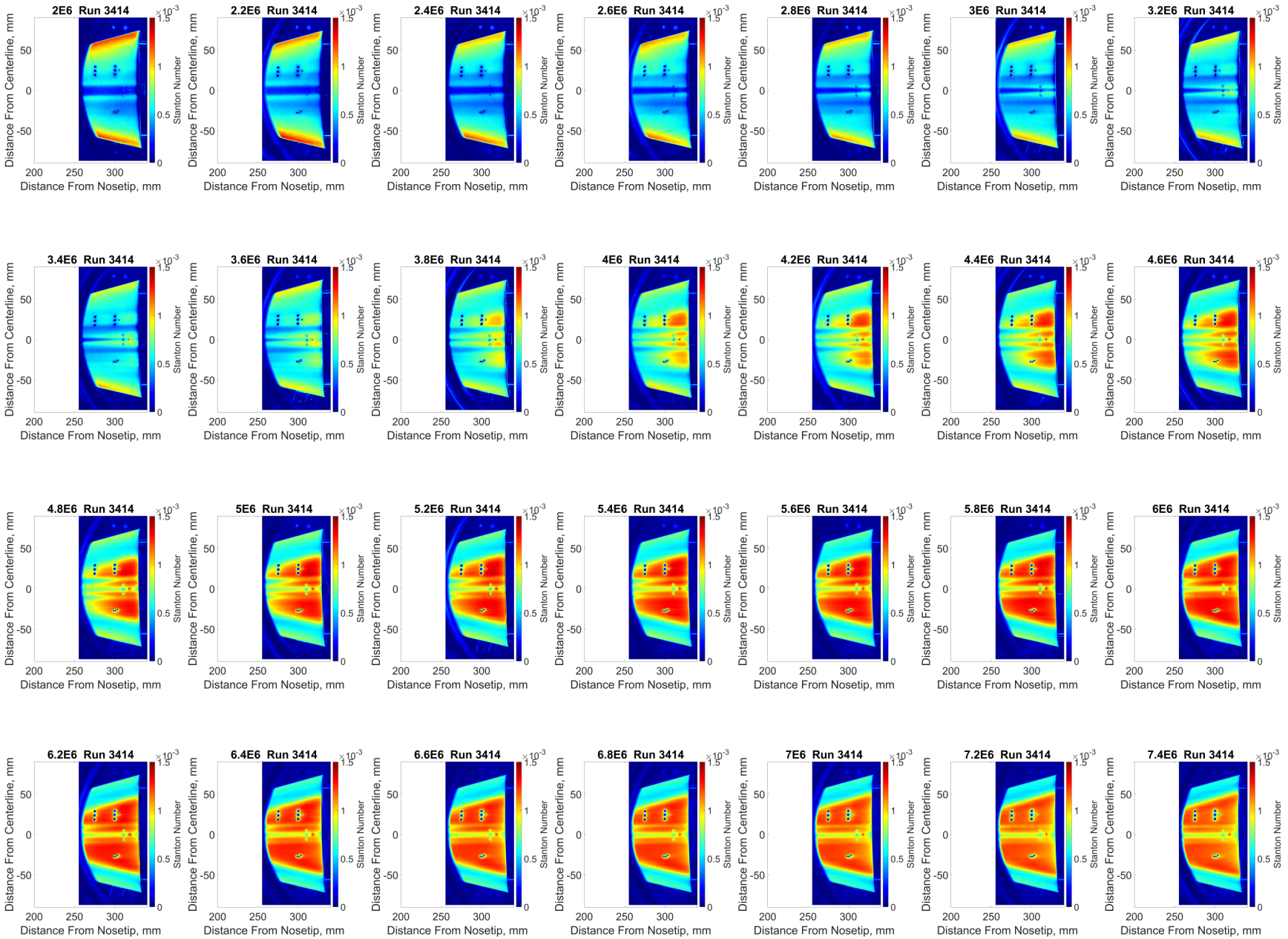

Figure D.10: St maps: ACE MID Station Run 3414.

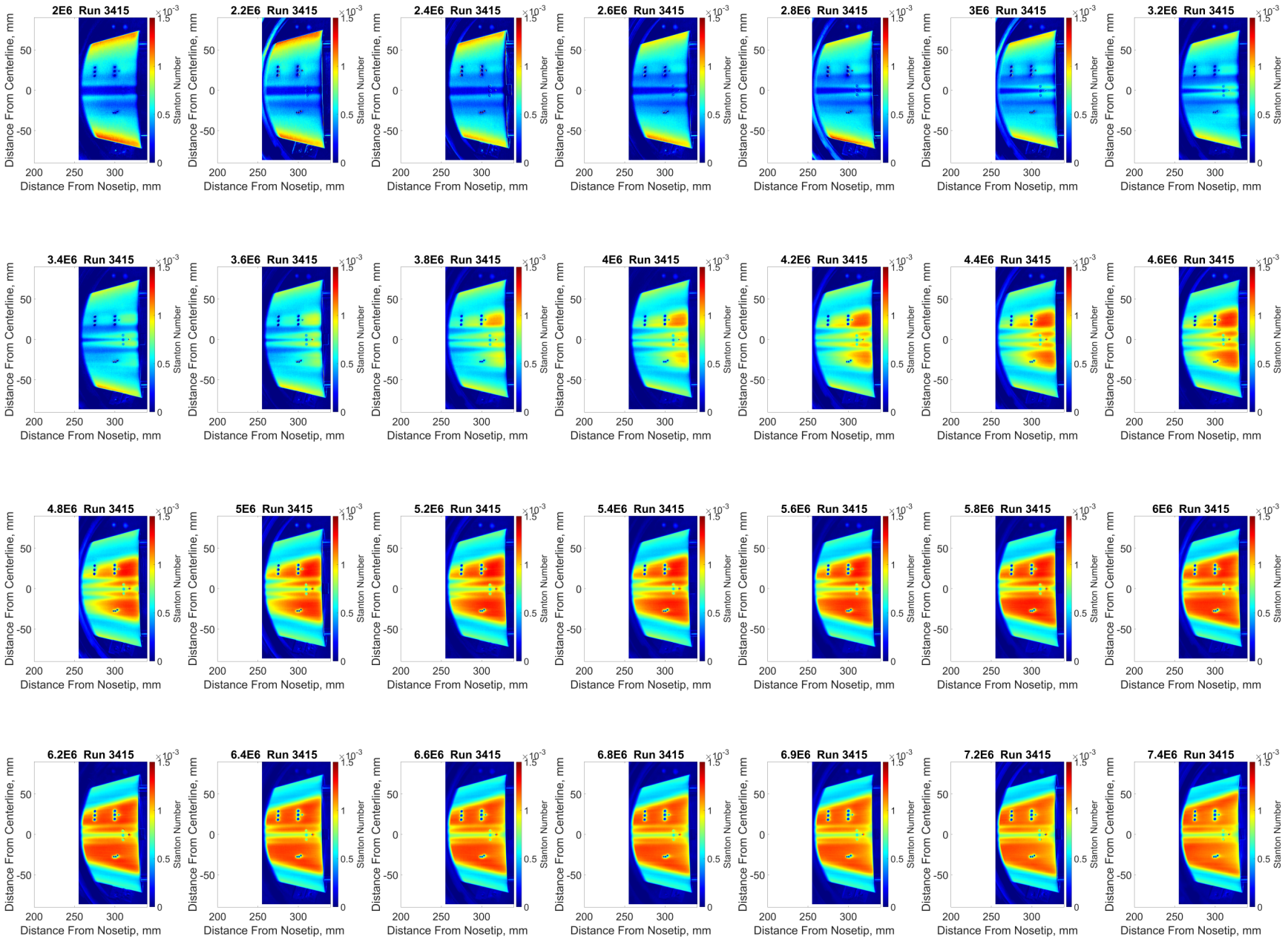

Figure D.11: St maps: ACE MID Station Run 3415.

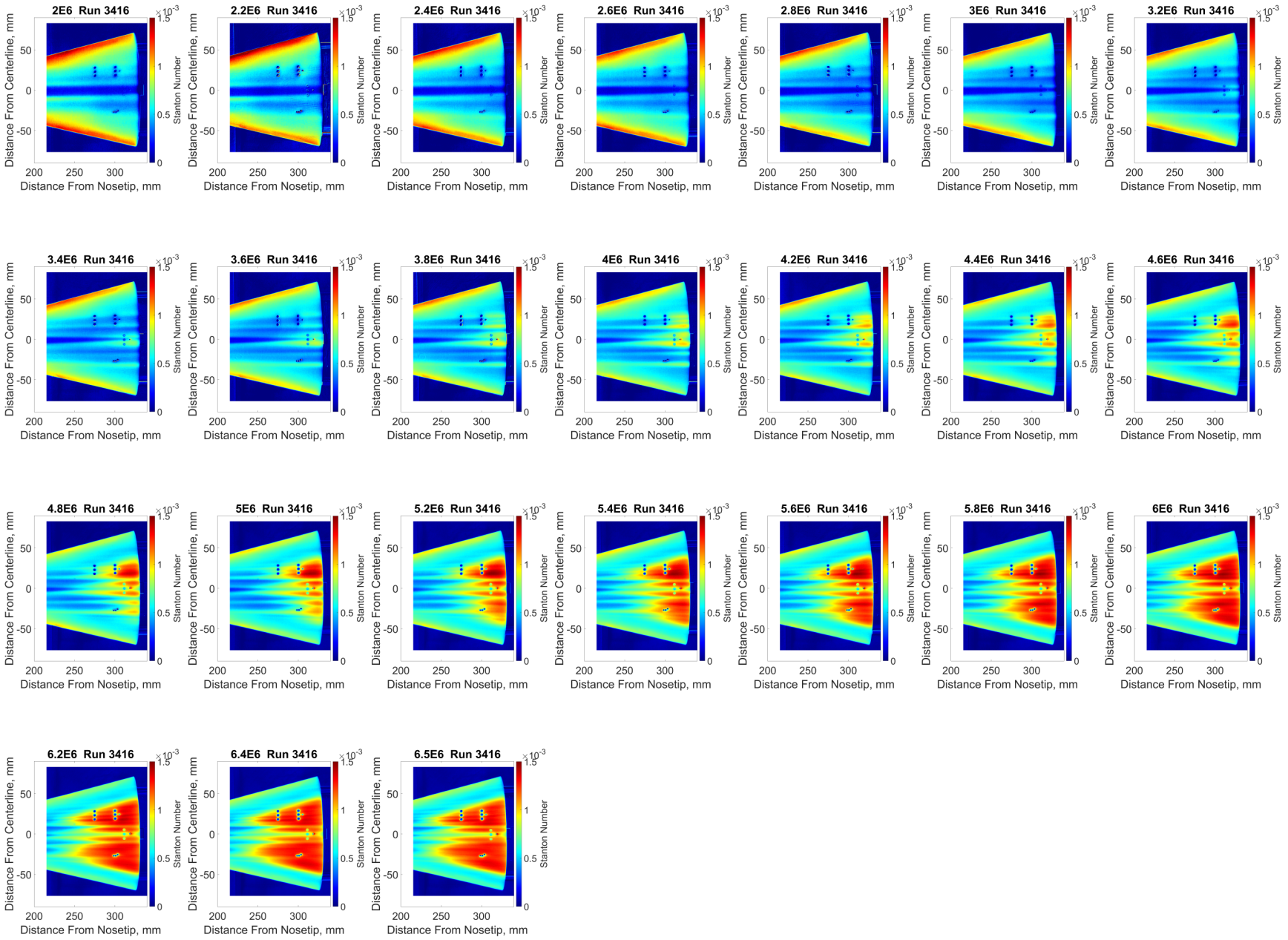

Figure D.12: St maps: ACE US Station Run 3416.

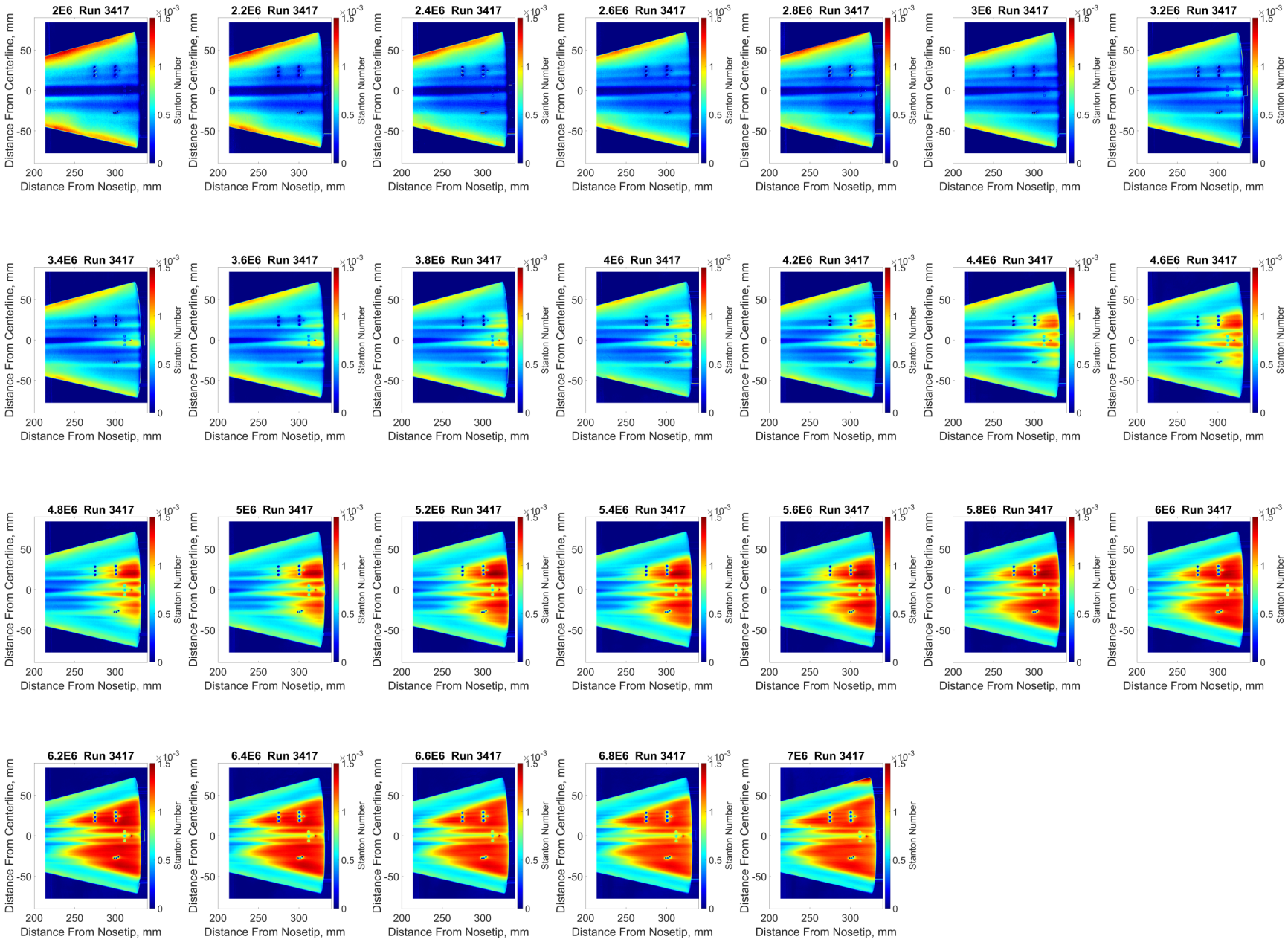

Figure D.13: St maps: ACE US Station Run 3417.

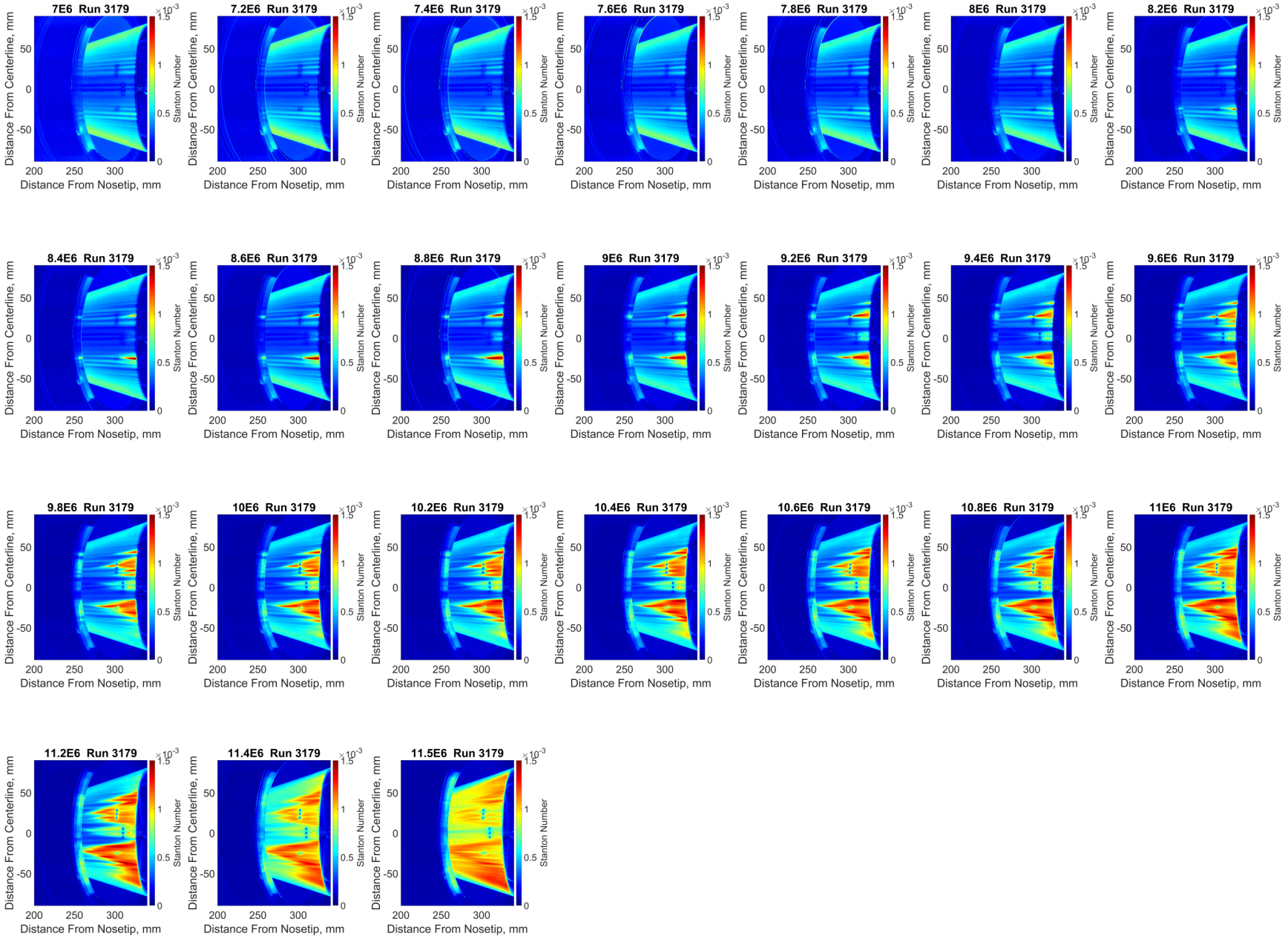

Figure D.14: St maps: M6QT Run 3179

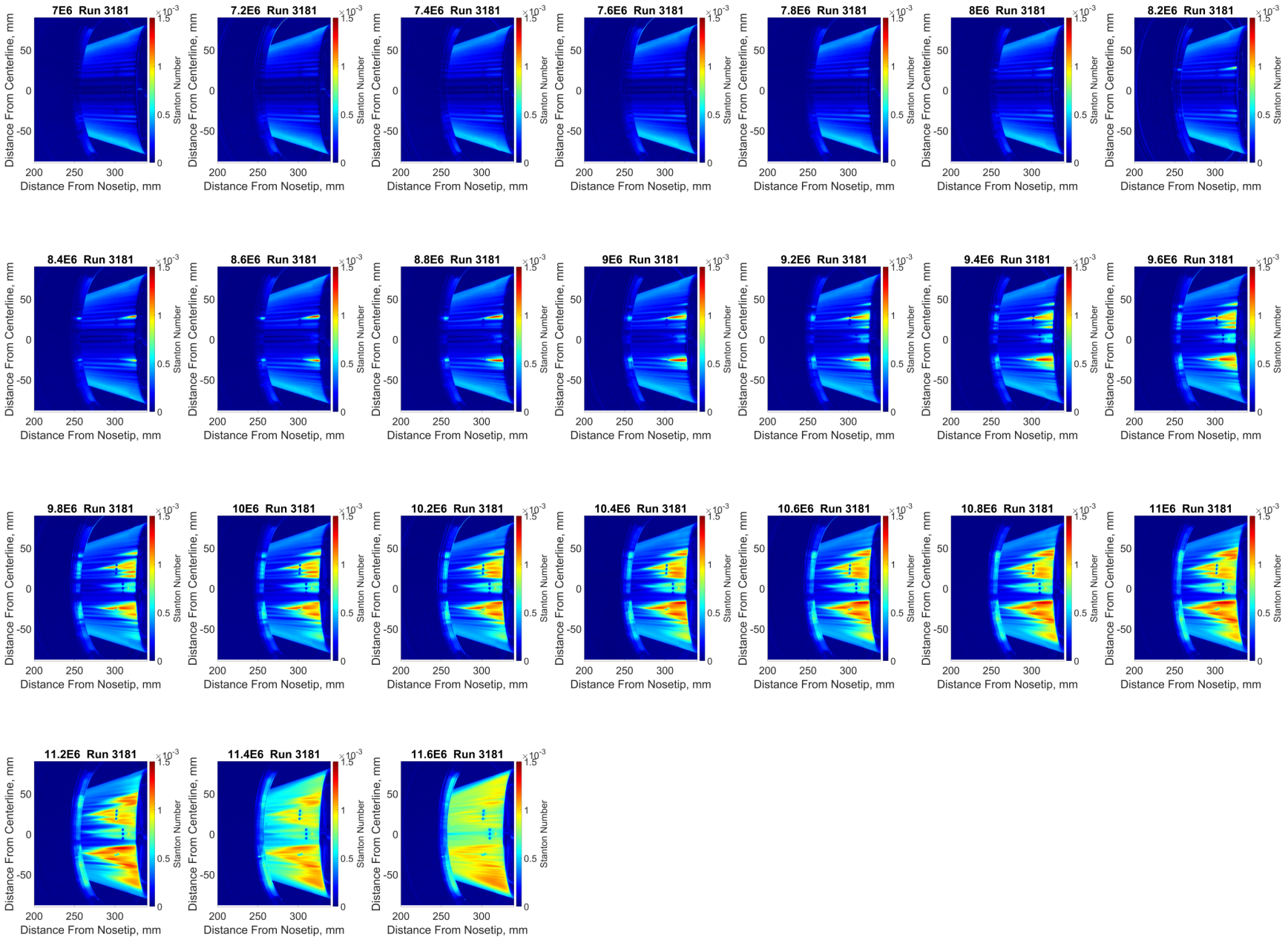

Figure D.15: St maps: M6QT Run 3181.

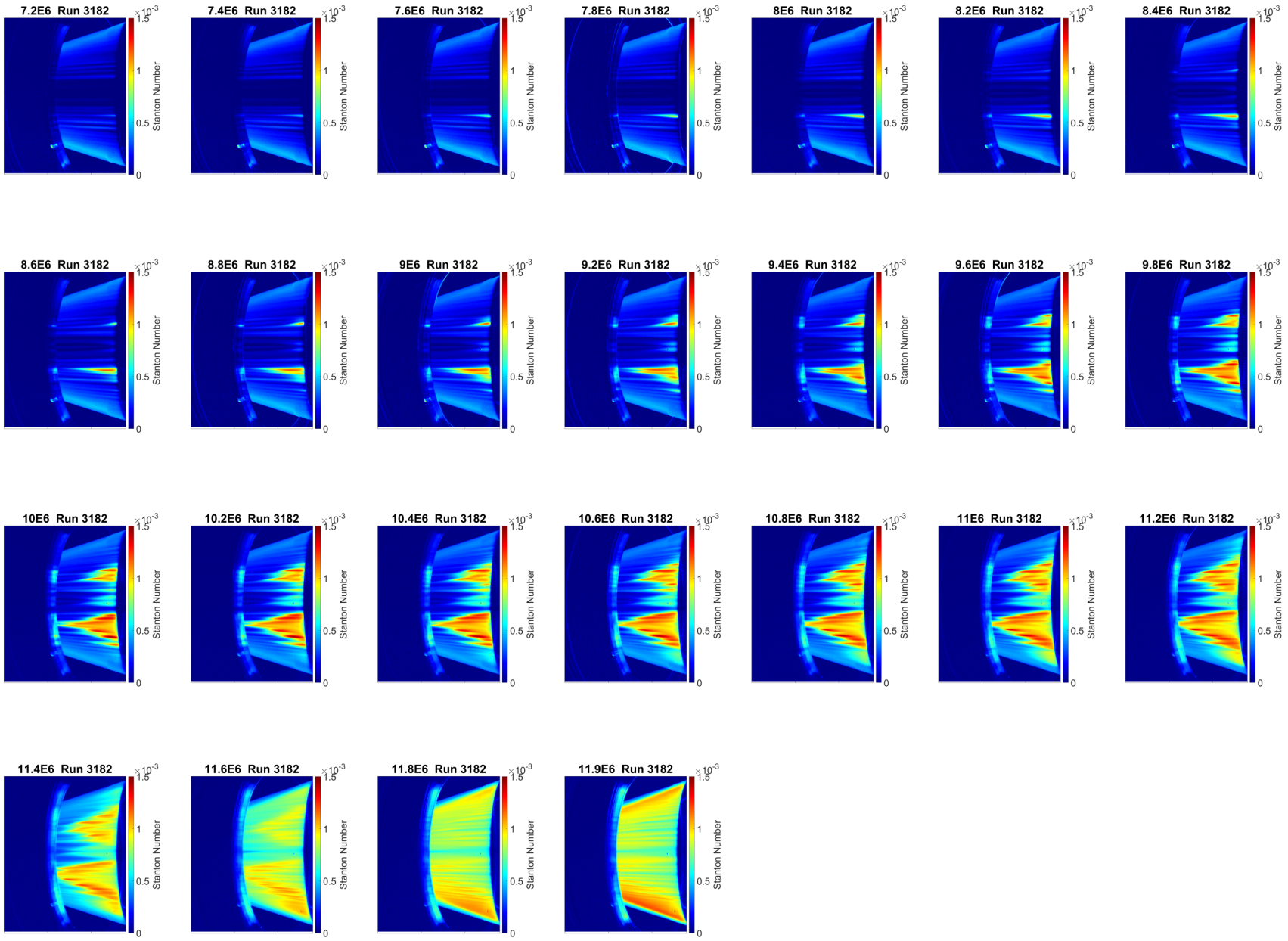

Figure D.16: St maps: M6QT Run 3182.

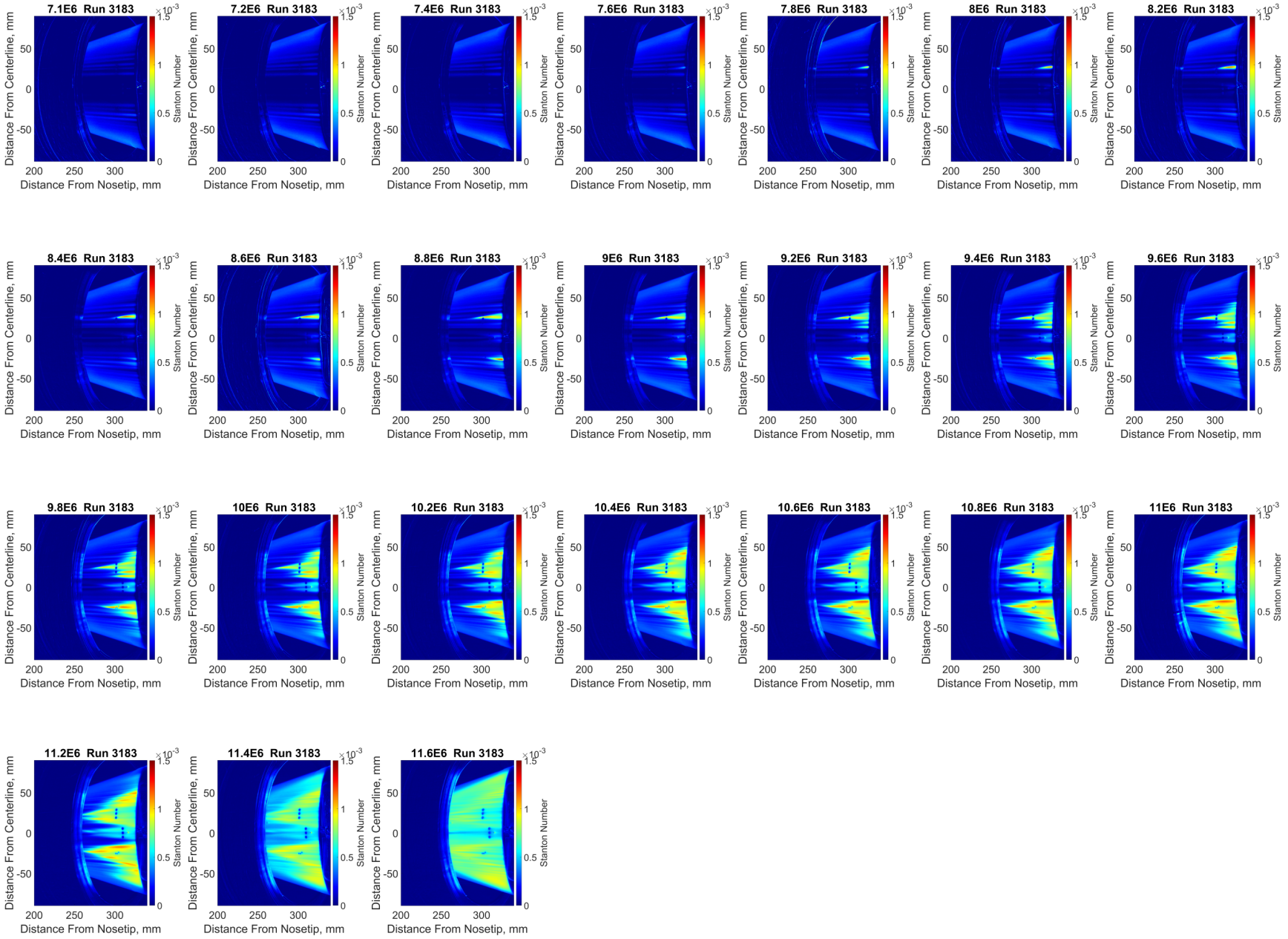

Figure D.17: St maps: M6QT Run 3183.

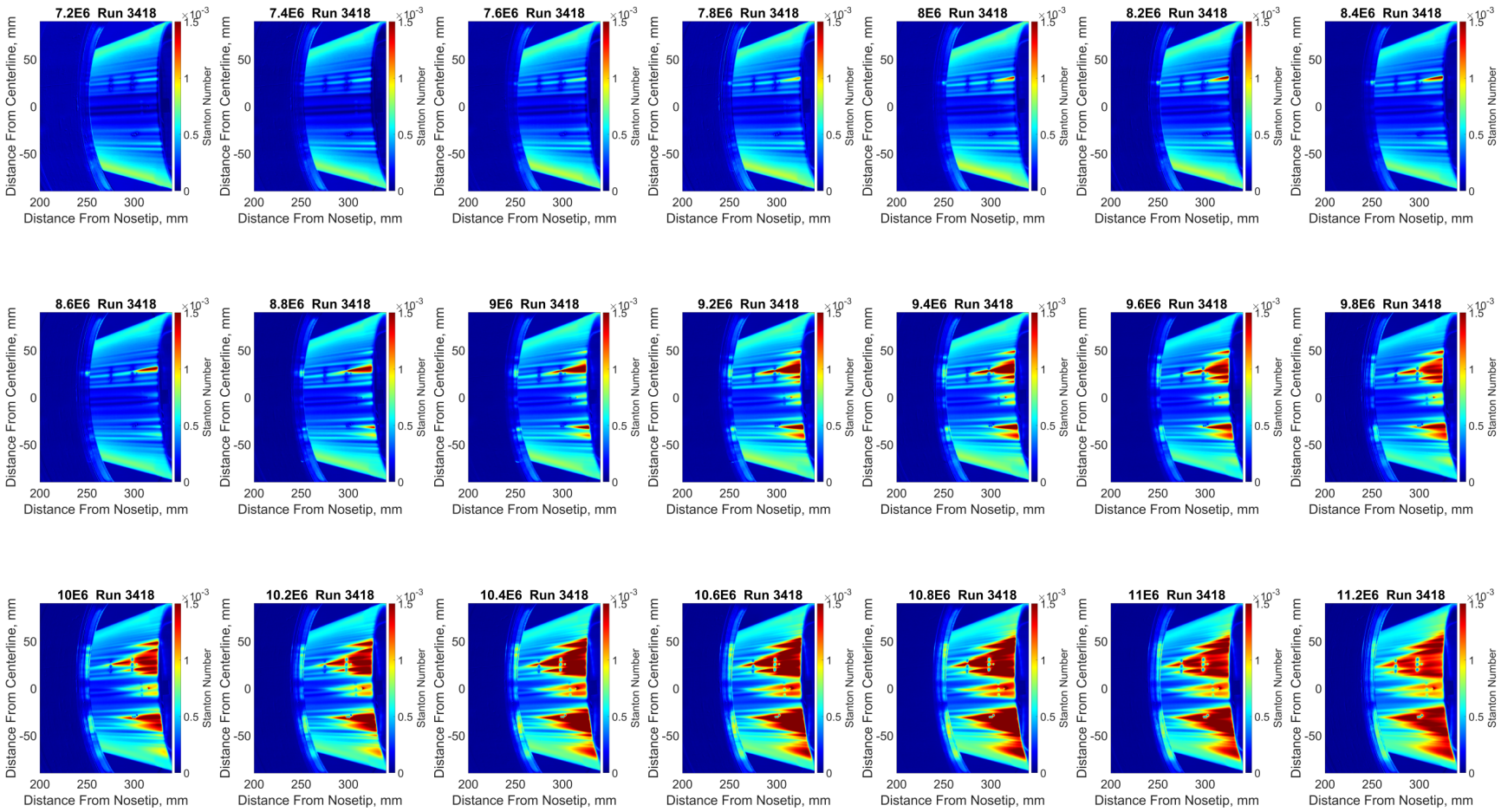

Figure D.18: St maps: M6QT Run 3418.

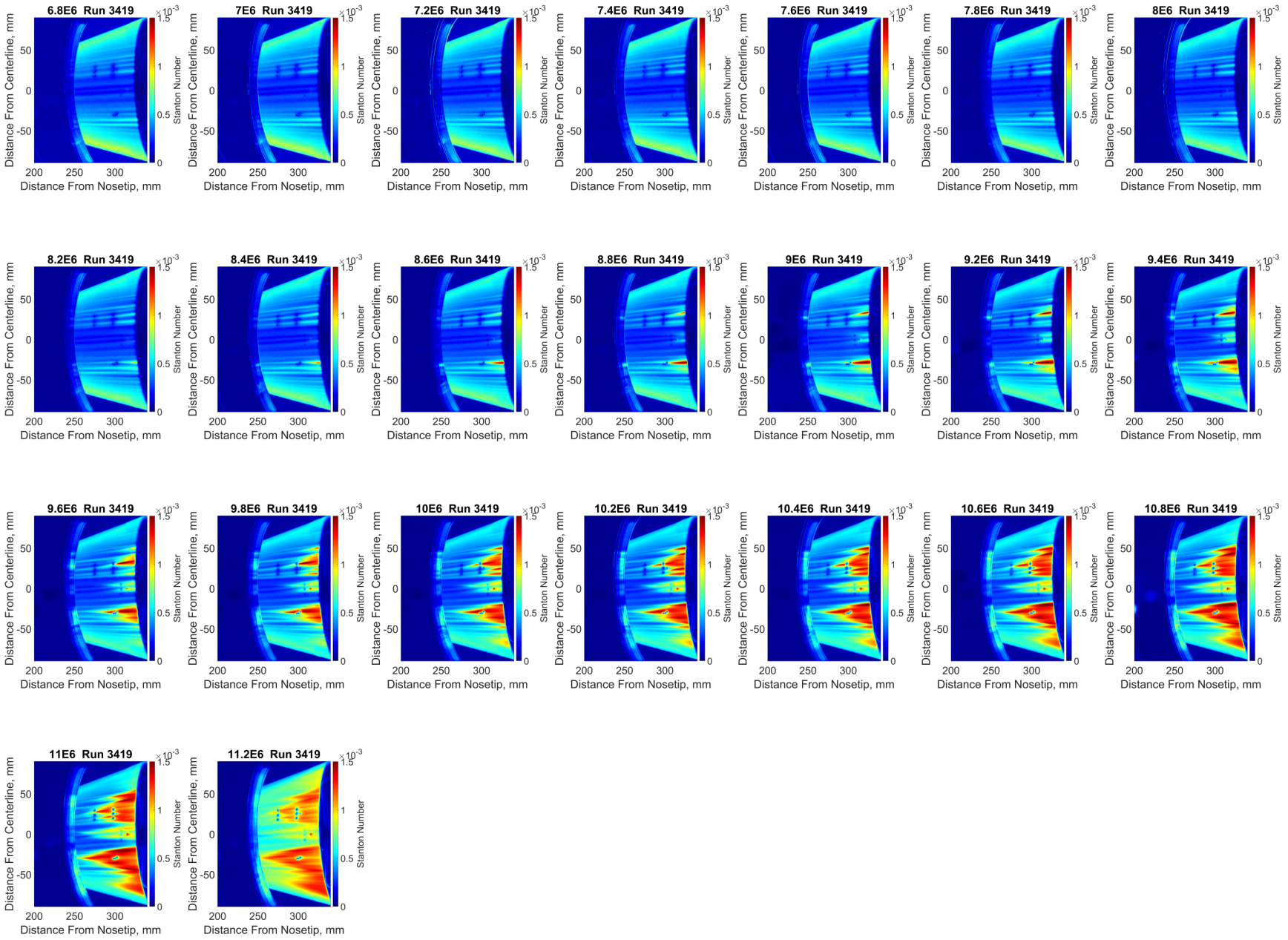

Figure D.19: St maps: M6QT Run 3419.

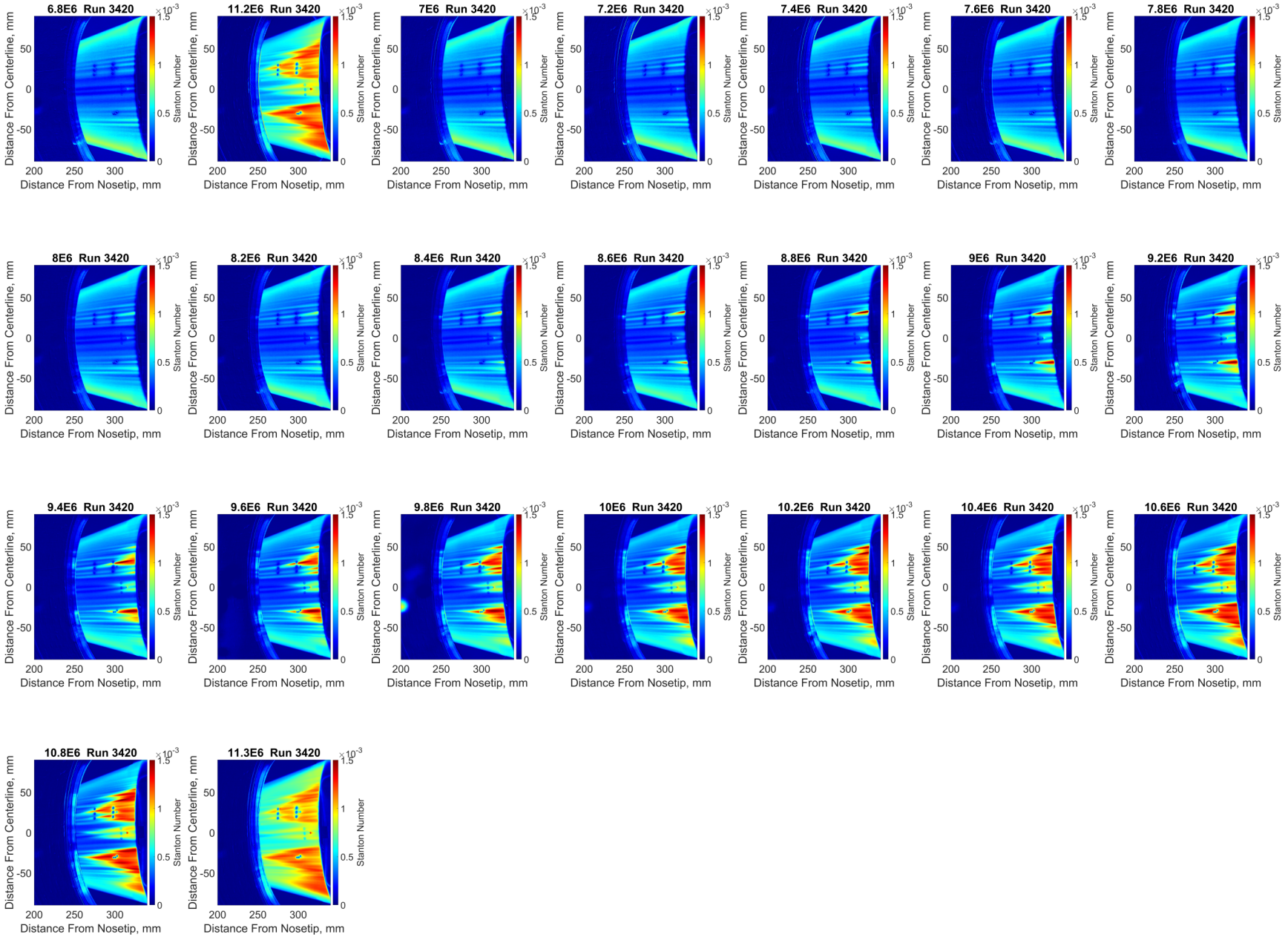

Figure D.20: St maps: M6QT Run 3420.

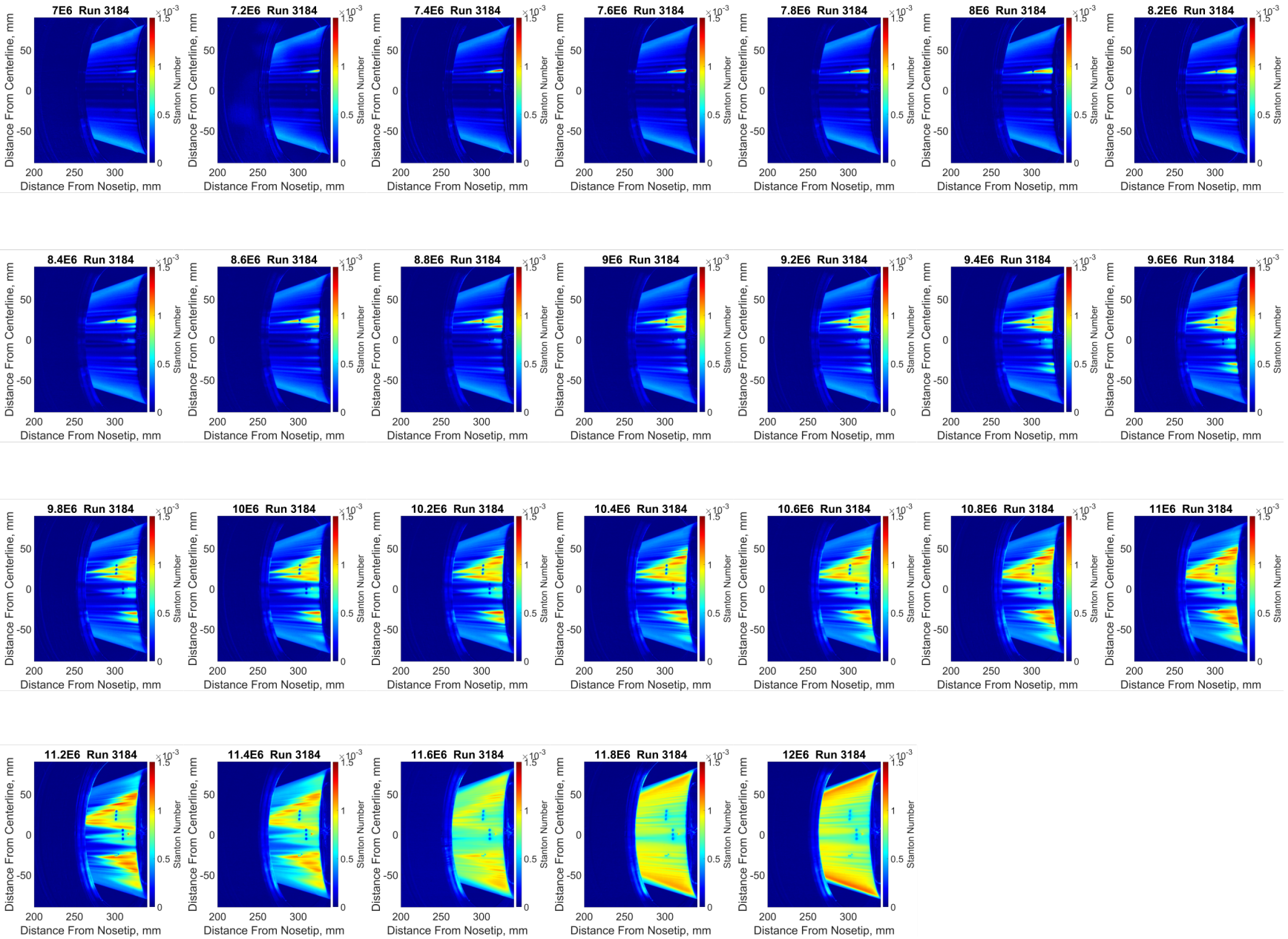

Figure D.21: St maps: M6QT Run 3184.

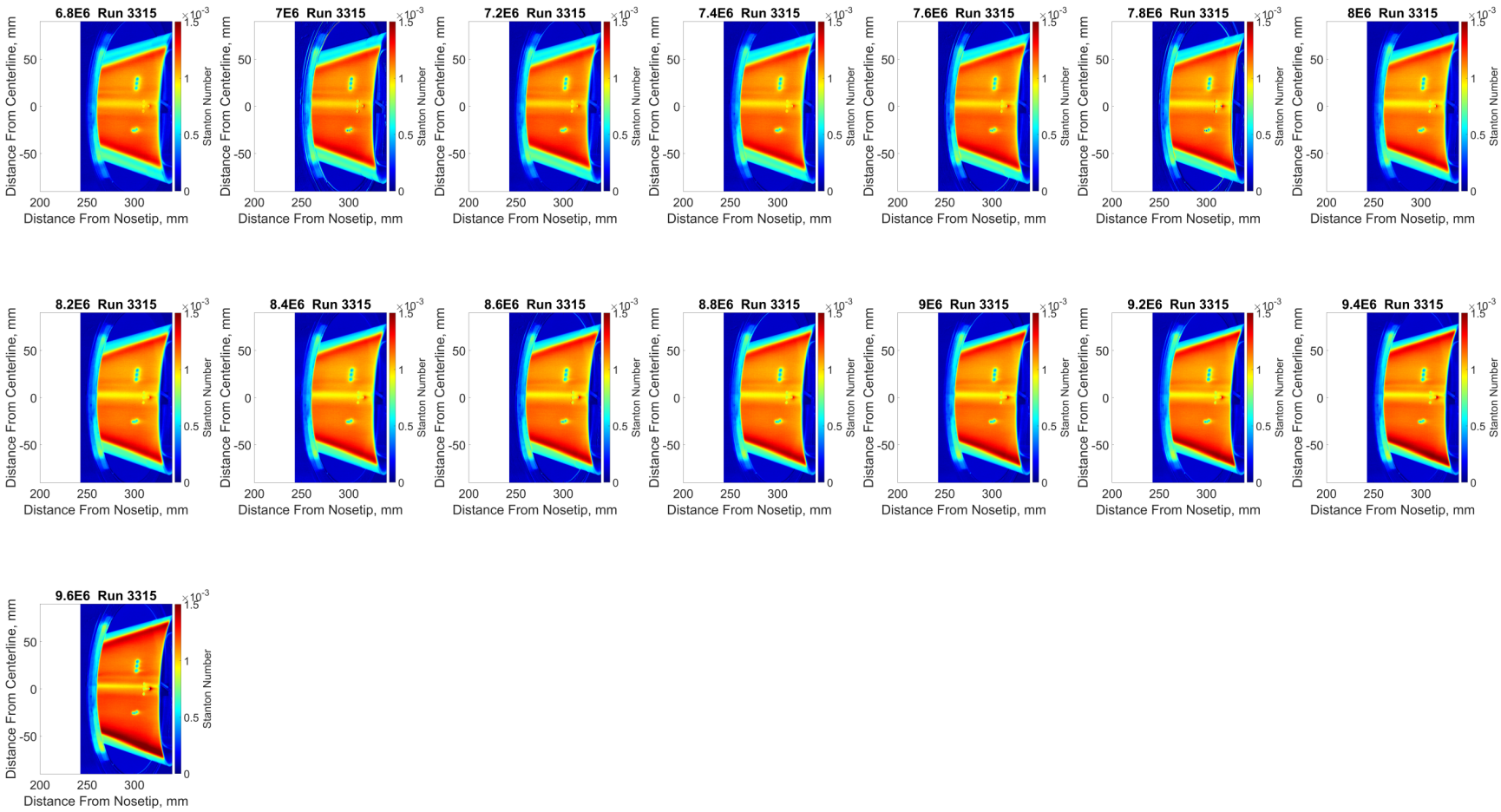

Figure D.22: St maps: M6QT Run 3315 Noisy.

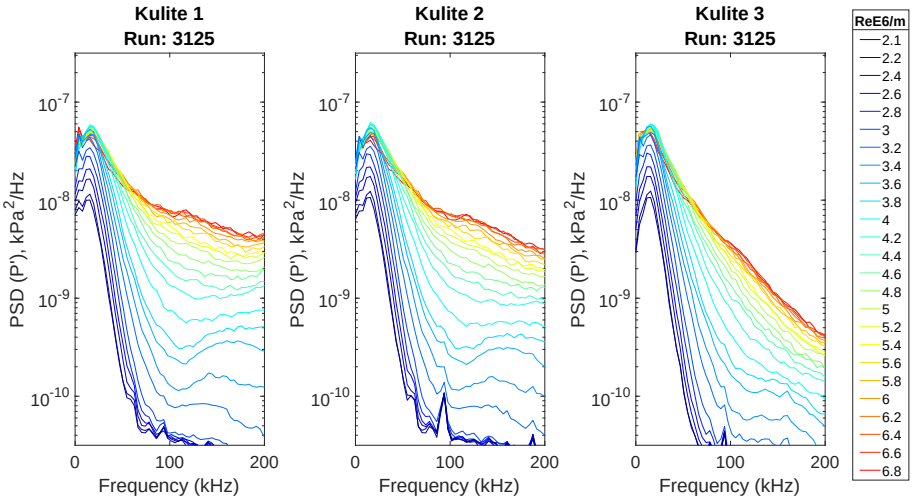

(a)

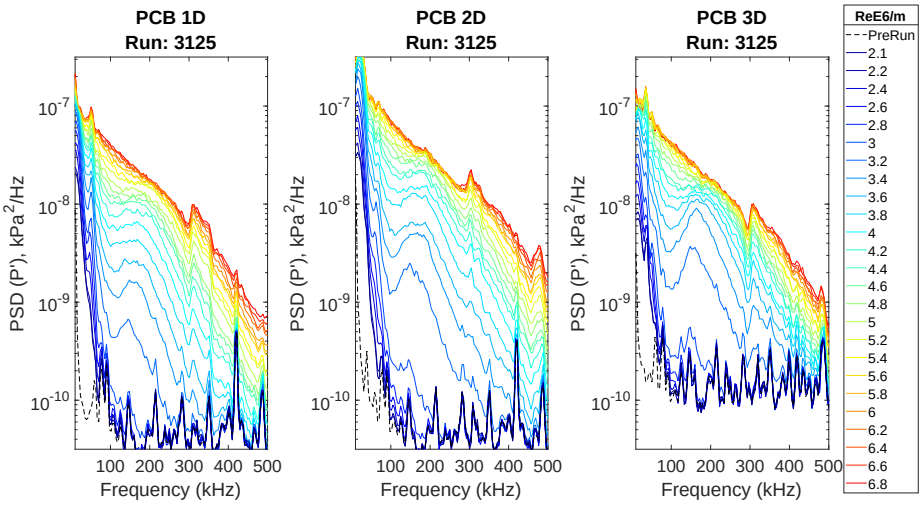

(b)

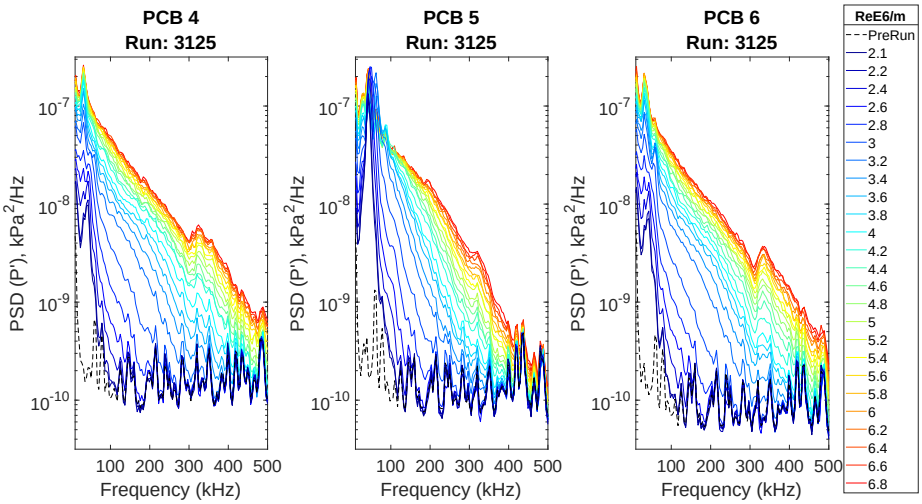

(c)

Figure D.23: Line plot PSD of fluctuating pressure for each transducer cluster Run 3125; ACE tunnel; DS station. (a) Kulites, (b) Downstream Shoulder PCB, (c) Centerline PCB

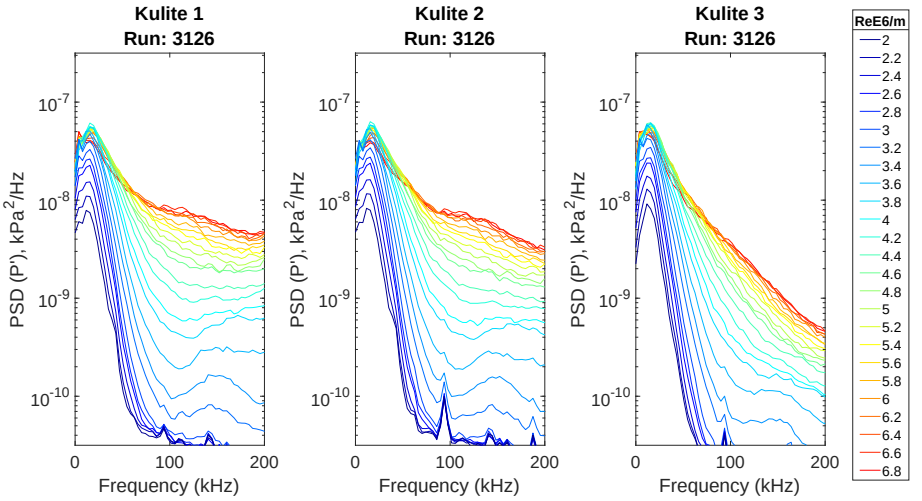

(a)

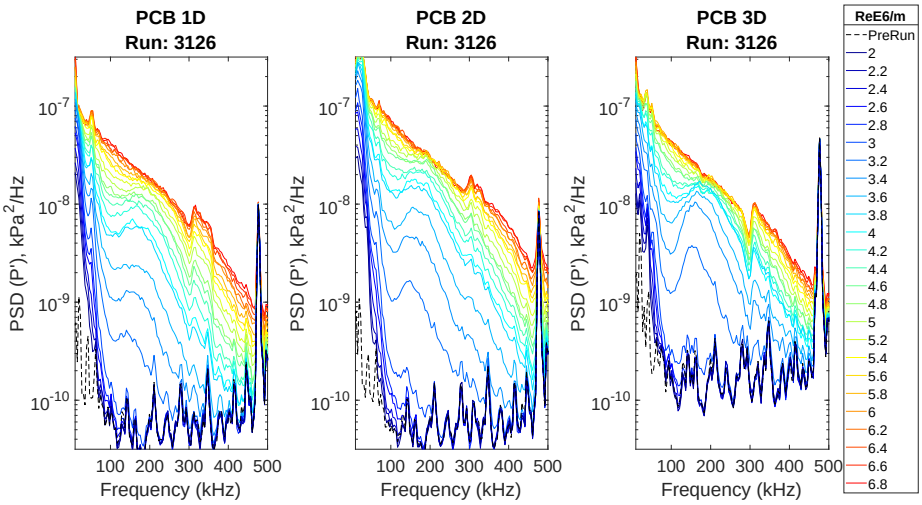

(b)

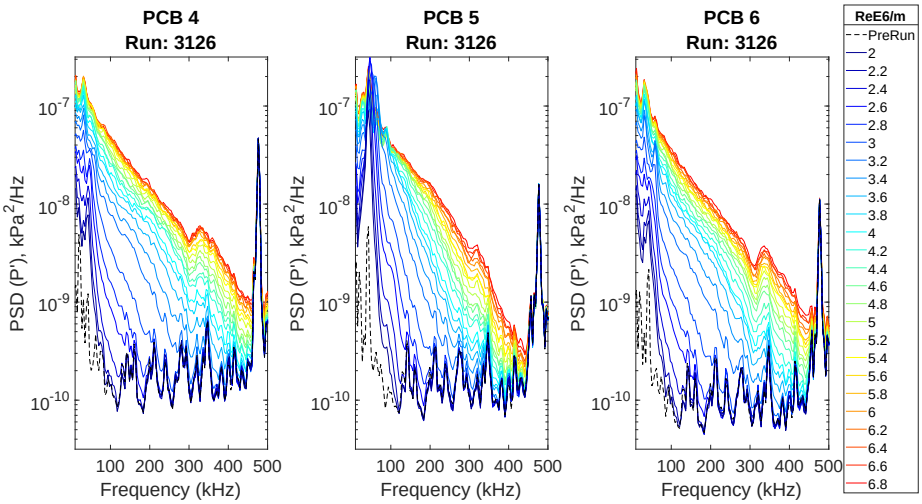

(c)

Figure D.24: Line plot PSD of fluctuating pressure for each transducer cluster Run 3126; ACE tunnel; DS station. (a) Kulites, (b) Downstream Shoulder PCB, (c) Centerline PCB

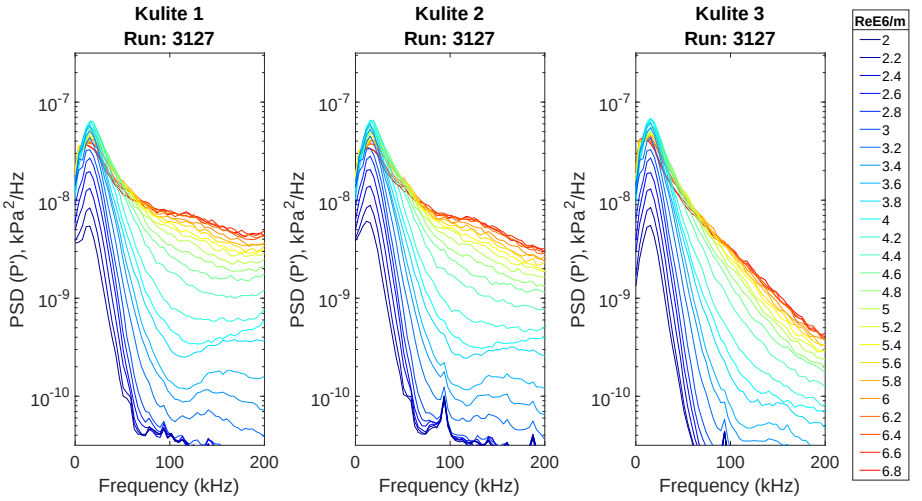

(a)

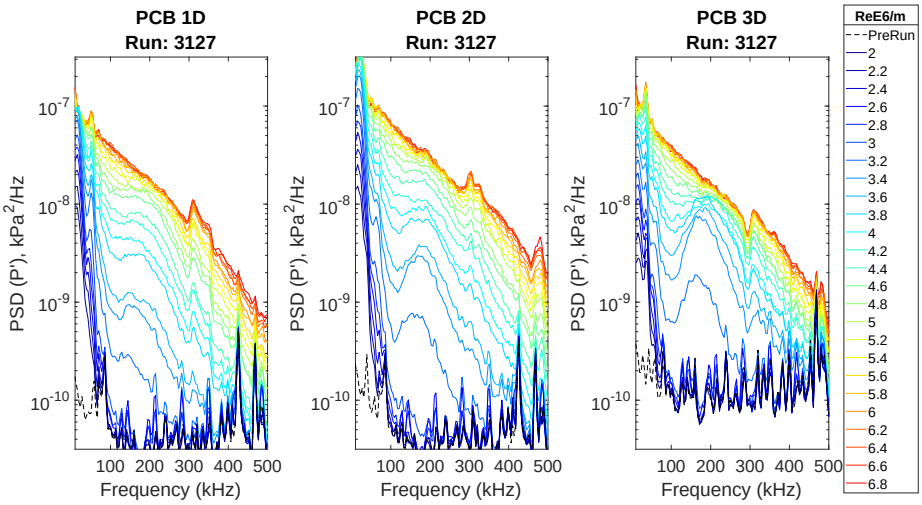

(b)

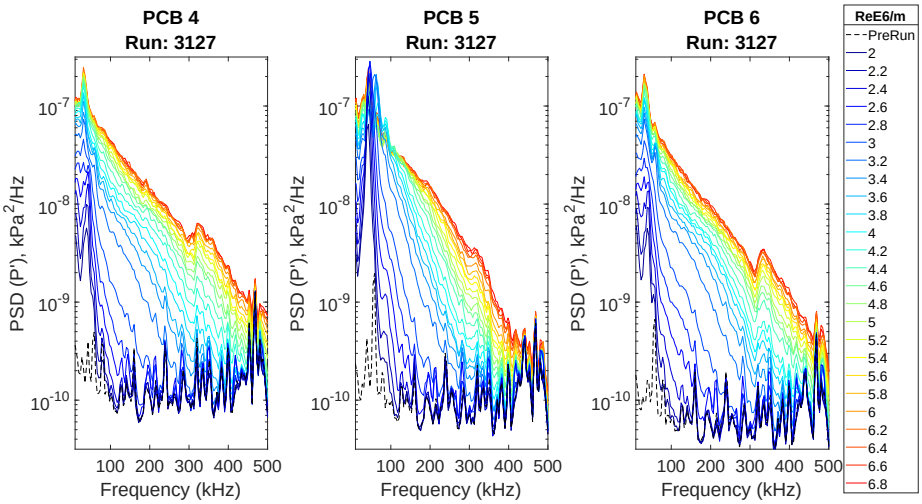

(c)

Figure D.25: Line plot PSD of fluctuating pressure for each transducer cluster Run 3127; ACE tunnel; MID station. (a) Kulites, (b) Downstream Shoulder PCB, (c) Centerline PCB.

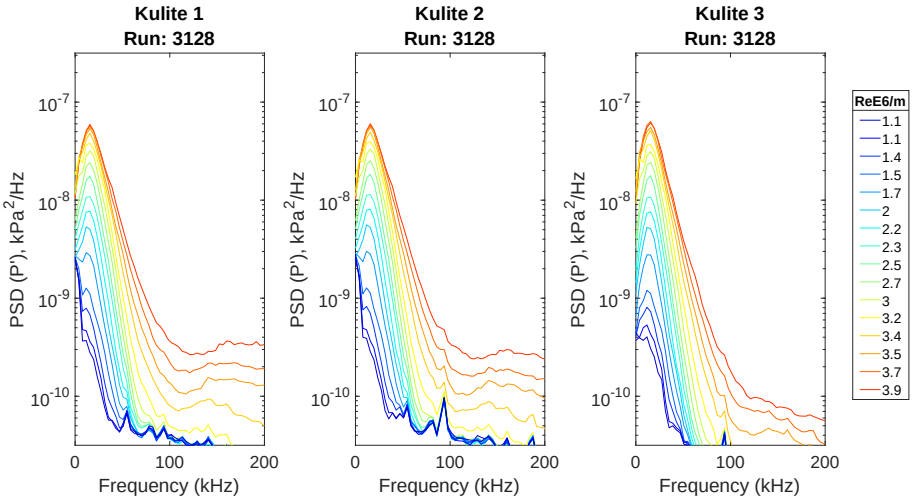

(a)

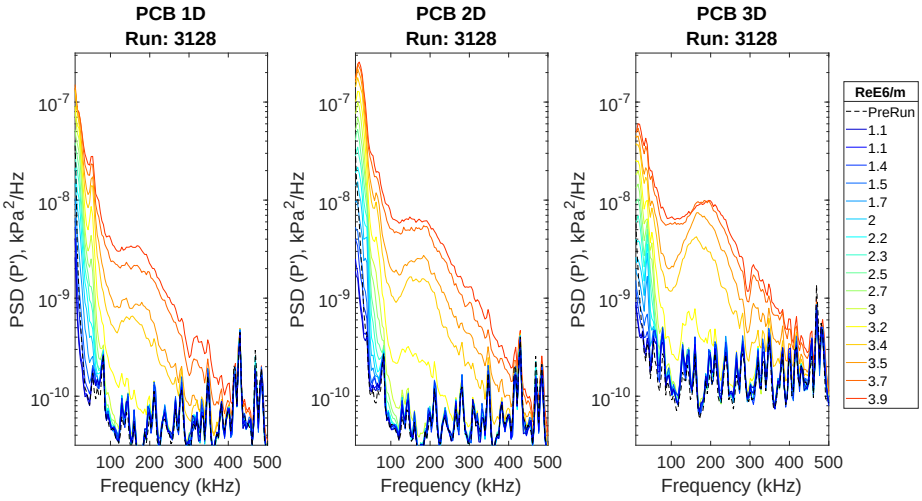

(b)

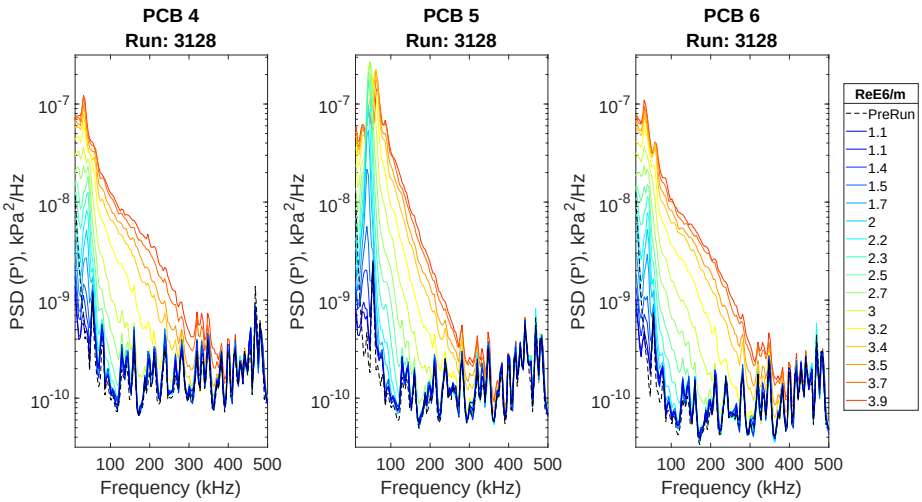

(c)

Figure D.26: Line plot PSD of fluctuating pressure for each transducer cluster Run 3128; ACE tunnel; MID station. (a) Kulites, (b) Downstream Shoulder PCB, (c) Centerline PCB.

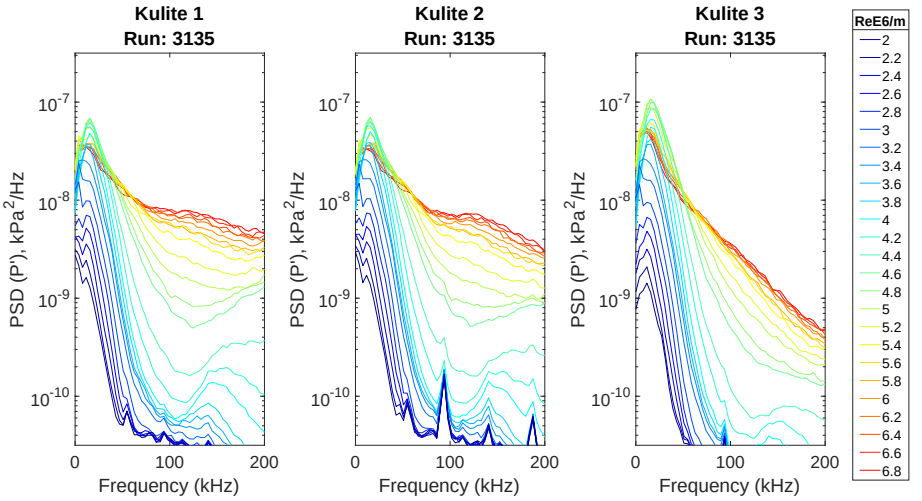

(a)

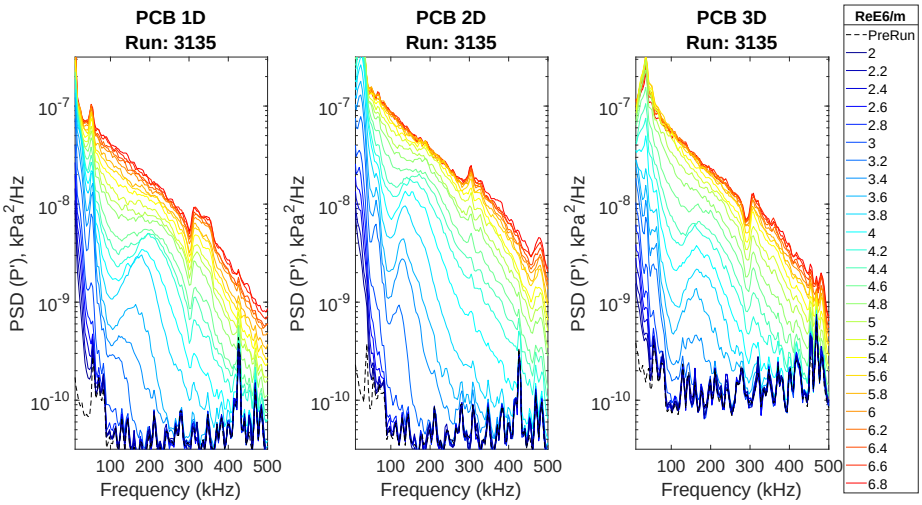

(b)

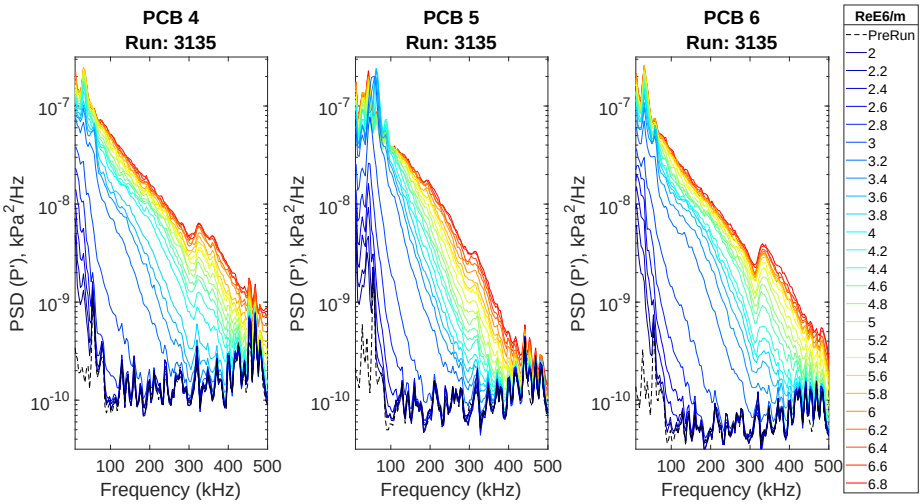

(c)

Figure D.27: Line plot PSD of fluctuating pressure for each transducer cluster Run 3135; ACE tunnel; US station. (a) Kulites, (b) Downstream Shoulder PCB, (c) Centerline PCB.

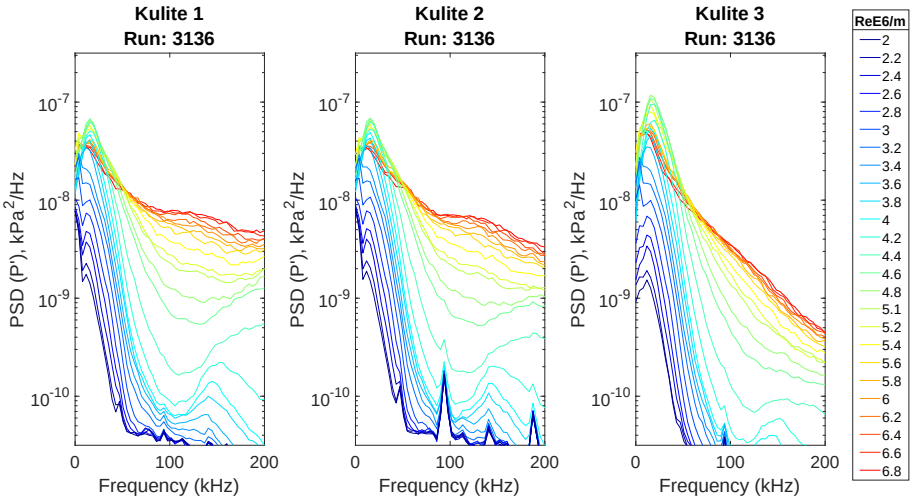

(a)

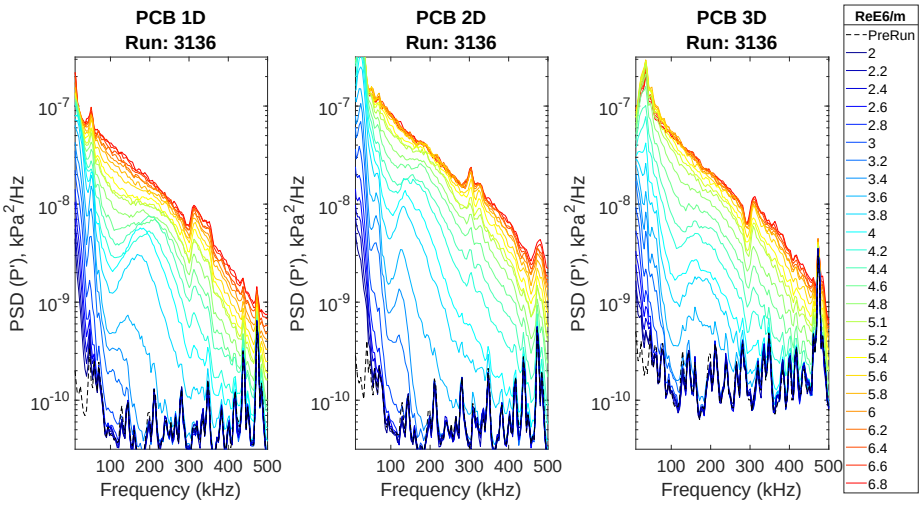

(b)

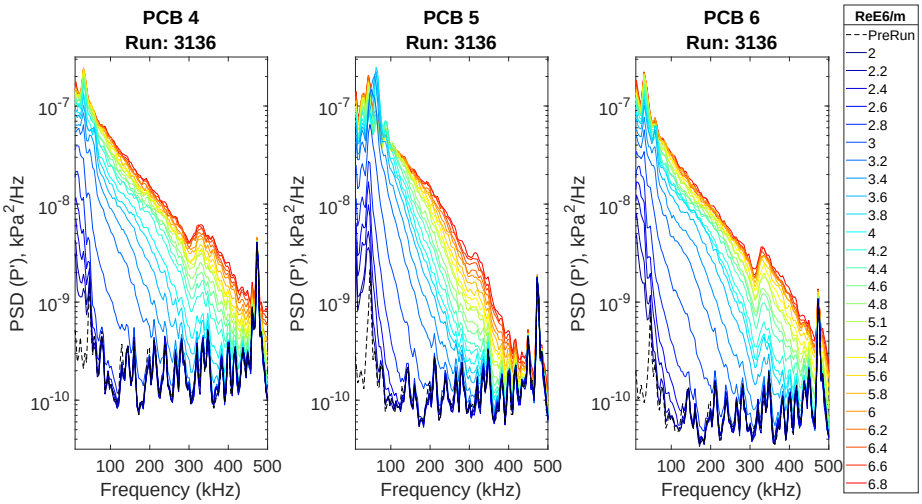

(c)

Figure D.28: Line plot PSD of fluctuating pressure for each transducer cluster Run 3136; ACE tunnel; US station. (a) Kulites, (b) Downstream Shoulder PCB, (c) Centerline PCB.

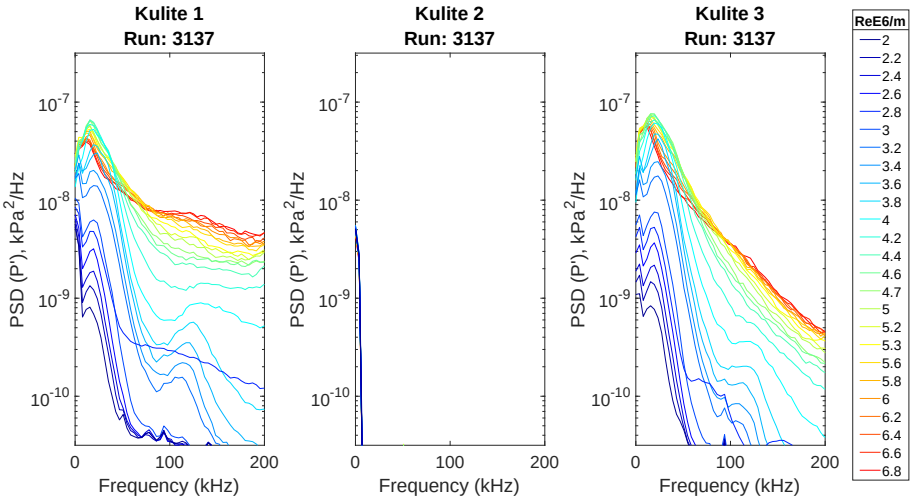

(a)

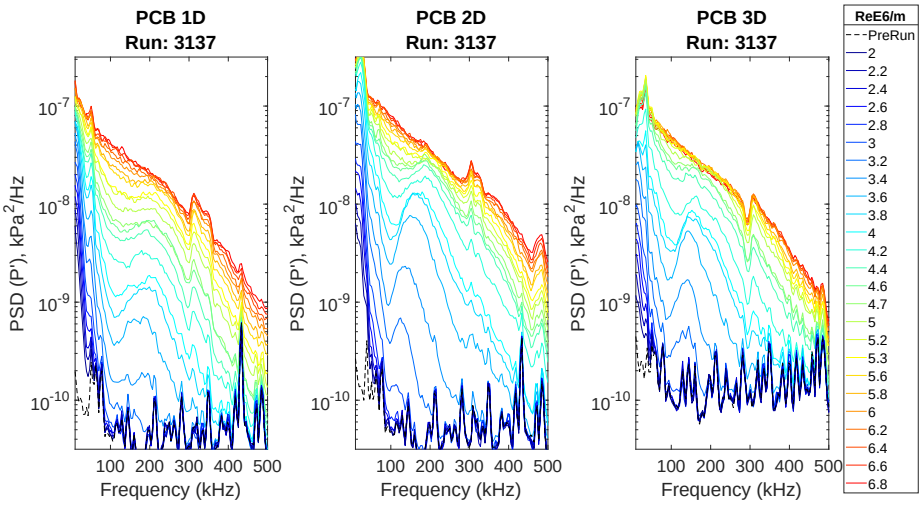

(b)

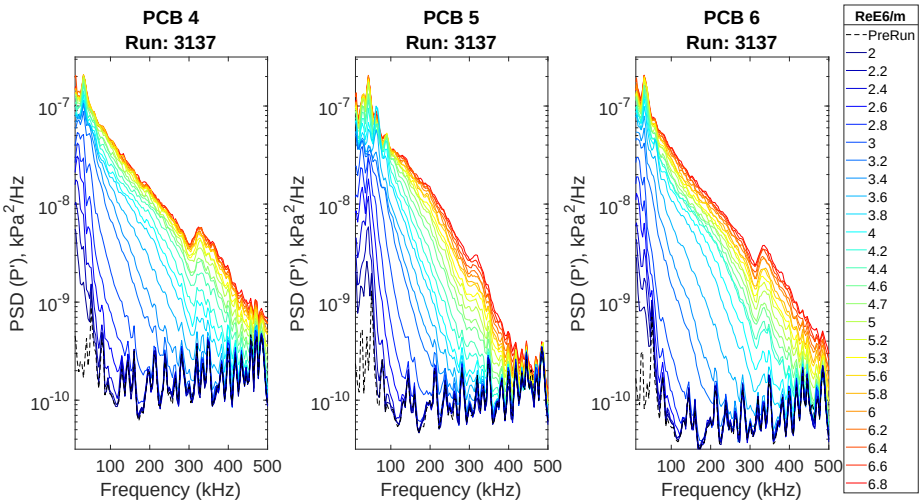

(c)

Figure D.29: Line plot PSD of fluctuating pressure for each transducer cluster Run 3137; ACE tunnel; US station. (a) Kulites, (b) Downstream Shoulder PCB, (c) Centerline PCB.

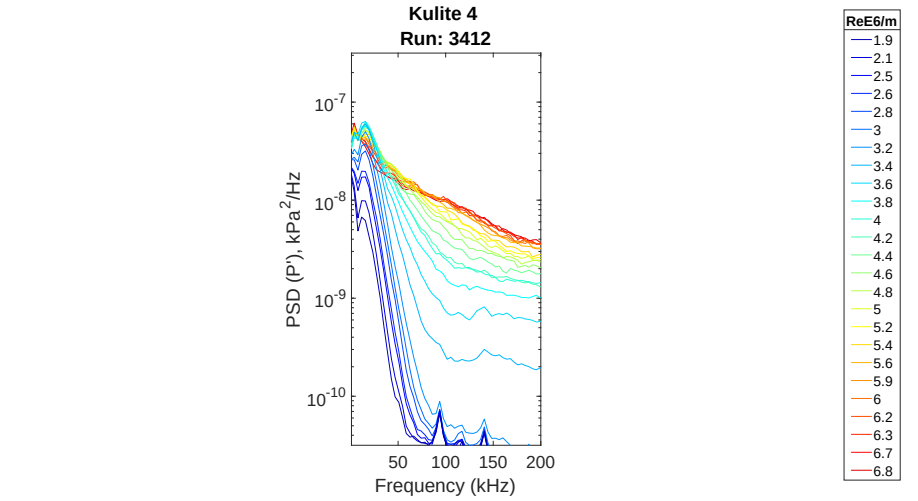

(a)

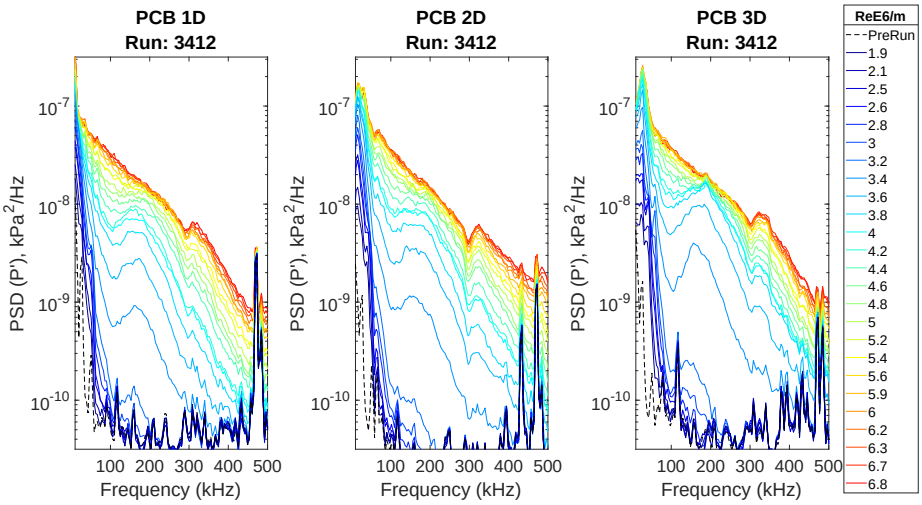

(b)

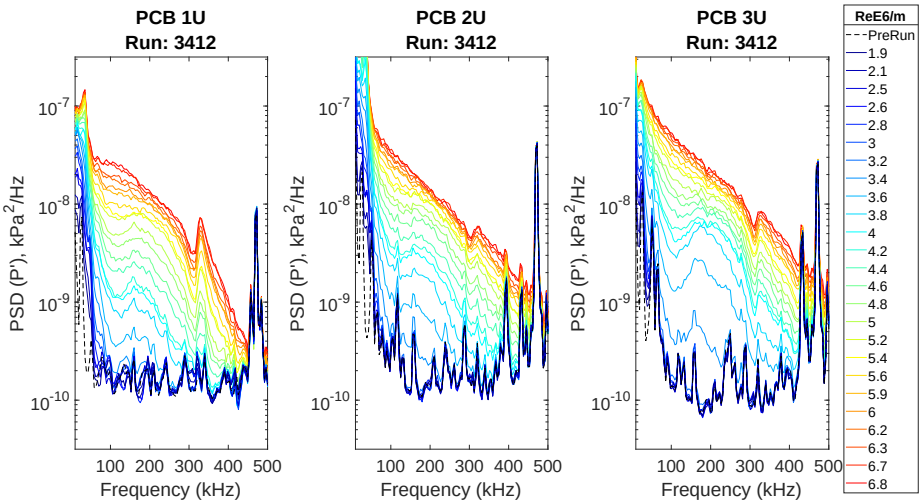

(c)

Figure D.30: Line plot PSD of fluctuating pressure for each transducer cluster Run 3412; ACE tunnel; DS station. (a) Kulite 4, (b) Downstream Shoulder PCBs, (c) Upstream shoulder PCBs.

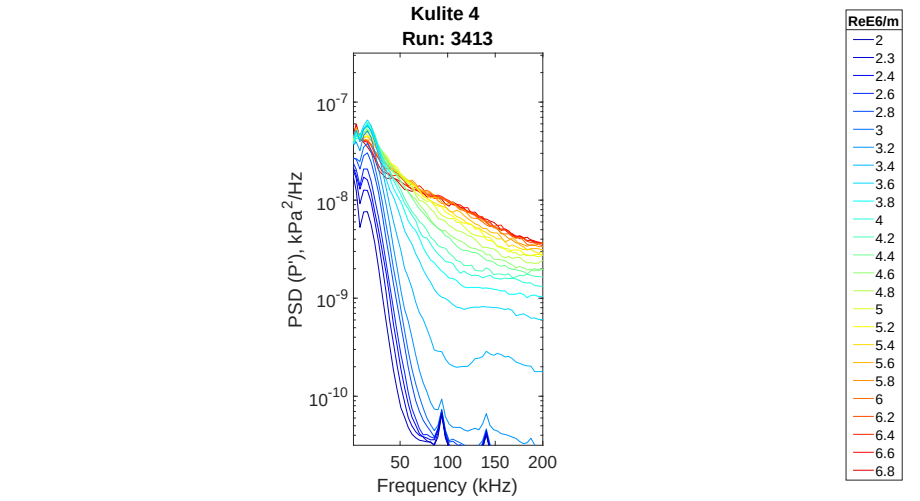

(a)

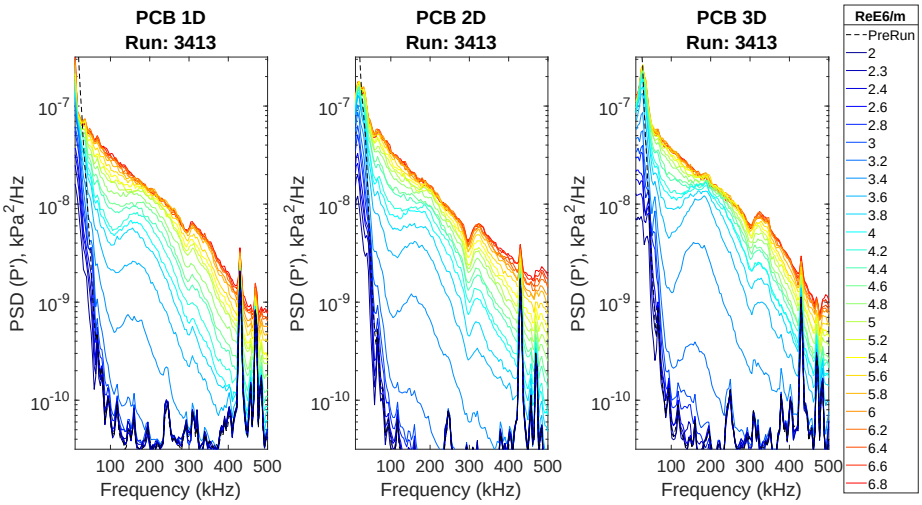

(b)

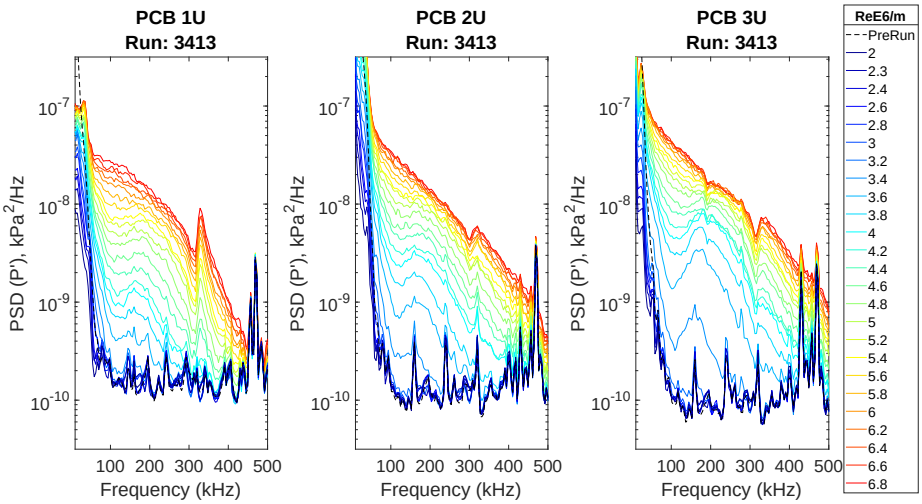

(c)

Figure D.31: Line plot PSD of fluctuating pressure for each transducer cluster Run 3413; ACE tunnel; DS station. (a) Kulite 4, (b) Downstream Shoulder PCBs, (c) Upstream shoulder PCBs.

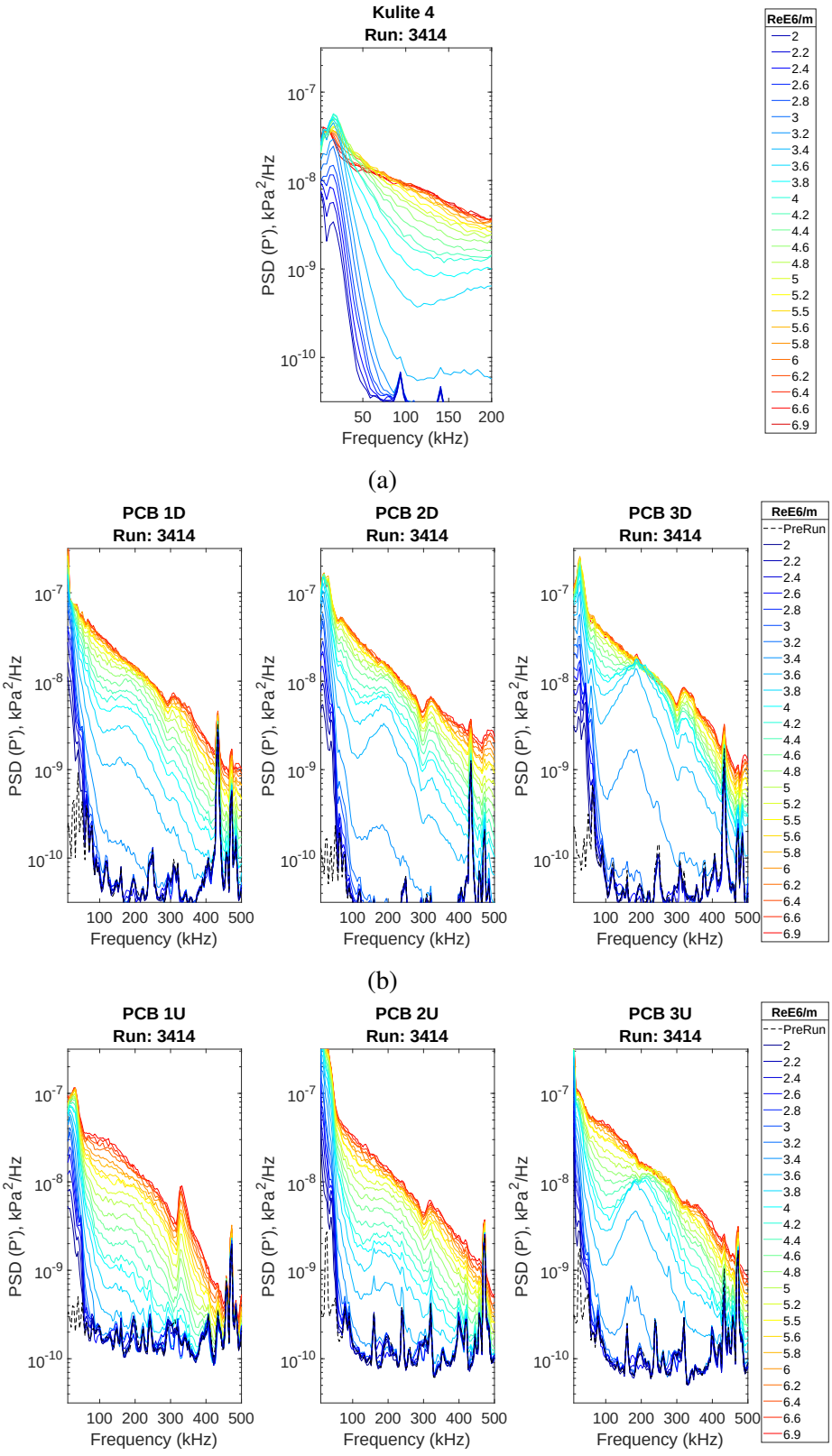

Figure D.32: Line plot PSD of fluctuating pressure for each transducer cluster Run 3414; ACE tunnel; MID station. (a) Kulite 4, (b) Downstream Shoulder PCBs, (c) Upstream shoulder PCBs.

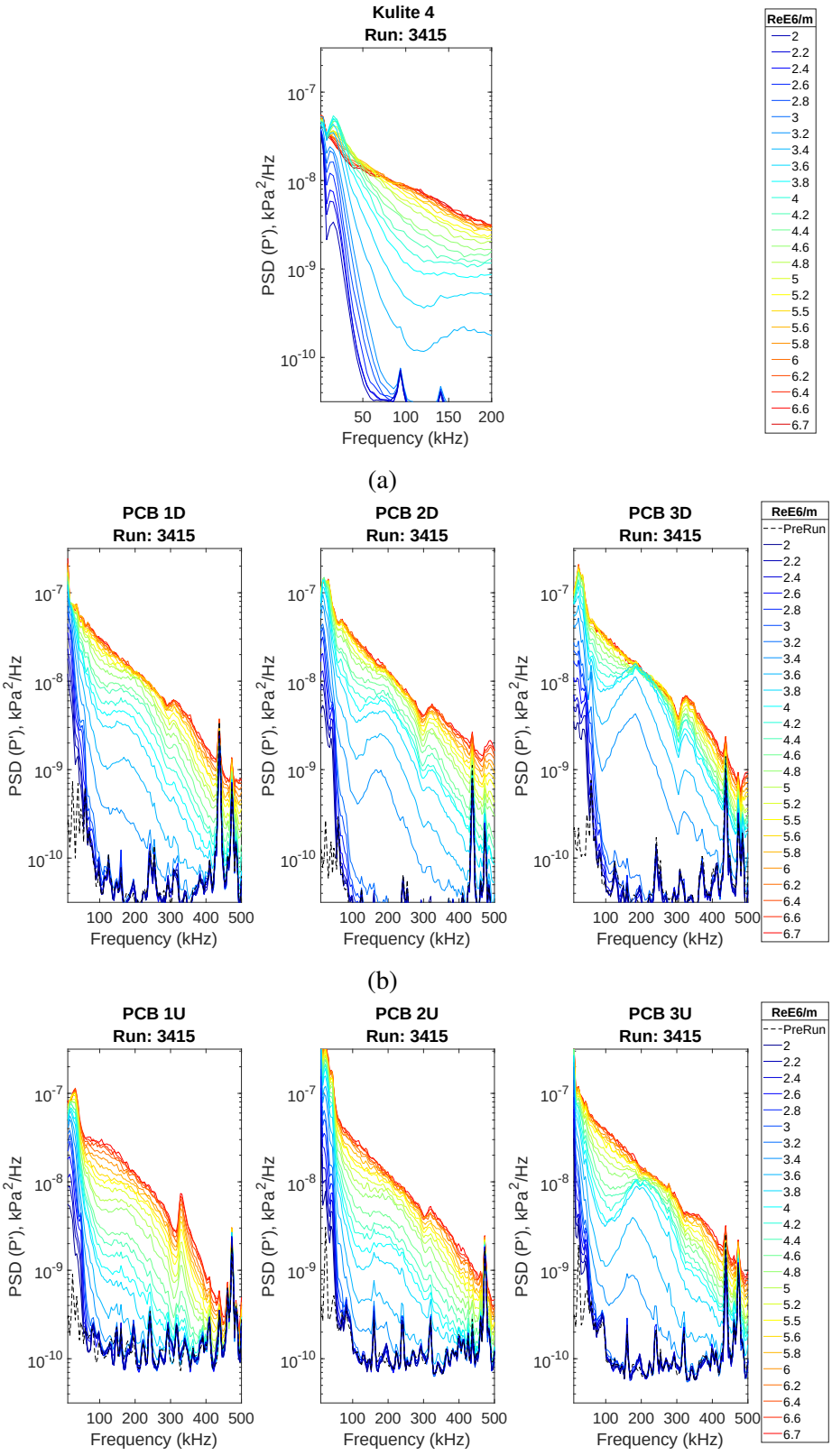

Figure D.33: Line plot PSD of fluctuating pressure for each transducer cluster Run 3415; ACE tunnel; MID station. (a) Kulite 4, (b) Downstream Shoulder PCBs, (c) Upstream shoulder PCBs.

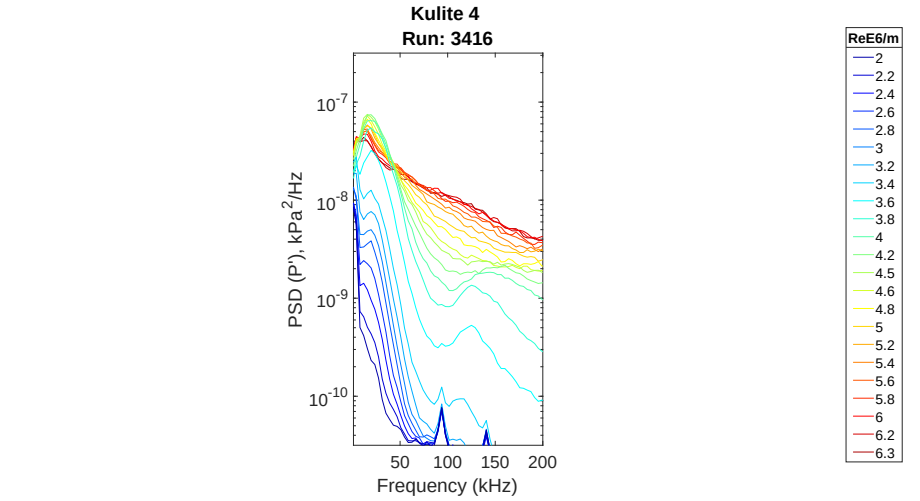

(a)

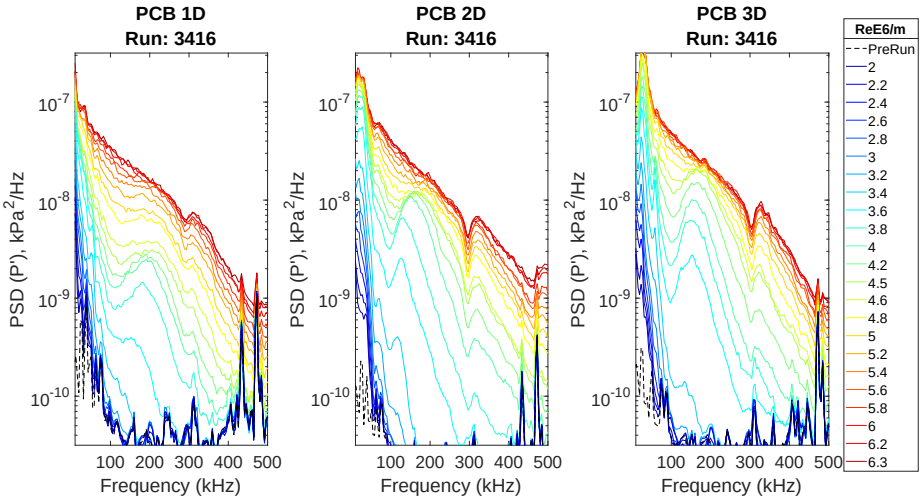

(b)

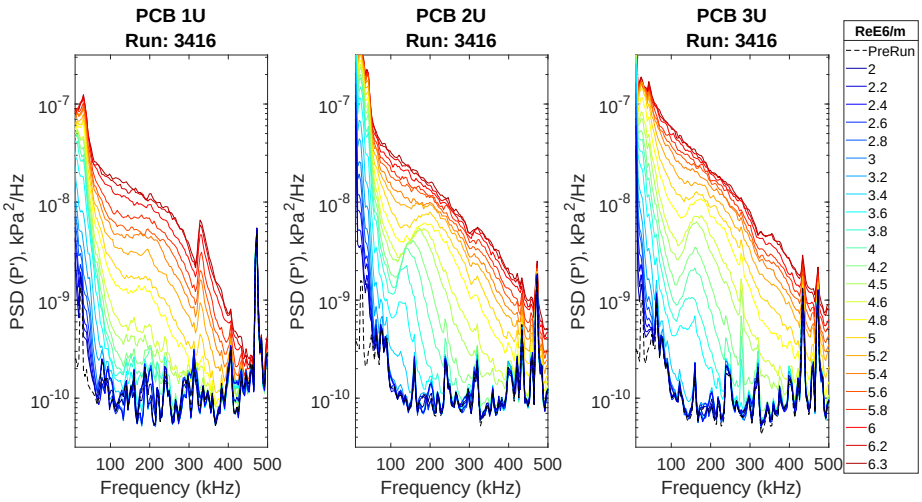

(c)

Figure D.34: Line plot PSD of fluctuating pressure for each transducer cluster Run 3416; ACE tunnel; US station. (a) Kulite 4, (b) Downstream Shoulder PCBs, (c) Upstream shoulder PCBs.

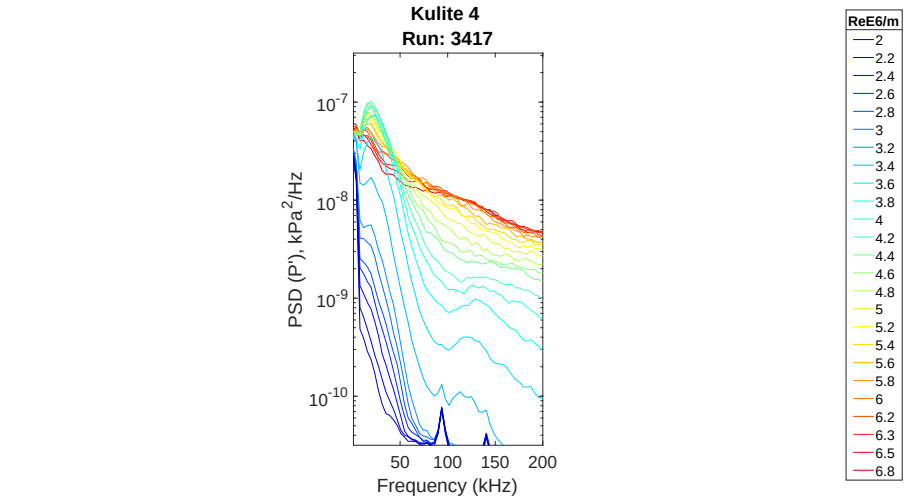

(a)

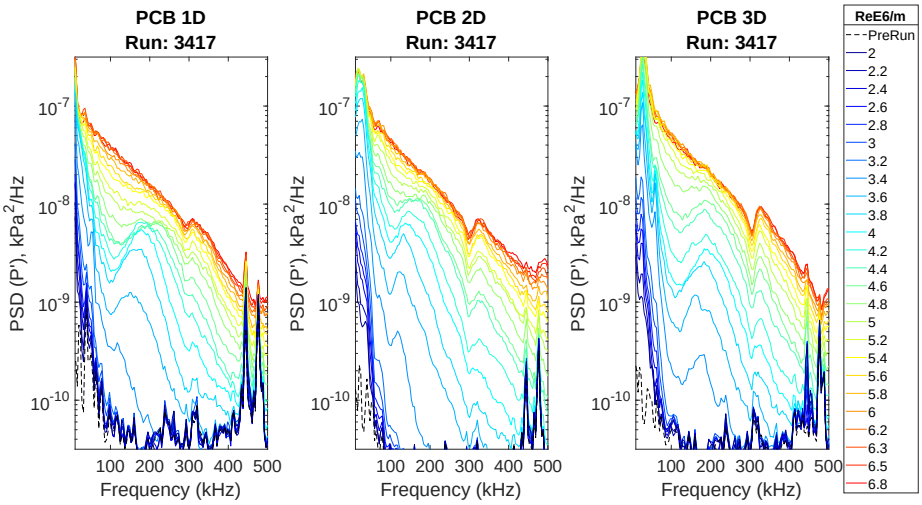

(b)

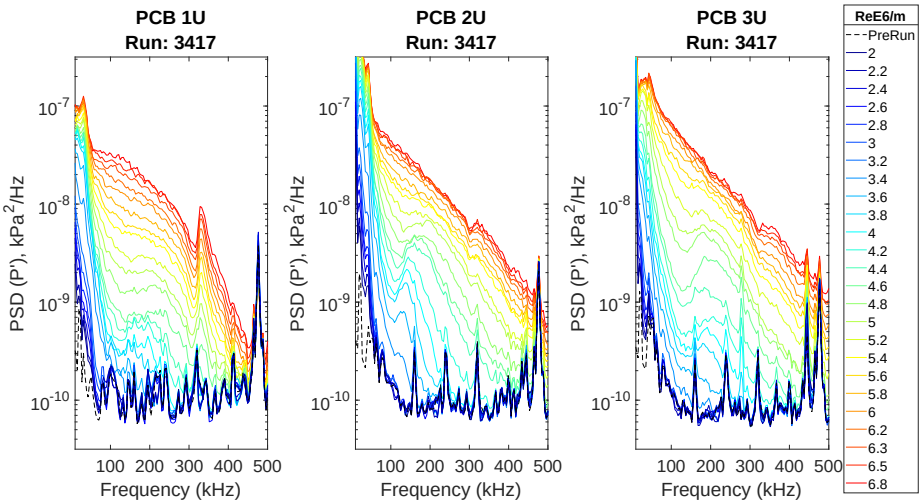

(c)

Figure D.35: Line plot PSD of fluctuating pressure for each transducer cluster Run 3417; ACE tunnel; US station. (a) Kulite 4, (b) Downstream Shoulder PCBs, (c) Upstream shoulder PCBs.

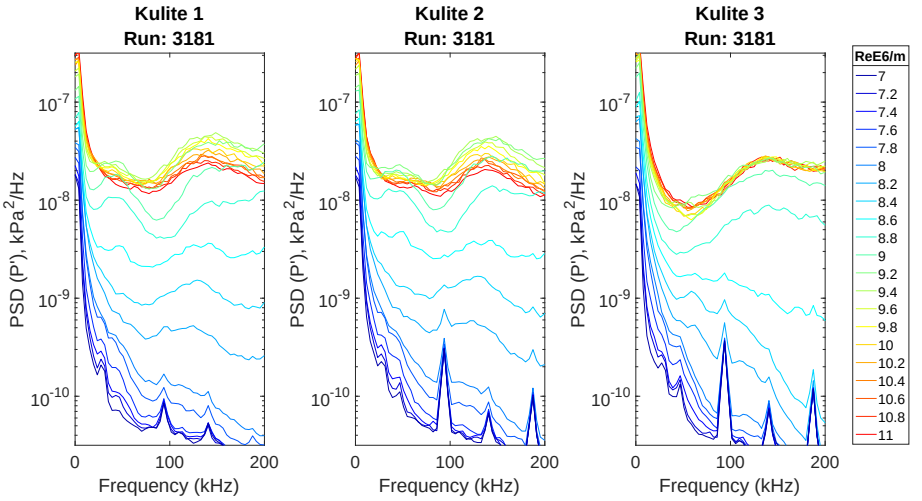

(a)

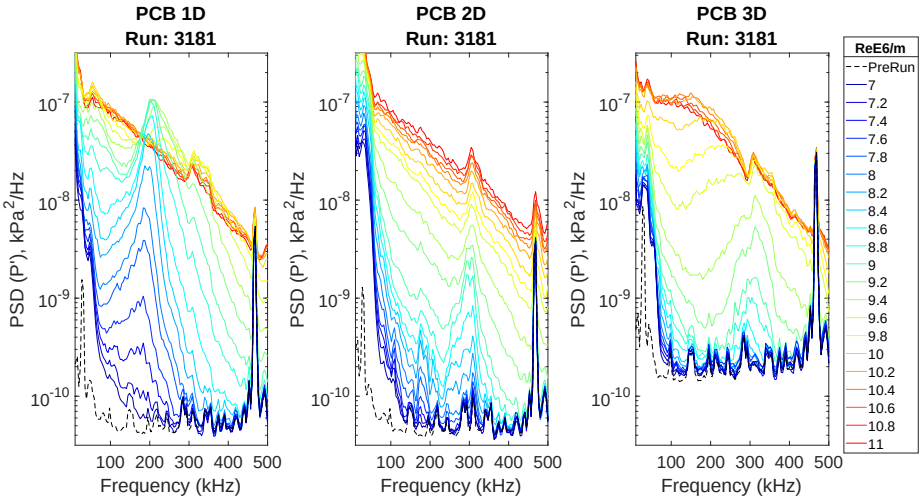

(b)

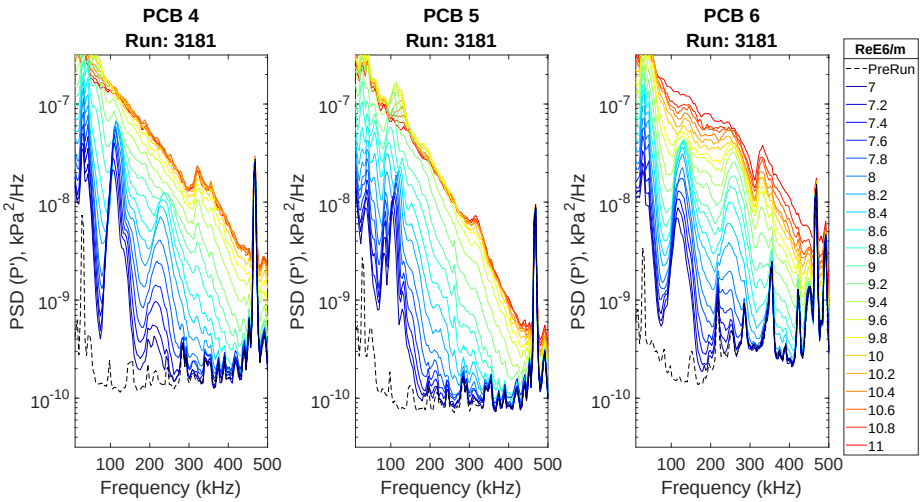

(c)

Figure D.36: Line plot PSD of fluctuating pressure for each transducer cluster Run 3181; M6QT. (a) Kulites, (b) Downstream Shoulder PCB, (c) Centerline PCB.

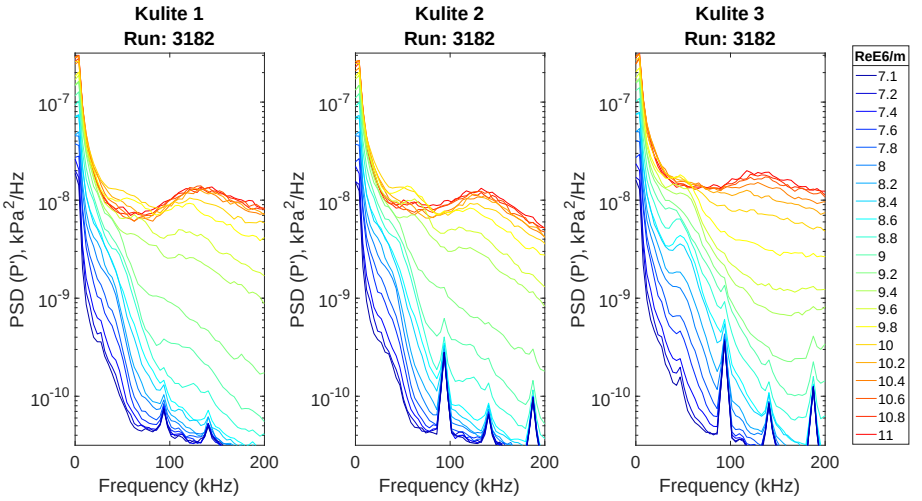

(a)

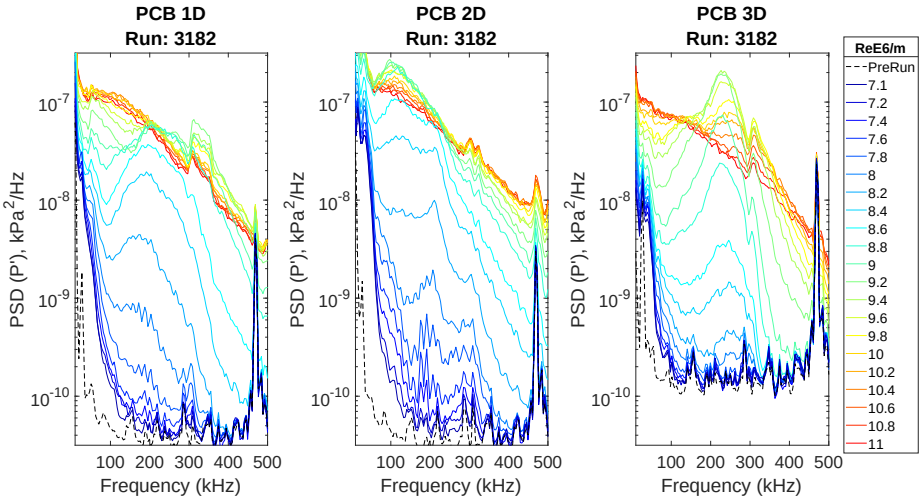

(b)

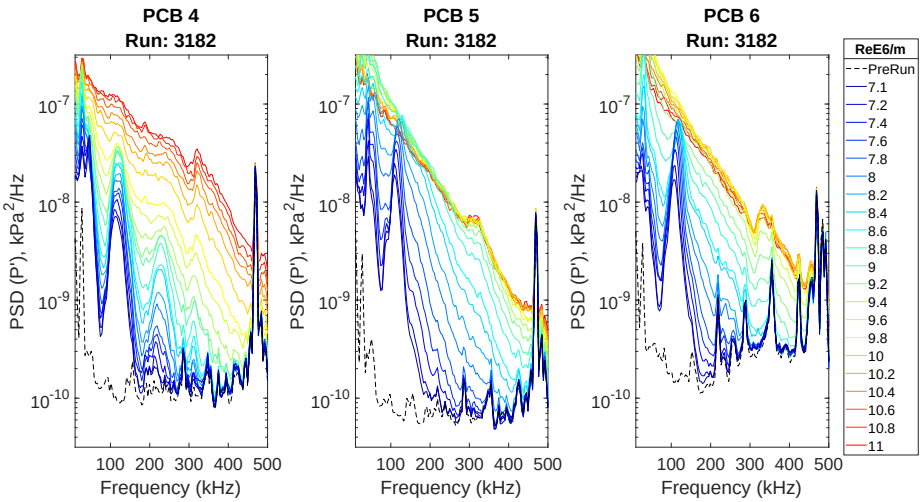

(c)

Figure D.37: Line plot PSD of fluctuating pressure for each transducer cluster Run 3182; M6QT. (a) Kulites, (b) Downstream Shoulder PCB, (c) Centerline PCB.

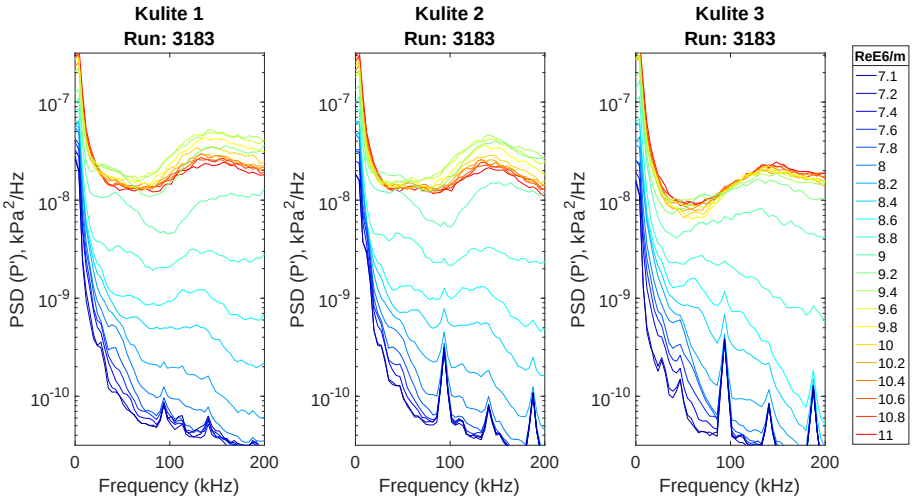

(a)

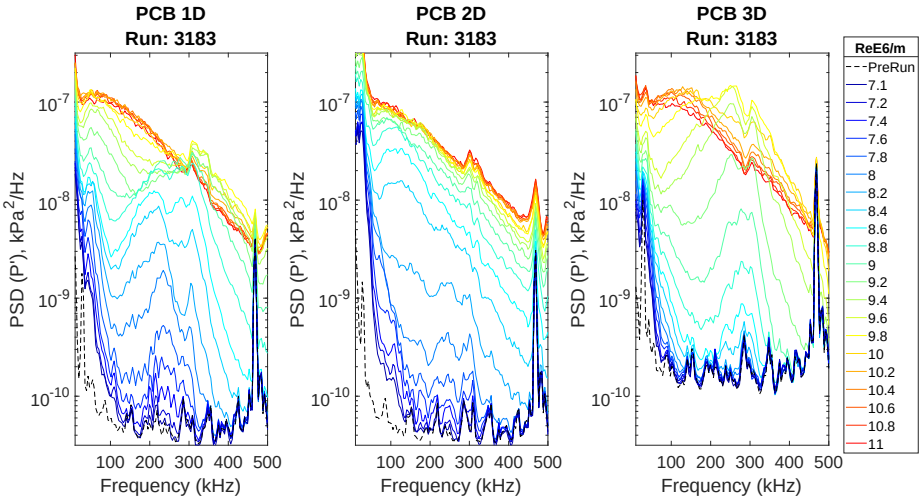

(b)

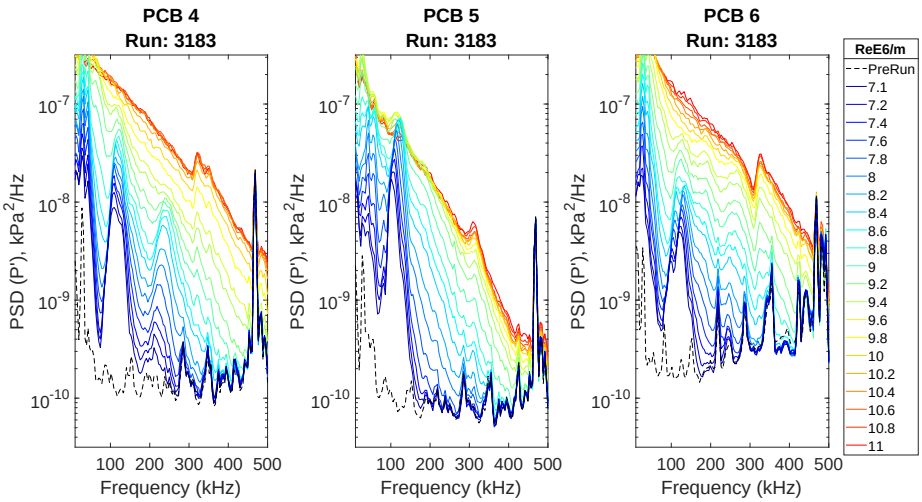

(c)

Figure D.38: Line plot PSD of fluctuating pressure for each transducer cluster Run 3183; M6QT. (a) Kulites, (b) Downstream Shoulder PCB, (c) Centerline PCB.

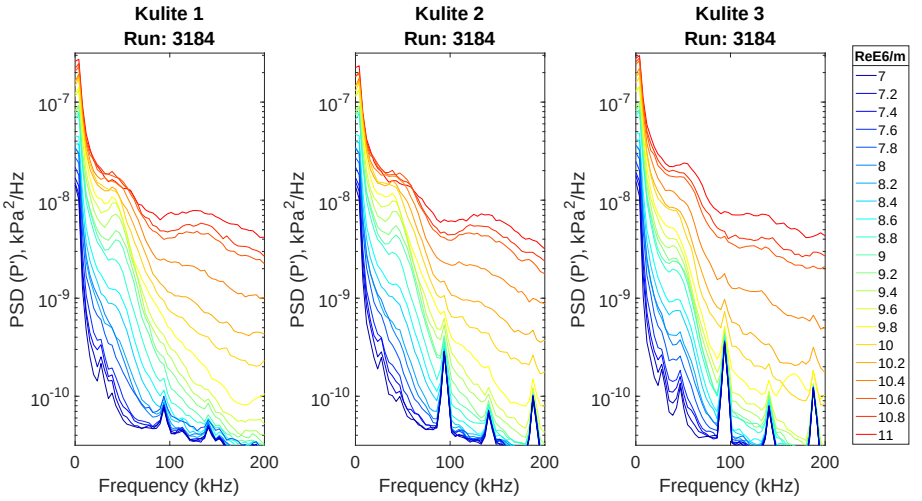

(a)

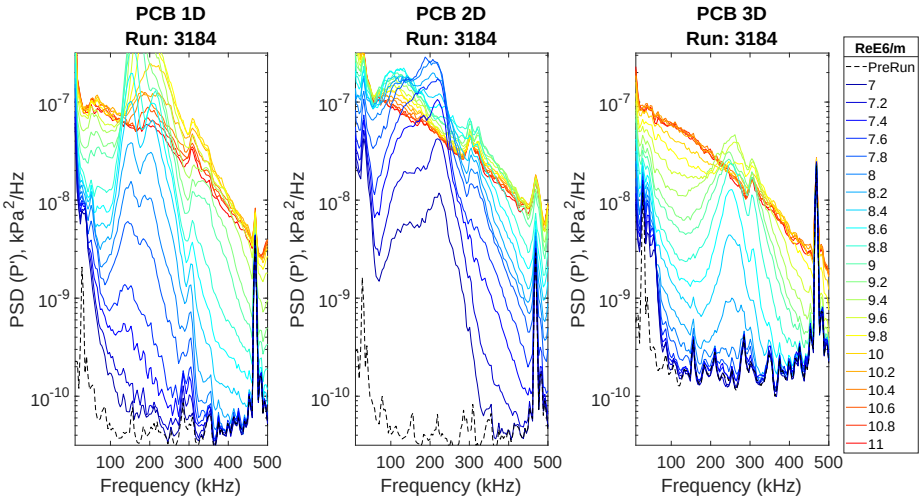

(b)

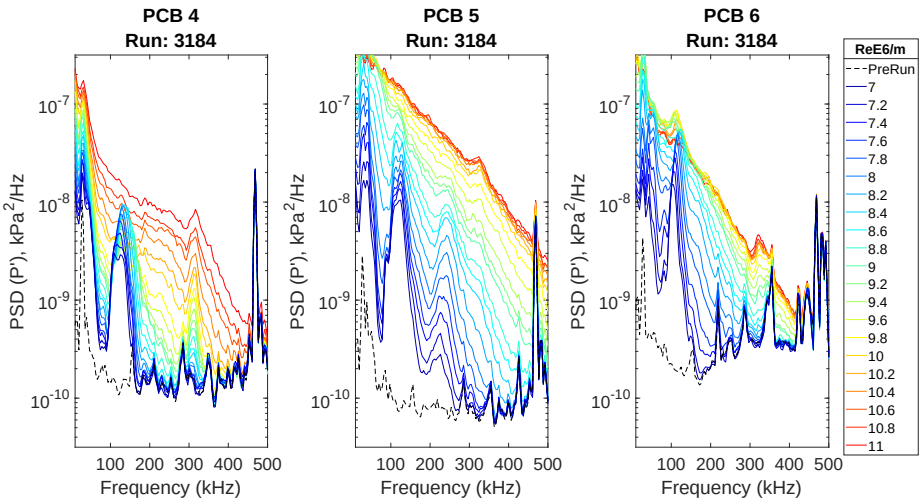

(c)

Figure D.39: PSD of Fluctuating Pressure for Each transducer cluster Run 3184; M6QT. (a) Kulite, (b) Downstream Shoulder PCB, (c) Centerline PCB

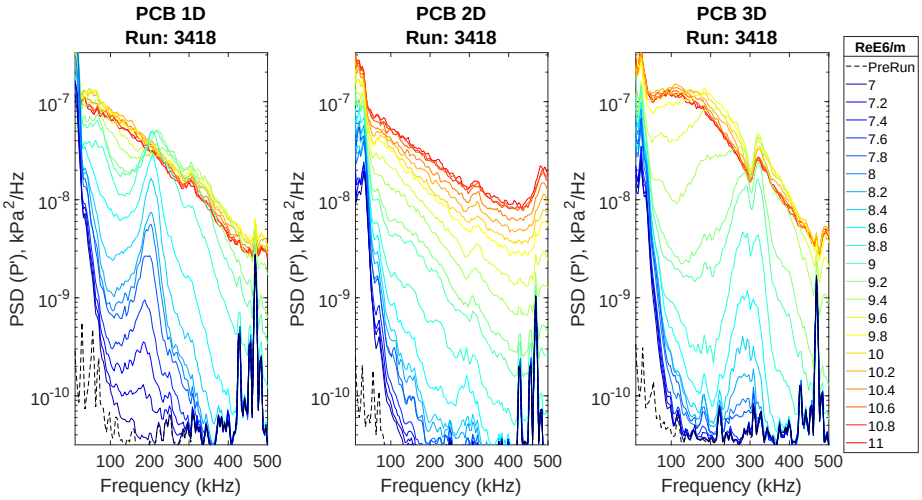

(a)

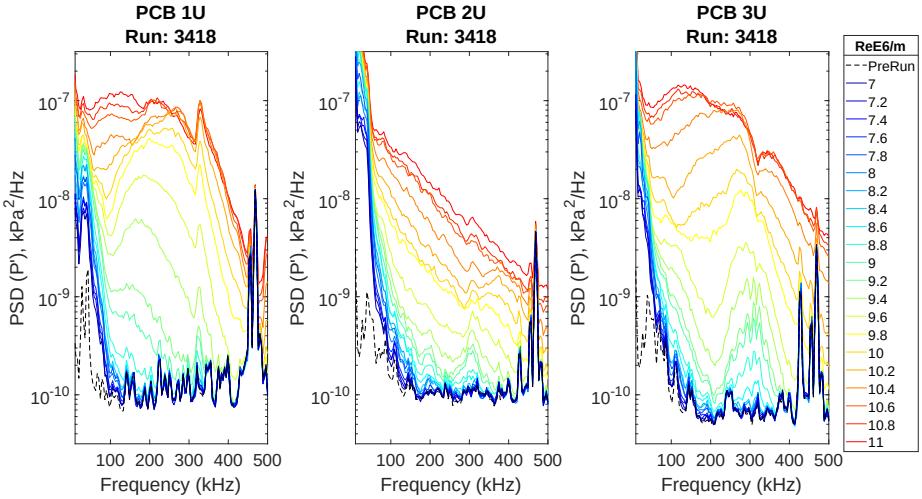

(b)

Figure D.40: Line plot PSD of fluctuating pressure for each transducer cluster Run 3418; M6QT. (a) Downstream shoulder PCBs, (b) Upstream shoulder PCBs.

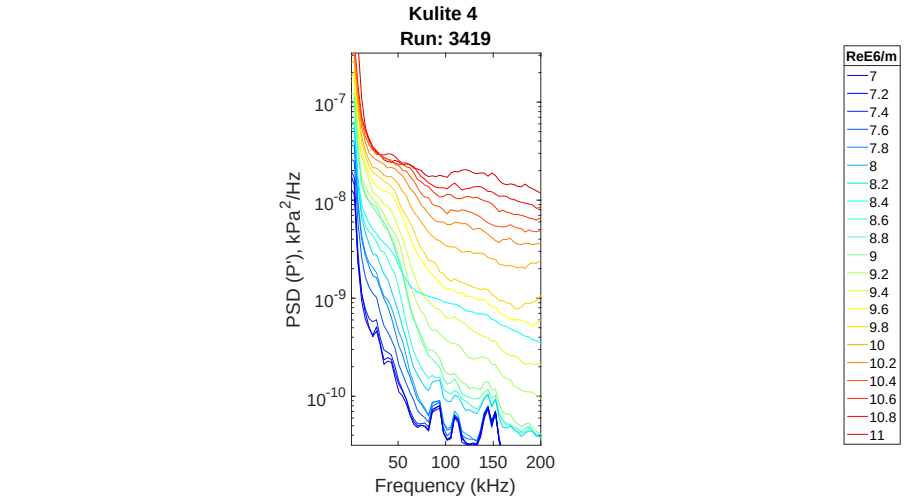

(a)

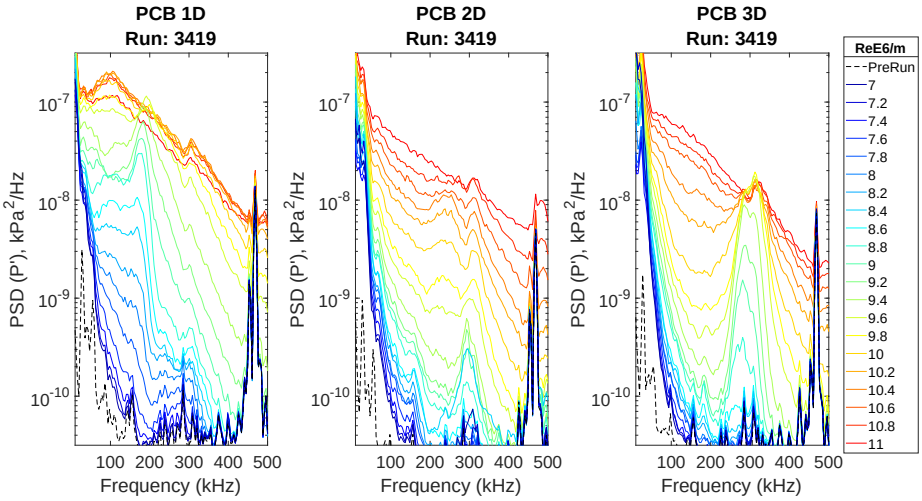

(b)

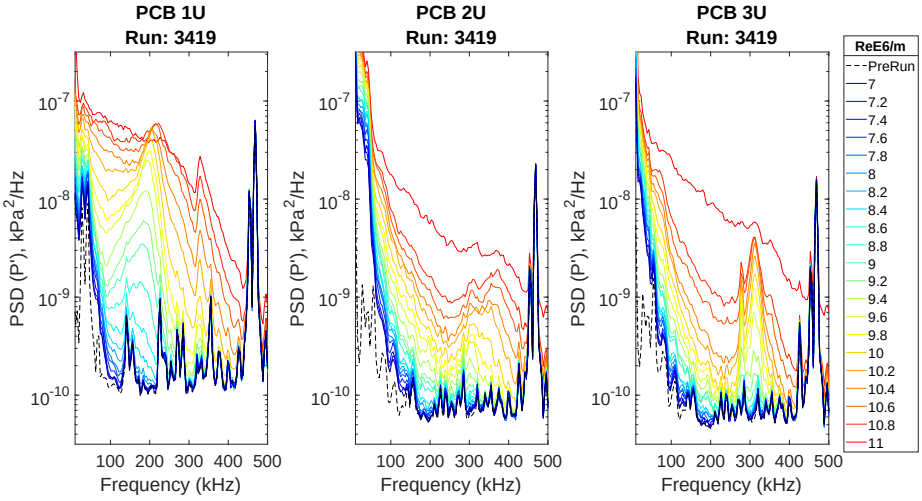

(c)

Figure D.41: Line plot PSD of fluctuating pressure for each transducer cluster Run 3419; M6QT. (a) Kulite 4, (b) Downstream shoulder PCBs, (c) Upstream shoulder PCBs.

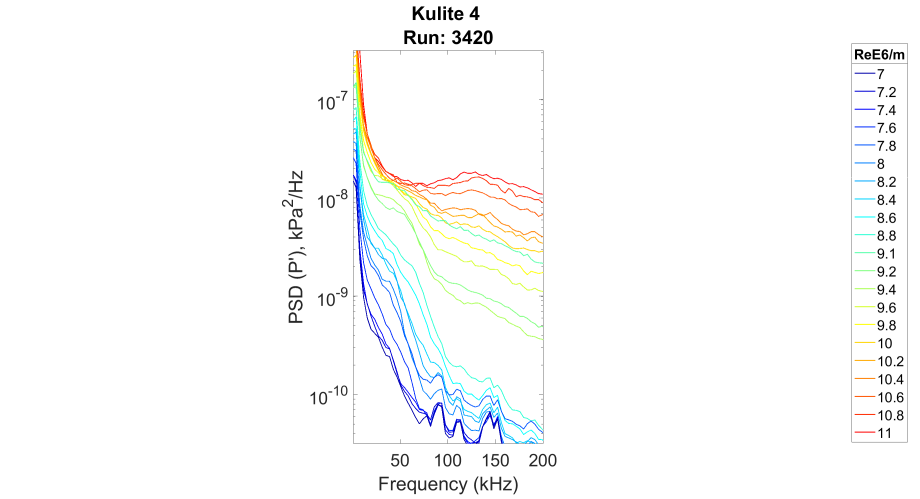

(a)

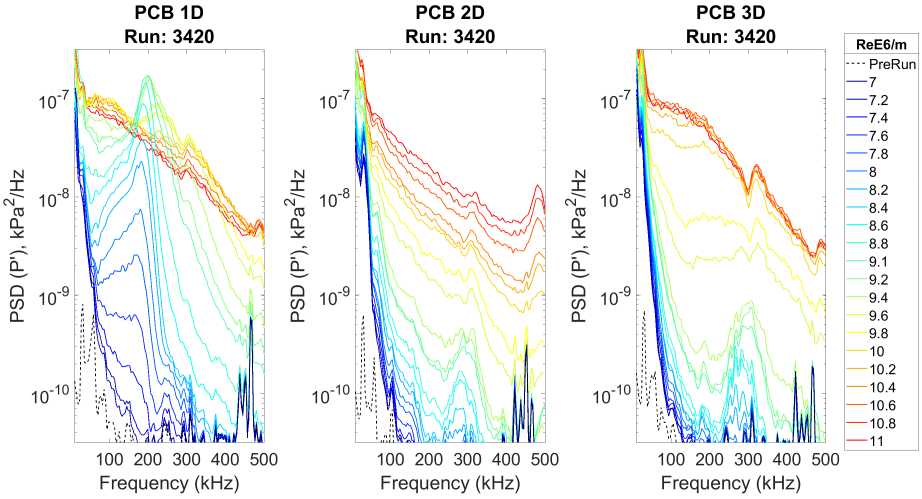

(b)

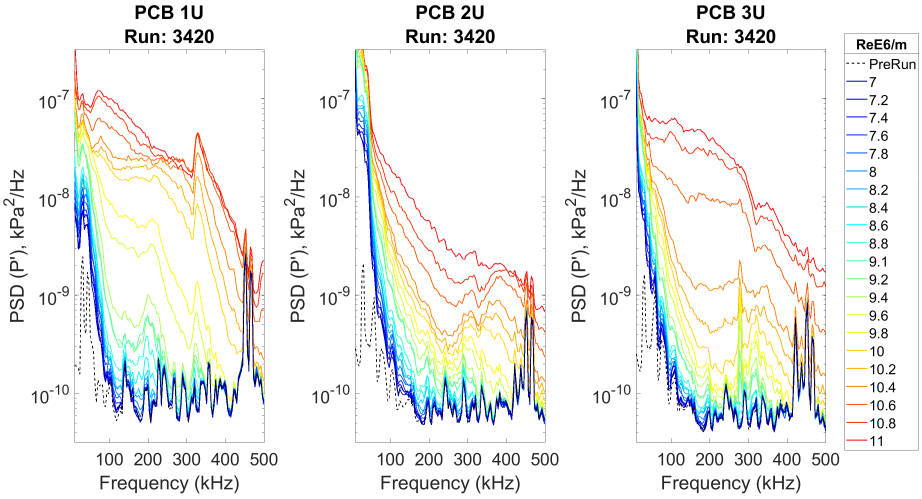

(c)

Figure D.42: Line plot PSD of fluctuating pressure for each transducer cluster Run 3419; M6QT. (a) Kulite 4, (b) Downstream shoulder PCBs, (c) Upstream shoulder PCBs.

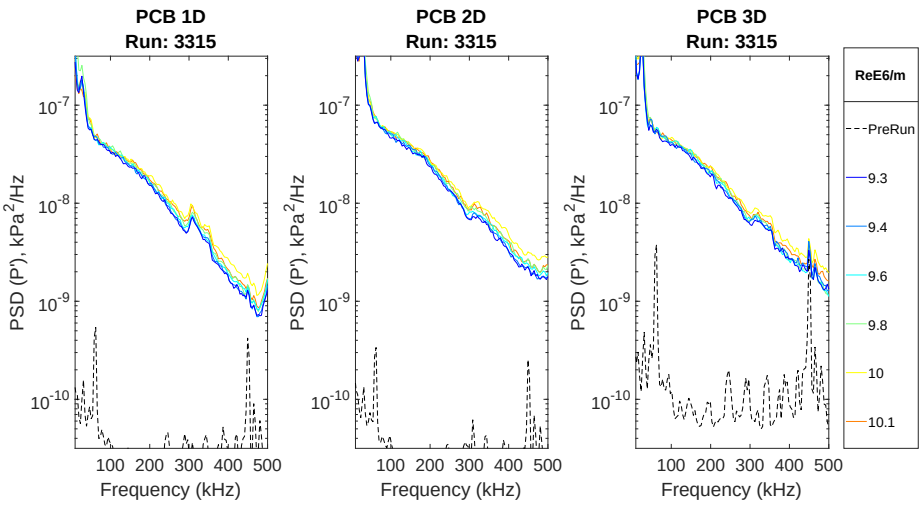

Figure D.43: Line plot PSD of fluctuating pressure for each transducer cluster Run 3419; M6QT noisy. (a) Kulite 4, (b) Downstream shoulder PCBs, (c) Upstream shoulder PCBs.

APPENDIX E

SAMPLE PROCESSING CODE

Sample MATLAB processing codes are presented below. Sec. E.1 gives the forward time central space finite difference code used for calculation of model temperature distribution. Sec. E.2 gives the roughness processing code used to analyze profilometer data. Sections of the roughness processing code was created using examples from Muralikrishnan & Raja (2009).

E.1 Heat Flux Calculation Code

```
function [q,T] = Neeldiff_Updated(k,cp,rho,Time,dt,len,surfacetemps,bc2 )
%% This function uses a forward time central space scheme to approximate the
    unsteady heat conduction equation to solve for the temperature
   distribution within the model and approximates heat flux via a 3 point
   approximation at the surface
%% inputs
% k, cp, rho, Material Properties (SI Units)
% Time,dt (seconds)
% len (meters) material thickness (Depth temperature bc2 is assumed)
% surfacetemps (Kelvin) surface temperature array as measured by IR camera
% bc2 depth constant temperature boundary condition

a=(k/(rho*cp)); % Compute a

% Set dx using s<= 5 rule for ftcs scheme stability
s=0.5;
dx=sqrt(a*dt/s);

%% Setup times and loop sizes for calculation
Maxtime = Time(end)-Time(1); %final time step
Jmax = round(len/dx+1);  % number of nodes into the surface
Maxex = Jmax-1;

jmap = Jmax-1;
AJM = jmap;

% Create array of X locations for plotting if desired
x=zeros(1,Maxex+1);
```

```
for i=2:Maxex+1
    x(i)=x(i-1)+dx;
end

%% initial and boundary conditions
T= NaN(size(surfacetemps,1),AJM+1);
%initial conditions (Sets T distribution at t=0 to backface temperature bc2)
for i = 2:(size(T,2)-1)
    T(1,i)= bc2;
end

% Boundary Conditions (Sets temperature boundary conditions to the measured
% surface temperature surfacetemps, and the backface temperature bc2)
for i= 1:size(T,1)
    T(i,1)=surfacetemps(i);
    T(i,end)=bc2;
end

%% FTCS Finite Difference Loop
t=zeros(1,size(T,1)); %(time vector for plotting)
for n=2:size(T,1) %loop time n
    for j=2:size(T,2)-1  %loop space j
        T(n,j)=s*T(n-1,j-1)+(1-2*s)*T(n-1,j) +s*T(n-1,j+1);
    end
    t(n) = t(n-1)+dt; % Build time vector (again for plotting)
end

% Compute heat flux at each of the points.
q=zeros(1,size(Time,2));
for i=1:size(Time,2)
    q(i)=-k*((-(3/2)*T(i,1)+2*T(i,2)-0.5*T(i,3))/(dx));
end

end
```

E.2 Roughness Processing Code

```
%%This code Analyzes roughness profiles form the Keyance Profilometer
   constructed at the TAMU FRL by Brian Crawford, Tom Duncan, and David West
%
%% House Keeping
clear
%close all
%% Read in roughness Scans
% Scan file in chosen directory
```

```
[filename,PathName] = uigetfile('*.dat','Select the MATLAB code file');
 oldfolder=cd(PathName);
full=load(filename);
cd(oldfolder)
[pathstr,name,ext] = fileparts(filename);
%% Filter settings
Medianbox = 5;   % Removes any spurious returns
order =int8(1);  % Order of least squares polynomial fit
lambdac =0.8;% cutoff wavelength in mm between roughness and "waviness"
%% Plotting?
plotflag=true;
%% Loop for each column in a scan
for ii=1:size(full,2)

raw_scan=full(:,ii); % Choose column containing desired scan
raw_scan(isnan(raw_scan))=[]; % Remove NaNs from edges of scan

%% Define x scale for scan
x=zeros(length(raw_scan),1);
for i = 1:length(raw_scan)
   x(i) = ((i-1)*25.4/(4.0*200.0*16.0));  %Scaling parameters set by
      profilometer traverse system
end

x0=x;
%% Median Filter 5 measurement window (Smooths oversampled Profilometer data
   ) Filter is smaller than laser head size
median_filtered=zeros(length(raw_scan),1);
for i=1:length(raw_scan)
    low = max(1,i-5);
    high = min(length(raw_scan),i+5);
    raw_scan(low:high);
    median_filtered(i)=median(sort(raw_scan(low:high)));
end

%% Least Squares polynomial (for form removal)
[fit,~,mu]=polyfit(x,median_filtered,order); % choose order for best fit
form = polyval(fit,x,[],mu); % create profile from fit

%% 0'th order Gaussian regression filter
dx=x(2)-x(1);
n=length(x); % sample length in points
z=median_filtered-form;
xg = (-lambdac:dx:lambdac)';  % x axis for generating filter
const = sqrt(log(2)/2/pi/pi);
```

```
w=zeros(length(raw_scan),1);
p=(1:1:n)';
for k=1:n % For each position k (center of the filter), generate the filter
    over the entire profile length
S = (1/sqrt(2*pi)/const/lambdac).*exp(-0.5*((k-p)*dx/const/lambdac).^2);  %
    generate weighting function
SMOD = S/sum(S);     % normalize filter to unit sum
w(k,1) = sum(SMOD.*(z));  % sum of products (this step replaces the
    convolution of a standard Gaussian filter)
end

%% Chop edges (Often the filter has relatively large error near the edges of
     the profile which skew the results.
chop = round(0/dx);
rough=(median_filtered-form)-w;
rough(end-chop:end)=[];
rough(1:chop)=[];
w(end-chop:end)=[];
w(1:chop)=[];

median_filtered(end-chop:end)=[];
median_filtered(1:chop)=[];
x(end-chop*2:end)=[];
form(end-chop:end)=[];
form(1:chop)=[];


%% Roughness parameters
% Roughness parameters can be computed for waviness and roughness profiles
% The calculations preformed adhere to
[Ra, Rq, Rp, Rv, Rt,Rzi,Rz] = myAmplitudeParameters(rough, lambdac);
[Wa, Wq, Wp, Wv, Wt,Wzi,Wz] = myAmplitudeParameters(w,lambdac);

%% PSD of raw profile
l=max(x); % length of the profile
n=l/dx;
zf=fft((median_filtered));     % perform FFT
PSD_raw = dx/n*(abs(zf).^2);
j=(2:1:floor(n/2)+1)'; % generate the wavelength array
lambda=n*dx./(j-1);    % generate the wavelength array

%% PSD of roughness profile
zf=fft(rough);
PSD_rough = dx/n*(abs(zf).^2);% perform FFT
Roughpsd= (PSD_rough(2:floor(n/2)+1,1));
```

```
%% PSD of waviness profile
zf=fft(w); % perform FFT
PSD_Wavy = dx/n*(abs(zf).^2);

%% Plotting
if plotflag==true
figure
%roughness profiles
subplot(3,2,1)
plot(x0,raw_scan)
hold on
plot(x+dx*chop,median_filtered)

hold on
plot(x+dx*chop,form)
title('Raw Scan Profile')
xlabel('Distance (mm)')
ylabel('Amplitude (\mum)')
legend ('raw','Median Filtered','Least Squares')


subplot(3,2,3)
title('Waviness Profile')
plot(x,median_filtered-form,'g',x,w,'r');
xlabel('Distance (mm)');
ylabel('Amplitude (\mum)');

subplot(3,2,5)
title('Roughness Profile')
plot(x,rough-mean(rough));
 Roughness = (median_filtered-form)-w;


subplot(3,2,2)
    plot(lambda,PSD_raw(2:floor(n/2)+1,1)); % plot half of the FFT array
    title('Raw PSD')
    xlabel('Distance (mm)')
    ylabel('PSD (\mum^3)')
    subplot(3,2,4)
    plot(lambda, PSD_Wavy(2:floor(n/2)+1,1));% % plot half of the FFT array
    title('Waviness profile PSD')
    xlabel('Distance (mm)')
    ylabel('PSD (\mum^3)')
    subplot(3,2,6)
    plot(lambda,PSD_rough(2:floor(n/2)+1,1));
```

```
    xlim([0,(lambdac+1)])
    title('Roughness PSD')
    xlabel('Distance (mm)')
    ylabel('PSD (\mum^3)')
end

Average_roughness = Ra;
RMS_roughness = Rq;

data{ii} = struct('filename',filename,...
                  'x',x,...
                  'Lambdacutoff',lambdac,...
                  'Scan_Number',ii,...
                  'form',form,...
                  'median_filtered',median_filtered,...
                  'Waviness',w,...
                  'Rough',rough,...
                  'Ra',Ra,...
                  'Rq',Rq,...
                  'Rz',Rz,...
                  'Rt',Rt,...
                  'Rv',Rv,...
              'Raw',raw_scan,...
              'fftlambda',lambda,...
              'Roughpsd',Roughpsd);

end
[pathstr,name,ext] = fileparts(filename);
save(strcat(name,'.mat'),'data');
```